

Narrow-linewidth Si/III-V lasers: A study of laser dynamics and nonlinear effects

Thesis by

Yaakov (Yasha) Vilenchik

In Partial Fulfillment of the Requirements
for the Degree of
Doctor of Philosophy



California Institute of Technology
Pasadena, California

2015

(Defended June 4, 2015)

© 2015

Yaakov (Yasha) Vilenchik

All Rights Reserved

Acknowledgments

These last few years at Caltech have been a time of immense personal and intellectual growth for me. I would like to take the opportunity to thank the many people I've learned from and with.

First and foremost, I would like to thank and acknowledge my advisor, Professor Amnon Yariv. Professor Yariv provided me with the opportunity to work at the forefront of science, and has succeeded in convincing me that nothing is impossible. His guidance has shaped me into a researcher who strives to combine a top-level scientific bird's-eye-view, with a down-to-earth understanding of technical challenges.

I deeply appreciate the time and effort of my thesis committee members, Professors Kerry Vahala, Oskar Painter and Andrei Faraon. This committee is truly the “dream team” for my thesis, and I am very privileged to have them in my corner.

I would like to thank Professor Bruno Crosignani for his support and encouragement over the years. His unique approach to problem-solving in all fields — from physics to politics and philosophy — has deeply enriched me and made me a better researcher and critical thinker.

I cannot thank enough the members of the Yariv group. I couldn't have done any of the work presented in this thesis without them. Scott Steger has guided me through the III-V fabrication process, and played a huge role in the fabrication of the lasers used in this thesis. Many of the important insights in this work are a result of our long discussions. Christos Santis has always been a model for hard-work and perfectionism in the clean-room. His contribution was crucial both in the conception of some of the initial ideas, and the implementation of the high-Q silicon resonators that were used in this work. I would also like to thank Naresh Satyan, whom I always sought for advice,

and his input was crucial time after time. Our collaboration has yielded an order of magnitude improvement in both the characterization setup, and my experimental skills. I must thank Dongwan Kim for his help in the fabrication effort, and for our many conversations which helped me to constantly improve my understanding of every aspect of this project. I would also like to thank Mark Harfouche for his frequent advice, that always provided me with new insights. This project benefited a lot from his wide range of expertise, that never ceased to amaze me. Other members of the Yariv group — Jacob Sendowski, Arseny Vasilyev, Sinan Zhao, Xiankai Sun, Hsi-Chun Liu, Avi Zadok, Paula Popescu and Marilena Dimotsantou — have all contributed to this work, each in their unique way, and for that I am thankful. A special thanks goes to group-members in the broader sense, Reg Lee and George Rakuljic, for their useful input and advice.

The staff members at KNI were a source of both knowledge and help. The support and advice I got from Guy DeRose, Melissa Melendes and Steven Martinez was indispensable. I would like to thank Christy Jenstad and Mabel Chik for helping me to navigate life and research at Caltech. I would especially like to thank Connie Rodriguez, who enabled me to do science, without needing to worry about the immense amount of paperwork. She made sure that my environment never got too cold, too warm or too loud — both literally and metaphorically.

The Israeli community at Caltech has provided an important support net, and helped me transition smoothly to a new country and culture. My time at Caltech would not have been as vibrant without them. I also thank Chabad of Pasadena and the Pasadena Jewish Community for enriching my spiritual life here.

Last, but absolutely not least, I would like to thank my family. My parents, who have supported me over the years, and encouraged me to seek knowledge and happiness. My children, Daniel and Mattan, who were *the* source of joy and pride in my life, and helped me keep my priorities straight. Most of all I would like to thank my partner in life, Neta, who has been an amazing pillar of support and strength in my life. She even helped proofread this entire work — a true test of spousal dedication. Thank you!

Abstract

Narrow-linewidth lasers play an important role in a wide variety of applications, from sensing and spectroscopy to optical communication and on-chip clocks. Current narrow-linewidth systems are usually implemented in doped fibers and are big, expensive, and power-hungry. Semiconductor lasers compete favorably in size, cost, and power consumption, but their linewidth is historically limited to the sub-MHz regime. However, it has been recently demonstrated that a new design paradigm, in which the optical energy is stored away from the active region in a composite high-Q resonator, has the potential to dramatically improve the coherence of the laser.

This work explores this design paradigm, as applied on the hybrid Si/III-V platform. It demonstrates a record sub-KHz white-noise-floor linewidth. It further shows, both theoretically and experimentally, that this strategy practically eliminates Henry's linewidth enhancement by positioning a damped relaxation resonance at frequencies as low as 70 MHz, yielding truly quantum limited devices at frequencies of interest.

In addition to this empirical contribution, this work explores the limits of performance of this platform. Here, the effect of two-photon-absorption and free-carrier-absorption are analyzed, using modified rate equations and Langevin force approach. The analysis predicts that as the intra-cavity field intensity builds up in the high-Q resonator, non-linear effects cause a new domain of performance-limiting factors. Steady-state behavior, laser dynamics, and frequency noise performance are examined in the context of this unique platform, pointing at the importance of nonlinear effects.

This work offers a theoretical model predicting laser performance in light of non-

linear effects, obtaining a good agreement with experimental results from fabricated high-Q Si/III-V lasers. In addition to demonstrating unprecedented semiconductor laser performance, this work establishes a first attempt to predict and demonstrate the key impact of nonlinear effects on silicon-based lasers.

Contents

Acknowledgments	iii
Abstract	v
1 Introduction	1
1.1 Narrow-linewidth semiconductor lasers	2
1.2 Laser sources for coherent communication	5
1.3 Linear and non-linear performance limiting factors	6
2 Hybrid Si/III-V as a platform for narrow linewidth	9
2.1 Noise in conventional semiconductor lasers	10
2.2 Hybrid Si/III-V platform	14
2.3 Noise reduction in hybrid Si/III-V	16
2.3.1 High-Q silicon resonator	16
2.3.2 Modal gain and loss	17
2.3.2.1 General description	18
2.3.2.2 The spacer lasers	20
2.3.3 Schawlow-Townes linewidth	21
3 Non-linear effects in hybrid Si/III-V	24
3.1 Two-photon-absorption in silicon	26
3.2 Free-carrier-absorption	28
3.2.1 General methodology	30
3.2.2 Bulk recombination	30

3.2.3	Surface recombination	32
3.2.4	Carrier diffusion	34
3.2.5	Effective carrier lifetime	35
4	Modified rate equations	40
4.1	Flat-mode approximation	40
4.2	Working with densities or total numbers?	42
4.3	Pump	43
4.4	Linear loss	44
4.5	Gain	45
4.5.1	The quantum-well: a two or three dimensional creature?	45
4.5.2	Active confinement factor	46
4.5.3	Material gain	47
4.6	Spontaneous emission	47
4.6.1	Model for the population inversion factor	48
4.7	Two-photon-absorption	49
4.8	Spontaneous recombination in the QW	50
4.9	Rate equation for free-carriers in silicon	51
4.10	Free-carrier-absorption	52
4.11	Total loss rate	52
4.12	The modified rate equations	53
5	Steady-state operation - Theoretical analysis	55
5.1	Steady-state carrier density in silicon	55
5.2	Gain saturation	56
5.3	Threshold current	56
5.4	Output power	58
5.4.1	Wall-plug efficiency	58
5.4.2	L-I curve	59
5.4.3	Slope efficiency	61
5.5	Schawlow-Townes linewidth	64

6	Steady-state operation - Experimental results	68
6.1	Threshold current	69
6.2	L-I curves	71
6.3	Schawlow-Townes noise floor	73
7	Dynamic operation - Theoretical analysis	77
7.1	Small-signal analysis	77
7.2	Intensity modulation response	79
7.2.1	Analytical investigation	81
7.2.1.1	Low nonlinear loss regime:	82
7.2.1.2	High nonlinear loss regime:	83
7.2.2	Numerical investigation	84
7.3	Frequency modulation response	86
7.3.1	Effect of Quantum Well carriers	89
7.3.1.1	Gain compression	89
7.3.1.2	Henry's alpha parameter	90
7.3.1.3	Frequency modulation response curve	91
7.3.2	The effects of free-carriers in silicon	92
7.3.2.1	Plasma effects in silicon	93
7.3.3	The total frequency chirp	94
8	Dynamic operation - Experimental results	99
8.1	Intensity modulation response	99
8.2	Frequency modulation response	105
9	Noise performance - Theoretical analysis	110
9.1	Methodology - Langevin noise sources	111
9.2	Source of noise - fluctuations	112
9.2.1	Photon density	116
9.2.2	Carriers in the quantum wells	119
9.2.3	Free-carriers in silicon	120

9.2.4	Temperature	122
9.3	Frequency noise	124
9.3.1	Spontaneous emission	125
9.3.2	Henry's linewidth enhancement	126
9.3.3	Noise due to the plasma effect in silicon	127
9.3.4	Noise due to the thermo-optic effect in silicon	131
9.3.5	Total noise spectrum	133
10	Noise performance - Experimental results	138
11	Conclusion	144
11.1	Summary of key results	144
11.2	Future directions	146
	Bibliography	149
A	Fabrication process	165
A.1	Silicon processing	165
A.1.1	Chrome deposition	165
A.1.2	Lithography	168
A.1.3	Etch	168
A.1.4	Oxidation	169
A.2	Wafer bonding	169
A.2.1	Surface treatment	170
A.2.2	Bonding	170
A.2.3	Substrate removal	170
A.3	III-V processing	172
A.3.1	Ion implantation	172
A.3.2	P-metal deposition	172
A.3.3	Mesa formation	173
A.3.4	N-Metal deposition	175
A.3.5	Cleaving	176

B	Characterization setups	177
B.1	Mounting and probing the lasers	178
B.1.1	Mounting of laser bars	178
B.1.2	Thermal management	178
B.2	L-I curves	179
B.2.1	CW excitation	179
B.2.2	Pulsed excitation	179
B.3	Intensity modulation response	180
B.3.1	Setup and equipment	180
B.3.2	Calibration and measurement procedures	181
B.3.2.1	Photodetector response	181
B.3.2.2	Driving circuitry response	181
B.3.2.3	Calculating the small-signal current	182
B.3.2.4	Delay compensation	183
B.4	Frequency modulation response	183
B.4.1	Setup and equipment	183
B.4.2	Calibration and measurement procedure	185
B.4.2.1	Balancing photodetectors	185
B.4.2.2	Photodetector response	186
B.4.2.3	Voltage swing	186
B.4.2.4	Delay compensation	188
B.4.2.5	Measurement procedure	188
B.4.2.6	Calculating the frequency response from the measurement	189
B.5	Frequency noise spectrum measurement	191
B.5.1	Setup and equipment	192
B.5.2	Calibration and measurement procedures	192
B.5.2.1	Balanced PD and amplifier	192
B.5.2.2	Measurement procedure	194
B.5.2.3	Calculating the noise spectrum from the measurement	196

List of Figures

1.1	Constellation diagrams. (a) Binary Amplitude Phase Shift Keying (b) 16 Quadrature Amplitude Modulation.	5
1.2	Phasor diagram demonstrating the effect of a spontaneous emission event	8
2.1	Hybrid Si/III-V laser schematics	15
2.2	Band structure of the mode-gap resonator. The parabolic potential-well supports one optical mode	17
2.3	(a) Quality factor of hybrid Si/III-V composite resonator (b) Mode profile of a traditional III-V laser (c) Profile of a high-Q hybrid Si/III-V laser	19
2.4	Confinement in III-V and in QWs vs. spacer thickness	21
3.1	Schematic description of two-photon-absorption	25
3.2	Model for FCA in silicon. Model #1 by [58, 101]. Model #2 by [70]	29
3.3	Waveguide structure used for analysis of FCA	30
3.4	Model for the ambipolar diffusion coefficient of silicon	35
3.5	Carrier density profile for several different surface recombination profiles	36
3.6	Effective lifetime of carrier in silicon for $S=1\frac{cm}{sec}$	37
3.7	Effective lifetime of carriers in Si (low photon excitation regime)	38
4.1	Flat mode approximation for the optical mode and the electron density	42
4.2	Symmetrical quasi-Fermi level model	49

4.3	Comparison between different loss mechanisms vs. photon density. $Q_{si} = 10^6$, typical absorption in III-V is assumed (i.e., 10cm^{-1}), confinement factor in III-V of 1% and effective lifetime of carriers in Si of $\tau_{eff} = 30\text{ns}$.	53
5.1	Threshold current vs. confinement factor in III-V for different quality factors of the Si resonator	57
5.2	Efficiency (left axis) and total Q (right axis) vs. mirror Q. $Q_{si}^{int} = 10^6$; $\eta_i = 1$; $\frac{I}{I_{tr}} = 10$ (a) 30nm spacer (b) 100nm spacer (c) 150nm spacer .	60
5.3	Efficiency of different spacer design vs. total-Q	61
5.4	L-I curves for different values of confinement factors with and without nonlinear effects for $Q_{si}^{int} = 10^6$ (a) spacer 150nm (b) spacer 100nm (c) spacer 30nm	62
5.5	Normalized slope efficiency at $I = 4 \cdot I_{th}$	63
5.6	Schawlow-Townes linewidth vs. confinement in III-V for different silicon resonators, with and without nonlinear effects at $I = 4 \cdot I_{th}$	65
5.7	Impact of nonlinear effects on linewidth for changing quality factors. Calculated at $I = 5 \cdot I_{th}$	66
5.8	Impact of nonlinear effects on linewidth for changing pump current. Calculated at $I = 5 \cdot I_{th}$ for $Q_{Si} = 10^6$	66
6.1	Threshold current for different spacer designs. (a) 1560nm lasers (b) 1575nm lasers	70
6.2	Normalized L-I curves for three spacer designs. The non-normalized output powers at $I=150\text{mA}$ are: 0.89mW, 0.62mW, and 10.2mW for the 200nm, 100nm, and 30nm spacers, respectively	72
6.3	L-I curves of the 150nm spacer. (a) For varying stage temperatures (b) In pulsed operation (duty cycle = 1%)	74
6.4	Schawlow-Townes linewidth vs current offset from threshold for the three spacer lasers. The dotted lines represent expected $1/P$ dependence . .	75

7.1	Intensity modulation response curves with and without nonlinear effects. $I = 4I_{th}$, $Q_{Si} = 10^6$ (a) 30nm spacer (b) 100nm spacer (c) 150nm spacer	85
7.2	Intensity modulation response curves for different spacer thicknesses. $I = 4I_{th}$, $Q_{Si} = 10^6$ (a) amplitude (b) phase	87
7.3	Intensity modulation response curves for different spacer thicknesses. $I = 10I_{th}$, $Q_{Si} = 10^6$ (a) amplitude (b) phase	88
7.4	Frequency modulation response due to quantum well electrons for different values of spacer thickness. $\alpha_H = 7$, $I = 2 \cdot I_{th}$, $Q_{Si} = 10^6$	91
7.5	Frequency modulation response due to free carriers in silicon for different values of spacer thickness. $\alpha_H = 7$, $I = 2 \cdot I_{th}$, $Q_{Si} = 10^6$	94
7.6	Frequency modulation response for several different spacer thicknesses, with and without nonlinear effects for $\alpha_H = 7$, $I = 2 \cdot I_{th}$, $Q_{Si} = 10^6$. (a) 30nm spacer (b) 100nm spacer (c) 150nm spacer	95
7.7	Frequency modulation response for several different spacer thicknesses for $\alpha_H = 7$, $I = 2 \cdot I_{th}$, $Q_{Si} = 10^6$	96
7.8	Effect of pump current on frequency modulation response for two different spacer thicknesses $\alpha_H = 7$, $I = 2 \cdot I_{th}$, $Q_{Si} = 10^6$. (a) 30nm spacer (b) 150nm spacer	97
8.1	Intensity modulation response of 30nm spacer laser (Chip 1, bar 5, Slot 1, device 7) for different bias currents. 3.5mA current modulation. Measured with New-Focus 1544B photodetector and HP 8722C RF network analyzer (a) Normalized magnitude (b) Phase	101
8.2	Intensity modulation response of 100nm spacer laser (chip 1, bar 1, slot 2, device 19) for different bias currents. 6mA current modulation. Low frequency response (<50MHz) was measured using New-Focus 1544B photodetector and Agilent 4395A network analyzer. High frequency response (>50 MHz) was measured using HP 8722C RF network analyzer (a) Normalized magnitude (b) Phase	102

8.3	Intensity modulation response of 150nm spacer laser (chip 1, bar 1, slot 2, device 19) for different bias currents. 3.3mA current modulation. Measured using New-Focus 1544B photodetector and Agilent 4395A network analyzer (a) Normalized magnitude (b) Phase	103
8.4	Intensity modulation response (magnitude in a.u.) of different spacer lasers for pump current offset of 40mA.	104
8.5	Frequency modulation response of 30nm spacer laser (Chip 1, bar 5, Slot 1, device 7) for different bias currents. 0.1mA current modulation. Measured with Optilab BPR-20-M balanced photodetector and HP 8722C RF network analyzer, using MZI with FSR = 7.06GHz	105
8.6	Frequency modulation response of 100nm spacer laser (Chip 1, bar 1, Slot 2, device 19) for different bias currents. 35nA current modulation. Measured with Optilab BPR-20-M balanced photodetector MZI with FSR = 1.56GHz. Low frequencies (<500 MHz) were measured using Agilent 4395A network analyzer and high frequencies (>500MHz) using HP 8722C analyzer. Curves from the two analyzers are plotted together without any additional post-processing (stitching)	106
8.7	Frequency modulation response of 150nm spacer laser (Chip 1, bar 1, Slot 2, device 19) for different bias currents. 0.1mA current modulation. Measured with Optilab BPR-20-M balanced photodetector and Agilent 4395A network analyzer, using MZI with FSR = 1.56GHz	106
8.8	Frequency modulation response of different spacer lasers for pump current offset of 50mA.	107
9.1	Particle reservoir picture of the system	113
9.2	PSD of the photon density (150nm spacer, $Q_{Si} = 10^6$, $I = 4I_{th}$) (a) Comparison of conventional terms (terms which don't involve TPA-generated free-carriers in Si) (b) Comparison of these conventional terms to free-carrier related terms	118

9.3	Comparison of the different terms of the PSD of QW-carrier density (150nm spacer, $Q_{Si} = 10^6$, $I = 4I_{th}$)	119
9.4	Noise spectrum of silicon carrier density for shot-noise model (150nm spacer, $Q_{Si} = 10^6$, $I = 4I_{th}$)	120
9.5	Frequency noise due to spontaneous emission and QW carrier density fluctuations using Langevin shot-noise model. $Q_{Si} = 10^6$, $I = 4I_{th}$, $\alpha_H = 3$	127
9.6	The effect of Si-carrier fluctuation on the frequency noise spectrum: Effective recombination model vs recombination-diffusion model. 150nm Spacer, $Q_{Si} = 10^6$, $I = 2I_{th}$	129
9.7	Frequency noise spectrum due to Si carrier fluctuations for different pump currents. 150nm Spacer, $Q_{Si} = 10^6$	130
9.8	Frequency noise spectrum due to Si carrier fluctuations for different spacers. $Q_{Si} = 10^6$, $I = 2 \cdot I_{th}$	131
9.9	The different components of the frequency noise spectrum due to temperature fluctuations (150nm spacer, $Q_{Si} = 10^6$, $I = 2 \cdot I_{th}$)	133
9.10	Frequency noise related to temperature fluctuations for different spacer designs ($Q_{Si} = 10^6$, $I = 2 \cdot I_{th}$)	134
9.11	The different components of the total frequency noise spectrum ($Q_{Si} = 10^6$, $I = 2 \cdot I_{th}$). (a) 150nm spacer (b) 100nm spacer (c) 30nm spacer	135
9.12	Predicted frequency noise spectrum of different spacer designs ($Q_{Si} = 10^6$, $I = 2 \cdot I_{th}$)	136
9.13	Predicted frequency noise spectrum for the 150nm spacer designs at different pump powers ($Q_{Si} = 10^6$)	136
10.1	Effect of BOA amplification on frequency noise spectrum. All data was taken with the same 150nm spacer at constant laser pump current. Only BOA pump current changed from curve to curve	139
10.2	Frequency noise of 150nm spacer, amplified using BOA and EDFA	140

10.3	Frequency noise spectrum vs. pump current for different spacer designs (a) 150nm spacer (threshold @ 66mA) (b) 100nm spacer (threshold @ 28mA) (c) 30nm spacer (threshold @ 55mA)	141
10.4	Frequency noise spectrum for different spacer designs at $I - I_{th} = 33\text{mA}$	142
A.1	Spacer laser device Schematics	166
A.2	Flow diagram of the silicon processing steps	167
A.3	Flow diagram of the III-V processing steps	172
A.4	SEM images of mesa formed using the two mask process (a) Entire mesa and Si waveguide (b) Sidewalls of mesa and InGaAs layers (c) Etch and under-cut of the QW layer	175
B.1	Schematics of L-I curve characterization setup	179
B.2	Schematics of the experimental setup used for intensity modulation re- sponse measurements	180
B.3	Measured response of NF1544B photodetector. The PD response was subtracted from measured laser response	182
B.4	Schematics of the experimental setup used for frequency modulation response measurements	184
B.5	Schematics of the electronic feedback PCB used to lock the MZI to quadrature	185
B.6	Response curves of balanced PDs (a) New Focus 1817 (b) Optilab BPR 20-M	187
B.7	Schematics of the experimental setup used for frequency noise spectrum measurements	193
B.8	Intensity noise measured for different input powers by the balanced pho- todetector (Optilab BPM-20)	194
B.9	Intensity noise vs calculated dark+shot noise for different input power to the balanced PD (a) 0.25mW per detector (b) 0.5mW (c) 1 mW . .	195

List of Tables

4.1	Parameters used for rate equations	54
A.1	Device dimensions. Notations is based on Figure A.1	166
A.2	III-V wafer structure	167
A.3	Conditions of Cr evaporation	168
A.4	Steps for E-Beam lithography	168
A.5	ICP etch steps and conditions	169
A.6	Oxidation/Anneal steps and conditions	170
A.7	Steps and conditions for wafer bonding	171
A.8	Substrate removal steps and conditions	171
A.9	Parameters used for ion implantation	173
A.10	Steps and conditions used to deposit P metal stack	174
A.11	Steps and conditions for lift-off photo-lithography	174
A.12	steps and conditions used to form the mesa	175
A.13	Steps and conditions used for N-metal deposition	176

Chapter 1

Introduction

For decades, semiconductor lasers have been considered reliable, inexpensive everyday light sources. However, they lack high quality coherence properties. On the other hand, narrow-linewidth lasers, i.e., fiber or solid-state devices, have been considered exotic, bulky, and expensive. A new technology — the hybrid Si/III-V platform [75]; and a new laser design paradigm [106], were recently combined to demonstrate a record narrow-linewidth semiconductor laser [88]. This demonstration might be the first milestone towards the penetration of semiconductor lasers to the narrow-linewidth laser industry, with a potentially dramatic impact on the narrow-linewidth industry.

Work pioneered by John Bowers et al. (i.e., [76, 75, 113, 34]) has enabled the integration of direct-bandgap semiconductor devices with a low-loss material, mainly silicon. The work by Amnon Yariv et al. (i.e., [132, 88]) used this platform to demonstrate a hybrid Si/III-V laser with 18 KHz white-noise floor linewidth. The mechanism of noise reduction was further developed by Yariv et al., who portrayed a path towards further reduction [106]. However, experimental results in that work were inconclusive, and did not overcome the ~ 18 KHz barrier.

The work presented in this thesis is a direct continuation of the work by Steger and Christos Santis [89]. It relies on the design and fabrication of high-Q Si resonators [88], and on the linewidth reduction approach by modal engineering and the control of spontaneous emission into the mode [106]. The novelty and contribution of this work is three-fold:

1. It provides a conclusive experimental validation for the new design approach - experiments demonstrating a record sub-KHz linewidth are presented in this work for the first time. A conclusive linewidth reduction trend is also presented, portraying the path for further improvement.
2. A theoretical analysis and experimental results of laser dynamics of this unique platform are also presented in this work for the first time. Intensity and frequency modulation response measurements were performed, showing unique characteristics of the hybrid platform, i.e., relaxation resonance frequencies as low as 100 MHz.
3. It provides a theoretical model and experimental validation of the impact of nonlinear effects, i.e., two-photon-absorption and the attendant free-carrier-absorption on laser performance. It is shown that as the intra-cavity intensity builds up these nonlinear processes limit the achievable linewidth and alter the laser dynamics. Others have shown that free-carrier-absorption in Si affects device performance [85, 57, 37, 112, 133]. However, this is the first time these effects are considered and experimentally demonstrated in the context of high-Q Si-based lasers. The analysis in this work provides a limit to the achievable device performance, and also offers directions to overcome these limits in silicon.

1.1 Narrow-linewidth semiconductor lasers

A laser is a light source that emits coherent radiation. The temporal coherence of a laser refers to the spectral purity of the electromagnetic field emitted by it. A related concept — the spatial coherence — refers to the correlation between the laser field at different points in space. The spatial coherence properties of a laser allow for tight beam focusing, as well as low-divergence beams. A convenient metric to quantify the coherence of a laser device is by the width of the spectral line of the electromagnetic field, also known as the linewidth. In this work, the use of this metric will imply a single mode laser, unless stated otherwise.

Semiconductor lasers (SCLs), in the context of this work, are high-coherence light sources constructed using direct band-gap semiconductor materials. These lasers can be pumped either optically or electrically. However, the main advantage of SCLs is their ability to be pumped electrically using standard current sources. For this reason, in the remainder of this work I will assume electrical pumping whenever SCLs are described. SCLs have many other advantages: they are lightweight, efficient in converting electrical energy into optical energy, and inexpensive, as well as have a small footprint. They can also be easily integrated with other electronic components to allow for control and manipulation of the laser field. However, the coherence properties of SCLs are usually inferior in comparison to other laser platforms, such as fiber lasers, solid-state lasers or gas lasers. The linewidth of SCLs is historically limited to the sub-MHz regime. The reasons for that will be described in detail in Chapter 2.

Narrow-linewidth lasers have been used in many fields. High-coherence light sources are so useful since there are many systems in which the narrow-linewidth sources translate directly into high-resolution. For example, in an interferometric ranging experiment high coherence translates into superior depth resolution. In spectroscopy, narrow-linewidth operation results in higher spectral resolution. In atomic clocks that are based on coherent population trapping (CPT), low-noise operation is essential for good temporal resolution of the clock.

To understand the basis behind this linewidth-resolution relationship it is useful to refer to a simple experiment: the Mach-Zehnder interferometer (MZI). Consider a laser beam (assume perfect spatial coherence for simplicity) that is split into two arms. One arm is delayed by a time delay of τ compared to the other, and the two beams are then combined and detected on a photodetector (PD). Assume the detected signal is measured for a time period much longer than the coherence time, such that the signal Fourier-limited width is much narrower than the linewidth of the laser. Neglecting amplitude noise, the complex laser field can be expressed as:

$$E(t) = Ae^{j(\omega t + \delta\phi(t))} \quad (1.1)$$

The power at the PD can be written as (assume equal power and polarization in both arms):

$$P(t) = \frac{1}{4}|E(t) + E(t - \tau)|^2 = \frac{A^2}{2}(1 + \cos(\omega\tau + \delta\phi(t) - \delta\phi(t - \tau))) \quad (1.2)$$

If we assume for simplicity that the constant phase term is biased such that $\omega\tau = 2\pi m + \frac{\pi}{2}$, where m is an integer, we get

$$P(t) \approx \frac{A^2}{2}(1 + \Delta\phi(t, \tau)) \quad (1.3)$$

where we have defined

$$\Delta\phi(t, \tau) = \delta\phi(t) - \delta\phi(t - \tau) \quad (1.4)$$

and assumed $\Delta\phi(t, \tau) \ll \pi$. The power spectral density (PSD) of the stationary and stochastic phase change term $\Delta\phi$ is related to the PSD of the laser frequency noise $W_{\dot{\phi}}$ by [78]:

$$W_{\Delta\phi} = W_{\dot{\phi}} \frac{\sin^2(\omega\tau/2)}{(\omega/2)^2} \quad (1.5)$$

Assuming a white frequency noise, the phase change can be found analytically by integration [78]:

$$\langle \Delta\phi(t, \tau)^2 \rangle = W_{\dot{\phi}}\tau \quad (1.6)$$

It can be seen from 1.6 and 1.5 that the noise at the PD output scales with the laser frequency noise. If, for example one wishes to detect small changes of the optical delay τ , the laser's noise term will eventually limit the achievable resolution. The same line of arguments can be made for many other systems, relating laser linewidth to resolution in the broader sense. Implementation of such high resolution devices using semiconductors can potentially bring these devices to the hand-held consumer electronics industry, such as cell-phones.

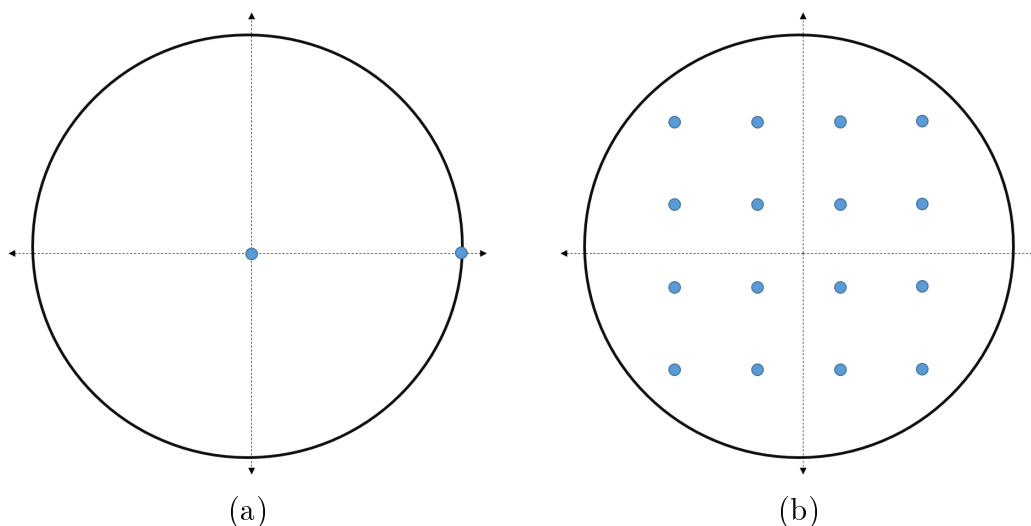


Figure 1.1: Constellation diagrams. (a) Binary Amplitude Phase Shift Keying (b) 16 Quadrature Amplitude Modulation.

1.2 Laser sources for coherent communication

Semiconductor lasers have been driving the optical communication industry for several decades. Direct (intensity) modulation is the most common modulation scheme. However, as the demand for data increases rapidly, phase modulation schemes gain popularity. Among other advantages, phase modulation scheme can pack more bits per symbol, hence increasing the data content efficiency of the channel. The concept of high data content per symbol is demonstrated in Figure 1.1. The bit error rate will be a function of the phase noise accumulated within one modulation period [134] and the distance between two consecutive states on the phasor diagram. In the realm of communication networks, this puts a linewidth requirement for the laser source, for a given modulation scheme.

Another way to increase data rates is to increase the modulation speed. Going this route would relax the linewidth requirement discussed above. This is due to the short time period between consecutive symbols. As modulation speed increases, the phase noise accumulated during one period decreases. This can be seen from Equation 1.6: as τ decreases the RMS phase deviation $\Delta\phi(t, \tau)$ decreases by the same factor. For a given modulation scheme, i.e., 16-QAM, the system can tolerate higher laser phase

noise, w_{ϕ} , if τ is smaller. These two competing trends merit some discussion when trying to evaluate the requirements from future optical communication light sources.

The increase in modulation speed is mostly driven by advances in the miniaturization of light modulators. Low capacitance is often required and sets a demand for smaller footprint devices. On the other hand, the increase of data rate by packing more bits per symbol is driven by advancements in digital signal processing (DSP). Faster parallel electronics is needed to encode multi-bit signals. This in turn is also driven by progress in high-speed electronics. These two market trends, faster modulators and faster DSPs, often go hand in hand. In the context of light sources for future optical communication networks, this means that the rate of increase in demand for narrower linewidth lasers for telecom should stagnate somewhat due to these competing trends.

The argument above implies that in the near future, it might not be necessary to portray a fast path towards constant reduction of laser linewidth. However, today's semiconductor lasers are incompatible with the transition to coherent communication, requiring alternative solutions. For example [94], to transmit 64 bits per symbol at frequency of 20 GHz, while requiring Bit Error Rate (BER) of 10^{-4} and sensitivity penalty of 2dB using feed-forward phase estimation techniques would require a laser with linewidth of 1.2 KHz. Today's state of the art DFB lasers that are commonly employed in communication networks are limited to a linewidth of about 100 KHz. Therefore, an improvement of about 2 orders of magnitude in linewidth is required to support near-future coherent communication.

1.3 Linear and non-linear performance limiting factors

The performance metrics for a laser is strongly dependent on the specific application. For narrow linewidth lasers, the important metric is often the amount of phase noise at the relevant frequency range. However, other metrics such as power output, side mode

suppression, and wall plug efficiency are often as important, for practical reasons.

Laser linewidth, or noise, are fundamentally related to losses. Here I refer to loss in the broader sense by defining it as a mechanism that couples “useful” energy — laser mode electromagnetic energy or pump electrical energy — to a thermal bath or a continuum of modes. For example, optical loss through scattering couples the mode to the free-space continuum. Dissipation through resistive heating couples pump current to the thermal bath. A very fundamental theorem, the fluctuation-dissipation theorem, relates the dissipation through these channels to fluctuations in the cavity. This theorem implies that the same mechanism that couples energy to the “outside world” also couples fluctuation from the outside world to the cavity.

Despite the universal nature of the fluctuation-dissipation theorem, it is not very useful for describing laser noise in a quantitative way. Text-book laser theory usually “attacks” noise by engaging the specific physics of a laser system. Losses in the cavity force us to pump the laser harder, such that gain overcomes loss. This in turn will yield larger density of excited electrons. These excited electrons will relax randomly to the ground state, adding random phase to the laser field through the process of spontaneous emission. In this case, the relaxation of excited electrons to the ground state is due to the interaction with the vacuum state corresponding to the laser mode and not the free-space continuum. This approach can be shown to be directly related to the the fluctuation-dissipation theorem [52].

In addition to fluctuations, losses limit the amount of energy we can store in the cavity. The addition of random phase through spontaneous emission will add noise to the laser field, and will have bigger impact if there are fewer stored photons. This is demonstrated in the phasor diagram of Figure 1.2. No matter which approach or argument is used to calculate the exact noise characteristics, it is obvious that loss is a fundamentally root cause of noise or fluctuations. We will divide loss mechanisms into two categories:

1. Linear loss: this is the most common and basic loss mechanism. In general,

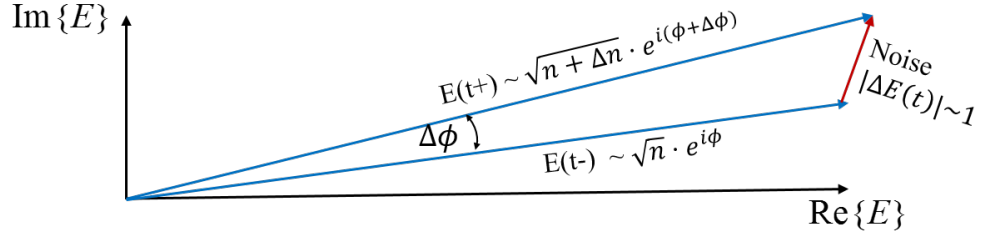


Figure 1.2: Phasor diagram demonstrating the effect of a spontaneous emission event

linear loss can be described through the equation:

$$\frac{dI}{dt} = -\alpha I \quad (1.7)$$

where I is a generic quantity, e.g., photon density or EM energy. The decay in this case is exponential with a rate that depends only on the constant α .

2. Non-linear loss: this loss refers to a mechanism in which the decay rate α depends on the quantity I through some non-constant function:

$$\frac{dI}{dt} = -\alpha(I) \cdot I \quad (1.8)$$

In the context of this work, non-linear loss refers to optical losses that depend on the photon density itself. Despite the more complex nature of this loss mechanism, the same arguments implied in the fluctuation-dissipation theorem are valid, and non-linear loss will have an impact on laser coherence.

In Chapter 2 I will analyze linear loss and will describe a strategy to decrease it for narrow-linewidth operation. We will see in chapter 3 that low-loss high-Q operation will yield an increase of non-linear loss. In Chapters 3-9 I will analyze the effect of these non-linear processes on noise performance and other important metrics.

Chapter 2

Hybrid Si/III-V as a platform for narrow linewidth

Semiconductor lasers are notorious for their low coherence properties. Despite the tremendous progress in micro fabrication and wafer growth this limit has hardly been broken. Some of the more successful attempts include a 64 KHz laser [32], a 28 KHz laser [38], and a 3.6 KHz laser [71]. Common to these results is the implementation of a large-mode-area, small confinement factors, and low-loss cavities. In [71] linewidth improvement was achieved also by suppression of spectral hole burning.

As we shall see in this chapter a key requirement for linewidth suppression is the reduction of modal loss. However, semiconductor lasers based on common III-V epistuctures require high density of dopants and carriers to maintain a low resistance current path for carrier injection into the quantum wells (QW). The high carrier density interacts with the mode and induces extra loss through radiation and dissipation. The fact that the III-V-only platform requires current path through the same volume in which the optical mode is stored renders this platform inconsistent with low-loss. Even though some improvement can be made for III-V lasers by decreasing QW confinement and reducing losses elsewhere, this platform is inherently limited.

In science and technology, a big milestone is often achieved only after improvements are made on the material-science front. New materials can overcome barriers that earlier were considered a fundamental limit. As we shall see in this chapter, the development of a new platform at the University of California, Santa Barbara

(UCSB), the hybrid Si/III-V platform [75] opened up a path to narrow linewidth semiconductor lasers. This path was followed by researchers from Caltech [88], demonstrating 18 KHz lasers. The work by Yariv et al. has portrayed a path towards further linewidth reduction on this platform. However, experimental results [106] were inconclusive. In this work I will provide theory describing the limits of performance of this platform and conclusive experimental results supporting the theory and demonstrating record-breaking performance.

2.1 Noise in conventional semiconductor lasers

There is a vast amount of research on the physics of noise in semiconductor lasers. [131] attacks the problem from fundamental quantum mechanics, [13] has a nice discussion on some phenomenological aspects of noise analysis, [78] have a detailed discussion on characterization and measurement of noise in lasers. Detailed derivations of semiconductor noise is outside the scope of this work. However, it is important to understand a few key concepts and results.

The electromagnetic laser field has magnitude and phase. In general, noise can appear in both. In common laser systems amplitude noise is vastly suppressed by gain saturation, providing a restoring force for the laser amplitude. In fact, in many practical laser systems, amplitude noise is at or very close to the shot-noise limit. On the other hand, the phase of the electromagnetic field doesn't have the same restoring force. Laser phase is fluctuating in a random walk process. For this reason, for most applications laser noise is dominated by phase noise. Thus, in this work I will refer to phase noise as laser noise, unless otherwise stated.

Laser frequency noise spectrum has several components. Equation 2.1 can be used to describe it in a general way:

$$W_{\dot{\phi}} = \sum_{i=1}^{\infty} \frac{a_i}{f^i} + C \quad (2.1)$$

The first sum in Equation 2.1 is often called “one over f” noise. The source of these

noise terms can be traced to several mechanisms. Some of them tend to be technical (e.g., mechanical vibration of the stage), and some of them are more fundamental (e.g., thermal diffusion). A nice review of generic $1/f$ noise can be found in [66]. Due to the illusive nature of these $1/f$ noise terms they are often treated as “technical noise”. In this work I will use the same notation even though in some cases the source of this noise could be fundamental. The constant C of the second term in Equation 2.1 is referred to as Schawlow-Townes white noise floor. In most semiconductor lasers, this term becomes dominant over $1/f$ terms at frequencies as low as few KHz. For this reason, laser noise analysis often emphasizes this white noise floor level. The ideas and strategies laid out in this chapter will focus on the reduction of this dominant term.

The analysis of white noise in semiconductor lasers can be laid out in several steps:

1. The main source of noise in SCLs is spontaneous emission. This refers to the stochastic radiative decay of excited electrons to the ground state. Every spontaneous emission event adds on the average one photon to the laser mode [31]. The field of this photon has a random phase compared to the laser coherent field and is thus source of phase fluctuations. The lack of restoring force for the laser’s phase means that over time the phase will go through a random walk process. The mean square of the phase deviation will be proportional to observation time τ . If the frequency noise is white (setting $a_i = 0$ in Equation 2.1) the mean square of the phase deviation will follow Equation 1.6.
2. Above laser threshold the modal gain of the laser is clamped at the modal loss level. A gain term that is exceeding the losses would imply the unphysical situation of diverging exponential photon density. In fact, due to spontaneous emission, the gain is only approaching losses from below; however, for any practical purposes we can set them as equal:

$$\Gamma G_m(n, \nu) = \alpha \tag{2.2}$$

Here G_m is material gain in units of sec^{-1} and is a function of both the lasing frequency ν and the density of excited electrons n . Γ is the confinement coefficient that describes the confinement of optical energy in the active (gain) region, such that ΓG_m is the modal gain. α describes modal loss in inverse time units. This includes intrinsic loss due to absorption and scattering, but also external mirror loss.

3. There is a fundamental relationship between stimulated and spontaneous emission. The gain, or stimulated emission rate, depends on the level of population inversion, i.e., the difference between the density of excited electrons and ground state electrons. The spontaneous emission process depends only on that of the number of excited electrons. The inversion level and the density of excited carriers are tied together using the quasi Fermi levels of the pumped semiconductor [13]:

$$R_{sp} = \Gamma G_m n_{sp} \quad (2.3)$$

Where R_{sp} is the spontaneous emission rate into the mode (photon number per unit time) and n_{sp} is the population inversion factor defined as:

$$n_{sp} = \frac{1}{1 - e^{(E_{21} - \Delta E_f)/KT}} \quad (2.4)$$

where E_{21} is the bandgap energy and ΔE_f is the difference between the quasi Fermi levels. The value of this population inversion factor is on the order of 1, but can quickly diverge in cases where the laser is operated very close to transparency ($E_{21} \approx \Delta E_f$).

4. Modal loss α can be expressed using the cavity/mode quality factor Q :

$$Q = \frac{\omega}{\alpha} \quad (2.5)$$

5. Laser white noise level due to spontaneous emission can be expressed using the spontaneous emission rate R_{sp} and the total number of stored photons in the

cavity N_p [31, 131, 13]:

$$W_{\dot{\phi}} = \frac{R_{sp}}{2N_p} \quad (2.6)$$

6. The photon storage capability of the resonator is a function of its quality factor. At threshold, the stimulated emission rate will reach the loss rate to maintain steady state. From Equation 2.5 it is clear that this rate is defined by the quality factor. Above threshold, each added photon due to injection will contribute to the growth of photon number in the cavity in a rate set by the fixed gain:

$$N_p = \eta_i \frac{(I - I_{th}) Q}{q \omega} \quad (2.7)$$

where q is the electron charge and η_i is the injection internal efficiency and I_{th} is the threshold current.

7. The linewidth is enhanced beyond the quantum limit due to relationship between the imaginary and real parts of the refractive index [31, 116]. This relationship exists in semiconductors due to the non-symmetrical gain spectrum. As discussed previously, photon number fluctuation induces gain fluctuations. These in turn cause fluctuations in the refractive index that induce phase noise. The effect of that process is a broadening of the Schawlow-Townes linewidth by a factor of $(1 + \alpha^2)$, where α is a material-dependent parameter usually in the range of 2-5 [107].
8. Putting together Equations 2.2, 2.3, 2.5, 2.6, and 2.7 we get the famous modified Schawlow-Townes formula that relates laser white noise PSD to the inverse of the square of the quality factor and the inverse of the output power:

$$W_{\dot{\phi}} = \frac{q\omega^2 n_{sp}}{2Q^2(I - I_{th})\eta_i} (1 + \alpha^2) \quad (2.8)$$

Equation 2.8 shows that increasing the quality factor of a resonator would yield a power-law reduction of noise. As we shall see in the next sections, this can be done in the hybrid Si/III-V platform. Moreover, this platform will lend itself towards the

effective elimination of the linewidth enhancement factor.

2.2 Hybrid Si/III-V platform

In the past decade the amount of academic research on silicon photonics devices and systems has grown rapidly. Silicon-based devices were demonstrated commercially, and much industrial effort has been devoted to this platform. This rapid growth was mainly motivated by several elements:

- CMOS compatibility - Realizing complex photonic integrated circuits using mature CMOS processes has the potential to considerably decrease cost and to increase performance while maintaining scalability.
- Integration with silicon-based electronics - Integration of optoelectronic devices with high-speed electronics can yield unprecedented control and manipulation capabilities of light in devices and systems.
- The high index contrast of Si can yield small footprint devices and support further miniaturization of standard devices.
- Silicon is transparent at telecom wavelengths - The low absorption loss together with reduced scattering thanks to advanced processing capabilities can yield very low-loss waveguides and devices. The typical loss figure is around 1-3 dB/cm; however, devices with losses as low as 0.3 dB/cm and lower have been demonstrated [9].
- CMOS compatible integration of Germanium with Si - The integration of Ge (strained [2] or SiGe [72]) for light detection is crucial for many applications.

The “explosion” of this field in recent years was followed by an attempt to integrate laser light sources on to this platform. Despite some success in monolithic growth of active material on Si [64, 124, 10] , the most common technology for laser-Si integration is the hybrid Si/III-V bonded platform. In this technology Si is patterned

2.3 Noise reduction in hybrid Si/III-V

In terms of coherence, the hybrid platform has many advantages over conventional III-V lasers. Silicon is a low-loss material for light of frequency above its bandgap. Linear absorption of light at telecom wavelength is practically negligible. Advanced silicon fabrication techniques together with a well-behaved silicon oxide allow for the fabrication of waveguides with minimal sidewall roughness, yielding reduced scattering losses. The hybrid structure is constructed such, that no current flows through silicon so that carriers and dopants don't have to be introduced into silicon to support the current flow. We shall see in the next sections that all these properties can be exploited for narrow-linewidth through careful design of the laser.

2.3.1 High-Q silicon resonator

As can be inferred from Equation 2.8, the first building block of a high-coherence laser is a high-Q resonator. Passive micro Si resonators with quality factors close to or bigger than a million were reported in the literature [25, 88]. These integrated Si-based implementations can yield small cavity sizes, compared to those used in commercial narrow-linewidth lasers.

Several resonator design topologies are available for high-Q. Common to all of them is the minimization of scattering through optimization of sidewall roughness and disorder. This is often done by designing waveguides that are weakly guiding, such that the mode is minimally interacting with the patterned core. One of the most common high-Q resonator designs is the ring [113] or disc resonator. One of the disadvantages of such a design is its large footprint. While the quality factor scales with the diameter of the ring, its area scales with the diameter squared. Since expensive III-V gain media should have a similar footprint, this strategy can quickly become prohibitively expensive. Two-dimensional photonic crystals were also utilized to demonstrate extremely high-Q cavities [95]. However, the commercialization viability of such technology is questionable.

One-dimensional photonic crystal offers good compromise in regards to footprint,

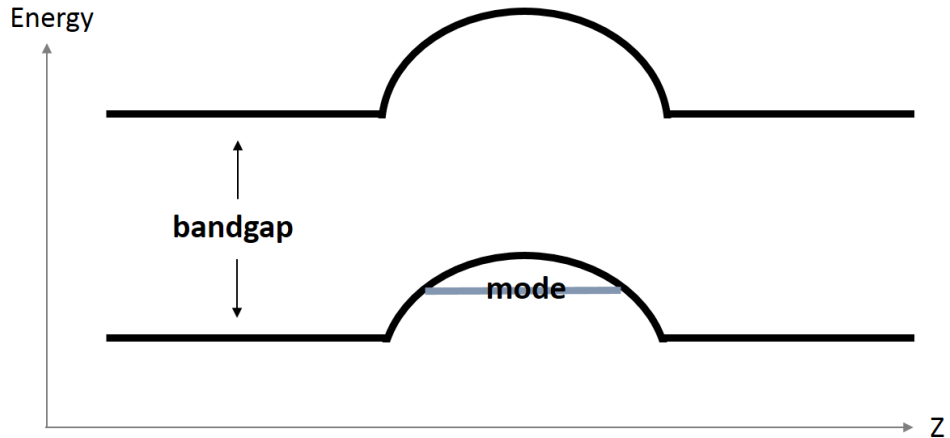


Figure 2.2: Band structure of the mode-gap resonator. The parabolic potential-well supports one optical mode

fabrication and design complexity and high-Q. Quality factors as high as 1.1 million were demonstrated [88, 46]. These inline resonators can easily be converted into dense arrays of lasers, suitable for applications, such as phase array and wavelength-division multiplexing (WDM).

In this work, we implement a mode gap resonator design, in which a 1-D grating is patterned. The grating has constant pitch, however, the dimensions of grating elements vary along the resonator length. The coupling coefficient κ is chirped such that the resulting photonic bandgap has a finite parabolic potential well. This well is designed such that only one mode is supported [100]. The photonic band diagram with the supported mode can be seen in Figure 2.2. Details on the exact structure and design methodology can be found in [89] and in [106].

2.3.2 Modal gain and loss

The availability of high-Q resonators on silicon does not immediately guarantee a narrow-linewidth laser. When the III-V is bonded to the high-Q resonator, it becomes an integral part of the resonator's structure. Losses induced by the bonded III-V can considerably lower the composite total Q and eliminate any benefit from the the low-

loss silicon. For that reason, it is important to engineer the structure such that the **composite** resonator is still high-Q, while supporting laser operation. In this section, I will describe such a design methodology. A detailed analysis of such an approach can be found in [106].

2.3.2.1 General description

Common doped III-V stacks have intrinsic losses with equivalent quality factor of $Q_{III-V} = 10^4$ [13]. The silicon resonators in this work may have unloaded Q as high as $Q_{Si} = 10^6$. The composite bonded structure will have quality factors in the range between these two extremes, depending on the exact modal composition. Total modal loss, which is related to the imaginary part of the effective refractive index, can be well estimated by using a weighted sum of material absorbance weighted by the confinement factor:

$$\alpha_{mode} = \sum_i \alpha_i \Gamma_i \quad (2.9)$$

For TE modes, as in our case, the appropriate approximation can be written as [121]:

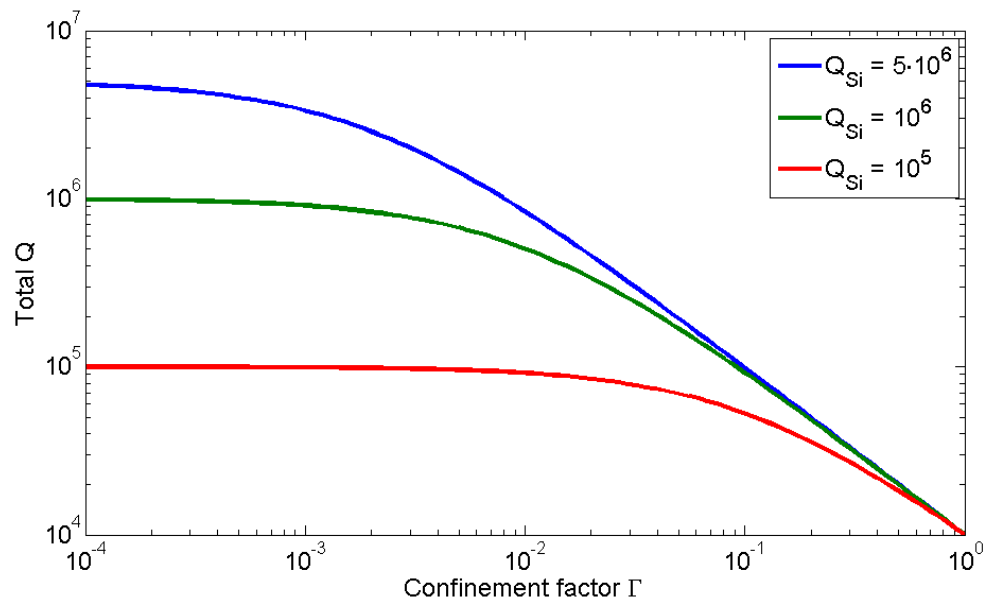
$$\Gamma_i = \frac{\int_i n_i(\mathbf{r}) |E(\mathbf{r})|^2 d^3\mathbf{r}}{n_{eff} \int_{all} |E(\mathbf{r})|^2 d^3\mathbf{r}} \quad (2.10)$$

where n_{eff} is the mode's effective index (real part), and the index i represents the desired material or region. Ignoring mirror loss for output coupling, we can express the total Q using:

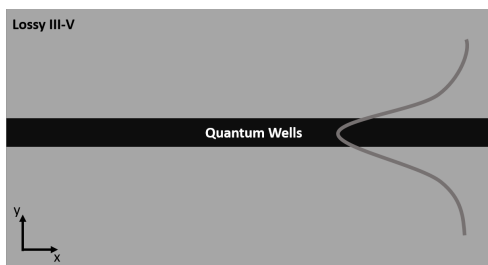
$$\frac{1}{Q} = \frac{\Gamma_{III-V}}{Q_{III-V}} + \frac{1 - \Gamma_{III-V}}{Q_{Si}} \quad (2.11)$$

A graphic representation of Equation 2.11 is shown in Figure 2.3. It is evident from Figure 2.3 (a) that one can reduce losses by reducing the overlap with the lossy III-V material, a process shown schematically in 2.3(b-c). In the high III-V confinement regime, the reduction in loss is a quasi-linear function of the confinement factor. At around the point where $\frac{\Gamma_{III-V}}{Q_{III-V}} = \frac{1 - \Gamma_{III-V}}{Q_{Si}}$ the total quality factor becomes sub-linear and eventually saturates at Q_{Si} .

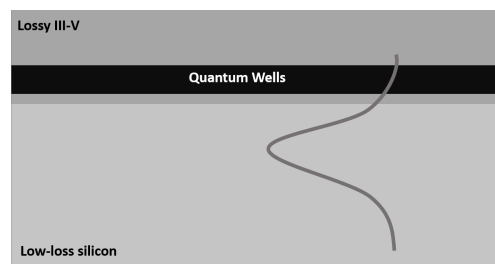
The modal gain can also be expressed using the same overlap integral as in Equa-



(a)



(b)



(c)

Figure 2.3: (a) Quality factor of hybrid Si/III-V composite resonator (b) Mode profile of a traditional III-V laser (c) Profile of a high-Q hybrid Si/III-V laser

tion 2.10. Since gain is only present at the quantum wells, we can express the gain (sec^{-1}) G using:

$$G = \Gamma_{QW}G_m \quad (2.12)$$

It is worth noting that even as the mode composition changes, i.e., is pushed down to Si, the ratio between Γ_{III-V} and Γ_{QW} stays constant for any practical purpose, as shown in Figure 2.4.

To reach lasing the gain only needs to compensate for the loss, as is evident from Equation 2.2. Since the modal gain is a linear function of Γ_{III-V} , in the regime where the loss is quasi-linear ($Q < \frac{1}{2}Q_{Si}$), the gain is reduced by the exact same amount that the loss is reduced and the threshold current remains nearly a constant as Γ_{QW} is reduced, yet the attendant reduction in loss translates to high coherence as implied from Equation 2.8.

2.3.2.2 The spacer lasers

Reducing the overlap of the mode with the III-V requires a physical mechanism to push the mode further down into the silicon. In this work, this is achieved using SiO_2 spacer layer [106]. The oxide is thermally grown on the Si device layer and separates between the high index silicon and the high index III-V. The thicker this oxide separation layer, the further the mode is pushed into Si. This is a very efficient method for modal engineering. Small changes in oxide thickness in the order of 10's of nanometers can change the confinement factor by orders of magnitude. For comparison, the size of an external cavity laser would have to scale by the required reduction in active confinement, yielding devices larger by orders of magnitude. The spacer transverse modal control allows us to achieve the same effect with very little compromise in footprint (the device might need to be slightly longer if the grating is weaker due to the spacer). The effect of spacer thickness on III-V confinement is shown in Figure 2.4.

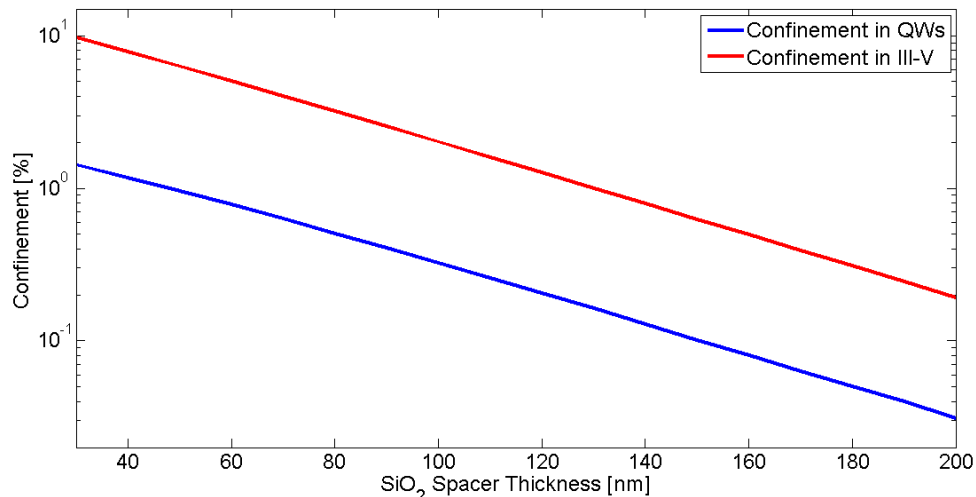


Figure 2.4: Confinement in III-V and in QWs vs. spacer thickness

2.3.3 Schawlow-Townes linewidth

The $\frac{1}{Q^2}$ dependence of the modified Schawlow-Townes linewidth formula of Equation 2.8 suggests that high quality factor will yield narrow linewidth. As we decrease losses further and further, the excited carrier density at threshold approaches the density required to reach transparency. Operating the laser close to the transparency point will be manifested in Equation 2.8 as very large population inversion factor n_{sp} . At this regime, the population inversion factor is very sensitive to changes in threshold gain, and we can no longer treat n_{sp} as constant. Since operating close to transparency is realistic and even desired in our case, I will introduce an approximation for n_{sp} that is more suited for this regime.

The spontaneous emission rate into the mode can be expressed using the phenomenological expression:

$$R_{SP} = \frac{\Gamma_{QW}\beta'_{sp}N_2}{\tau_{sp}} \quad (2.13)$$

where N_2 is number of excited electrons, τ_{sp} is the spontaneous radiative decay time of excited electrons into all modes, and β'_{sp} is the spontaneous emission factor. $\Gamma_{QW}\beta'_{sp}$ describes the fraction of photon that is coupled to the lasing mode out of all modes (notice that some textbooks define that as β_{sp}). The quantity $\frac{\beta'_{sp}}{\tau_{sp}}$ is material and

structure dependent. Very small changes in spacer thickness, which hardly change the cavity volume, are not expected to affect this quantity. The number of excited electrons can be broken into carriers needed to get to transparency and carriers needed to overcome loss:

$$N_2 = N_{tr} + (N_2 - N_{tr}) \quad (2.14)$$

We can then use a linearized expression for the gain (which is more accurate the closer we get to transparency):

$$G = \Gamma_{QW} G'_m (N_2 - N_{tr}) \quad (2.15)$$

where G'_m is the material differential gain. We can now use Equations 2.6, 2.7, 2.13, 2.14, and 2.15 to express the linewidth using:

$$W_{\dot{\phi}} = \frac{\beta'_{sp}}{\tau_{sp}} \frac{q\omega}{(I - I_{th})\eta_i} \left(\Gamma_{QW} \frac{N_{tr}}{Q} + \frac{\omega}{G'_m Q^2} \right) \quad (2.16)$$

Equation 2.16 implies some important conclusions:

- Far from transparency, where the second term in the bracket is dominant, increasing the quality factor Q yields a square power law improvement in linewidth. This is because the reduction in needed threshold gain lowers spontaneous emission rates, and because the photon density increases with increasing Q .
- As we get closer to transparency by increasing Q the square law improvement saturates into a linear improvement, as the first term in the bracket becomes the dominant one. This is because the spontaneous emission rate is now approximately a constant, set by the transparency carrier density, and only the photon number, N_P , increases with increasing Q .
- A reduction in Γ_{QW} will lower the spontaneous emission rate into the mode. The total spontaneous emission rate to all modes is constant, but less will be coupled to the lasing mode due to the weak interaction of the quantum well with this mode.
- In the hybrid platform, Γ_{QW} is our knob to reduce Q (see Equation 2.11).

Equation 2.16 teaches us that this strategy guarantees a $\frac{1}{\Gamma^2}$ dependence, both close and far from transparency, as long as we have not saturated the total Q .

In this chapter, I discussed noise in conventional lasers, and introduced hybrid Si/III-V as a platform for low-noise lasers. The spacer laser design was introduced as a simple mechanism to push noise performance to the limit of the platform. In the next chapter, I will describe the nonlinear effects that may be responsible for this limit.

Chapter 3

Non-linear effects in hybrid Si/III-V

As described in section 2.3 moving the energy of the optical mode (“pushing” it) into low-loss silicon resonator yields lasers with a very high-Q lasing mode. This mode exists mostly in silicon and interacts very weakly with the active (and lossy) III-V. The high intra-cavity field intensities that are a consequence of the high-Q and the small cavity volume enhance the probability of non-linear and multi-photon processes in silicon.

Si has a large non-linear $\chi^{(3)}$ coefficient compared to commonly used low-loss materials such as SiO_2 or Si_3N_4 . Both Raman scattering and optical Kerr effects have been reported in silicon. Brillouin scattering, which is often dominant in optical fibers, is much weaker than the Raman process in silicon, and is rarely observed [97].

Raman scattering is a non-linear process involving interaction with optical phonon. The Raman gain in silicon has a narrow linewidth response ($\sim 100\text{GHz}$) centered at a frequency of 15.6 THz (at room temperature) [29]. Silicon Raman lasers have been demonstrated by several authors, both pulsed [7] and CW [84]. Cascaded Si Raman lasers have also been demonstrated [86]. However, the single mode operation of our hybrid Si/III-V lasers and the narrow gain bandwidth of the quantum wells relative to the Raman frequency eliminates (first order) Raman scattering from interfering with the laser operation.

Kerr non-linearity involves light intensity-dependent alterations to the refractive index, both real and imaginary parts. Writing the third-order polarization for

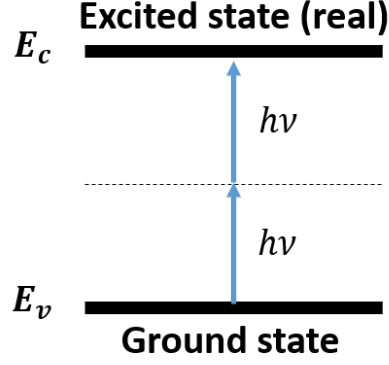


Figure 3.1: Schematic description of two-photon-absorption

monochromatic light $E(t) = \epsilon \cos(\omega t)$ as [6]:

$$P^{(3)}(t) = \chi^{(3)} E(t)^3 = \frac{1}{4} \chi^{(3)} \epsilon^3 \cos(3\omega t) + \frac{3}{4} \chi^{(3)} \epsilon^3 \cos(\omega t) \quad (3.1)$$

The second term of Equation 3.1 represents a contribution to polarization at the same frequency of light and hence an intensity-dependent refractive index. The real part of the refractive index can be expressed as:

$$n = n_0 + n_2 I \quad (3.2)$$

where n_0 is the linear (low-intensity) refractive index and I is the light intensity, such that [6]

$$n_2 = \frac{12\pi^2}{n_0^2 c} \text{Re} \{ \chi^{(3)} \} \quad (3.3)$$

The imaginary part of $\chi^{(3)}$ can phenomenologically describe two-photon-absorption (TPA), a process that is schematically described in Figure 3.1. The total attenuation in the presence of the nonlinearities now has the form [30]:

$$\frac{dI(z)}{dz} = -\alpha I(z) - \beta_T I^2(z) \quad (3.4)$$

where α is regular linear attenuation and β_T is the so-called two-photon-absorption coefficient.

Si has a bandgap that corresponds to a wavelength of $1.1\mu\text{m}$. Therefore TPA, which is wavelength dependent, can occur at wavelengths of $1.1\text{--}2.2\mu\text{m}$, and is around its peak at telecom wavelengths. In the hybrid Si/III-V laser, the field intensity builds up in the presence of gain and the high-Q resonator. As a consequence, non-linear processes such as TPA add extra loss [4] that would otherwise be negligible in the low-intensity passive version of the same resonator. TPA is a non-resonant fast process. Its time-constant is considerably smaller than any time-constant of interest in our system. We therefore treat it as instantaneous. As depicted in Figure 3.1 the absorption of two cavity photons conserves energy by exciting an electron to the conduction band. Since silicon is not a direct bandgap semiconductor, the electron is likely to recombine non-radiatively. As we shall see in the next sections, the conduction-band electrons can live quite a long time in the excited states before they recombine or diffuse away from the mode, and act as free carriers that can interact with the mode and add extra loss through Free-Carrier-Absorption (FCA) processes.

In this chapter I analyze phenomena related to non-linear loss mechanisms, such as TPA and FCA. In the following chapter I will analyze the effect of these processes on the high-Q hybrid Si/III-V lasers. A thorough review of non-linear effects in Si can also be found in [58].

3.1 Two-photon-absorption in silicon

Kerr nonlinearities impact the functionality of devices in many systems. In some cases these nonlinear effects have been used to create new functionality. Among other applications, the Kerr effect has been used to demonstrate all-optical modulation [69], continuum generation [73], pulse compression, and mode-locking [112]. In the context of laser noise TPA has been used to suppress relative intensity noise (RIN) [3], and to generate photon-number squeezed-light [36].

In other cases these nonlinearities have degraded or impacted performance. In silicon TPA often induce free carriers. In many examples of performance limiting nonlinearities it is those free carriers that are responsible for performance degradation.

The next section is devoted to FCA and some examples will be given there. In this section we will discuss only the physics of two-photon-absorption.

As has been discussed in previous sections TPA is manifested as the imaginary part of the index of refraction, and is non-zero whenever the photon's energy is larger than half the band-gap of silicon, as in the case of telecom wavelengths. The coefficient β_T relates the change of the imaginary part of the refractive index Δn_i to the field's intensity I using [58]:

$$\Delta n_i = \frac{c}{2\omega} \beta_T I \quad (3.5)$$

The coefficient β_T is wavelength-dependent, and its value at $1.55\mu m$ has been measured by several authors. Femto-second pulses and balanced Z-scan technique have been used to measure TPA coefficient experimentally. An empiric value of $\beta_T = 0.8 \frac{\text{cm}}{\text{GW}}$ has been obtained [17] at $1.54\mu m$ using that technique. Similar value was measured by [8]. Experimental data from nonlinear power transmission was also used to extract a value of $\beta_T = 0.45 \frac{\text{cm}}{\text{GW}}$ at the same wavelength [114]. Evidence of crystal anisotropy was also found for the third order susceptibility tensor, where a factor of 2.36 between tensor components was obtained [136]. In this work I will use the value:

$$\beta_T = 0.8 \frac{\text{cm}}{\text{GW}} \quad (3.6)$$

Optical loss induced by two-photon absorption in Si can be described by a nonlinear rate equation term for the average photon density n_p :

$$\frac{dn_p}{dt} = -\beta_T h\nu v_g^2 \Gamma_{Si}^2 n_p^2 \quad (3.7)$$

where $h\nu$ is the photon energy, v_g the group velocity, and Γ_{Si} is the confinement factor in Si, defined as in Equation 2.10 (with layer i being the Si layer). The nonlinear nature of TPA is manifested in this equation by the n_p^2 square power law in the right half side.

3.2 Free-carrier-absorption

For each TPA absorption event in Si, an electron-hole pair is generated. Long carrier recombination life time of conduction-band electrons in intrinsic silicon allows these carriers to accumulate and interact with the electromagnetic field. This interaction induces both extra loss through FCA and plasma-effect-related refractive index changes.

TPA-induced free-carrier-absorption was shown to alter and degrade the performance of many devices. In high-Q resonators, free-carriers have caused self-induced modulation of the transmitted light [37]. In Raman lasers and amplifiers, free-carriers alter the Raman gain and induce loss [85]. This loss has limited the available pump power in Raman lasers [57].

Free-carriers recombine and diffuse through a time-dependent process. Therefore, Unlike TPA, which is considered instantaneous, the interaction with free-carriers often adds some frequency response that would alter the dynamics of devices. FCA has been found to limit switching speeds in all-optical switching schemes [73]. It has been found to broaden intense pulses [112] and to alter spectrum of self-phase-modulation experiments in Si [133].

The electron and hole momentum relaxation times are longer than that of an optical cycle. Therefore, carriers can easily oscillate at optical frequencies. Optical energy will be attenuated through both radiation and heat. The strength of these damping effects can be well modeled using the Drude model [101] where the loss coefficient per unit distance α_{FCA} (as in Equation 3.4) and refractive index change n_{FCA} can be directly related to the electron and hole concentrations n_{Si} and p_{Si} , respectively.

There have been empirical measurements of absorption in doped p-type [92] and n-type [104, 92] Si. Comparison of the empirical results to the Drude model predictions was done by [101] and reviewed by [58]. The Drude model predictions were found to underestimate absorption by about a factor of two. [58] derived an empirical formula for free-carrier-absorption. For intrinsic silicon at $1.55\mu m$ the cross-section parameter

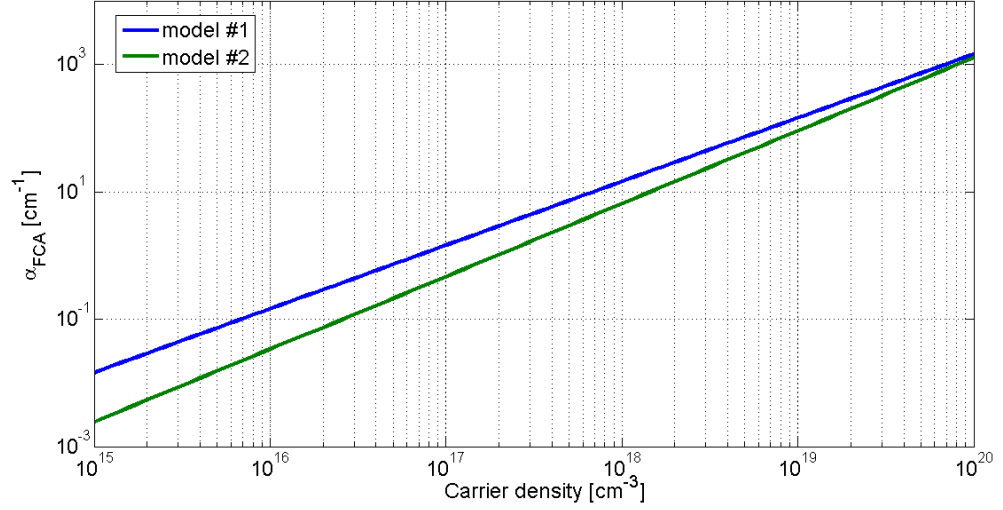


Figure 3.2: Model for FCA in silicon. Model #1 by [58, 101]. Model #2 by [70]

[58] σ_a is used to relate FCA loss (per unit length) to electron concentration n_{Si} :

$$\alpha_{FCA}^{(z)} = \sigma_a n_{Si} \quad (3.8)$$

Where n_{Si} is the electron and hole concentration in units of cm^{-3} and the value of σ_a is given by:

$$\sigma_a = 1.45 \cdot 10^{-17} \text{ cm}^2 \quad (3.9)$$

A more recent attempt to characterize FCA in Si was done by [70]. For wavelength of $1.55 \mu\text{m}$ the following formula was obtained for electron and hole concentration n_e and n_h , respectively:

$$\alpha_{FCA}^{(z)} = 8.88 \cdot 10^{-21} \cdot n_e^{1.167} + 5.84 \cdot 10^{-20} \cdot n_h^{1.109} \quad (3.10)$$

A graphic comparison between these two models is shown in Figure 3.2.

As can be seen from Figure 3.2, the two models are not drastically different, especially at the high carrier concentrations. In this work, I will use the model given by Equation 3.8.

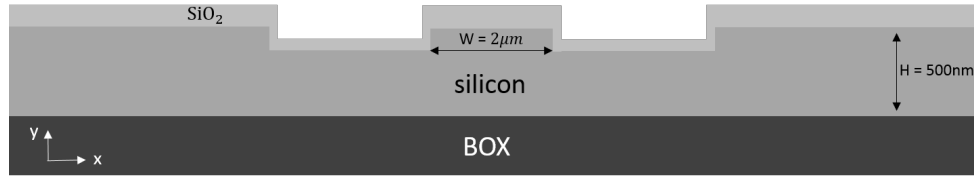


Figure 3.3: Waveguide structure used for analysis of FCA

3.2.1 General methodology

TPA-induced free carriers are generated instantaneously. Once generated, they can recombine at the bulk of the silicon or at its surface. The generated carrier density will vary along the waveguide since TPA depends on light intensity. More electrons will be generated at the peak of the mode than at its tail. Therefore, free carriers will also undergo a diffusion process. To properly model the optical loss due to FCA we will need to estimate how many carriers interact with the mode in the steady state, and what is their temporal response.

To estimate the number of free electrons in the steady state operation of the laser we need to solve the diffusion-recombination-generation equation. Since recombination at the bulk is a rather slow process in intrinsic silicon, surface recombination is expected to be dominant. The magnitude of the effect of surface recombination will depend on the specific waveguide geometry. For example, if the mode is located far away from any surface or interface then surface recombination will play a smaller role. For that reason, we need to take into account the exact waveguide geometry to account for surface recombination properly. The model I will use for our analysis is as depicted in Figure 3.3. Where the Si slab thickness is 500nm and the width of the waveguide is $2\mu\text{m}$.

3.2.2 Bulk recombination

Several physical processes are responsible for the carrier recombination at the bulk of the silicon (away from the surfaces and interfaces). The lifetime of an electron-hole

pair can be expressed using a contribution from all these processes as [33]:

$$\frac{1}{\tau_B} = \frac{1}{\tau_{SRH}} + \frac{1}{\tau_{Aug}} + \frac{1}{\tau_{rad}} \quad (3.11)$$

where τ_{SRH} is lifetime associated to Shockley–Read–Hall (SRH) recombination, τ_{Aug} is associated to Auger-type recombination, and τ_{rad} is radiative recombination lifetime.

Radiative recombination, where the annihilation of an electron-hole pair is accompanied by generation of a photon, can be modeled using the rate (per unit volume):

$$R_{rad} = Bn^2 \quad (3.12)$$

where $B \approx 1 \cdot 10^{-14} \frac{\text{cm}^3}{\text{sec}}$ [22], and n is the conduction band electron density. Since silicon is a non-direct bandgap material, radiative recombination is usually negligible compared to other processes.

The Auger recombination is a three-particle collision process, where the energy of the electron-hole recombination is transferred to a third electron or hole. The third electron or hole is then promoted to a higher energy in the same band, and relaxes back to the band edge by thermalization. The parametrization of Auger recombination was done by [40]. An approximate expression can be used for Auger recombination time constant [33] :

$$\frac{1}{\tau_{Aug}} = \gamma n^2 \quad (3.13)$$

where the parameter γ is carrier-concentration dependent:

$$\gamma = \gamma_{min} + \frac{\gamma_{max} - \gamma_{min}}{1 + \frac{n}{n_{ref}}} \quad (3.14)$$

where $\gamma_{min} = 4 \cdot 10^{-31} \frac{\text{cm}^6}{\text{sec}}$, $\gamma_{max} = 1.35 \cdot 10^{-30} \frac{\text{cm}^6}{\text{sec}}$, and $n_{ref} = 7 \cdot 10^{17} \text{cm}^{-3}$. As evident from Equation 3.13, the Auger recombination rate is higher at high carrier-densities.

Shockley–Read–Hall recombination refers to recombination through a trap in the

electronic bandgap [98]. For low carrier concentration this is the dominant recombination process. The rate of recombination can be described using the expression[98]:

$$R_{SRH} = \frac{n \cdot p - n_i^2}{\tau_p(n + n_1) + \tau_n(p + p_1)} \quad (3.15)$$

where n_1, p_1 are auxiliary variables that depend on the trap energy level, $\tau_{p,n}$ is a time constant related to the density of traps and temperature [21], and n_i is the equilibrium $p \cdot n$ product. As we shall see in this chapter, the bulk recombination lifetime is of secondary importance in our devices. The effective lifetime in our rib structure will be dominated by surface recombination, and will be in the range of 1-50ns. The bulk recombination lifetime is typically in the range of tens of μsec [16] to as high as 30msec [41]. For that reason the exact form and values in our approximations are of little to no consequence. I will therefore use a simpler approximation for the SRH recombination lifetime:

$$\frac{1}{\tau_{SRH}} = \frac{n^2 - n_i^2}{2\tau_t(n^2 + n \cdot n_i)} \quad (3.16)$$

where I estimate a fairly large effective time $\tau_t = 100\mu\text{sec}$ based on the assumption of a high-resistance, low-defect-density silicon.

3.2.3 Surface recombination

Dangling bonds and defects at the surfaces and interfaces of the silicon slab act as traps that promote recombination at the surface. The exact expression for the surface recombination rate is very similar to the SRH recombination, except that the density of traps is now expressed in two dimensions [93]. Those surfaces and interfaces act as carrier sink, which deplete the carrier density at the surface. Carriers from the bulk will therefore diffuse toward the low-concentration regime at the surface. The rate at which carriers diffuse toward the surface is characterized using the surface recombination velocity S in units of $\frac{\text{cm}}{\text{sec}}$, such that the two-dimensional rate is given by $R_S^{2D} = S \cdot n$ [93].

The optical mode in our lasers is confined to a 500nm thick Si slab. Carriers are

generated through TPA in the thin Si slab and diffuse quickly towards the surface where they recombine via surface traps. The fact that the slab thickness is narrower than the typical diffusion length of Si allows us to approximate the carrier density within the slab thickness as constant [16]. The recombination can be expressed using a three-dimensional rate ($\left[\frac{\text{cm}^{-3}}{\text{sec}}\right]$) by distributing the two-dimensional recombination process at the surface to the entire slab thickness using[16]:

$$R_S = \frac{S}{H}n \quad (3.17)$$

where H is the Si slab thickness as in Figure 3.3 and n is the excited carrier density in Si. This approximation neglects the spatial variation of the mode in the thin Si slab.

The value of the surface recombination velocity can vary a great deal depending on the quality of the Si surfaces and interfaces. For non-passivated surfaces, the velocity can reach several thousands [74]. Passivated Si wafers can have much lower surface recombination velocities, but the exact conditions of the passivization play an important role. Velocities of the order of 500-1800 $\frac{\text{cm}}{\text{sec}}$ were reported for non-optimized oxidation processes [47]. For optimized oxidation, such as that commonly employed in the fabrication of Si solar cells, velocities as low as 1-50 $\frac{\text{cm}}{\text{sec}}$ are reported [41].

Our lasers go through high temperature anneal and oxidation during the fabrication process. A very thick (up to 150nm) thermal oxide layer terminates the Si slab. The oxide is further sealed with the III-V chip. No direct measurement of surface recombination velocity was performed prior to bonding and it is therefore difficult to predict the resulting surface recombination velocity. However, given historical data from oxidized surfaces, a very low velocity will not be surprising. In later chapters, I will use an indirect measurement to estimate the recombination velocity and will show that its value is on the lower end of previously reported values.

3.2.4 Carrier diffusion

Carriers in silicon interact with the optical mode and induce loss and phase changes. Among the recombination processes described above, carriers that were generated locally by TPA will also diffuse to low carrier density areas. Therefore, the interaction time of the mode with these carriers will be limited to the length of time they spend in the vicinity of the mode. It is therefore important to add diffusion to our model. The diffusion equation governing this process is given by:

$$\frac{dn}{dt} = D\nabla^2 n \quad (3.18)$$

where D is the diffusion coefficient for silicon. For high carrier-densities we will have to use the ambipolar diffusion coefficient given by [87]:

$$D_a = \frac{2KT}{q} \left(\frac{1}{\mu_e} + \frac{1}{\mu_p} \right)^{-1} \quad (3.19)$$

where $\mu_{e,p}$ is the mobility of electrons/holes. When the carrier density is high, carrier-carrier scattering will increase. This will reduce the mobility of the carriers further at high densities. I will model the effect of carrier density on mobility using [39]:

$$\frac{1}{\mu_{e,p}} = \frac{1}{\mu_{e,p}^{(0)}} + \frac{\Delta n_{e,p} \cdot \ln(1 + 4.54 \cdot 10^{11} \Delta n_{e,p}^{-0.667})}{1.428 \cdot 10^{20}} \quad (3.20)$$

where $\Delta n_{e,p}$ is electron/hole density in [cm^{-3}] and the low-density mobility is taken to be:

$$\mu_e^0 = 1430 \frac{\text{cm}^2}{\text{V}\cdot\text{sec}} \quad (3.21)$$

$$\mu_p^0 = 495 \frac{\text{cm}^2}{\text{V}\cdot\text{sec}} \quad (3.22)$$

The effect of carrier density on the diffusion coefficient of silicon is shown in Figure 3.4

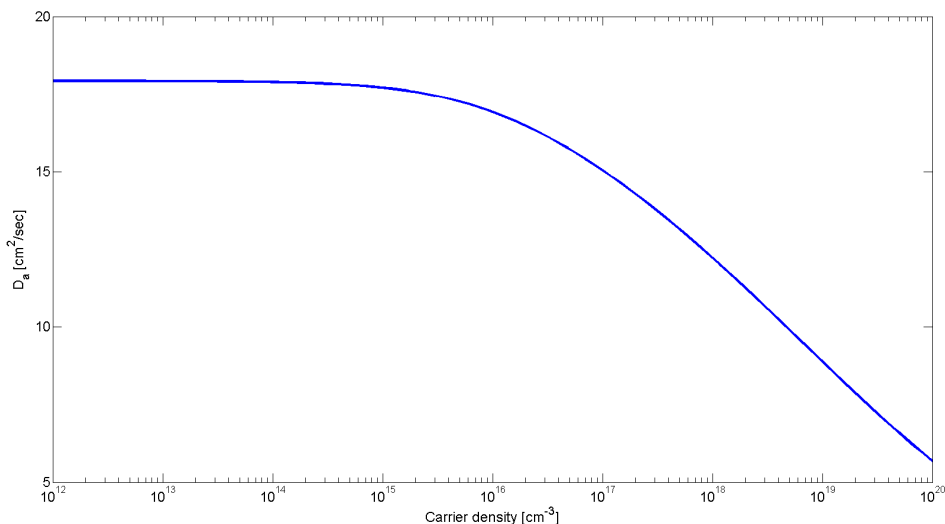


Figure 3.4: Model for the ambipolar diffusion coefficient of silicon

3.2.5 Effective carrier lifetime

The optical mode is confined within the three-dimensional cavity. In the longitudinal direction, the mode is designed to be a Gaussian with half-width in the order of hundreds of microns. In the transverse direction, the mode is confined to only a few microns. The orders of magnitude change in confinement between longitudinal and transverse direction motivates us to approximate the longitudinal direction as having a uniform photon distribution. The gradient in carrier density in the longitudinal direction is much weaker than that of the transverse. Therefore, diffusion in the longitudinal direction could be neglected. For the thin Si slab I can assume a uniform carrier density since the diffusion length is much larger than that thickness (y direction in Figure 3.3). For that reason, I can approximate the whole problem using a 1-D diffusion equation in the x direction only.

The generation-recombination-diffusion equation describing the dynamic of the carriers in Si can be expressed as [16]:

$$\frac{dn_{Si}}{dt} = \frac{\beta_T h\nu \Gamma_{Si}^2 V_g^2}{2} n_p^2 - \frac{n_{Si}}{\tau_b} - 2\frac{S}{H} n_{Si} + D_a \frac{d^2 n_{Si}}{dx^2} \quad (3.23)$$

where the first term on RHS represents generation due to TPA; the second term rep-

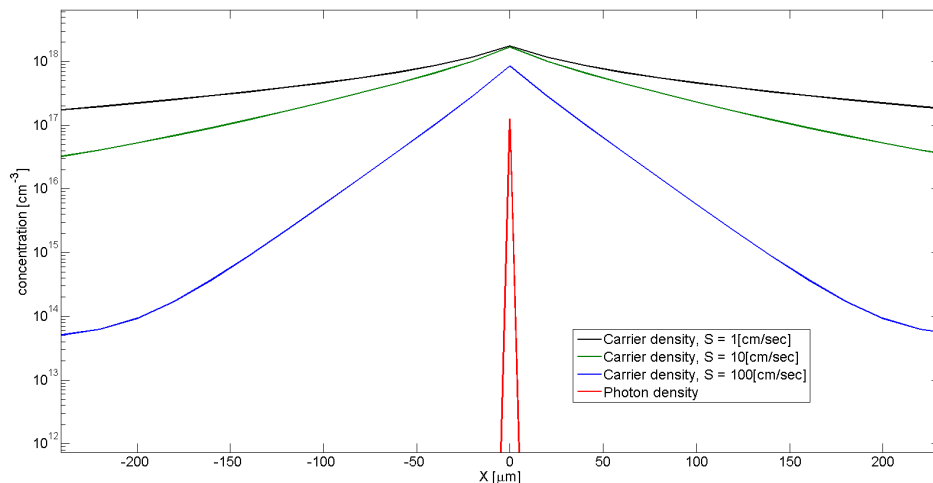


Figure 3.5: Carrier density profile for several different surface recombination profiles presents bulk recombination; the third term represents surface recombination, and the last term represents diffusion. To gain more insight into the typical carrier distribution I will assume that the generation of carriers is due to TPA induced by an optical mode with a Gaussian spatial profile:

$$n_p = \frac{n_{p,0}}{\sqrt{2\pi}} e^{-\frac{x^2}{2\sigma^2}} \quad (3.24)$$

where the width of the Gaussian is chosen to be equal to the waveguide ridge width $\sigma = 2\mu\text{m}$ (see Figure 3.3). $n_{p,0}$ would be the average photon density, if the mode were uniform within the waist area ($n_{p,0} = \frac{1}{\sigma} \int n_p(x) dx$).

A numerical solution to Equation 3.23 is shown in Figure 3.5. A few conclusions can be drawn from this figure:

- Even for very fast surface recombination, the carrier profile is much broader than the mode's profile. This will motivate us to approximate the carrier density as uniform in the vicinity of the mode.
- Surface recombination is the main mechanism of recombination. Mode profile depends almost solely on the surface recombination velocity.
- The steady-state carrier-density peak-height strongly depends on the surface

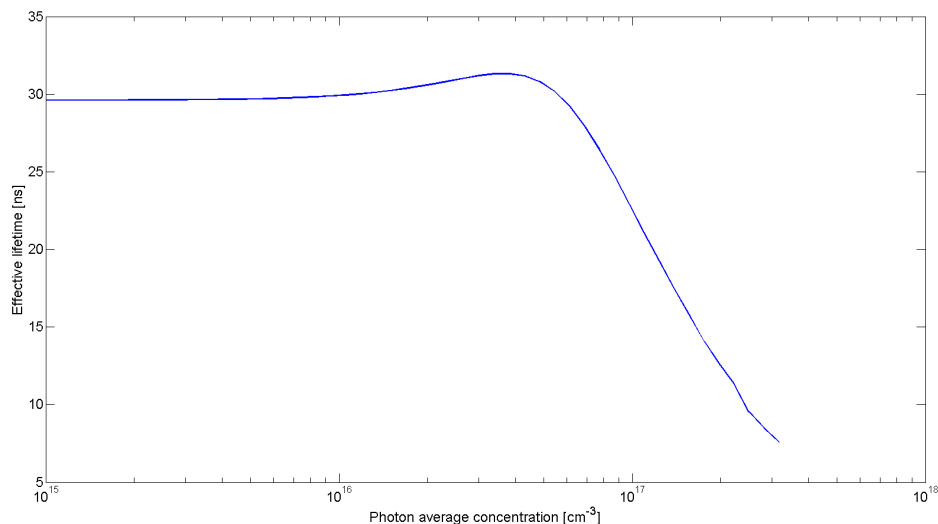


Figure 3.6: Effective lifetime of carrier in silicon for $S=1 \frac{\text{cm}}{\text{sec}}$

recombination velocity. However, as the surface recombination velocity becomes slower and slower the carrier-density peak eventually saturates.

Once I have numerically solved this equation for a given photon density profile, I can define an effective lifetime for carriers in Si for the given optical mode:

$$\tau_{eff} = \frac{2}{\beta_T h \nu_g^2 n_p^2} \frac{\int n_{Si}(x) n_p(x) dx}{\int n_p(x) dx} \quad (3.25)$$

The parameter τ_{eff} represents the average time in which generated electrons interact with the optical mode before they recombine at the surface or the bulk, or diffuse away from the mode's area. A similar approach was taken by [16]. The effect of surface recombination velocity on this time constant is shown in Figure 3.6. We can identify three regimes in this figure:

1. Low carrier densities - The effective lifetime is constant for a wide range of rather low densities. This corresponds to the flat area in the diffusion coefficient of Figure 3.4.
2. Intermediate carrier densities - The effective lifetime increases. This is due to carrier-carrier scattering that reduces the carrier mobility and hence slows down

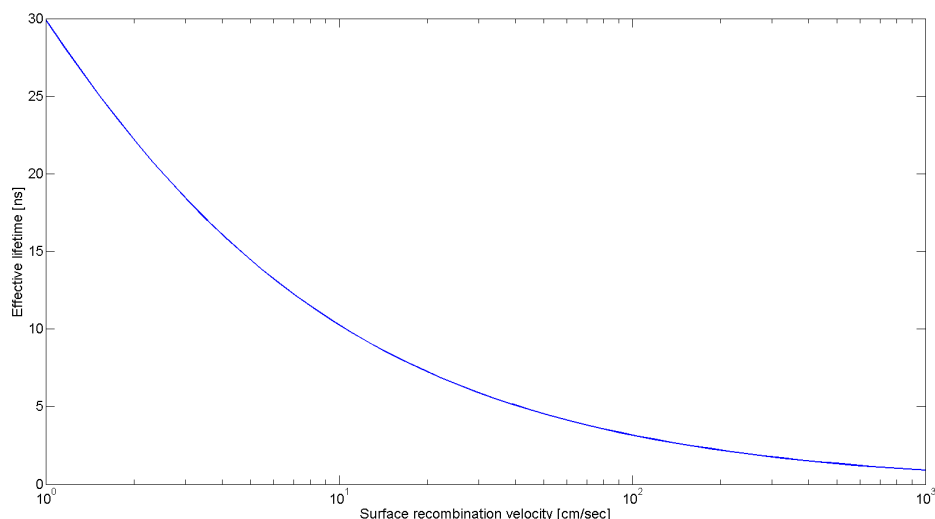


Figure 3.7: Effective lifetime of carriers in Si (low photon excitation regime)

diffusion.

3. High carrier densities - Effective lifetime reduces with density. This is due to Auger recombination at the bulk, which becomes dominant at high densities.

This behavior also explains the saturation of peak density shown in Figure 3.5 — Auger recombination processes limit the accumulation of carriers.

Finally, the effective lifetime of carriers in Si is shown in Figure 3.7 vs the surface recombination velocity, for low photon density excitation. According to this figure, the expected lifetimes are in the range 1–30ns for reported values of recombination velocities. Though the exact dynamics of carriers in Si is hard to monitor, the effective lifetime is often much easier to measure, or can be estimated indirectly. For example, effective lifetime of 25ns was estimated in Raman amplifiers [85]. In that work FCA associated with this relatively high time constant was shown to yield non-linear loss that effected Raman gain at high pump levels. In a different structure, lifetimes in the order of 10ns were observed in an all-optical modulation experiment [69], where free-carriers have affected modulation speed and quality at high powers.

Photo-generated free-carriers have been shown to affect the performance of many devices. The free carriers' effective lifetime, defined in this chapter, is a convenient

way to lump many physical processes into one time constant. It was shown that micron-scale devices with highly passivated surfaces, as in the case of our Si high-Q laser-resonator, can have lifetimes in the order of tens of nanoseconds.

In this chapter I have laid the foundation for the consideration of nonlinear effects in the context of high-Q Si/III-V lasers. In the next chapter, I will incorporate TPA and FCA in a model describing our lasers. Later chapters will show that these effects have a considerable impact on laser performance.

Chapter 4

Modified rate equations

As described in the last chapter, TPA and FCA can impact laser performance and dynamics. To investigate these effects, I will start with the classical rate equations. These equations can be found in almost any laser physics textbook (i.e., [13, 131, 99]). For the purpose of noise estimation, I shall use a spontaneous emission source term in the rate equation. The origin of spontaneous emission is quantum mechanical in nature; however, once an expression was derived using quantum theory, it is plugged into the rate equation as a classical term. The same is done for noise calculation: quantum mechanical results are implemented in the framework of these classical rate equations. Modifications to the classical rate equations will be done to account for non-linear effects. Terms for TPA and FCA will be added to the rate equations, and another equation for the density of free-carriers in silicon will be introduced.

This chapter will describe the general methodology and will construct, step by step, the modified rate equations. This will be the foundation for the laser performance analysis in later chapters.

4.1 Flat-mode approximation

Formal rate equations include spatial variation of the electromagnetic field, the electron density, and the semiconductor mesoscopic polarization. The phase of both the optical field and polarization should also be taken into account in a rigorous study. Therefore, at least five variables are required. A system of such rate equa-

tions based on a density matrix approach was constructed and discussed by several authors [111, 1, 129]. One of the first discussions, by C.L. Tang, has shown that in the limit where the coherence time of the atomic system is much shorter than both the photon lifetime in the cavity and the relaxation time of the atomic transition, the classical rate equation is obtained and two equations are sufficient [111]. In semiconductor lasers it was shown that for very short pulses, such that the polarization can't respond fast enough, the classical rate equations don't hold [129] (in fact, gain and refractive index can't even be defined in such cases). Moreover, in semiconductor lasers, intra-band relaxation has to be assumed faster than other lifetimes in the system in order to use the classical rate equations [5]. It is also the case in our lasers that the optical mode and electron density profile vary along the resonator's volume. However, the resonator is designed such that these spatial variations are slow to avoid spatial hole burning, and thus local spikes, which might change the entire dynamics, are not an issue in our lasers.

Though spatially-dependent density matrix formulation is possible in our system, it will make the numerical analysis difficult and might shadow some of the important nonlinear physics. Therefore, in order to numerically investigate non-linear laser-dynamics, it is advantageous to simplify the model. To that end, I will neglect all spatial variations and approximate our mode as constant within a rectangular box. The size of the box will be equivalent to the full-width-half-max (FWHM) volume of the mode, and the amplitude will be taken as the average amplitude within that rectangle.

The electron density in the QWs will also be taken constant within a box. Since I am only interested in the QW electrons that have significant contribution to the modal gain, I will choose the size of that box to correspond to the dimension of the optical mode, in the x and z dimensions (referring to Figure 4.1). The third dimension (y) will represent the thickness of the QW layer, since the optical mode is approximately fixed over nanometer scale.

The interaction strength between photons and electrons will be calculated using the overlap integral for TE mode defined in Equation 2.10. This methodology, ex-

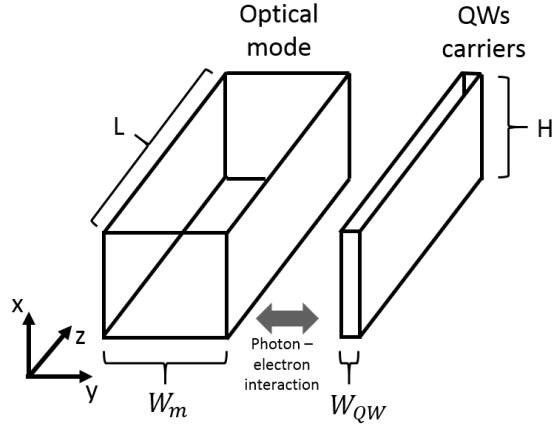


Figure 4.1: Flat mode approximation for the optical mode and the electron density

pressed graphically in Figure 4.1, will allow me to neglect any spatial profile of both photons and electrons, while accounting for the interaction between the two. It is worth noting that in many textbooks the quantum wells are localized at the peak of the mode. In these cases it is common to use the volume of the quantum well to calculate the strength of the interaction. This approach is not valid in our case, since the QWs are located at the far tail of the optical mode.

4.2 Working with densities or total numbers?

After neglecting any spatial dependence, one has to decide whether to express the rate equations using the total numbers of photon/electrons or their density. There is a certain elegance in expressing the rate equations in total number, as the equation for photon and electron becomes symmetrical. For example, the rate of generation (absorption) of the total number of photons N_p in the box will be calculated using the material gain (loss) G_m :

$$\frac{dN_p}{dt} = \Gamma_{QW} G_m N_p \quad (4.1)$$

Conservation of energy during radiative recombination of QW electrons and the quantum nature of photons will force the rate equation for the generation of total number

of electrons to be exactly the same (with an opposite sign):

$$\frac{dN_e}{dt} = -\Gamma_{QW}G_mN_p \quad (4.2)$$

Furthermore, one could associate fluctuations due to spontaneous emission as addition of a single photon to the cavity [31], which will be easily evident in the total number representation.

However, my main goal here is to consider the effect of non-linear effects. TPA, and other $\chi^{(3)}$ processes depend on the **intensity** of light. For that reason, the size of the “box” does matter. Furthermore, the magnitude of the gain term G_m will depend on **density** of QW electrons. For all these reasons, writing the rate equations in terms of total numbers will be futile. On the other hand, some features that distinguish our hybrid spacer lasers from conventional lasers will become more evident in the density representation. I will therefore use the **density** of photons/electrons to construct the rate equations.

4.3 Pump

Our laser is electrically pumped through the contact pads shown in Figure 2.1. The current flow through the path is defined by the ion implantation mask. Fabrication tolerances and non-optimized ion-implant processes will be manifested as leakage: a fraction of the pump electrons will leak to areas of little interest (outside the mode area). Furthermore, the QWs themselves have some quantum efficiency associated with them. In this work, I will lump all factors that reduce the pump efficiency to one parameter: η_i . The rate of change of the density of QW electrons n_e due to pump current I will be given by:

$$\frac{dn_e}{dt} = \frac{\eta_i I}{qV_{QW}} \quad (4.3)$$

where V_{QW} is defined as the effective volume of the QW electron box (see Figure 4.1).

4.4 Linear loss

The linear loss in our laser is defined as the combination of intrinsic loss, dominated by scattering, and mirror loss. It is convenient to describe the total loss α (in units of sec^{-1}) using the quality factor Q :

$$\frac{1}{Q} = \frac{\Gamma_{III-V}}{Q_{III-V}^{int}} + \frac{1 - \Gamma_{III-V}}{Q_{Si}^{int}} + \frac{1}{Q^{mirror}} \quad (4.4)$$

$$\alpha = \frac{2\pi\nu}{Q} = \text{photon decay rate } [\text{sec}^{-1}] \quad (4.5)$$

Where Q_{Si}^{int} and Q_{III-V}^{int} are the intrinsic losses in Si and in III-V, respectively and Q^{mirror} is the external mirror loss. Q_{Si}^{int} is dominated by scattering loss and will depend on the mode profile. I can therefore interpret the term $\frac{1 - \Gamma_{III-V}}{Q_{Si}^{int}}$ as loss due to sidewall scattering in Si experienced by the **composite** hybrid Si/III-V mode. For designs that mostly utilize Si, the intrinsic loss of the composite mode will be very close to loss in the passive Si-only resonator. I therefore use the passive loss to approximate Q_{Si}^{int} .

The output power will depend on how much light we couple as useful output through the mirrors. If the mirrors are too strong, the intra-cavity intensity will be higher, but the laser will be inefficient since most of the loss is not due to useful output. If the mirror loss is too high, the total loss will be dominated by it, and the Q will be low. A good balance between output power and linewidth can be achieved in the ‘‘optimal coupling’’ point, defined as the point in which [99]:

$$\frac{1}{Q_c} = \frac{2}{Q^{mirror}} \quad (4.6)$$

At this point, the intrinsic loss is equal to the external loss. Beyond optimal coupling, we can only increase the total Q by at most a factor of two, at the expense of a major reduction in output power (approaching zero at the limit).

4.5 Gain

The gain for the laser is provided by the monolithically grown quantum wells in the III-V. The amount of gain depends on the strength of the interaction between the carriers in the quantum wells and the lasing mode. The theoretical treatment describing QW gain in the literature often has somewhat of a dissonance; the density of states is calculated using quantum mechanics and is considered to be a two-dimensional quantity, while the gain is often calculated using the confinement factor, which assigns finite volume to the quantum well. In the next sub-section, I will address this ambiguity and describe my approach to expressing the modal gain.

4.5.1 The quantum-well: a two or three dimensional creature?

A ‘textbook’ quantum well is usually described using a potential well of small dimension in one axis (i.e., z direction) with infinite energy barriers. The k -vectors of the resulting quantized electron wave-function will be sparsely spaced in the k_z direction. The energy levels in the well will also be discrete where each level corresponds to a well-defined wave-function in the z -direction. Therefore in a QW laser, where most transitions are from the ground state of the QW, the wave-function of the electrons in the z -direction is well-defined, and the electrons behave like a two-dimensional electron gas. For this reason, a quantum well is inherently a two-dimensional creature. If we treat it as two-dimensional, we should express the density of states per **unit area** $\rho_a^{(2D)}$ and the interaction with the optical mode will be restricted to a **single slice** z_0 . The modal gain will be proportional to the product of the density of state and the intensity [77]:

$$G \sim \rho_a^{(2D)} E^2(z_0) \quad (4.7)$$

where $\rho_a^{(2D)}$ doesn’t depend directly on the thickness of the QW W_{QW} .

In reality, we are using a stack of several QWs (five in our case) and they don’t have infinite potential barriers. The separation between them is large enough so that the wave-function of the electron is approximately a linear combination of the separate

wells. Each wave-function will be spread out due to the finite barrier size. In this case the QW stack is no longer a well-defined two-dimensional creature, though we can still treat it this way. Treating it as a three-dimensional object and assigning a volume to it will not change any of the results. The density of states per **unit volume** $\rho^{(2D)}$ will be inversely proportional to W_{QW} , but now the gain will be calculated using an overlap integral between the mode and the electron wave-function, and will be summed over all QWs in the volume.

It is a matter of choice how to represent the gain, either by using the field at a point $E^2(z_0)$, or by using the overlap integral and the confinement factor Γ_{QW} . Doing it with the latter provides more general results, because they could be easily converted to a bulk gain medium, or quantum dots. This representation is also more common in the literature. I will therefore adhere to the representation using the confinement factor.

4.5.2 Active confinement factor

The rate of the total electron and photon number of Equations 4.1 and 4.2 can be converted to densities by dividing the equation by the volume of the optical cavity and the QW, respectively. Referring to Figure 4.1, it is useful to define a geometrical confinement factor:

$$\Gamma_{geom} = \frac{W_{QW}}{W_m} \quad (4.8)$$

The rate equation for the densities representing gain could be written as:

$$\frac{dn_p}{dt} = \Gamma_{QW} G_m(n_e) n_p \quad (4.9)$$

$$\frac{dn_e}{dt} = -\frac{\Gamma_{QW}}{\Gamma_{geom}} G_m(n_e) n_p \quad (4.10)$$

As expected, the representation using densities is no longer symmetrical. In most lasers, the QWs are located exactly at the peak of the mode. In this case, the

confinement factor can be well-approximated using the geometrical confinement:

$$\frac{\Gamma_{QW}}{\Gamma_{geom}} \approx 1 \quad (4.11)$$

which is what most, if not all, textbooks show. The fact that this approximation is no longer valid in our special case will have major consequences on the small signal dynamics and on gain saturation.

4.5.3 Material gain

It is common to use the empirical formula for the material gain [13]:

$$G_m(n_e) = G_0 \ln \left(\frac{n_e}{n_{tr}} \right) \quad (4.12)$$

G_m is the material gain in units of sec^{-1} , where the differential gain is given by $\frac{dG_m}{dn_e} = \frac{G_0}{n_e}$, and n_{tr} is the transparency carrier-density. The low losses due to the high-Q resonator enable the laser to operate close to transparency. This allows us to define $G'_m = \frac{G_0}{n_{tr}}$ and write the material gain using the approximate linear expression:

$$G_m = G'_m(n_e - n_{tr}) \quad (4.13)$$

This will make some of the calculations and numerics easier.

4.6 Spontaneous emission

The rate of spontaneous emission into the mode is given by Equation 2.3. The rate for the photon density can be expressed by dividing the equation by modal volume:

$$R'_{sp} = \frac{\Gamma_{QW} G_m(n_e) n_{sp}}{V_p} \quad (4.14)$$

$$\frac{dn_p^{(sp)}}{dt} = R'_{sp} \quad (4.15)$$

It is evident here that the reduced QW confinement factor Γ_{QW} , i.e., reduced rate of spontaneous emission, which is a characteristic of our high-Q platform, minimizes the spontaneous emission rate into the mode. It is also important to note that our rate equations only express photon density, and completely ignore the phase. The spontaneous emission term in the rate equations is important because it provides an initial photon source for lasing, and a straightforward way to estimate the S-T linewidth. In Chapter 9 I replace this term with properly normalized Langevin forces.

4.6.1 Model for the population inversion factor

It is common in the literature to set the population inversion coefficient n_{sp} to a constant. Values of 1-2 are common [13]. However, in our case this might lead to gross errors. Since our low-loss lasers are working very close to transparency this term can reach very high values. To calculate n_{sp} exactly we need to know the exact form of the quasi-Fermi levels. In general, the two quasi-Fermi levels are different and are not symmetrical with respect to the center of the electronic bandgap. This could be a consequence of doping or the different effective masses for electrons and holes [77]. However, to simplify our calculation while still getting the right trends and physics, I shall assume that the two quasi-Fermi levels are exactly symmetrical with respect to the center of the bandgap, and that the Fermi-level is exactly at the center of the bandgap. This situation is depicted in Figure 4.2. Exploiting the symmetry in this model, I can express the distance of the electrons quasi-Fermi level from the conduction band using the bandgap and quasi-Fermi level separation:

$$2(E_2 - E_{f,c}) = E_{21} - \Delta E_f \quad (4.16)$$

At transparency (in any SCL) $\Delta E_f = E_{21}$, and due to the symmetry I can further write $E_{f,c} = E_2$. I will use this relationship to express the conduction band electrons above transparency using:

$$n_e = \frac{2 \cdot n_{tr}}{1 + e^{(E_2 - E_{f,c})/KT}} \quad (4.17)$$

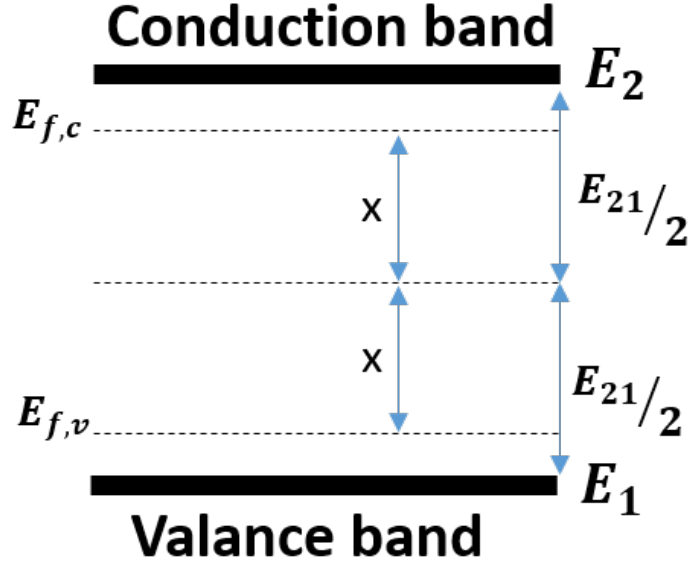


Figure 4.2: Symmetrical quasi-Fermi level model

Finally, I can use Equation 2.4, 4.16 and 4.17 to express the population inversion factor using useful macroscopic quantities:

$$n_{sp} = \frac{1}{1 - \left(\frac{2n_{tr}}{n} - 1\right)^2} \quad (4.18)$$

Though this is a very approximated expression that should be used with caution, it gives a simple way to calculate the population inversion factor that gives the correct behavior. It is unity in complete inversion (in this model full inversion is at $n = 2n_{tr}$), and blows up very close to transparency.

4.7 Two-photon-absorption

The flat-mode approximation makes our calculations much simpler since it neglects spatial variations and assigns an average photon density to a fixed box. In terms of TPA, this approximation is a bit problematic. TPA depends on the local intensity of the mode, and loss rate scales as the intensity square. By taking an average value lower than the peak's intensity, we might underestimate TPA. The exact (local) equation

in Si:

$$\frac{dn_p(\mathbf{r})}{dt} = -\beta_T h\nu v_g^2 n_p^2(\mathbf{r}) \quad (4.19)$$

can be averaged by integration:

$$\frac{1}{V_p} \int \frac{dn_p(\mathbf{r})}{dt} d^3r = -\beta_T h\nu v_g^2 \frac{1}{V_p} \int_{Si} n_p^2(\mathbf{r}) d^3r \quad (4.20)$$

Notice that the integral in the RHS is with respect to the density **squared**. It is therefore different from the definition of the confinement factor, which is linear in the photon density. To express the averaged equation I define the factor M_{TPA} and express the integral on the RHS by:

$$\frac{1}{V_p} \int_{Si} n_p^2(\mathbf{r}) d^3r = \frac{M_{TPA}}{V_p^2} \left(\int_{Si} n_p(\mathbf{r}) d^3r \right)^2 \quad (4.21)$$

such that now the integral in the RHS can be expressed using the confinement factor in Si Γ_{Si} and the average photon density n_p :

$$\frac{1}{V_p} \int_{Si} n_p^2(\mathbf{r}) d^3r = M_{TPA} \Gamma_{Si}^2 n_p^2 \quad (4.22)$$

Where M_{TPA} is defined from Equation 4.21 as:

$$M_{TPA} = V_p \frac{\int_{Si} |E(\mathbf{r})|^4 d^3\mathbf{r}}{\left(\int_{Si} |E(\mathbf{r})|^2 d^3\mathbf{r} \right)^2} \quad (4.23)$$

The total loss rate for TPA will be given by:

$$\frac{dn_p}{dt} = -\beta_T h\nu v_g^2 M_{TPA} \Gamma_{Si}^2 n_p^2 \quad (4.24)$$

4.8 Spontaneous recombination in the QW

The excited electrons in the QWs have a finite lifetime, as was the case in Si (see section 3.2.2). However, unlike the case in silicon, InGaAsP is a direct bandgap

semiconductor. Therefore, radiative spontaneous recombination (spontaneous emission) will play a bigger role. Other recombination mechanisms are also important: non-radiative recombination via SRH or Auger processes. I will lump all the recombination processes, radiative and non-radiative, into one time constant τ_r that will enter the rate equation for electrons in the QWs:

$$\frac{dn_e}{dt} - \frac{n_e}{\tau_r} \quad (4.25)$$

It is possible to capture the dependence of the time constant on the density of electrons to better account for radiative and Auger recombination. However, this will clutter our expressions and slow down the numerical analysis. Furthermore, the goal of this work is to evaluate the effect of non-linear TPA and FCA. Adding nonlinearities in the form of a density-dependent lifetime might shadow some important physics. I therefore treat this lifetime as constant.

4.9 Rate equation for free-carriers in silicon

Following the discussion in section 3.2 I will use the effective lifetime τ_{eff} of carriers in silicon to account for recombination in the bulk, the surface, and diffusion of the carriers away from the mode. The total number of carriers generated by TPA can be given by half the total number of photons absorbed by TPA (since two photons generate one carrier). When writing a rate equation for the **density** of carriers in silicon, I consider only the volume that is occupied by silicon. Therefore, I can construct a rate equation for the density of silicon carriers n_{Si} :

$$\frac{dn_{Si}}{dt} = \frac{1}{2}\beta_T h\nu v_g^2 M_{TPA} \Gamma_{Si} n_p^2 - \frac{n_{Si}}{\tau_{eff}} \quad (4.26)$$

This will add an extra rate equation for the system of equations, which is another contribution of this work compared to conventional lasers analysis.

4.10 Free-carrier-absorption

As described in section 3.2, I will use the empirically measured cross-section σ_a to account for optical absorption by free-carriers in silicon. Only portions of the mode confined in Si will be affected by silicon FCA so that the loss scales with the confinement factor Γ_{Si} . The rate equation for the loss in photon density due to FCA is therefore given by:

$$\frac{dn_p}{dt} = -v_g \sigma_a n_{Si} \Gamma_{Si} n_p \quad (4.27)$$

It is worth noting that on first glance, this equation looks like an extra linear loss term. However, the loss rate term is also proportional to the n_{Si} . It is clear from Equation 4.26 that in the steady state ($\frac{d}{dt} = 0$) the number of carriers in silicon is proportional to n_p^2 :

$$n_{Si,0} = \frac{1}{2} \tau_{eff} \beta_T h \nu v_g^2 M_{TPA} \Gamma_{Si} n_{p,0}^2 \quad (4.28)$$

Therefore the FCA absorption loss rate in the steady state will take the form:

$$\left. \frac{dn_p^{(\text{FCA loss})}}{dt} \right|_{\text{steady state}} = -\frac{1}{2} v_g \sigma_a \Gamma_{Si}^2 \tau_{eff} \beta_T h \nu v_g^2 M_{TPA} n_{p,0}^3 \quad (4.29)$$

It is now evident that FCA can in fact be considered, at least mathematically, as a three-photon-absorption process since it is proportional in the steady-state to n_p^3 . It is therefore expected that when the photon density is high, FCA might be dominant.

4.11 Total loss rate

So far I have identified the main three loss mechanisms in our lasers: linear loss, TPA, and FCA. From sections 4.4, 4.7, and 4.10 I can compare these three mechanisms to gain some insight on the magnitude of each. For example, a comparison of different loss mechanisms is shown in Figure 4.3. As can be shown in Figure 4.3, loss due to FCA can exceed that due to the linear loss at sufficiently high photon densities. To gain some insight on the order of magnitude of photon densities it is worth noting that for typical waveguide dimensions (i.e., cross-section of $(1\mu\text{m})^2$), photon density

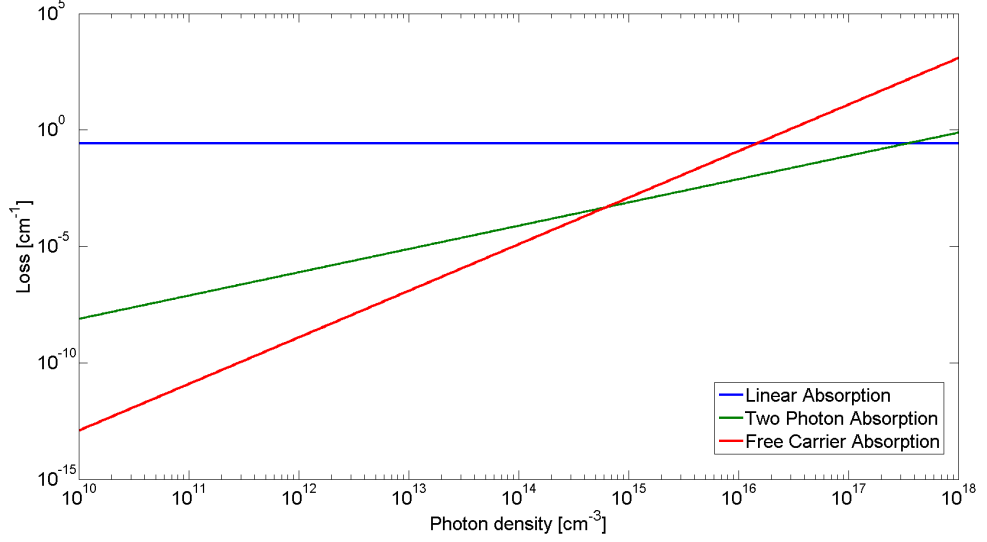


Figure 4.3: Comparison between different loss mechanisms vs. photon density. $Q_{Si} = 10^6$, typical absorption in III-V is assumed (i.e., 10cm^{-1}), confinement factor in III-V of 1% and effective lifetime of carriers in Si of $\tau_{eff} = 30\text{ns}$.

of $10^{17}[\text{cm}^{-3}]$ represents intra-cavity power of about 1 Watt.

4.12 The modified rate equations

I can now express the complete system of rate equations:

$$\frac{dn_e}{dt} = -\frac{n_e}{\tau_r} - \frac{\Gamma_{QW}}{\Gamma_{Geom}} G_m(n_e) n_p + \frac{\eta_i I}{qV_{QW}} \quad (4.30)$$

$$\begin{aligned} \frac{dn_p}{dt} = & (\Gamma_{QW} G_m(n_e) - \alpha) n_p - \beta_T h\nu_g^2 M_{TPA} \Gamma_{Si}^2 n_p^2 \\ & - v_g \sigma_a n_{Si} \Gamma_{Si} n_p + R'_{sp} \end{aligned} \quad (4.31)$$

$$\frac{dn_{Si}}{dt} = \frac{1}{2} \beta_T h\nu_g^2 M_{TPA} \Gamma_{Si} n_p^2 - \frac{n_{Si}}{\tau_{eff}} \quad (4.32)$$

The parameters I will use for the rate equation analysis are summarized in table 4.1.

This chapter formally incorporated TPA and FCA in the rate equations and pinpointed some unique characteristics of the high-Q hybrid platform. This analysis will

¹Measured experimentally. Measurement technique and details appear in later chapters.

Parameter	Description	Value	Units
τ_r	Recombination life time (including non-radiative)	$50 \cdot 10^{-9}$	sec
G_m	Material gain	Equation 4.13	sec^{-1}
G'_m	Differential material gain	$1 \cdot 10^{-19}$	m^2
n_{tr}	QWs transparency density	$2 \cdot 10^{24}$	m^{-3}
η	Quantum efficiency (including current leakage)	0.3	-
I	Pump current	(sweep)	Amper
q	Electron charge	$1.6 \cdot 10^{-19}$	Coulombs
V_{QW}	Quantum well effective volume	$4.2 \cdot 10^{-17}$	m^3
V_p	Effective mode volume	$6 \cdot 10^{-16}$	m^3
α	Linear loss rate in the cavity	Equation 4.5	sec^{-1}
Γ_{QW}	QW confinement factor	Equation 2.10	-
Γ_{geom}	Geometrical confinement factor	0.07	-
v_g	Mode's group velocity	$c/3.53$	$\frac{\text{m}}{\text{s}}$
β_T	TPA coefficient	$8 \cdot 10^{-12}$ [17, 8]	$\frac{\text{m}}{\text{W}}$
M_{TPA}	TPA magnification factor	Equation 4.23	-
σ_a	FCA cross section	$1.45 \cdot 10^{-21}$ [58]	m^2
Γ_{Si}	Si confinement factor	eq. 2.10	-
R_{sp}	Spontaneous emission rate into mode	Equation 4.14	sec^{-1}
τ_{eff}	Si carriers effective lifetime	30ns^1	sec

Table 4.1: Parameters used for rate equations

lay the foundation for a detailed exploration of laser performance in the following chapters.

Chapter 5

Steady-state operation - Theoretical analysis

In the previous chapter, I developed a set of rate equations that describes the laser operation and included nonlinear effects such as TPA and FCA. The first step towards understanding the effect of the nonlinear terms on the laser performance is to solve the set of equations for the steady-state point. I will therefore set all $\frac{d}{dt} = 0$ in the LHS of Equations 4.30-4.32.

5.1 Steady-state carrier density in silicon

The third equation for the Si carriers is the simplest to solve:

$$n_{Si,0} = \frac{1}{2} \beta_T h \nu_g^2 M_{TPA} \Gamma_{Si} n_p^2 \tau_{eff} \quad (5.1)$$

The average density of the Si carriers is proportional to the square of the density of photons and to τ_{eff} . As expected, increasing the intra-cavity intensity would quickly increase the Si carrier density and will yield increased losses through FCA. From Chapter 3.2 we know that the effective lifetime of carriers in Si can vary by two orders of magnitude, depending on the surface quality and device dimensions. It is now clear that the carrier density in Si (and therefore FCA) scale with this time constant.

5.2 Gain saturation

I will now deal with the first rate Equation 4.30 for the electron density in the QW. To make the expressions analytical I will use the linear material gain model of Equation 4.13. setting $\frac{dn_e}{dt} = 0$, I get the expression for the modal gain:

$$\Gamma_{QW}G'_m(n - n_{tr}) = \frac{\Gamma_{QW}G'_m(n_{pump} - n_{tr})}{1 + G'_m \frac{\Gamma_{QW}}{\Gamma_{geom}} \tau_r n_{p,0}} \quad (5.2)$$

where I have defined

$$n_{pump} = \frac{\eta_i I}{qV_{QW}} \tau_r \quad (5.3)$$

Notice that the density defined by n_{pump} is the steady-state density if we set $n_p = 0$. Therefore we can interpret n_{pump} as the steady-state carrier density we pump into the QWs. Equation 5.2 is a familiar saturated gain term, with gain saturation coefficient:

$$\epsilon_s = G'_m \frac{\Gamma_{QW}}{\Gamma_{geom}} \tau_r \quad (5.4)$$

such that:

$$G'_m(n_p) = \frac{G'_m}{1 + \epsilon_s n_p} \quad (5.5)$$

There is one noticeable difference in the gain saturation coefficient compared to conventional lasers: the dependence on the ratio $\frac{\Gamma_{QW}}{\Gamma_{geom}}$. In a conventional laser, this term is usually unity. Since the QWs in our lasers are located at the tail of the optical mode, the gain saturation coefficient is much lower than the value in a conventional laser.

5.3 Threshold current

Just below threshold, the intra-cavity intensity is very low and nonlinear effects are negligible. Therefore, the threshold current is not effected by TPA and FCA. Above transparency, the current has to be increased to the point in which the gain overcomes loss in order to start lasing oscillation. Different spacer designs have different modal

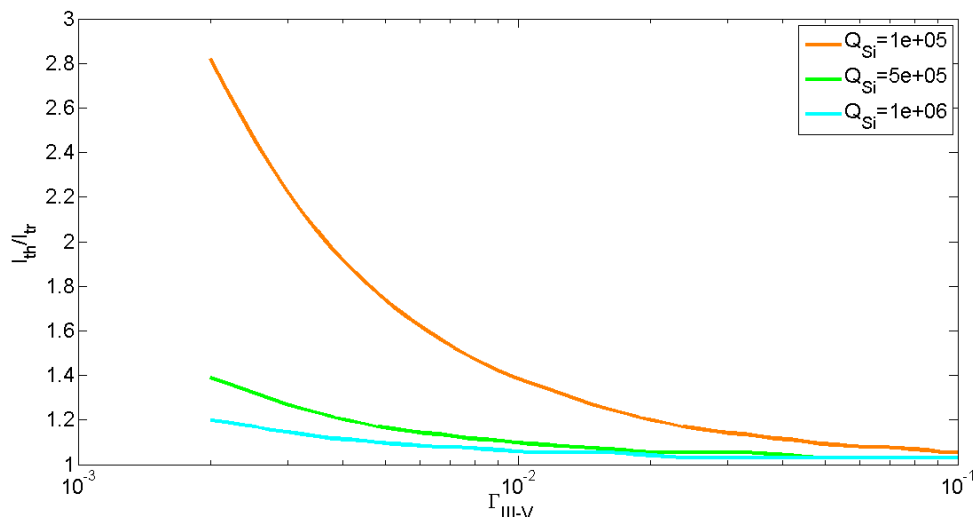


Figure 5.1: Threshold current vs. confinement factor in III-V for different quality factors of the Si resonator

gain values, since the interaction with the QWs is reduced with thicker spacers. However, the modal loss is also reduced as a consequence of the increased overlap with the low-loss material and the reduced overlap with the lossy materials. This is one of the key features and strengths of this platform and design approach.

As long as the total-Q remains lower than the silicon-Q (intrinsic and external), a small increase in spacer thickness will yield a linear reduction in the total loss. This is demonstrated in the quasi-linear portion of the plot in Figure 2.3. When the thickness is increased to a point in which the total-Q is approaching the silicon-Q, the reduction in loss starts to saturate. Since the reduction in gain is always linear with the confinement factor, the lasing condition will now be met at a higher level, and threshold is increased.

This behavior is demonstrated in Figure 5.1, which was obtained using the numerical solution to the rate equations. Figure 5.1 demonstrates a very important feature of the hybrid Si-III-V platform: starting with a high-Q silicon resonator allows us to increase the total-Q by increasing spacer thickness without trading off threshold current. However, if we overdo it by working too close to the silicon-Q, we pay a penalty in threshold current.

5.4 Output power

Output power is one of the most important metrics for almost every application. Narrow-linewidth lasers are often used for sensing or ranging, where output power is crucial to ensure enough photons fall on the photodetector so the signal is well above the instrumental noise. In coherent communication, a combination of output power and linewidth is used to calculate bit-error-rate. External amplification of the output power might result in the corruption of the initial high coherence.

5.4.1 Wall-plug efficiency

Every laser has an unavoidable intrinsic loss, as well as a mirror loss. The mirror loss couples the stored energy in the cavity to the outside world as useful output. The energy lost due to the intrinsic part is connected to heat or to the modes of the free-space continuum, and is thus “wasted”. The total quality factor of a generic laser can be written as:

$$\frac{1}{Q} = \frac{1}{Q^{int}} + \frac{1}{Q^{mirror}} \quad (5.6)$$

The rate of output photons P_N (photons/sec) given using the product of the total number of photons stored N_p and the mirror loss rate is:

$$P_N = \frac{\omega N_p}{Q^{mirror}} \quad (5.7)$$

The total number of photons in the cavity can be calculated using Equation 2.7. We can define the external efficiency η_e as the ratio between the rate of output photons and input electrons:

$$\eta_e = \eta_i \left(1 - \frac{I_{th}}{I}\right) \frac{Q}{Q^{mirror}} \quad (5.8)$$

We can further express the threshold current I_{th} using the transparency current and total loss from the lasing condition (gain = loss) and assuming a linear gain model as in 4.13:

$$I_{th} = \frac{qV_{QW}}{\eta_i\tau_r} \left(n_{tr} + \frac{\omega}{Q\Gamma_{QW}G'_m} \right) \quad (5.9)$$

The external efficiency will now take the form:

$$\eta_e = \eta_i \left(1 - \frac{I_{tr}}{I} \right) \cdot \frac{Q^{int}}{Q^{int} + Q^{mirror}} - \eta_i \xi \frac{I_{tr}}{I} \cdot \frac{1}{Q^{mirror}} \quad (5.10)$$

where I_{tr} is the transparency current and we have defined the parameter ξ as:

$$\xi = \frac{\omega}{\Gamma_{QW}G'_m n_{tr}} \quad (5.11)$$

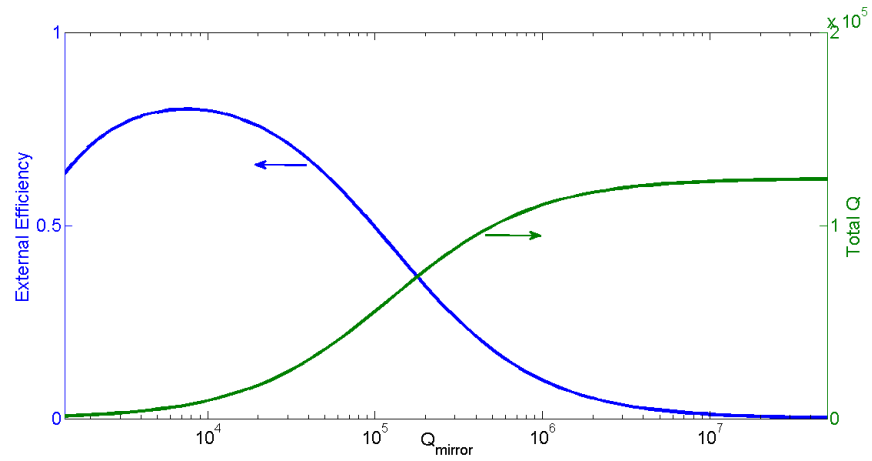
Our hybrid Si/III-V lasers have a unique form for the intrinsic and mirror quality factors given by Equation 4.4. For a given Q_{si}^{int} and a given Γ_{III-V} , I can calculate the external efficiency using Equation 5.10. An example is shown in Figure 5.2 for $Q_{si}^{int} = 10^6$ and for several values of confinement factors.

As can be seen from Figure 5.2 there is some trade off between efficiency and total Q. For the efficiency, there is an optimal mirror-Q. Increasing it to increase the total-Q for narrower linewidth will take its toll on the output power. The definition of optimal coupling defined in Equation 4.6 can now be better understood: at the optimal coupling point, where the total Q is exactly half the intrinsic Q, the efficiency is below optimal levels, but only slightly. Increasing the mirror-Q above that point can only yield a factor of two improvements in total-Q, but efficiency will quickly go to extremely low values.

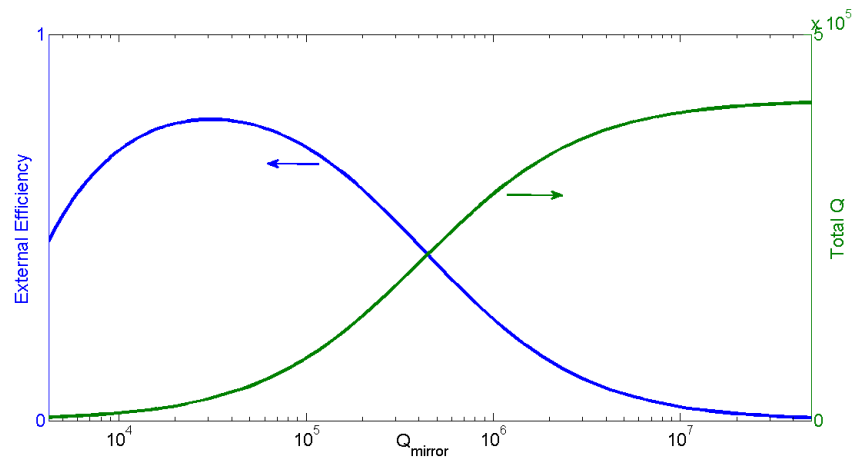
The total quality factor is a measure of the resulting linewidth of the laser. Different spacer designs yield different linewidths and efficiencies. A comparison between different designs and the exact trade-offs between quality factor and efficiency of each design are shown in Figure 5.3.

5.4.2 L-I curve

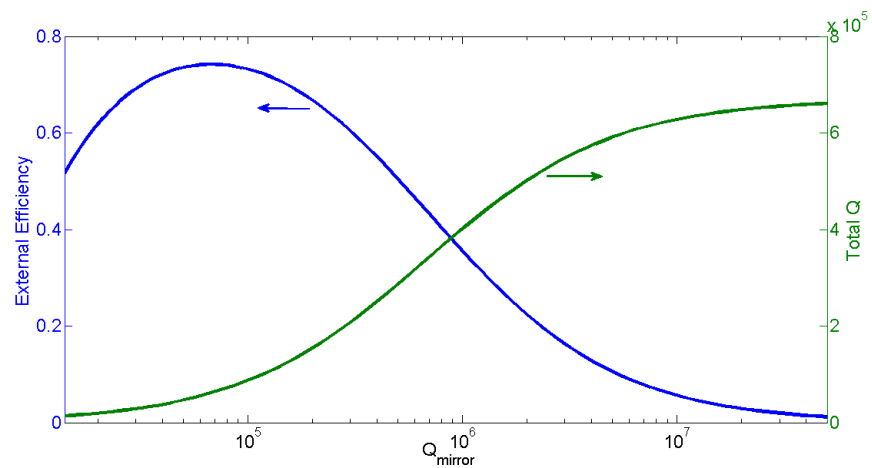
I can now solve the system of rate equations numerically in the steady state for different silicon quality factors and different confinement factors in III-V. The solution



(a)



(b)



(c)

Figure 5.2: Efficiency (left axis) and total Q (right axis) vs. mirror Q. $Q_{si}^{int} = 10^6$; $\eta_i = 1$; $\frac{I}{I_{tr}} = 10$ (a) 30nm spacer (b) 100nm spacer (c) 150nm spacer

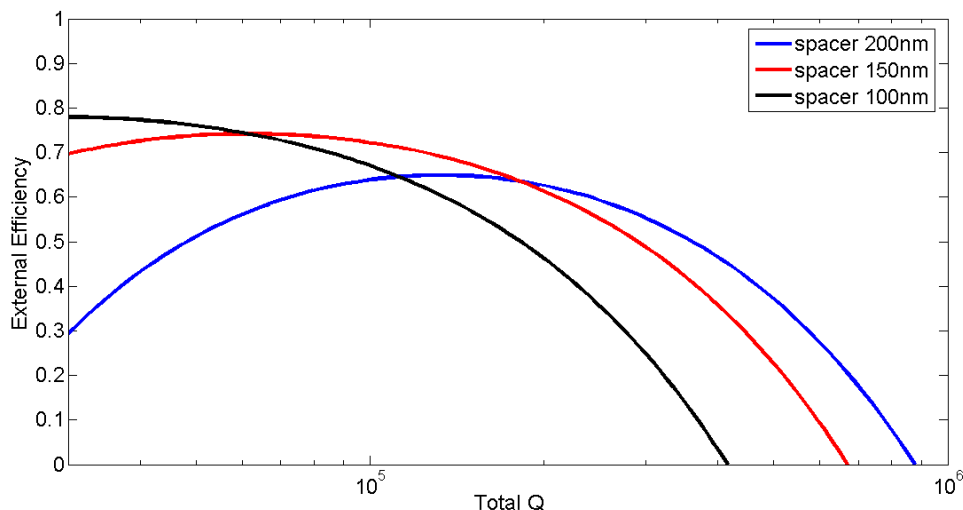


Figure 5.3: Efficiency of different spacer design vs. total-Q

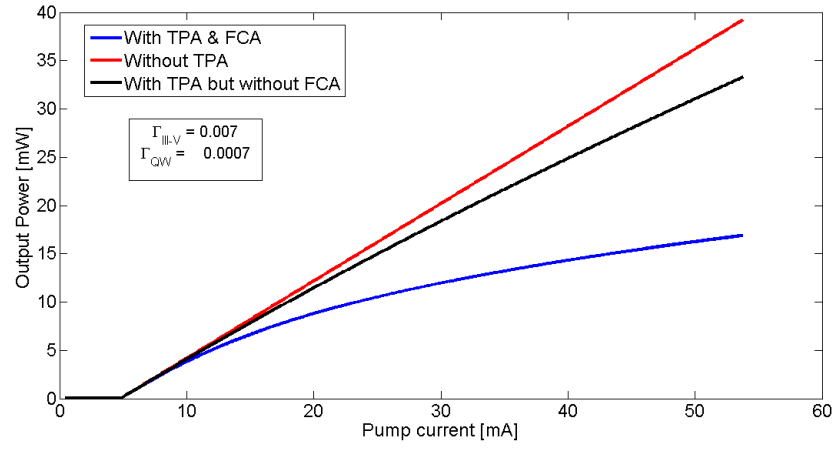
will yield the steady states photon density in the cavity, which we can convert to output power by assuming optimal coupling ($Q^{mirror} = Q^{int}$) and using:

$$P_{out} = \frac{2h\nu^2 n_p V_p}{Q^{int}} \quad (5.12)$$

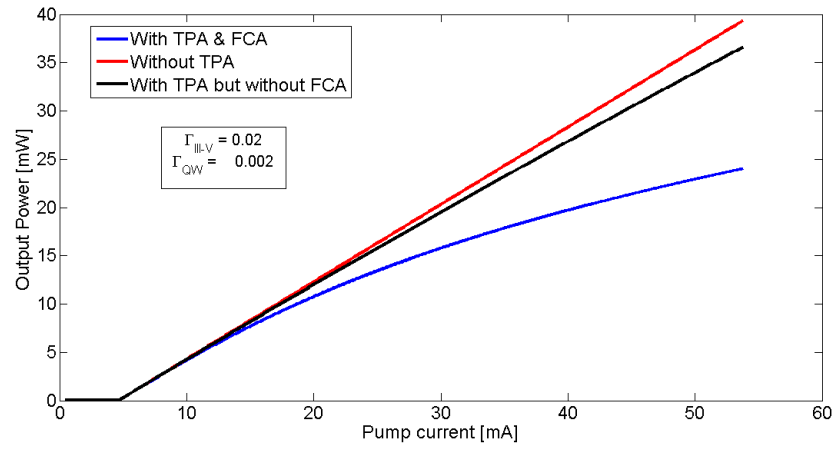
Numerically obtained L-I curves for $Q_{st}^{int} = 10^6$ for different values of confinement factors are shown in Figure 5.4, with and without the inclusion of nonlinear effects. As the intra-cavity intensity builds up, TPA and FCA processes become more and more dominant, and introduce excess loss. When the current pump increases, the intensity-dependent loss increases, and the total-Q of the cavity is reduced. As a result, the cavity cannot increase its photon storage at the same rate as the current pump and the L-I curve becomes nonlinear. As can be seen in Figure 5.4, though TPA itself affects the linearity of the L-I curve, FCA has a much bigger impact.

5.4.3 Slope efficiency

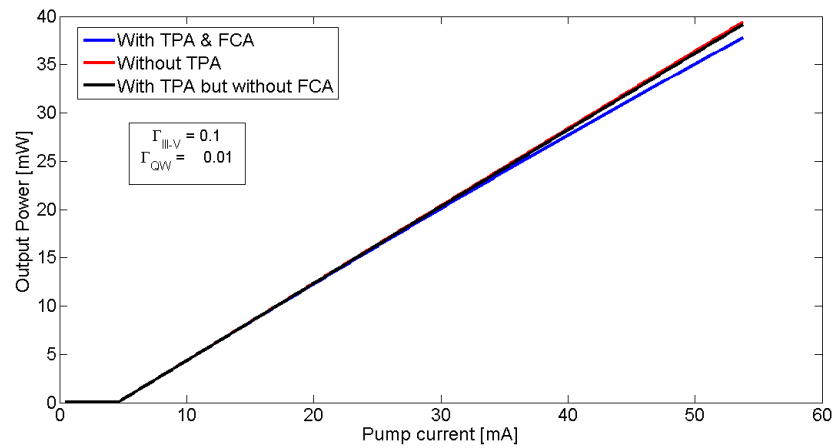
It is evident from the L-I curves of Figure 5.4 that the slope of the curve reduces with pump current due to nonlinear effects such as TPA and FCA. For high pump currents, the output power and the slope of the L-I curves are both highly affected



(a)



(b)



(c)

Figure 5.4: L-I curves for different values of confinement factors with and without nonlinear effects for $Q_{si}^{int} = 10^6$ (a) spacer 150nm (b) spacer 100nm (c) spacer 30nm

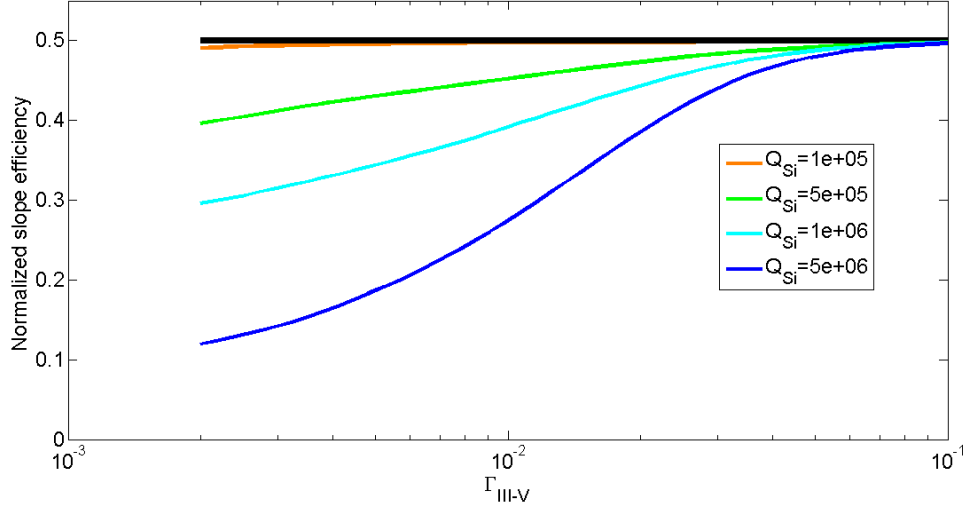


Figure 5.5: Normalized slope efficiency at $I = 4 \cdot I_{th}$

by nonlinear effects. I can define a local slope efficiency at a pump value I as the increase in number of photons at the output for every electron at the input.

$$\eta_s(I) = \frac{dN_p^{out}}{dN_e^{in}} \quad (5.13)$$

Using this definition, I can examine the impact of nonlinear effects on the power extraction efficiency for different spacer designs. For ease of interpretation of this figure of merit I will assume that the mirror-Q is exactly half the total cold-cavity-Q. In such a setup, if there were no nonlinear effects, exactly half the input energy above threshold would go to useful output. The effect of nonlinear loss is shown in Figure 5.5 for different silicon-Qs. For more aggressive designs (i.e., higher silicon-Q or lower confinement in III-V) I expect to have higher-Q, and therefore nonlinear loss would be higher for these designs. The nonlinear loss will reduce the slope efficiency and the external efficiency, as shown in Figure 5.5. Therefore, the efficiency plots of Figures 5.2 and 5.3 will change with pump current in the presence of strong TPA and FCA.

5.5 Schawlow-Townes linewidth

If a laser has only white frequency noise with a constant power spectral density $W_{\dot{\phi}}$ the spectrum of the field $E(t)$ is a Lorentzian with spectral width of [78]:

$$\Delta\nu = \frac{W_{\dot{\phi}}}{2\pi} \quad (5.14)$$

This linewidth is also known as the Schawlow-Townes linewidth.

A realistic laser will have other noise components. However, these components usually decay with frequency and have the form $1/\nu^\alpha$ for some positive α . At the high frequencies, the laser noise will usually be dominated by the S-T linewidth. If we are only interested in the high frequencies components of the signal, as in optical communication, the S-T linewidth will set an effective linewidth for the purpose of that measurement. If the frequency range of interest is below the relaxation oscillation frequency then the S-T floor is multiplied by a factor of $(1 + \alpha_H^2)$ due to coupling between amplitude and phase fluctuations [31] (the Henry linewidth enhancement).

To estimate the S-T noise floor I will use Equation 2.6 that relates the spontaneous emission rate into the mode to the frequency noise PSD floor. We estimate the spontaneous emission rate using Equation 4.14 that relates spontaneous emission to the laser's gain. The population inversion factor is calculated using the symmetrical quasi-Fermi level approximation of Equation 2.4. For a given pump power, the gain and the photon density are calculated numerically from the steady-state rate equation, and the S-T noise floor is derived.

The S-T Linewidth [91] is known to be inversely proportional to Q^2 and inversely proportional to the output power P . For laser resonators with nominally high quality factors, the nonlinear loss effectively limits the Q by introducing excess intensity-dependent loss, thus preventing the intra-cavity intensity from rising. As demonstrated in Figure 5.6, this effect increases the linewidth compared to the S-T linewidth of an equivalent resonator without TPA and FCA. For a given silicon resonator quality factor, reducing confinement in III-V increases the total-Q and re-

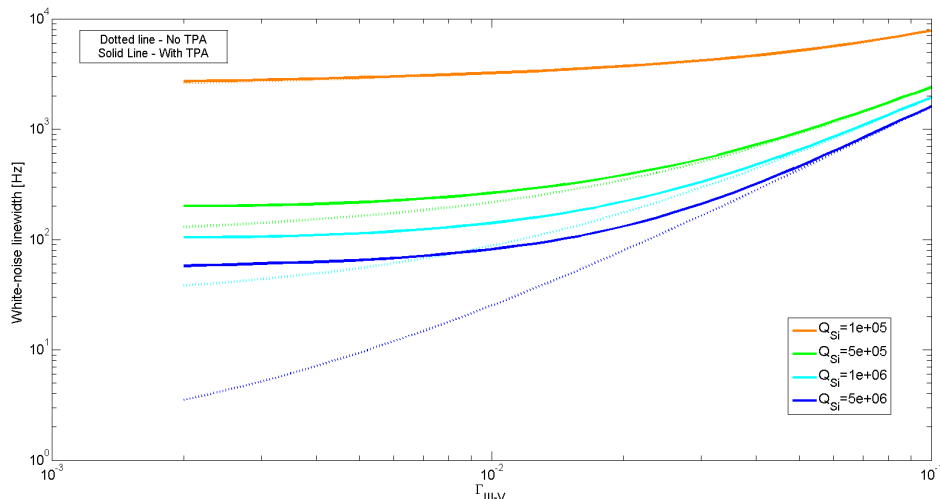


Figure 5.6: Schawlow-Townes linewidth vs. confinement in III-V for different silicon resonators, with and without nonlinear effects at $I = 4 \cdot I_{th}$

duces spontaneous emission to the lasing mode. In the absence of nonlinear loss, this process will result in quick reduction of linewidth. However, nonlinearities, such as TPA and FCA, limit the total-Q and the resulting linewidth is somewhat clamped. For example, Figure 5.6 shows that for 200nm spacer increasing the silicon-Q from 10^6 to $5 \cdot 10^6$ should result in an improvement of an order of magnitude in linewidth, and should yield S-T linewidth as low as 4Hz. However, due to TPA and FCA the improvement is limited to a factor of two, down to a value of 60 Hz. At silicon-Qs of about one million, the linewidth is limited by nonlinearities to around 100 Hz, and performs very similar to a device with quality factor of half a million. It is thus demonstrated that nonlinear loss limits the achievable linewidth, to a point where it is no longer so attractive to fabricate ultra-high-Q ($Q > 10^6$) resonators in silicon for hybrid lasers. This argument is further demonstrated in Figure 5.7. The $1/Q^2$ dependency of the linewidth is retrieved in the numerical calculation in the absence of nonlinear effects. However, in the presence of TPA and subsequent FCA this form no longer holds for high-Q. As the quality factor increases, the linewidth tends to saturate at a few tens of Hz.

The saturation of stored energy due to TPA and FCA also occurs when the pump current increases. As a consequence, the linewidth would decrease at a smaller rate

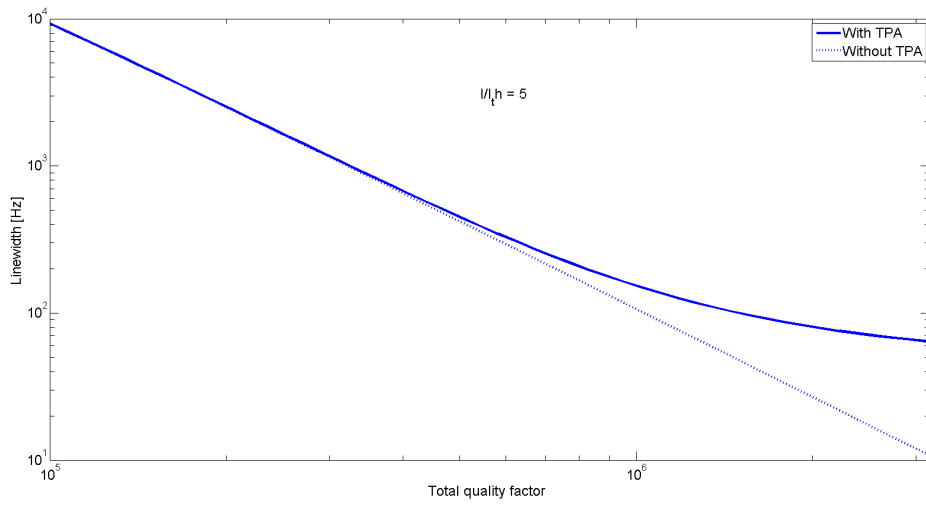


Figure 5.7: Impact of nonlinear effects on linewidth for changing quality factors. Calculated at $I = 5 \cdot I_{th}$

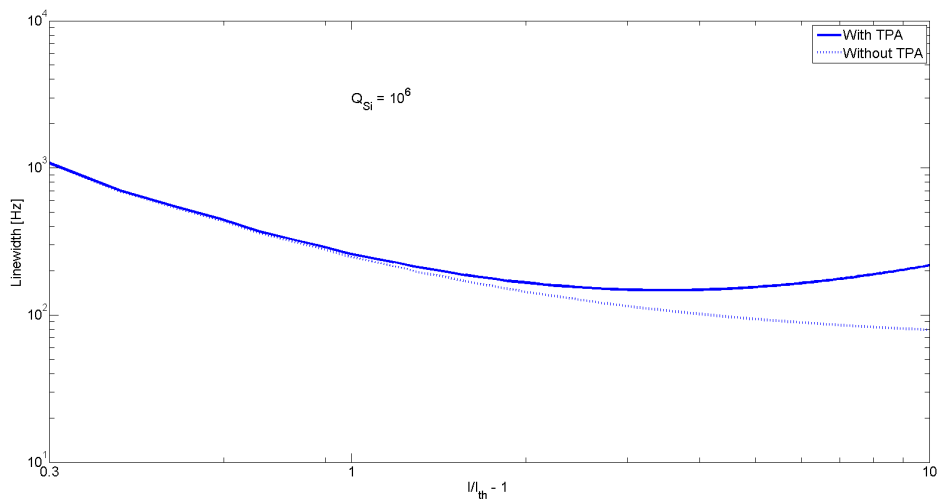


Figure 5.8: Impact of nonlinear effects on linewidth for changing pump current. Calculated at $I = 5 \cdot I_{th}$ for $Q_{Si} = 10^6$

than the expected $(I - I_{th})^{-1}$. This can be seen in Figure 5.8. Moreover, not only do nonlinear effects saturate the linewidth improvement with increased power, but even cause re-broadening of the linewidth. This is due to the increased total loss by TPA and FCA; the gain has to compensate for the excess non-linear loss by increasing the QW carrier density. This, in turn, increases the spontaneous emission rate into the mode. This effect is accompanied by the saturation of the stored energy in the cavity and leads to a broadening of the linewidth at higher currents.

In this chapter, I analyzed the steady-state performance of the lasers in light of nonlinear effects such as TPA and FCA. It was predicted that L-I curves of narrow-linewidth lasers might show nonlinear behavior. As we saw, the frequency noise-floor of these lasers will deviate from the familiar S-T formula, and may saturate or even broaden at high-power. It was also shown that although some tradeoff between wall-plug efficiency and linewidth exists, it is possible to design ultra-narrow linewidth lasers with reasonable efficiency.

Chapter 6

Steady-state operation - Experimental results

We have fabricated and characterized hybrid Si/III-V spacer lasers with several laser designs. Details on the laser design and fabrication process can be found in appendix A, while details on the measurement techniques and procedures can be found in appendix B. Steady-state performance of similar hybrid spacer lasers are also reported in [106]. Here, I will focus on results that are relevant to the observation of nonlinear effects, or new results that are absent in [106].

In the design and fabrication of the spacer lasers we have swept several parameters:

1. Wavelength - Three different grating periods — 240nm, 242.5nm, and 245nm — corresponding to the three different lasing wavelengths were fabricated.
2. Spacer thicknesses - Four different spacers were fabricated — 30nm, 100nm, 150nm and 200nm. The most aggressive design — the 200nm spacer thickness — didn't lase at all. It is possible that the modal gain for this spacer thickness was too low, indicating that the total-Q was past the point of saturation at the silicon-Q (as suggested by Figure 5.1). In this chapter, I will present results from the remaining operational three spacer designs.
3. Mirror section length - Devices were cleaved to yield five different bar lengths, corresponding to varying mirror-Qs. The exact mirror quality factor value depends strongly on etch depth and profile, which fluctuate considerably between

different fabrication runs. Therefore, a quantitative estimation of the mirror-Q is unreliable. Furthermore, we ended up with lasers with relatively low power, and for experimental reliability we had to work with lasers that have reasonable output. Therefore, this chapter will only include results from the shortest bars. Despite this fact, there is evidence to indicate that mirror-Q is still high enough to be considered under-coupled (in the regime to the right of the optimum peak in Figure 5.2). For example, overall low efficiency and decreasing output power with increasing mirror-Q, both indicate under-coupling.

4. Potential-well depth - Two designs were fabricated, with 100GHz and 120GHz well-depth (see Figure 2.2). However, designs with deeper potential wells are more confined to the defect region and therefore have an effectively stronger mirror grating. Since all devices turned under-coupled, we chose to work with the shallow-well designs to obtain more output power.

6.1 Threshold current

Threshold current was extracted from the L-I curves by locating the intersection of the slopes before and after threshold. All threshold data presented here are for stage temperature of $20^{\circ}C$. The different designs are of comparable physical dimensions. The same current channel was defined by the ion implantation steps, and the same III-V wafer was used in all cases. I therefore expect that the biggest impact on threshold current will be due to variation in modal loss, compared to modal gain between designs. The scatter plot of Figure 6.1 compares threshold currents for different spacer designs for two different lasing frequencies. Several conclusions can be drawn from Figure 6.1:

1. The spread of threshold current values is much bigger for thicker spacers. This is expected, since as the spacer thickness increases the total-Q is dominated by the silicon-Q, which varies considerably due to small variations in dimensions due to fabrication conditions. The laser bar of the 150nm spacer had only three

lasing devices. We would have most likely seen a spread with higher thresholds as well; however, these didn't lase due to thermal effects decreasing the material gain.

2. The low threshold devices of the 100nm spacer have the same threshold as the 30nm spacer. This indicates that for these devices, the silicon-Q is high enough to be in the regime where threshold is no longer affected by reduced active confinement, as suggested by Figure 5.1.
3. The spread of threshold current values is very small for the thin 30nm spacer design. This indicates that losses are dominated by the III-V intrinsic loss, which has very little variation.

6.2 L-I curves

Different spacer designs were fabricated in separate fabrication runs. Small and unavoidable variations in etch depth can have a big impact on the grating strength, and therefore on the amount of output coupling in the mirror sections of the lasers. The fabricated lasers are all under-coupled. The overall efficiency is low, and laser bars with longer mirror sections have low output power. Furthermore, there is variation in the quality of the facets, as they were cleaved but not polished. For these reasons, it is very hard to compare the efficiency between different spacer lasers: the arbitrary output coupling acts as an unknown scaling factor. It is therefore nearly impossible to draw conclusions that are based on the absolute output power across lasers. It is worth noting that though this is true for the absolute power, it is not the case for the linewidth; all the lasers are under-coupled, and therefore the loss is dominated by the intrinsic-Q and not the mirror-Q. This fact causes the linewidth of different lasers to be almost independent of the mirror transmission.

Though the absolute output power of different lasers is somewhat arbitrary, the shape of the L-I curve within a single laser contains much information. Figure 6.2 shows a comparison between typical L-I curves of the three different spacer designs.

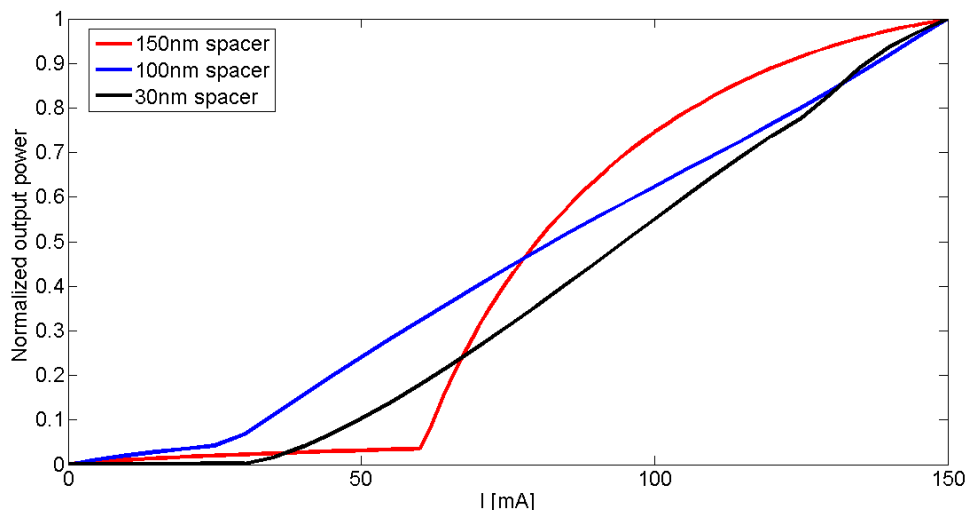


Figure 6.2: Normalized L-I curves for three spacer designs. The non-normalized output powers at $I=150\text{mA}$ are: 0.89mW , 0.62mW , and 10.2mW for the 200nm, 100nm, and 30nm spacers, respectively

The absolute magnitude of different curves was altered and normalized to ensure that all curves are on the same scale for better comparison. It is evident from Figure 6.2 that while the 30nm and 100nm spacers have a nearly linear L-I curve, the 150nm spacer is very nonlinear.

One has to be careful, though, in attributing nonlinear L-I curves to TPA and FCA. Power roll-offs are common in many laser systems. In fact, every laser will roll off (or even burn) at sufficiently high pump currents. “Standard” power roll-off is usually attributed to thermal effects [79]. Increase in pump current elevates the temperature through Joule heating, Thomson Heating, and non-radiative recombination heating. The elevated temperature lowers the gain due to the widening of the Fermi spreading of carriers. To maintain lasing at this lower gain, the carrier density increases. This in turn elevates electron leakage, Auger recombination, spontaneous recombination, and SRH recombination. It was suggested [80] that electron leakage is the main source of power roll-off.

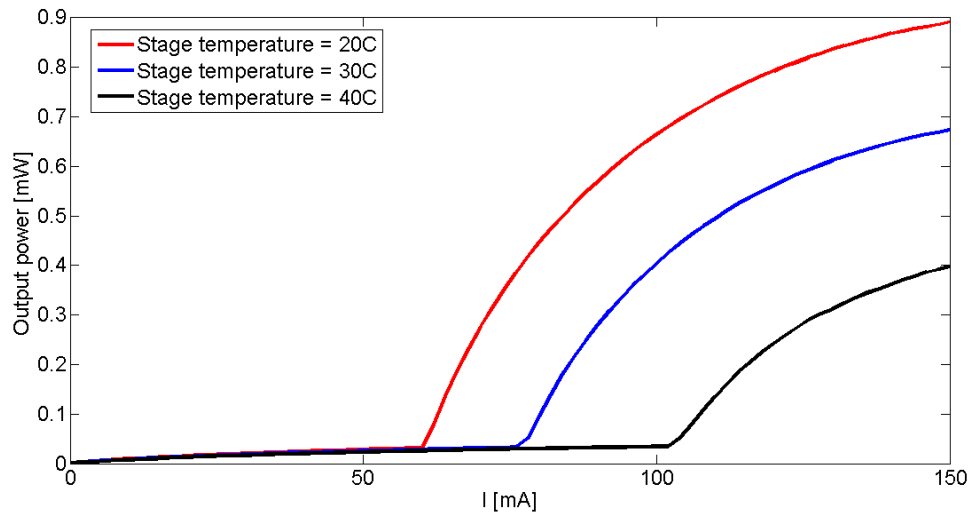
The chain of events causing power roll-off begins with Joule heating. It was found [80] that Thomson heating, which is a consequence of the capture of electrons in the QW, is of lesser impact and is compensated by Thomson cooling (due to escape

of electrons from the QW). Figure 6.3(a) shows the effect of stage temperature on the L-I curve. Furthermore, to isolate the effect of thermal power roll-off, a pulsed current source was used. Figure 6.3(b) shows L-I curves from a pulsed power source, with pulse width of $1\mu\text{sec}$ and $10\mu\text{sec}$. The short pulses and the small duty cycle guarantee that thermal effects are minimized. It is shown in Figure 6.3 that even in pulsed operation, the L-I curve of the thick spacer laser is nonlinear, in agreement with the theoretical analysis of Chapter 5 that attributed the nonlinearity to free-carrier-absorption.

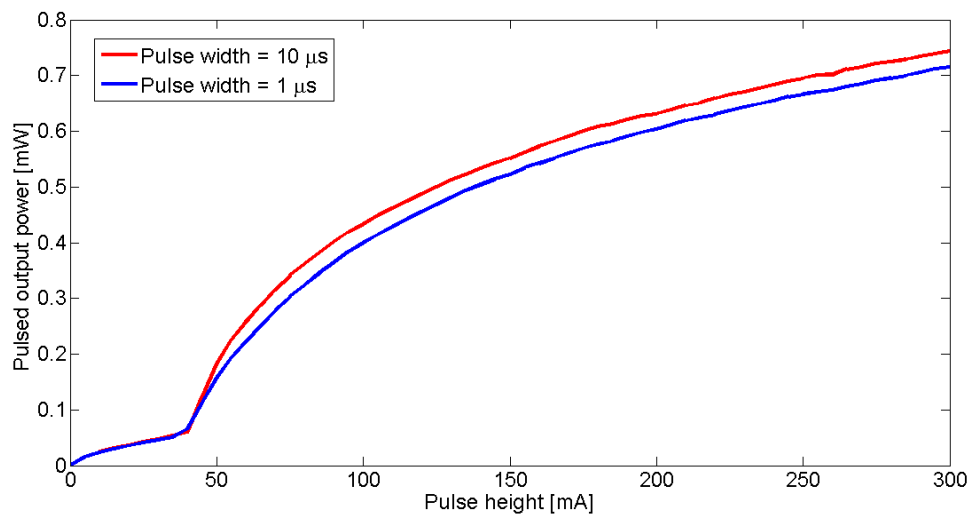
6.3 Schawlow-Townes noise floor

The Schawlow-Townes linewidth represents the spectral width of the electromagnetic field when the frequency noise spectrum consists of white noise only. In a practical laser, the noise spectrum is not a flat white noise curve. Though the noise floor is limited by the S-T linewidth, there are other noise sources that dominate in some frequency ranges. The low frequency is dominated by technical noise and thermal-fluctuations noise. This is common to almost all laser systems. Since our lasers had relatively low output power ($\sim 1\text{mW}$), we needed an amplifier to get a reliable measurement of the frequency noise. For that reason, the high-frequency noise was dominated by phase-noise added by the amplifier. The effect of the amplifier on the noise measurements is discussed in detail in Chapter 10.

The S-T noise floor was extracted from an experimental noise spectrum from the intermediate regime of $100\text{MHz} - 1\text{GHz}$. The single sided PSD of the frequency noise was multiplied by π according to Equation 5.14 (notice that in the equation $W_{\dot{\phi}}$ is the PSD of the angular frequency), to obtain the equivalent white noise linewidth. Figure 6.4 shows the S-T linewidth for different pump currents and for the three different spacer designs. It is evident from Figure 6.4 that the $1/(I-I_{th})$ dependence that is expected from the S-T linewidth formula is maintained at the lowest threshold, at least when the pump current is not too high. As the pump current increases, the linewidth saturates. The more aggressive designs, 100nm and 150nm spacers,



(a)



(b)

Figure 6.3: L-I curves of the 150nm spacer. (a) For varying stage temperatures (b) In pulsed operation (duty cycle = 1%)

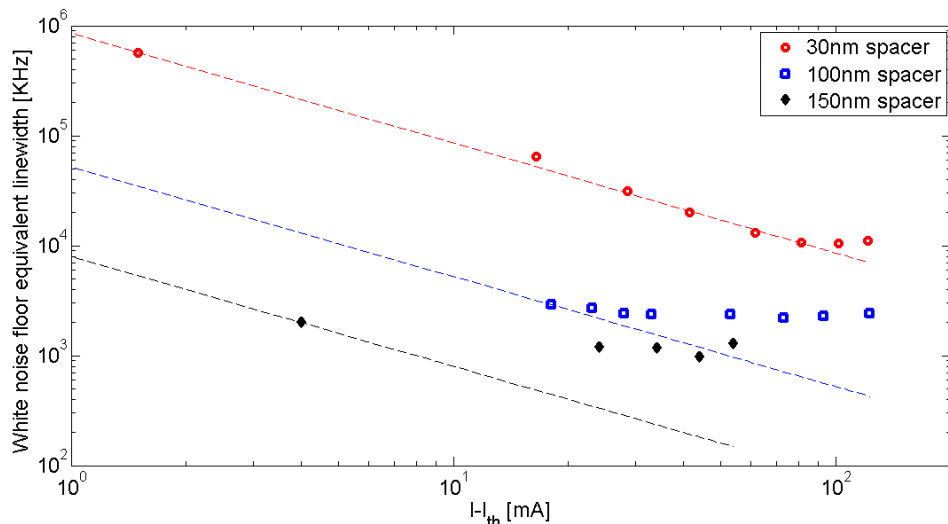


Figure 6.4: Schawlow-Townes linewidth vs current offset from threshold for the three spacer lasers. The dotted lines represent expected $1/P$ dependence

deviate considerably from the $1/(I-I_{th})$ dependence, in agreement with the theoretical predictions made in regards to TPA and FCA. The rate of linewidth reduction with pump current slows down below $1/(I-I_{th})$ and at high pump currents the linewidth even broadens. It is worth noting that measured linewidth in the 150nm spacer is limited by the measurement setup, due to the presence of the amplifier. Therefore, the white noise floor could not be observed and the specified values for these devices (150nm spacer) only represent upper bound and should be taken with a grain of salt.

In this chapter I have presented experimental results regarding the steady-state operation of narrow-linewidth hybrid Si/III-V lasers. One of the most striking experimental results in the steady-state operation of these lasers is their noise performance. The 150nm spacer, in which less than 1 percent of the light resides in the III-V material, yielded lasers with Schawlow-Townes linewidth of ~ 1 KHz. In fact, this figure is limited by the measurement, and the actual laser linewidth is sub-KHz. This is, to the best of our knowledge, the lowest noise ever reported for a stand-alone semiconductor laser, without an externally-coupled cavity. The trend from Figure 6.4 is also very clear: pushing the mode into silicon yields lasers with superior noise performance.

In the context of nonlinear phenomena in silicon there are several indications for

the significance of these effects. First, the aggressive spacer designs showed very nonlinear L-I curves as expected from the theoretical analysis. Moreover, the improvement in linewidth with pump current saturates quickly for the thick spacer lasers. These observations are in agreement with theoretical analysis that predicts the same effect due to nonlinear loss in the Si. These two facts are initial indications for the impact of TPA and FCA on laser performance. In the next sections, I will analyze the dynamical behavior of the lasers in the presence of nonlinear loss, both theoretically and experimentally.

Chapter 7

Dynamic operation - Theoretical analysis

The semiconductor laser is one of the pillars of the optical communication field and of other high-speed applications. Their fast output power vs. injection current response is being exploited for direct modulation of the laser using its pump current. Modulation speeds of tens of GHz are commonly achieved [62, 125, 35, 137] in direct (current) modulation communication schemes. The modulation response of the laser is also important for its noise characteristics. Random fluctuations in the input current will cause intensity and phase fluctuations, which follow the same modulation response transfer functions.

On the other hand, in coherent communication, where information is encoded in the phase of the field, external modulators are usually used. In this case, a “slow” response, which doesn’t extend to modulation frequencies, is advantageous since it will suppress phase and amplitude fluctuations due to inevitable current-source noise at the high frequencies of interest. In this chapter, I use the rate equations developed in Chapter 4 to examine how the laser responds to a small perturbation of the pump current around the steady-state, which was analyzed in Chapter 5.

7.1 Small-signal analysis

In Chapter 5 I set all time-derivatives to zero to find the steady-state. To account for fluctuations around the steady-state we will need to keep those time derivatives in our

current analysis. Unfortunately, the rate equations are nonlinear, even without TPA, and cannot be solved analytically. To get a closed-form solution, I will assume small fluctuations compared to the average values and linearize all the equations, neglecting higher-order terms.

I will start by expressing all the dynamic variables using the steady-state value plus small perturbation. Since the resulting system of equations is linearized, I will then analyze the equations in the complex Fourier domain, using the definitions of section 4.12:

$$n_e = n_{e,0} + \Delta n_e \cdot e^{i\omega t} \quad (7.1)$$

$$n_p = n_{p,0} + \Delta n_p \cdot e^{i\omega t} \quad (7.2)$$

$$n_{Si} = n_{Si,0} + \Delta n_{Si} \cdot e^{i\omega t} \quad (7.3)$$

$$I = I_0 + \Delta I \cdot e^{i\omega t} \quad (7.4)$$

The resulting linearization of 4.30-4.32 yields the following system of linear equations:

$$\begin{pmatrix} A_{11} & A_{12} & A_{13} \\ A_{21} & A_{22} & A_{23} \\ A_{31} & A_{32} & A_{33} \end{pmatrix} \begin{pmatrix} \Delta n_e \\ \Delta n_p \\ \Delta n_{Si} \end{pmatrix} = \begin{pmatrix} \frac{\Delta I}{qV_{QW}} \eta_i \\ 0 \\ 0 \end{pmatrix} \quad (7.5)$$

Where

$$A_{11} = i\omega + \frac{1}{\tau_r} + \frac{\Gamma_{QW}}{\Gamma_{Geom}} G'_m n_{p,0} \quad (7.6)$$

$$A_{12} = \frac{\Gamma_{QW}}{\Gamma_{geom}} G'_m (n_{e,0} - n_{tr}) \quad (7.7)$$

$$A_{13} = A_{31} = 0 \quad (7.8)$$

$$A_{21} = -\Gamma_{QW} G'_m n_{p,0} \quad (7.9)$$

$$A_{22} = i\omega - \left(\Gamma_{QW} G'_m (n_{e,0} - n_{tr}) - \alpha \right) + 2Bn_{p,0} + Cn_{Si,0} \quad (7.10)$$

$$A_{23} = Cn_{p,0} \quad (7.11)$$

$$A_{32} = -2Dn_{p,0} \quad (7.12)$$

$$A_{33} = i\omega + \frac{1}{\tau_{eff}} \quad (7.13)$$

And I have defined the parameters:

$$B = \beta_T h\nu v_g^2 M_{TPA} \Gamma_{Si}^2 \quad (7.14)$$

$$C = v_g \sigma_a \Gamma_{Si} \quad (7.15)$$

$$D = \frac{1}{2} \beta_T h\nu v_g^2 M_{TPA} \Gamma_{Si} \quad (7.16)$$

The steady-state gain term $\Gamma_{QW} G'_m (n_{e,0} - n_{tr})$ will be calculated using the clamped gain (gain = loss) to eliminate $n_{e,0}$ from the expression:

$$\Gamma_{QW} G'_m (n_{e,0} - n_{tr}) = \alpha + Bn_{p,0} + Cn_{Si,0} \quad (7.17)$$

Notice the spontaneous emission term was omitted, since well above threshold it is negligible compared to the stimulated emission.

7.2 Intensity modulation response

During modulation of the input current, the intensity changes based on the intensity-modulation transfer-function. In most semiconductor lasers, the transfer-function is

a second-order low-pass filter, of the generic form $H(s) = \frac{\omega_n^2}{s^2 + 2\xi\omega_n s + \omega_n^2}$. The low frequencies ($\omega \ll \omega_n$) propagate without distortion, while frequencies above the natural frequency ($\omega > \omega_n$) are suppressed. Notice, that in most laser systems the response is under-damped, such that the natural frequency ω_n provides a good estimate for the relaxation-oscillation frequency. It is worth noting that there are two factors that affect the modulation response [65]:

1. Internal laser dynamics - The interplay between QW carriers and cavity photons that yields the relaxation oscillation.
2. Capacitance-related response - The capacitance due to package parasitics will alter the way input-current propagates through the device.

Though these mechanisms are fundamentally different, in practice it is hard to distinguish between the two. In this section, I will analyze only the basic internal laser dynamics, and will ignore parasitics, which are package-dependent. Experimental results will validate that in the frequency range of interest, this is justified in our case.

Most semiconductor laser designs attempt to push the relaxation resonance to as high a frequency as possible, so that modulation frequencies fall within the constant portion of the response. This is usually done by choosing materials that have large differential gain (e.g., AlGaInAs), working at low temperatures, decreasing the active region volume, and working at high powers [128]. Pushing the resonance frequency further by driving the laser harder has an important yet limited effect. Thermal issues and increased damping usually limit the bandwidth to ~ 30 GHz. Optical injection locking was found useful in taking care of damping effects, and resonance at 70 GHz or more was demonstrated [127].

On the other hand, narrow-linewidth lasers, e.g., fiber lasers, have a very low relaxation oscillation resonance frequency, often sub-MHz, or tens of KHz. The resonance in these lasers is also typically highly peaked, at 20dB or more. These characteristics often limit their usefulness, and fiber-laser designs attempt to suppress the resonance peak. Several techniques are used to that end: active feedback [26], intra-cavity loss

elements with feedback [138], locking to a master laser [59, 27], and incorporation of non-linear loss elements [11, 108, 3]. Out of these techniques, the latter is most relevant to our study. TPA, which is a nonlinear loss mechanism, is capable of suppressing intensity noise. When the intensity noise is very high, as in the case of a relaxation peak, the nonlinear loss is also high, and the noisy peak is suppressed.

7.2.1 Analytical investigation

The matrix in Equation 7.5 can be solved analytically, and simplified using Equation 7.17. The transfer function $H(s)$ can be defined using the Laplace transform :

$$\Delta n_p(s) = H(s)\Delta I(s) \quad (7.18)$$

which relates modulation of intra-cavity photon density to input current modulation . To relate it to the output power, one can use Equation 5.12. The resulting expression has the form:

$$H(s) = \frac{\Gamma_{QW}G'_m n_{p,0} \left(\frac{1}{\tau_{eff}} + s \right) \frac{\eta_i}{qV_{QW}}}{(s + 2\xi\omega_n) \left[(s + Bn_{p,0}) \left(\frac{1}{\tau_{eff}} + s \right) + 2CDn_{p,0}^2 \right] + \left(\frac{1}{\tau_{eff}} + s \right) \omega_n^2} \quad (7.19)$$

Where the natural frequency ω_n and the damping factor ξ are defined as:

$$\omega_n^2 = \frac{\Gamma_{QW}}{\Gamma_{geom}} G'_m n_{p,0} \alpha_T \quad (7.20)$$

$$\xi = \frac{\frac{1}{\tau_r} + \frac{\Gamma_{QW}}{\Gamma_{geom}} G'_m n_{p,0}}{2\omega_n} \quad (7.21)$$

and the total loss rate, linear and nonlinear, is defined as:

$$\alpha_T = \alpha + Bn_{p,0} + Cn_{Si,0} \quad (7.22)$$

The transfer function of Equation 7.19 has in general one zero and three poles. Unfortunately, the roots of the third-order polynomial in the denominator cannot be

expressed analytically. I will study this transfer function by looking at two different regimes: low and high nonlinear losses.

7.2.1.1 Low nonlinear loss regime:

Written explicitly, the second term in the denominator is:

$$2CDn_{p,0}^2 = \frac{2}{\tau_{eff}} v_g \sigma_a n_{Si,0} \Gamma_{Si} = \frac{2}{\tau_{eff}} \alpha_{FCA} \quad (7.23)$$

Where we have used the steady-state silicon carrier-density from Equation 5.1, and defined the loss rate due to FCA α_{FCA} in units of $[\text{sec}^{-1}]$. I can now compare a few terms in the square bracket of Equation 7.19. If the FCA loss rate is slower than some frequency ω of interest:

$$2\alpha_{FCA} \ll \omega \quad (7.24)$$

then the term $2CDn_{p,0}^2$ can be neglected. In this case, the $\left(\frac{1}{\tau_{eff}} + s\right)$ term cancels out everywhere, and the transfer function is reduced to the familiar form:

$$H(s) = \frac{\Gamma_{QW} G'_m n_{p,0}}{s^2 + 2\xi\omega_n s + \omega_n^2} \quad (7.25)$$

which is the typical second-order low-pass filter.

The exact location of the poles ω_p of the transfer-function is given by:

$$\omega_p = \omega_n \left(-\xi \pm \sqrt{\xi^2 - 1} \right) \quad (7.26)$$

When the damping factor is smaller than unity, the knee frequency can be well-approximated by the value of ω_n and the resonance is under-damped. When the damping factor is larger than unity, there will be two real poles and the system will be highly damped.

It is interesting to study how the relaxation resonance behavior changes with different spacer designs. Most textbooks have a similar expression as Equation 7.20, except that for a traditional laser $\frac{\Gamma_{QW}}{\Gamma_{geom}} \approx 1$, so the dependance on Γ_{QW} is often

obscured. I will use the relationship between the photon density and the total loss rate:

$$n_{p,0} = \eta \frac{(I - I_{th})}{eV_p \alpha_T} \quad (7.27)$$

such that:

$$\omega_n^2 = \frac{\Gamma_{QW}}{\Gamma_{geom}} G'_m \eta \frac{(I - I_{th})}{eV_p} \quad (7.28)$$

It is now clear that in our spacer design, where unlike the case of a conventional laser, the quantum wells reside deeply in the exponential tail of the mode, such that $\frac{\Gamma_{QW}}{\Gamma_{geom}} \ll 1$, and we expect to see very small relaxation oscillation resonance frequencies with the trend:

$$\omega_n \sim \sqrt{\Gamma_{QW}} \quad (7.29)$$

The damping factor in our system can also be evaluated. Assuming we are operating in a regime where $\frac{1}{\tau_r} < \frac{\Gamma_{QW}}{\Gamma_{geom}} G'_m n_{p,0}$, which is a reasonable assumption for practical photon densities and confinements, we can express the damping factor as:

$$\xi \approx \frac{1}{2} \sqrt{\frac{\Gamma_{QW}}{\Gamma_{geom}} \frac{n_{p,0}}{\alpha_T}} \quad (7.30)$$

Since the total loss is also a function of Γ_{III-V} in the regime where the total-Q is not saturated by the silicon-Q, we can write: $n_{p,0} \sim \frac{1}{\alpha_T} \sim \frac{1}{\Gamma_{QW}}$ and get the form:

$$\xi \sim \frac{1}{\sqrt{\Gamma_{QW}}} \quad (7.31)$$

and we expect an increasingly damped response with reduced III-V confinement.

7.2.1.2 High nonlinear loss regime:

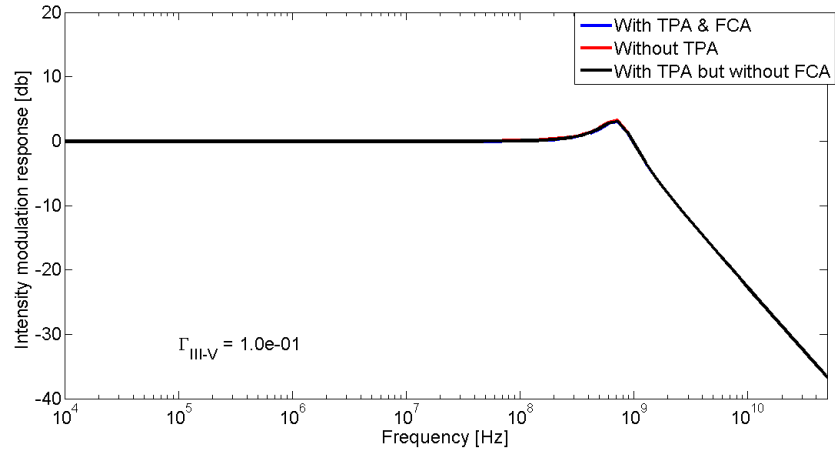
When the FCA loss is high and the second term in the square bracket of Equation 7.19 cannot be neglected, we are back to the regime in which an analytical expression cannot be obtained. However, there are some conclusions we can draw from the general form of the transfer function:

1. The existence of a zero of the transfer function at $\omega_z = \frac{1}{\tau_{eff}}$. In the low nonlinear regime, this zero was effectively masked by a pole at the same frequency. In the high nonlinear regime this is no longer the case, and we expect to see a zero of the transfer function.
2. The existence of three poles of the transfer function. In general, these can be three real poles, or a pair of complex-conjugate poles and a real pole. Several types of behavior will be possible, depending on strength of FCA, and on the location of the zero/poles. For example, if the system is highly damped we can expect to see a pole of the transfer function at low frequency, then a zero at an intermediate frequency, and the pole pair at high frequencies. If the system is less damped, we expect to see the zero at low frequency and three poles at higher frequencies. Due to the complex nature of the transfer function, and the fact that $n_{p,0}$, Γ_{QW} , Q_{Si} , and τ_{eff} all depend on each other, a numerical analysis is needed.

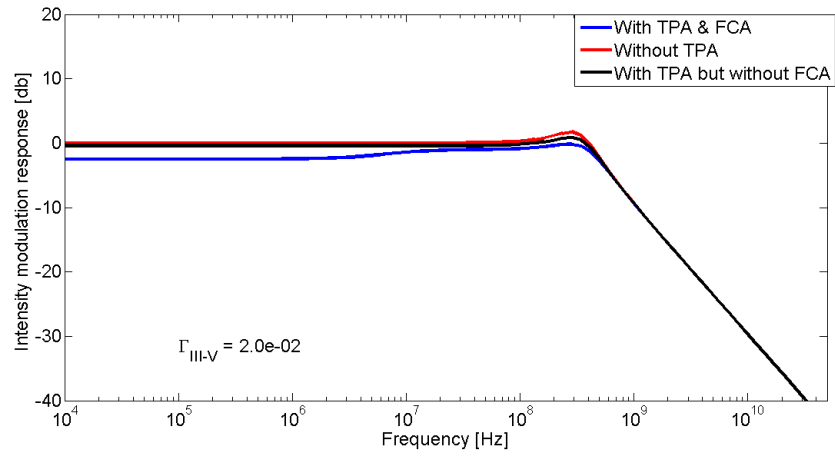
7.2.2 Numerical investigation

In this section, I will study the small-signal response numerically. First, a steady-state solution is obtained as in Chapter 5. Then, the linearized small-signal rate equations are solved numerically using Cramer's rule, and the previously obtained steady-state values. This process is repeated for several values of III-V confinement.

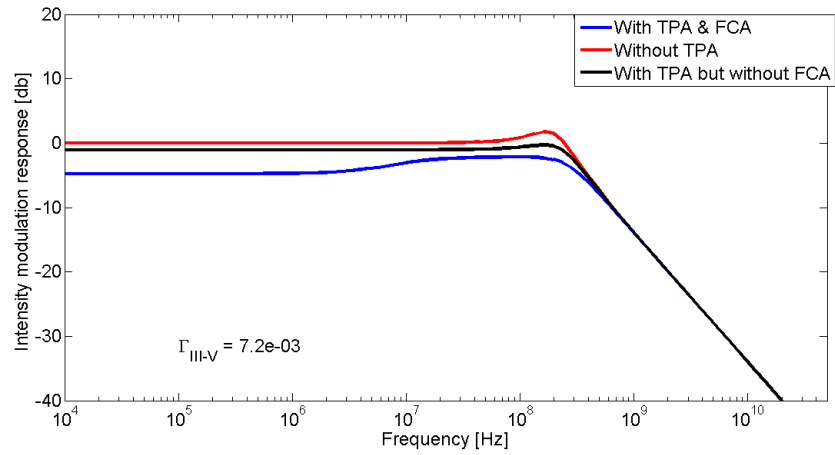
Figures 7.1(a)-(c) demonstrate the impact of nonlinear effects on the response curve. To isolate the effect of both TPA and FCA on the transfer function, I have repeated the study three times: first with all nonlinearities, then without FCA by setting $\sigma_a = 0$, and finally without TPA by setting $\beta_{TPA} = 0$. In 7.1(a) the 30nm spacer results in a relatively low-Q. Nonlinear effects are small and the three curves, including TPA and FCA and without them, are roughly equivalent. In Figure 7.1(c) the 150nm spacer yields a fairly high-Q, and the impact of nonlinear effects is evident. Without nonlinearities, the typical shape of the relaxation resonance curve is restored. The resonance peaks a few dB above the DC response. When TPA is turned on, but



(a)



(b)



(c)

Figure 7.1: Intensity modulation response curves with and without nonlinear effects. $I = 4I_{th}$, $Q_{Si} = 10^6$ (a) 30nm spacer (b) 100nm spacer (c) 150nm spacer

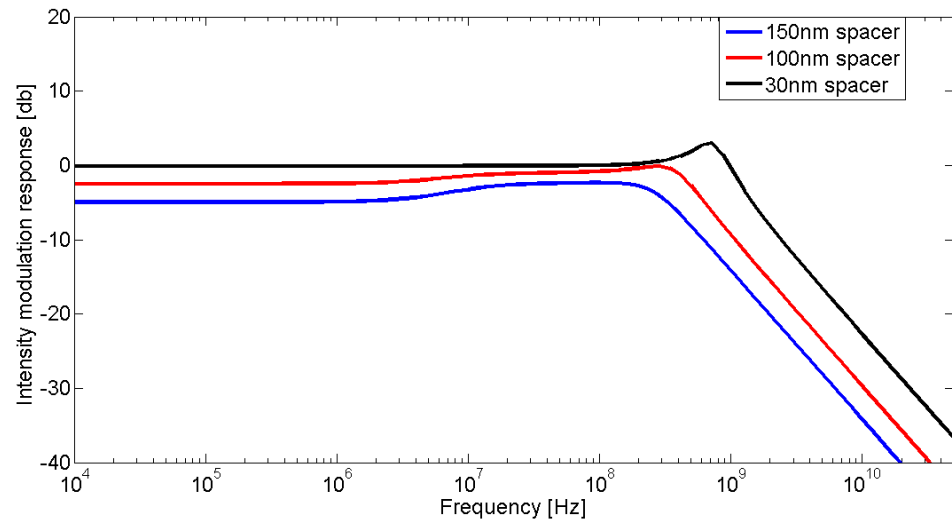
still without FCA, the shape of the curve is maintained, but the resonance peak is suppressed. This is due to the stronger TPA at higher intensities. When FCA is turned on, the entire curve changes: the zero of the transfer function appears at $f = \frac{1}{2\pi\tau_{eff}} = 5.3MHz$ and changes the resonance peak into a broad “hill” peak. Furthermore, the entire response curve drops. This can be understood by looking at the L-I curves of Figure 5.4: The DC value of the response curve represents the local slope at the working point, and with the nonlinear L-I curve this slope is reduced.

Another interesting feature of Figure 7.1 is the trend in the relaxation oscillation frequency. The bigger the spacer, the lower the resonance frequency. This is better demonstrated in Figure 7.2, where we compare both amplitude and phase of the three spacers on the same plot with nonlinear effects. In fairly good agreement with the analytical analysis of section 7.2.1, the relaxation resonance frequency scales with the square root of the confinement. Resonance frequencies as low as a few hundred MHz are expected from thick spacer lasers. Figure 7.3 shows the response curve for a higher bias point. Here, due to the stronger pump, nonlinear effects are evident, even in the thinner spacer design.

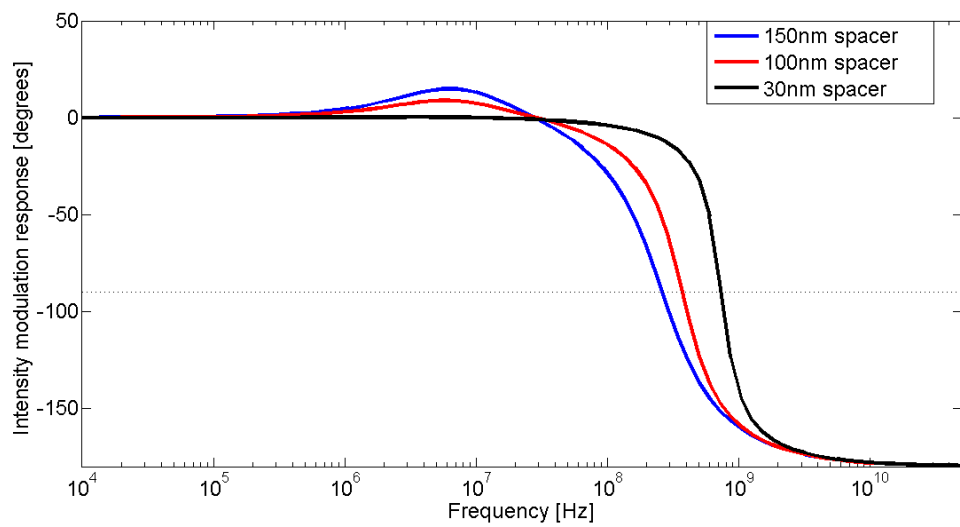
7.3 Frequency modulation response

When the input current to the laser is being modulated, the lasing frequency changes as well as the intensity. The low-frequency response is usually dominated by thermal effects; the medium’s refractive index is temperature-dependent, and the modulation of the input current changes the laser’s temperature. The thermo-optic coefficient is of the same order of magnitude in III-V and silicon [14, 12], about $\frac{dn}{dT} \approx 2 \cdot 10^{-4} [K^{-1}]$. We therefore expect the hybrid silicon laser to perform similarly to a conventional III-V laser as far as low-frequency thermal response is concerned. For that reason, I will ignore thermal effect in the following analysis, and will focus on the unique characteristics of the hybrid platform.

The change in lasing frequency of the laser will depend on changes of the effective refractive index of the lasing mode. Assuming these changes are small enough, we can

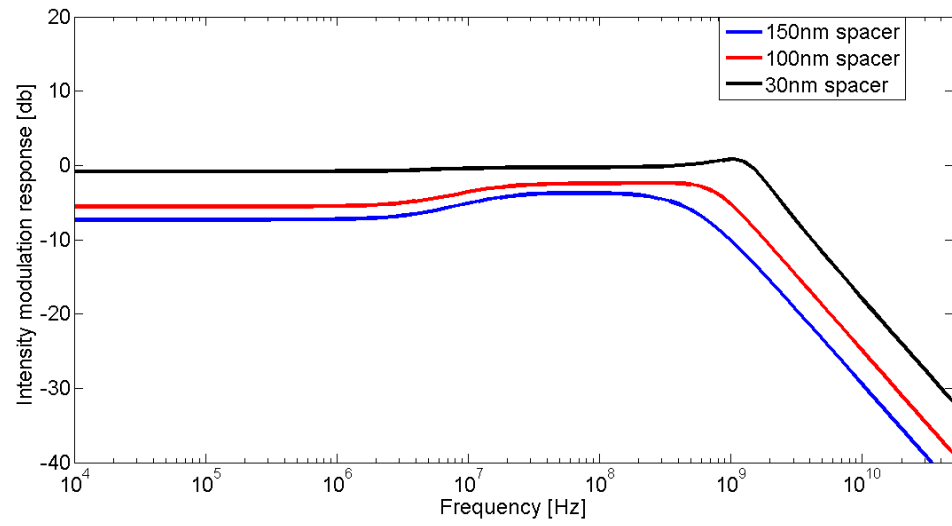


(a)

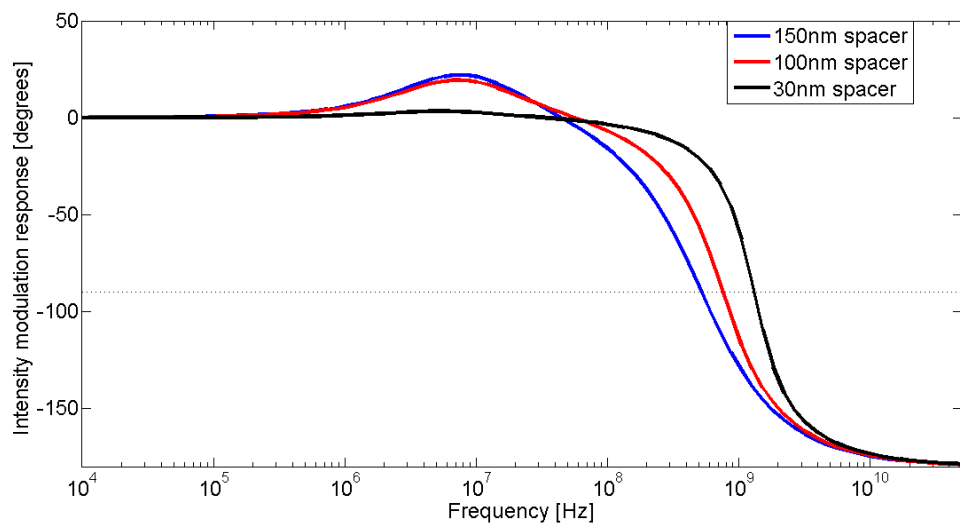


(b)

Figure 7.2: Intensity modulation response curves for different spacer thicknesses. $I = 4I_{th}$, $Q_{Si} = 10^6$ (a) amplitude (b) phase



(a)



(b)

Figure 7.3: Intensity modulation response curves for different spacer thicknesses. $I = 10I_{th}$, $Q_{Si} = 10^6$ (a) amplitude (b) phase

safely neglect changes in the modal profile and connect local changes of the refractive index to the effective index using the confinement factor. For example, if the index of silicon changes by $\Delta n_r^{(Si)}$, and the index of the QWs changes by $\Delta n_r^{(QW)}$, we can calculate the change to the effective index using:

$$\Delta n_r = \Gamma_{QW} \Delta n_r^{(QW)} + \Gamma_{Si} \Delta n_r^{(Si)} \quad (7.32)$$

The resulting frequency chirp $\Delta\nu$ is approximated using [13, 126]:

$$\Delta\nu = -\frac{v_g}{\lambda_0} \Delta n_r \quad (7.33)$$

7.3.1 Effect of Quantum Well carriers

The modulation of input current yields a change of the carrier density in the quantum wells. This in turn causes refractive index modulation through the plasma effect [44], which results in frequency chirping. In an ideal laser, the carrier density is clamped to its threshold value. This fact would mean that a DC modulation should result in zero frequency chirp. In practical laser systems this is not the case. Even at DC, the plasma effect causes frequency tuning, typically few hundred MHz per mA of input modulation [123, 78, 13, 126]. To explain this discrepancy I will have to consider **gain compression** in our model. This effect was of no significance in previous analysis. However, since the laser is extremely sensitive to refractive index changes, it is important to consider it in the analysis of the frequency modulation response.

7.3.1.1 Gain compression

It is an approximation to view the gain as clamped to its threshold value. In practice, the high photon density will compress the (unsaturated) gain. This non-linearity of the gain is often attributed to spectral hole burning and carrier heating (intra-band re-absorption of photons) [129]. A good model for this effect can be given by the

expression:

$$G'_m(n_p) = \frac{G'_m}{1 + \Gamma_{QW}\epsilon_c n_p} \quad (7.34)$$

where ϵ_c is the gain compression coefficient, which is derived empirically. When the laser pump current is modulated, the photon density responds, as described in section 7.2. The resulting compression of the gain would force the QW carriers to follow in order to compensate for the change in differential gain, and frequency chirp will be observed. In light of this modification to the model, the differential rate equations should be altered. Gain compression should be included in the differential rate Equations 7.6-7.13 by making the differential gain dependent on the photon density, thus making the substitution $G'_m \rightarrow G'_m(n_p)$. Moreover, the derivative of the gain with respect to the photon density has to be included. Specifically, this results in changes to two terms in the small-signal matrix 7.5:

$$A_{12} = \frac{\Gamma_{QW}}{\Gamma_{geom}} G'_m(n_p) \cdot (n_{e,0} - n_{tr}) \left[1 - \frac{\Gamma_{QW}\epsilon_c n_{p,0}}{1 + \Gamma_{QW}\epsilon_c n_{p,0}} \right] \quad (7.35)$$

$$A_{22} = i\omega + \alpha + 2Bn_{p,0} + Cn_{Si,0} - \Gamma_{QW} G'_m(n_p) \cdot (n_{e,0} - n_{tr}) \left[1 - \frac{\Gamma_{QW}\epsilon_c n_{p,0}}{1 + \Gamma_{QW}\epsilon_c n_{p,0}} \right] \quad (7.36)$$

7.3.1.2 Henry's alpha parameter

In laser analysis, it is useful to express changes to the refractive index n_r using changes to the imaginary part of the refractive index n_i , which is related to the material gain g . Henry's alpha parameter α_H can be defined as:

$$\alpha_H = \frac{dn_r/dn_e}{dn_i/dn_e} \quad (7.37)$$

and is used to connect the two using the expression [115]:

$$\frac{dn_r}{dn_e} = -\alpha_H \frac{\lambda_0}{4\pi} \cdot \frac{G'_m}{2v_g} \quad (7.38)$$

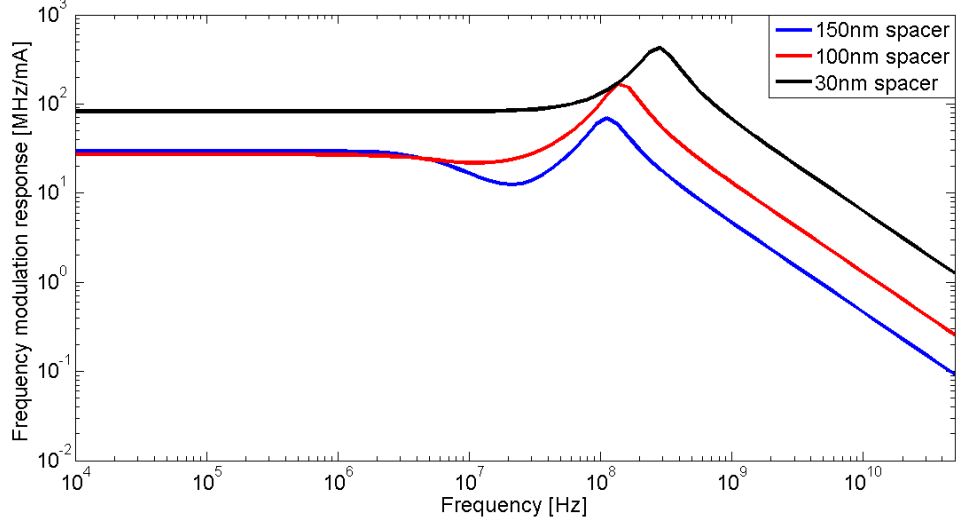


Figure 7.4: Frequency modulation response due to quantum well electrons for different values of spacer thickness. $\alpha_H = 7$, $I = 2 \cdot I_{th}$, $Q_{Si} = 10^6$

where we have used the explicit linear form of the gain (Equation 2.15) to calculate $\frac{dg}{dn_e}$. The minus was added to force α_H to be positive for the expected blue shift with carrier-density.

7.3.1.3 Frequency modulation response curve

I can now calculate the effect of quantum well carriers on the frequency modulation response. By combining Equations 7.33 and 7.38 I can express the frequency response as:

$$\frac{\Delta\nu_{QW}}{\Delta I} = -\frac{v_g}{\lambda_0} \frac{dn_r}{dn_e} \Delta n_e = \frac{\alpha_H}{8\pi} \Gamma_{QW} G'_m \frac{\Delta n_e}{\Delta I} \quad (7.39)$$

where $\frac{\Delta n_e}{\Delta I}$ is calculated directly from the small signal matrix 7.5. The exact expression can be presented analytically using the same assumption we have used in section 7.1:

$$\frac{\Delta\nu_{QW}}{\Delta I}(s) = \frac{\frac{\alpha_H}{8\pi} \Gamma_{QW} G'_m \frac{\eta_i}{eV_{QW}} \left(s + \frac{1}{\tau_{eff}} \right) \left[s + Bn_{p,0} + \alpha_T \frac{\Gamma_{QW} \epsilon_c n_{p,0}}{1 + \Gamma_{QW} \epsilon_c n_{p,0}} \right] + 2CDn_{p,0}^2}{(s + 2\xi\omega_n) \left[(s + Bn_{p,0}) \left(\frac{1}{\tau_{eff}} + s \right) + 2CDn_{p,0}^2 \right] + \left(\frac{1}{\tau_{eff}} + s \right) \omega_n^2} \quad (7.40)$$

The resulting response due to the plasma effect in the quantum wells can be seen in Figure 7.4. Several prominent new features are evident:

1. For the thin 30nm spacer, the response resembles that of a conventional semiconductor laser [43]. A flat response up to a few hundred MHz, of magnitude of roughly few hundred MHz/mA are very common for III-V lasers.
2. As the spacer thickness increases, say in the case of 100nm, the entire curve maintains its general shape, but decreases in magnitude. This is due to the decreased overlap between the the mode and the QW. Changes in the QW's refractive index have a smaller effect on the mode due to the low confinement factor.
3. The resonance frequency decreases with increasing spacer thickness, for the same reasons that were discussed in section 7.2.
4. For very thick spacers, i.e., 150nm, the response curve changes: a shallow dip due to FCA is revealed at $\omega = \frac{1}{\tau_{eff}}$.
5. In the case of the 150nm spacer, the magnitude of the response at low frequencies is comparable to the 100nm spacer, despite the reduced overlap with the quantum wells. This is due to nonlinear loss. TPA and FCA act as effective gain compression mechanisms; increased photon density increases nonlinear loss, and QW carrier density has to grow to increase the gain, such that gain=loss.

7.3.2 The effects of free-carriers in silicon

As we have seen in the previous section, the plasma effect due to quantum well carriers has a small impact on the frequency modulation response as we push the mode further and further into the silicon. Figure 7.4 suggests an order of magnitude reduction in DC frequency modulation compared to the typical 300 MHz/mA response [123, 78, 13, 126]. In the hybrid Si/III-V platform, the bulk of the mode is in silicon, especially in our narrow-linewidth design approach. It is therefore important to consider the impact of free-carriers in silicon on the frequency modulation.

As the pump current is modulated, the intra-cavity photon density follows the intensity modulation response. TPA, which is considered instantaneous, tracks the

changes in the photon density and the density of the free-carriers in silicon are modulated. This in turn causes refractive index changes, due to the plasma effect, which yields frequency chirping.

7.3.2.1 Plasma effects in silicon

Silicon modulators are studied intensively in the literature. A very common empirical model that relates the carrier density in silicon to the refractive index at 1550nm has the form [101, 81]:

$$\Delta n_r = \xi n_{Si} = -8.8 \cdot 10^{-22} n_{Si,e} - 8.5 \cdot 10^{-18} (n_{Si,p})^{0.8} \quad (7.41)$$

where $n_{Si,e/p}$ are the electrons and hole densities respectively in units of cm^{-3} . In our intrinsic silicon, I shall set the hole and electron densities as equal $n_{Si,e} = n_{Si,p} = n_{Si}$. The differential refractive index change depends on the carrier density due to the different effective masses of electrons and holes and is given by:

$$\frac{dn_r}{dn_{Si}} = \xi(n_{Si}) = -8.8 \cdot 10^{-22} - 8.5 \cdot 10^{-18} (n_{Si})^{-0.2} \quad (7.42)$$

in units of cm^3 .

Frequency modulation response curve

The frequency chirp due to the refractive index modulation in silicon is given by using Equations 7.33 and 7.41:

$$\frac{\Delta \nu_{Si}}{\Delta I} = -\frac{v_g}{\lambda_0} \Gamma_{Si} \xi \frac{\Delta n_{Si}}{\Delta I} \quad (7.43)$$

It can be calculated analytically from the system of differential rate equations:

$$\frac{\Delta \nu_{QW}}{\Delta I}(s) = \frac{-2 \frac{v_g}{\lambda_0} \Gamma_{Si} \xi(n_{Si}) \frac{\eta_i}{e V_{QW}} \Gamma_{QW} G'_m D n_{p,0}^2}{(s + 2\xi\omega_n) \left[(s + B n_{p,0}) \left(\frac{1}{\tau_{eff}} + s \right) + 2CD n_{p,0}^2 \right] + \left(\frac{1}{\tau_{eff}} + s \right) \omega_n^2} \quad (7.44)$$

The effect of silicon free-carriers on the frequency modulation response is demonstrated in Figure 7.5. The response follows the three-pole transfer function discussed

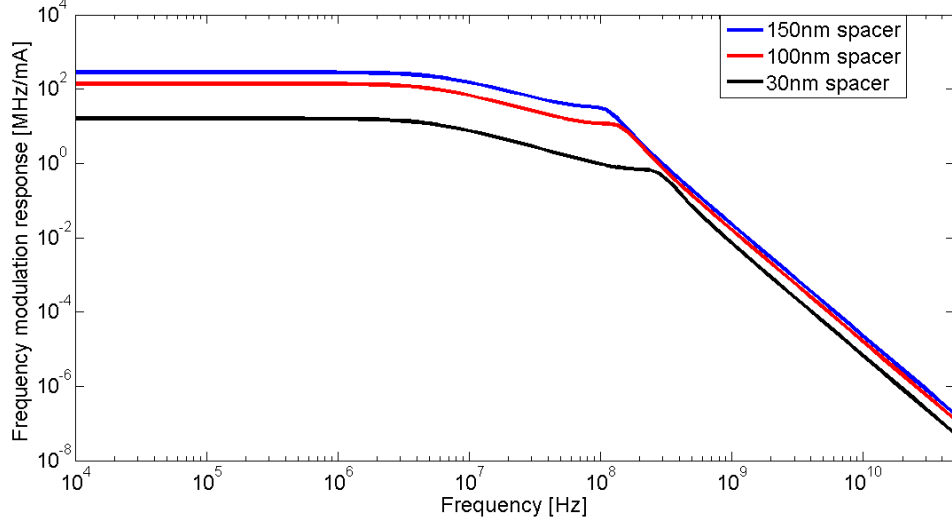


Figure 7.5: Frequency modulation response due to free carriers in silicon for different values of spacer thickness. $\alpha_H = 7$, $I = 2 \cdot I_{th}$, $Q_{Si} = 10^6$

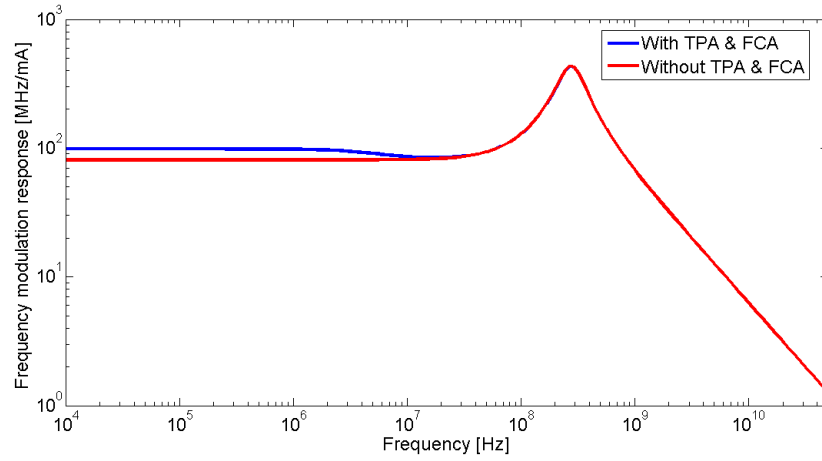
in Chapter 7.2. The first pole is at $\omega \approx \frac{1}{\tau_{eff}}$, while the other two poles are at the resonance frequency, which decreases with increasing spacer thickness. The magnitude of the response increases with spacer thickness. Since TPA is a nonlinear process and is proportional to n_p^2 , the differential response is dependent on the photon density. The thicker spacers have higher-Q and therefore higher stored photon density. Therefore, the plasma effect in silicon is expected to be stronger for higher-Q designs, such as the thick spacer.

7.3.3 The total frequency chirp

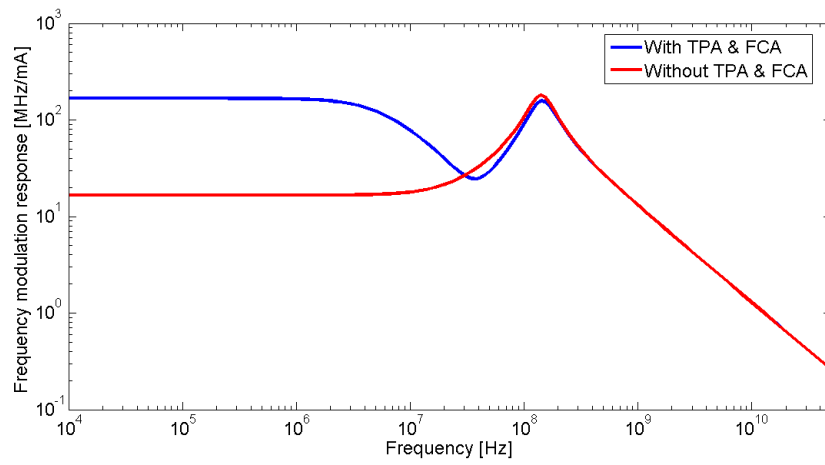
The combined frequency chirp due to QW and silicon plasma effects can be calculated using the partial derivatives:

$$\Delta\nu = -\frac{v_g}{\lambda_0} \left(\Gamma_{QW} \frac{dn_r}{dn_e} \Delta n_e + \Gamma_{Si} \frac{dn_r}{dn_{Si}} \Delta n_{Si} \right) \quad (7.45)$$

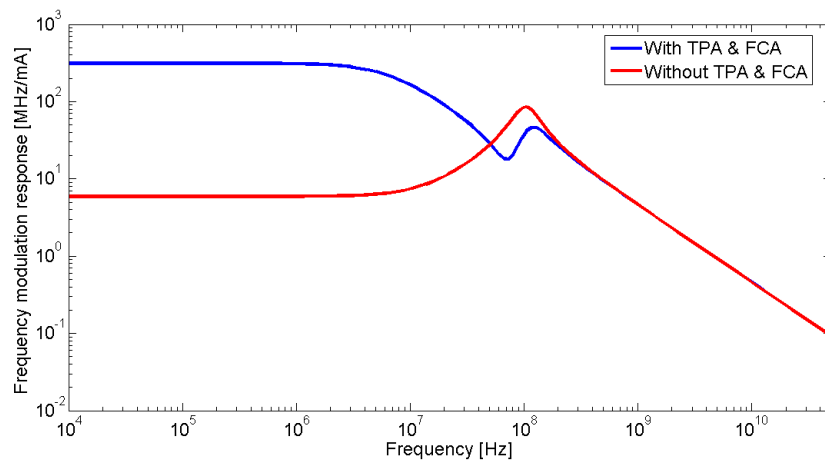
The exact phases of Δn_{QW} and Δn_{Si} have to be taken into account in the addition. Figures 7.6(a)-(c) show the (total) frequency modulation response vs. the same response in the absence of nonlinear effects. TPA and free-carriers in silicon have a



(a)



(b)



(c)

Figure 7.6: Frequency modulation response for several different spacer thicknesses, with and without nonlinear effects for $\alpha_H = 7$, $I = 2 \cdot I_{th}$, $Q_{Si} = 10^6$. (a) 30nm spacer (b) 100nm spacer (c) 150nm spacer

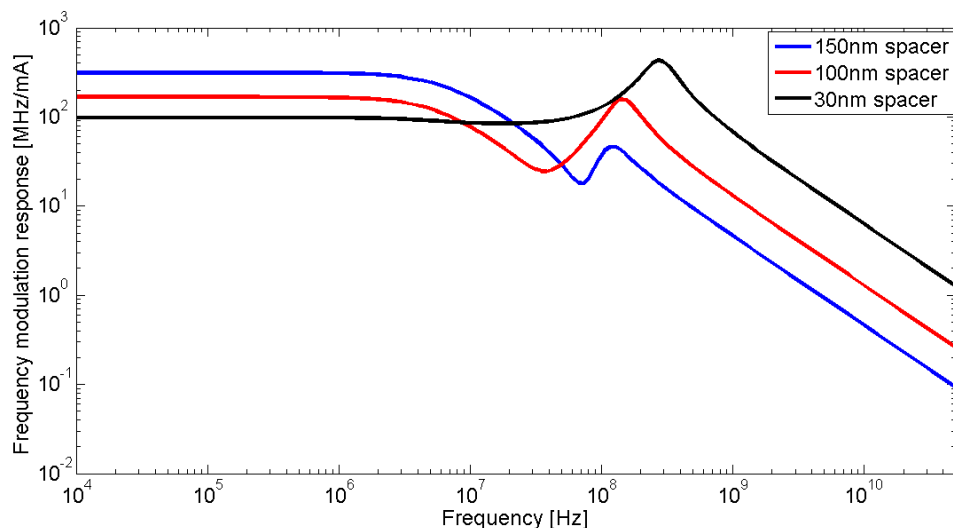
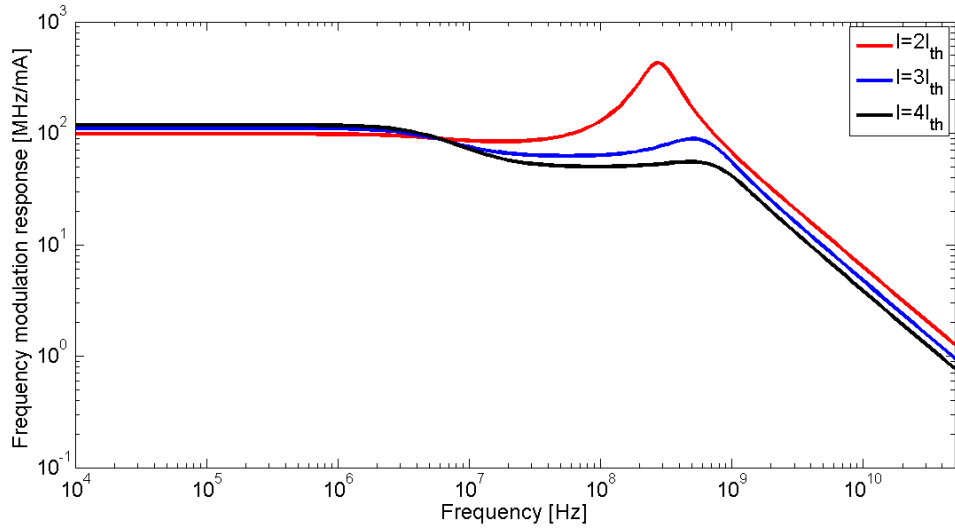


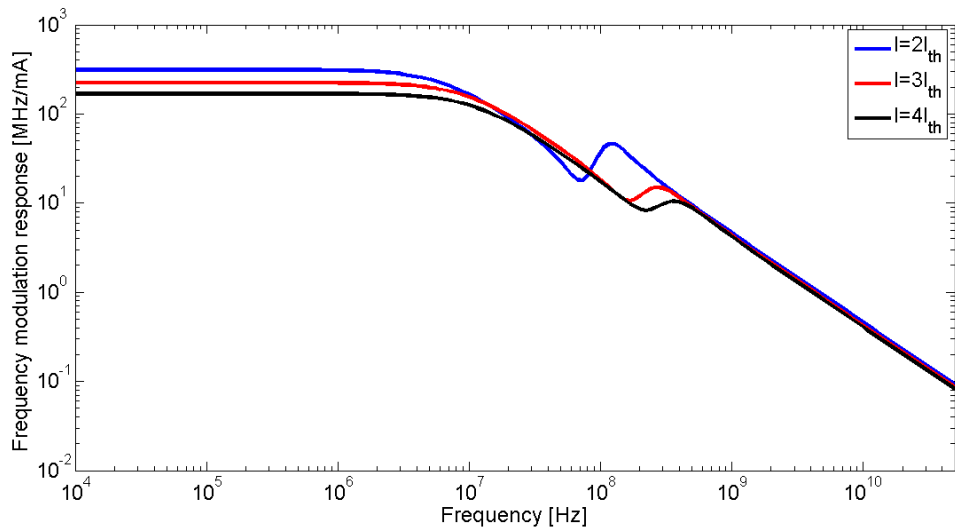
Figure 7.7: Frequency modulation response for several different spacer thicknesses for $\alpha_H = 7$, $I = 2 \cdot I_{th}$, $Q_{Si} = 10^6$

major impact on the frequency response in the thicker spacer designs. A very clear dip in the response curve, followed by a resonance, is a unique consequence of free-carrier-dispersion in silicon, and is very different from a conventional III-V, where TPA is negligible. The frequency modulation curves of the different spacer thicknesses are compared in Figure 7.7. The effect of pump current on the response curve is shown in Figure 7.8(a)-(b) for thin and thick spacers. In the thin 30nm spacer, as the pump current increases, the effect of free-carriers becomes more prominent, as indicated by the appearance of the extra pole before the resonance frequency. In the thick 150nm spacer, as the pump current increases, the resonance is pushed to higher frequencies, and the frequency response curve is altered accordingly.

In this chapter, I analyzed the laser dynamics in both the intensity and the frequency response. The analysis predicts much lower relaxation resonance frequencies than a conventional semiconductor laser. This is due to grossly reduced confinement in the QW, which reduces the induced transition rate. This is the base of this platform. The effect of free-carriers in silicon was also analyzed. It was predicted that it will add a zero to the intensity modulation transfer function, and a unique dip to the frequency modulation response. In the next chapter I will present experimental



(a)



(b)

Figure 7.8: Effect of pump current on frequency modulation response for two different spacer thicknesses $\alpha_H = 7$, $I = 2 \cdot I_{th}$, $Q_{Si} = 10^6$. (a) 30nm spacer (b) 150nm spacer

results from fabricated devices and compare them to these predictions.

Chapter 8

Dynamic operation - Experimental results

In this chapter, I will discuss the modulation response experiments that were performed with a number of different spacer designs. The experimental setup and procedures are described in detail in appendix B. The experimental results presented in this chapter are the first published results for the dynamics of low active confinement hybrid Si/III-V lasers. They will be used to point out some of the special characteristics of the low-noise spacer design, and to probe and quantify some of the nonlinear effects described in earlier chapters.

8.1 Intensity modulation response

Intensity modulation response experiments were conducted using the setup described in appendix B.3. The intensity modulation transfer function $H_{IM}(\nu)$ was calculated by computing the ratio between the relative intensity modulation and the laser's input current at a given modulation frequency:

$$H_{IM}(\nu) = \frac{\Delta P_{out}}{\Delta I} \cdot \frac{1}{P_0} \quad (8.1)$$

The response of the driving circuitry was divided out from this calculation to isolate the response of the laser only. Details on this calibration process can be found in appendix B.3.2.

Experimental results from intensity modulation experiments of different spacer lasers and at different bias currents are shown in Figures 8.1-8.3. Each figure shows the measured magnitude and phase of the amplitude modulation (AM) transfer function. Several interesting features are present in the AM transfer function of different spacer lasers:

1. Resonance frequency position vs spacer thickness - As expected from the theoretical analysis, the resonance frequency shifts towards lower frequencies as the overlap with the QW is reduced. The 150nm spacers show relaxation frequency as low as ~ 100 MHz. This is one to two orders of magnitude lower than conventional III-V lasers, and to the best of our knowledge, the lowest-ever reported for a semiconductor laser. Figure 8.4 compares the AM response of different spacer lasers for the same offset current from threshold. It is worth noting that though the trend is in perfect agreement with the theory, the theory predicts that the ratio between the resonance frequency at the 30nm spacer and the 150nm spacer should be:

$$\frac{\omega_n(30\text{nm spacer})}{\omega_n(150\text{nm spacer})} = \sqrt{\frac{\Gamma_{QW}(30\text{nm spacer})}{\Gamma_{QW}(150\text{nm spacer})}} \approx 4 \quad (8.2)$$

where the confinement factors used are based on Comsol simulation. Based on the experimental AM curve, the ratio is $\frac{\omega_n(30\text{nm spacer})}{\omega_n(150\text{nm spacer})} \approx 8$. Since theory predicts a square root relationship between confinement and resonance frequency, it might indicate that the 150nm spacer has lower confinement Γ_{III-V} (by about a factor of 4) than estimated by the simulation. If this is the case, and the simulation over-estimates the confinement in the QW, it can explain the low yield of the 150nm spacer and the zero yield of the 200nm spacer (the gain is reduced and is no longer compensated by an increase of Q).

2. The presence of a zero of the transfer function for the 150nm spacer (Figure 8.3) - What might look like very broad resonance in Figure 8.3 is in fact a zero of the transfer function. This observation is consistent with both the shape of the

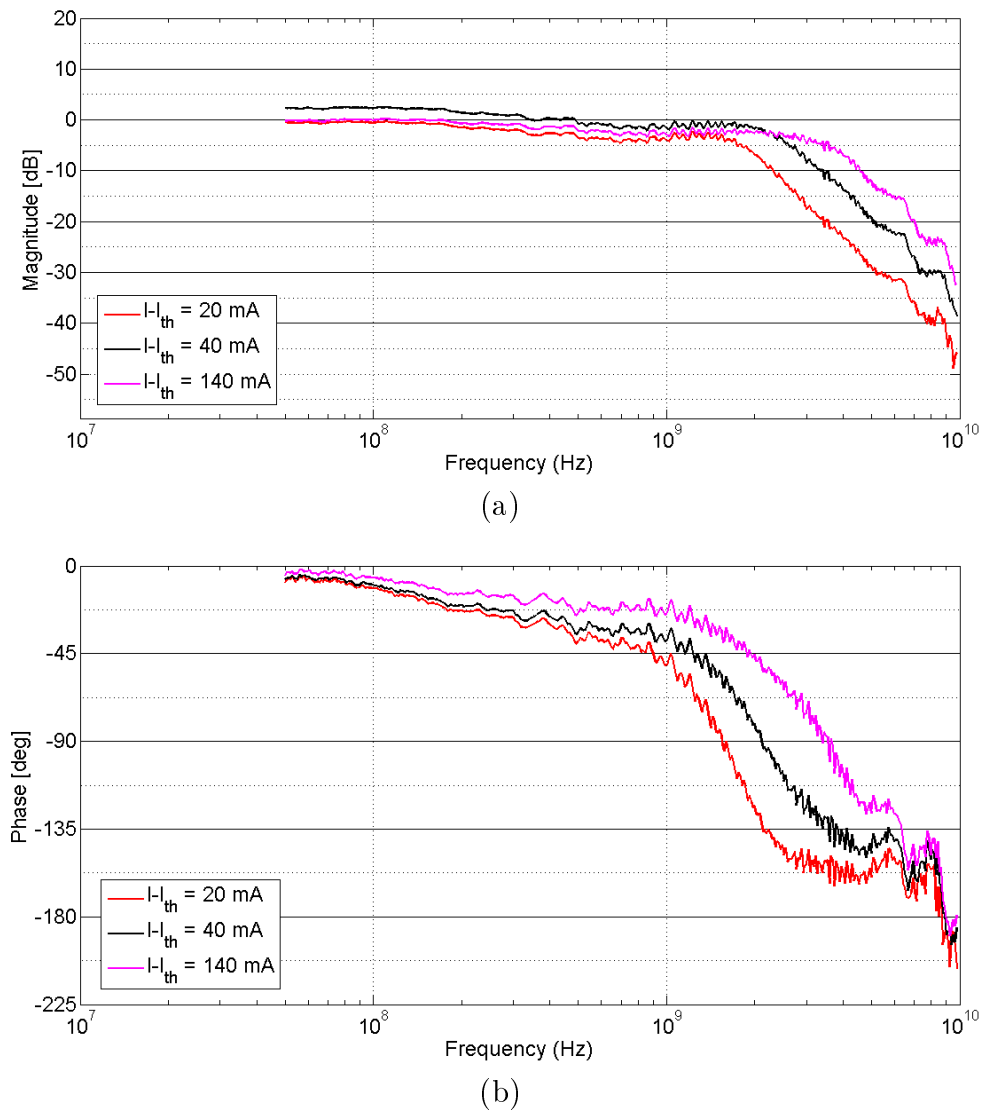


Figure 8.1: Intensity modulation response of 30nm spacer laser (Chip 1, bar 5, Slot 1, device 7) for different bias currents. 3.5mA current modulation. Measured with New-Focus 1544B photodetector and HP 8722C RF network analyzer (a) Normalized magnitude (b) Phase

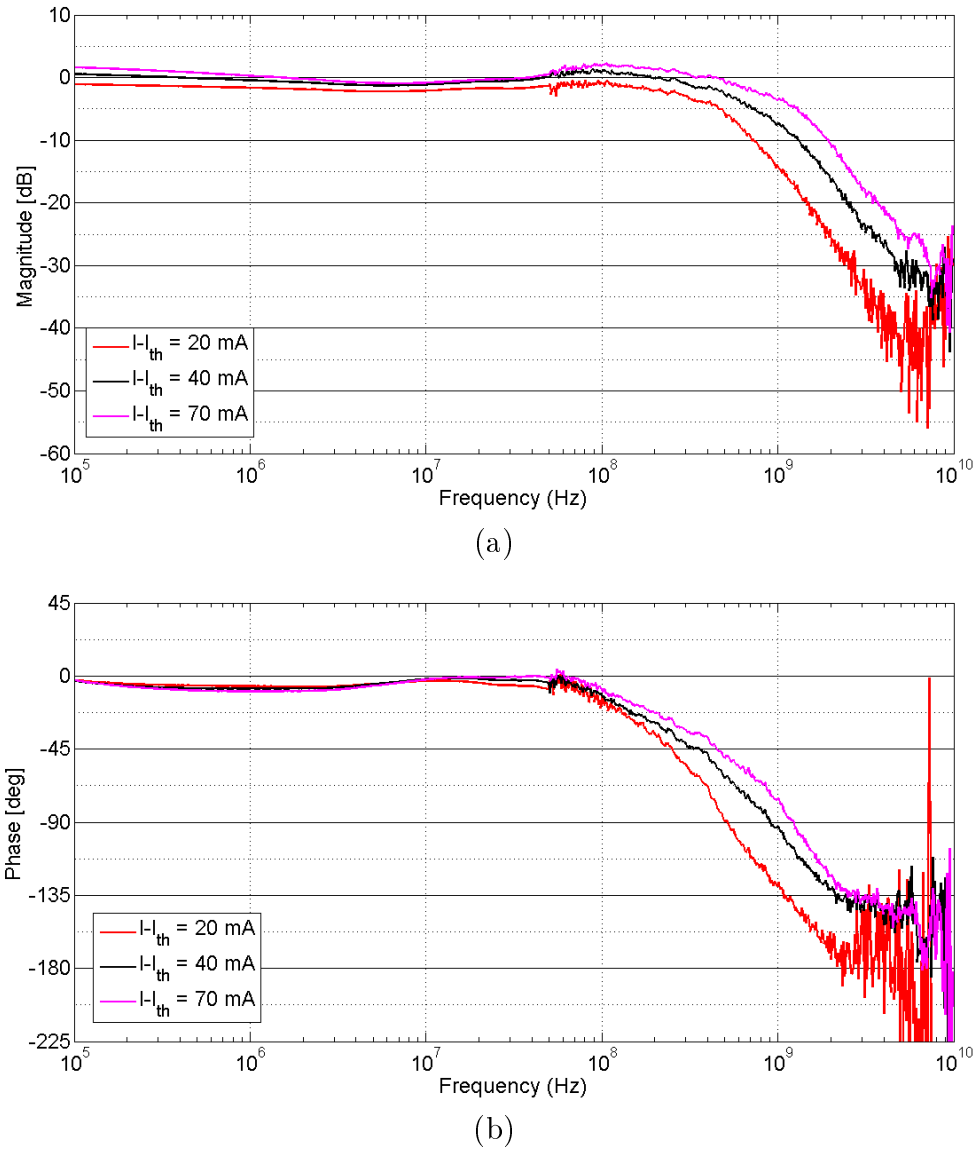
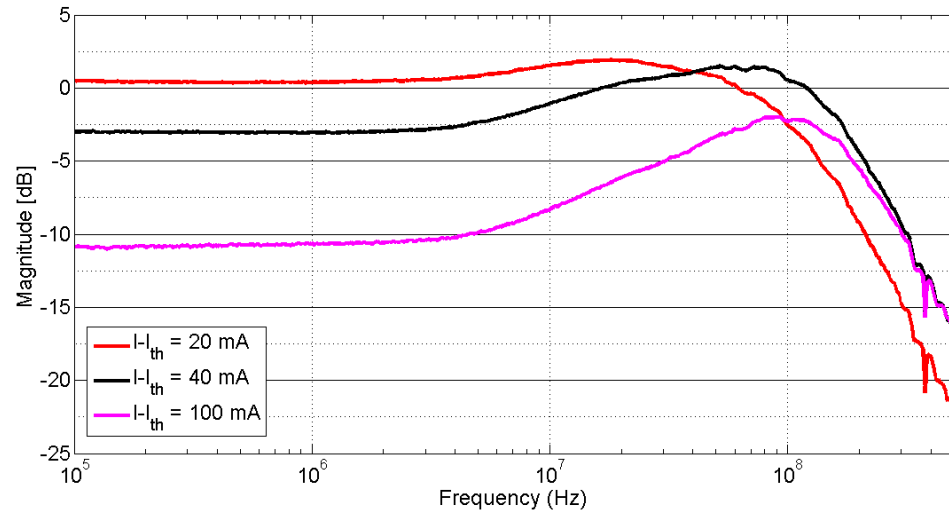
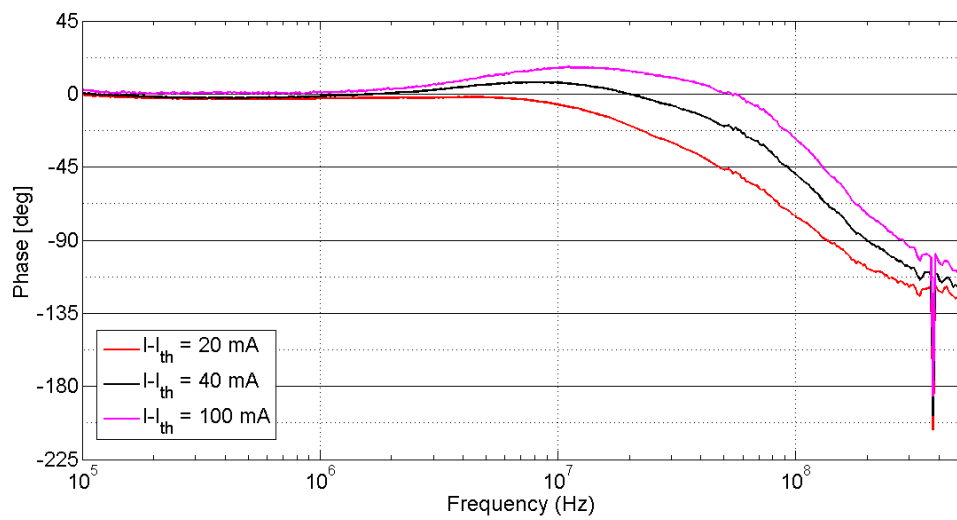


Figure 8.2: Intensity modulation response of 100nm spacer laser (chip 1, bar 1, slo t2, device 19) for different bias currents. 6mA current modulation. Low frequency response (<50 MHz) was measured using New-Focus 1544B photodetector and Agilent 4395A network analyzer. High frequency response (>50 MHz) was measured using HP 8722C RF network analyzer (a) Normalized magnitude (b) Phase



(a)



(b)

Figure 8.3: Intensity modulation response of 150nm spacer laser (chip 1, bar 1, slot 2, device 19) for different bias currents. 3.3mA current modulation. Measured using New-Focus 1544B photodetector and Agilent 4395A network analyzer (a) Normalized magnitude (b) Phase

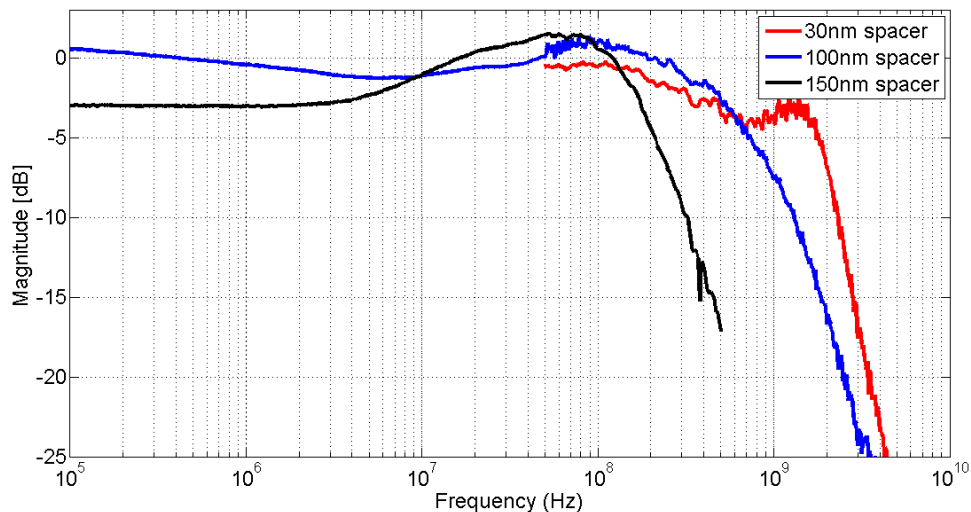


Figure 8.4: Intensity modulation response (magnitude in a.u.) of different spacer lasers for pump current offset of 40mA.

magnitude response curve, and the phase-lead in the phase response. This is in very good agreement with the theoretical analysis (see Figure 7.2), attributing the zero to free-carrier-absorption. The very clear zero of the transfer function at $\nu \approx 5MHz$, can be used to experimentally estimate the effective lifetime of carriers in Si, by comparing it to the theoretical transfer function of Equation 7.19. For the AM response of the 150nm spacer, the resulting experimental carrier lifetime is estimated to be:

$$\tau_{eff} \approx 30ns \quad (8.3)$$

This is, to the best of our knowledge, a novel experimental technique to measure the effective lifetime of carriers in Si, and the first time it is measured in Si/III-V lasers. As discussed in section 3.2.5, this value is comparable to previously reported values in the literature, but is at the high end of the range. It indicates that surface recombination velocity is diminished due to the high-quality of surfaces and interfaces induced by the high-temperature anneal and oxidation.

3. Resonance frequency position vs pump current - The resonance frequency is

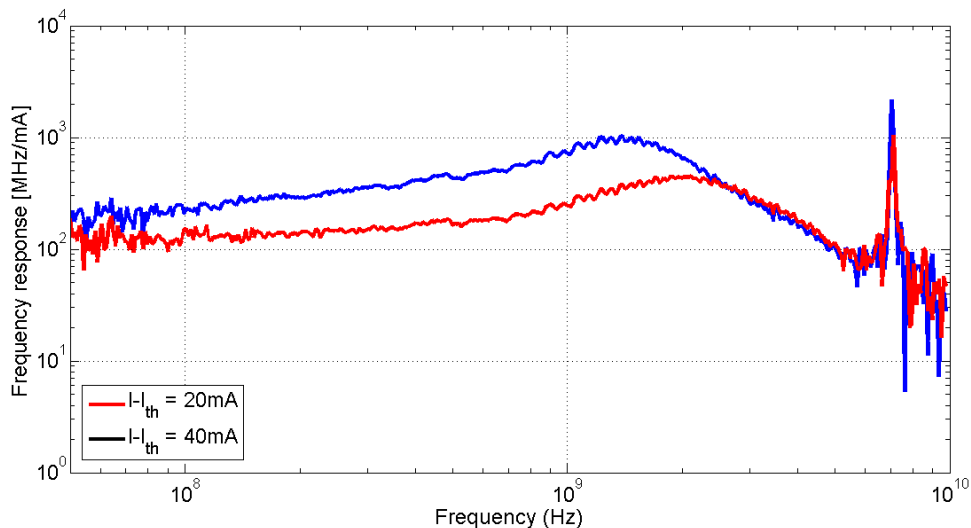


Figure 8.5: Frequency modulation response of 30nm spacer laser (Chip 1, bar 5, Slot 1, device 7) for different bias currents. 0.1mA current modulation. Measured with Optilab BPR-20-M balanced photodetector and HP 8722C RF network analyzer, using MZI with FSR = 7.06GHz

pushed to higher frequencies with pump current, as expected from classic laser dynamics theory.

4. Resonance frequency damping - All spacer lasers have damped relaxation resonance. This is expected due to the high-Q and TPA that suppresses intensity peaks.

8.2 Frequency modulation response

The setup used to perform frequency modulation response measurements is described in appendix B.4. The network analyzer's output was converted to units of GHz/mA using the calibration procedure described in appendix B.4.2. Figures 8.5-8.7 show experimental frequency response curves from the three spacer designs, and for different bias currents. The frequency response curves show some very unique characteristics that are very different from conventional III-V lasers. Some of the key observations are:

1. The thin 30nm spacer has a classic response curve for semiconductor lasers.

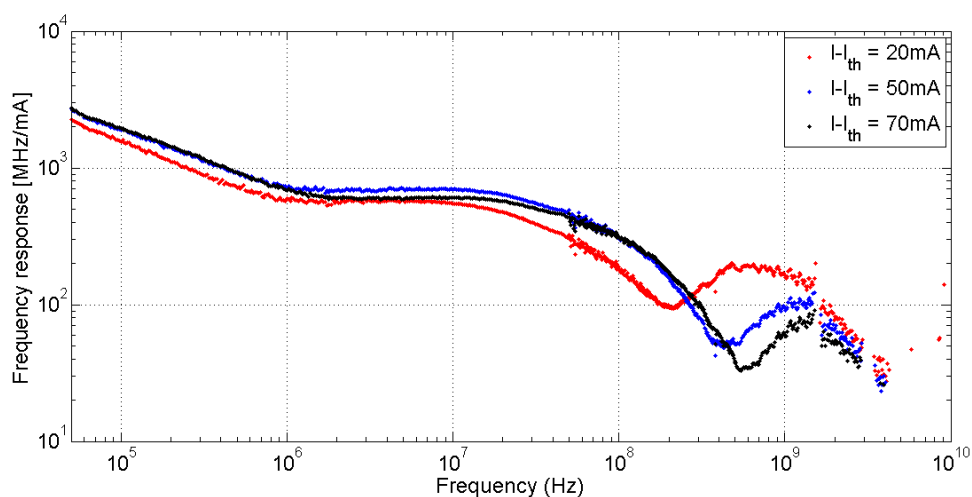


Figure 8.6: Frequency modulation response of 100nm spacer laser (Chip 1, bar 1, Slot 2, device 19) for different bias currents. 35nA current modulation. Measured with Optilab BPR-20-M balanced photodetector MZI with FSR = 1.56GHz. Low frequencies (<500 MHz) were measured using Agilent 4395A network analyzer and high frequencies (>500MHz) using HP 8722C analyzer. Curves from the two analyzers are plotted together without any additional post-processing (stitching)

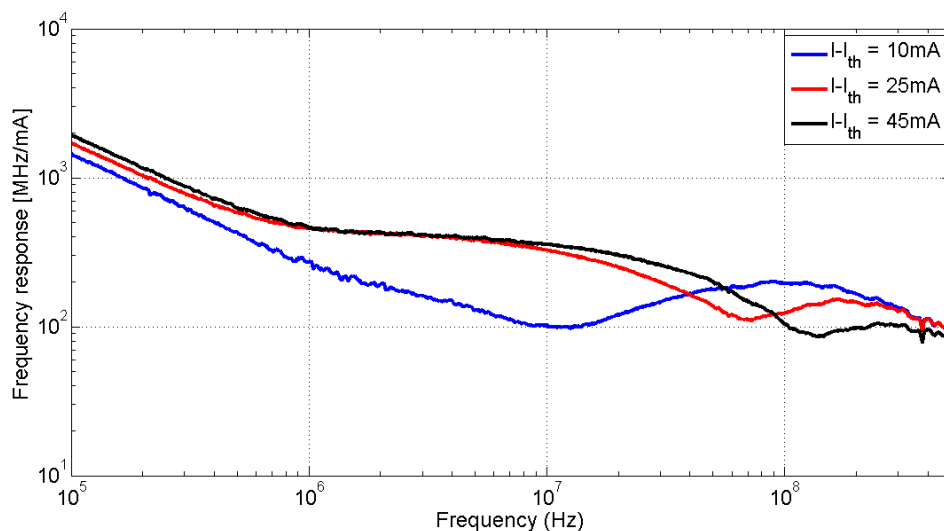


Figure 8.7: Frequency modulation response of 150nm spacer laser (Chip 1, bar 1, Slot 2, device 19) for different bias currents. 0.1mA current modulation. Measured with Optilab BPR-20-M balanced photodetector and Agilent 4395A network analyzer, using MZI with FSR = 1.56GHz

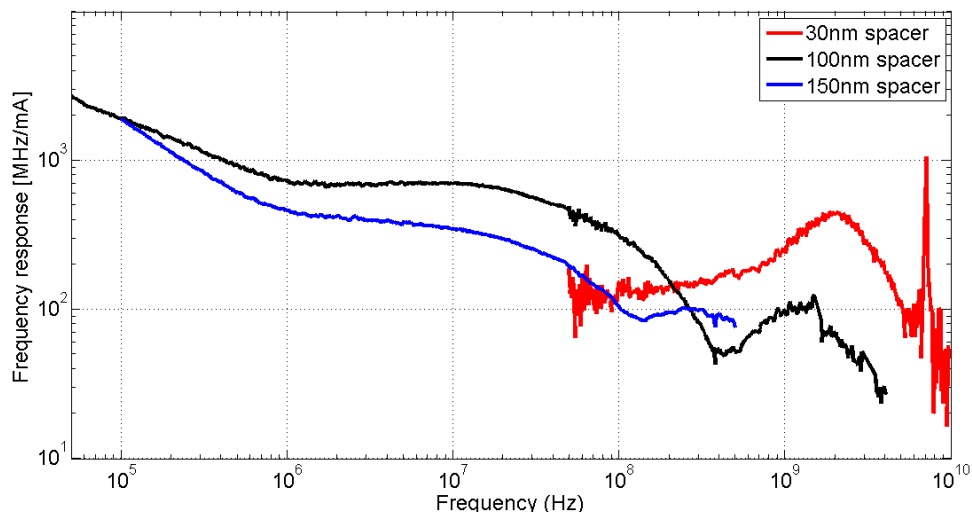


Figure 8.8: Frequency modulation response of different spacer lasers for pump current offset of 50mA.

It shows a response of few hundred MHz/mA of plasma dispersion effect, and a resonance peak at few GHz. The relaxation follows a zero of the transfer function as predicted from the (classic) rate equation analysis. This behavior is very typical of III-V lasers, as expected from thin spacer designs.

2. In all lasers, the very low frequency ($<1\text{MHz}$) is dominated by $1/f$ -like response that is attributed to thermal frequency drift.
3. The thicker spacer designs have a qualitatively different response: they feature dips of the frequency response curve, prior to the relaxation frequency. This is in very good qualitative agreement with the nonlinear rate equation analysis, which attributes this feature to Si free-carrier-dispersion.
4. The thick 150nm spacer in Figure 8.7 demonstrates a wide range of bias currents with a “close to threshold” measurement curve. This figure shows a much lower frequency response than at the higher bias currents. This is consistent with the nonlinear rate equation analysis that attributed the rise in the response to the accumulation of free-carriers in Si.

Figure 8.8 compares the three spacer design for a given offset from threshold. As

was also evident from the intensity modulation response, the resonance frequency shifts to extremely low frequencies when the mode is pushed further into silicon. It also demonstrates the different dynamics of the 30nm spacer, which is closer to the conventional design, compared to the thicker 100nm and 150nm spacer designs.

Despite the very good qualitative agreement with the theoretical analysis, there are still some characteristics that are not explained by the nonlinear model:

1. The position of the frequency response dip - Theory predicts that this unique dip will move to slightly higher frequencies with spacer thickness. In the experimental results, the dip is in fact pushed to lower frequencies.
2. The relative frequency response magnitude between the 100nm and 150nm spacers - The nonlinear model predicts that the thicker spacer will have a stronger frequency response at the low frequencies than the thinner spacer. In the experimental results of Figure 8.8 the 100nm spacer flattens at value of $\sim 700\text{MHz}/\text{mA}$ while the 150nm spacer does so at $350\text{MHz}/\text{mA}$

It is worth noting that at the root of these discrepancies lies the assumption that different spacer laser are identical in all parameters but spacer thicknesses. This is very unlikely. The two lasers were fabricated separately; they have different threshold currents, and hence operate at different temperatures. Heat management is less efficient for the thick spacer design, due to the thermally isolating oxide layer. They may also have different internal efficiencies, due to fabrication variations in the ion-implant. For all of these reasons, it is difficult to compare absolute values in different spacer lasers. However, the unique characteristics that were outlined in the theoretical analysis in Chapter 7 are observed in these lasers, and the trends within a specific spacer design are in agreement with the theory.

In this chapter I presented experimental results demonstrating the modulation response behavior of our lasers. The relaxation resonance was found to be at frequencies as low as $\sim 100\text{MHz}$, validating the theoretical predictions. Predictions regarding the role of free-carriers in Si were also validated: a zero of the intensity modulation

transfer function and a unique dip of the frequency modulation response were both empirically observed. The location of the transfer function's zero was used to estimate that the effective lifetime of carriers in Si is ~ 30 ns. This is the first time this lifetime has been measured in the context of hybrid Si/III-V lasers.

Chapter 9

Noise performance - Theoretical analysis

Chapter 5 considered the noise due to the spontaneous emission process. The analysis there was based on the Schawlow-Townes formula, which was derived by using Fermi's golden rule to calculate the rate of spontaneous decay and the coupling of this spontaneous radiation to the lasing mode. The resulting frequency noise spectra from the S-T formula is white. Further enhancement of the noise was considered by taking into account the coupling between the imaginary and real parts of the refractive index through Henry's alpha parameter. The modified Schawlow-Townes formula was derived, but was still considered white noise.

As was seen in Chapter 7, the dynamic response of the laser cannot be simplified by making it a constant, especially at high frequencies, where resonance effects appear. Furthermore, though the modified Schawlow-Townes formula withstood the test of time and was proven useful, our high-Q hybrid lasers have a new component which is absent from conventional lasers: the free-carriers in silicon. Fluctuations in the number of free-carriers in Si are bound to add excess noise to the system, and must be considered in the context of narrow-linewidth Si/III-V lasers. This chapter will use a different method to carry out the analysis, the Langevin noise source approach, to reconsider laser frequency noise in the presence of fluctuations of carriers, photons, and temperature. Experimental results are compared to the theoretical predictions in Chapter 10.

9.1 Methodology - Langevin noise sources

The use of Langevin noise terms in the context of lasers has many analogies to the original use of Paul Langevin (1872-1946) in the context of Brownian motion of particles. The same results that Albert Einstein derived by using advanced mathematical tools were derived by Langevin by using a simple, yet very different, technique. In his own words, Langevin describes his work “infinitely more simple” than Einstein’s [54]. Despite the simplification, his method is considered even more general than Einstein’s [54]. Langevin introduced a stochastic force that pushes the Brownian particle (in the velocity space), a concept that since then was generalized into a very useful class of methods in the study of continuous random processes.

Laser noise formulas were derived using the advanced mathematical tools of quantum mechanics. The inclusion of quantum-mechanical operators in that analysis makes this approach very cumbersome, and many simplifications must be made to obtain analytical results. The treatment of McCumber [63] in a paper from 1965 suggested the interpretation of quantum fluctuations of a system that is described by rate equations in terms of fictitious Langevin noise sources. This approach was later justified both in the context of classical self-sustained oscillators [53] and for laser oscillators [51]. The same approach was further justified and used to analyze quantum noise of semiconductor lasers [67, 28, 130, 117]. Carrier fluctuations and temperature diffusion were also included to successfully predict the noise spectrum of semiconductor lasers [50]. This approach provides a strong, yet simple, mathematical tool to estimate laser noise spectrum and was found to agree well with experimental results [28].

The strength of the Langevin noise approach is its simplicity: one can simply add a stochastic driving force term to the rate equations. These somewhat fictitious forces are “engineered” to recreate noise predicted from master equations or other fundamental approaches. In the context of recombination and generation of photons and carriers, the Langevin noise force that recreates quantum mechanical results is simply shot-noise [63]. Quantum fluctuations can be described using delta-function

impulses with integrated intensity of one (in the total number description). This implies that one can infer the magnitude of the noise-term just by looking at the form of the dynamic equations. A Langevin noise source suitable for diffusion processes can also be derived. In the next section, Langevin noise terms are added to the differential rate equations, and their statistical properties are discussed.

9.2 Source of noise - fluctuations

Fluctuations of the carriers and photon density can be considered by inserting Langevin noise driving terms in the system of rate Equations 7.5. I will set the current modulation to zero ($\Delta I = 0$) and write the noise-driven rate equations in the matrix form:

$$\begin{pmatrix} A_{11} & A_{12} & A_{13} \\ A_{21} & A_{22} & A_{23} \\ A_{31} & A_{32} & A_{33} \end{pmatrix} \begin{pmatrix} \Delta n_e \\ \Delta n_p \\ \Delta n_{Si} \end{pmatrix} = \begin{pmatrix} F_{n_e} \\ F_{n_p} \\ F_{n_{Si}} \end{pmatrix} \quad (9.1)$$

where the RHS represents the stochastic noise terms, and the matrix elements are the same as in Equations 7.6-7.13. The statistical properties of the different noise terms will be discussed in the following subsections. Since shot-noise describes the statistics of many of these noise terms, it is convenient to look at a particle reservoir picture of the different variables, as shown in Figure 9.1. In Figure 9.1 α is linear loss, α_{TPA} is loss due to TPA, α_{FCA} is loss due to FCA, η_i is the internal efficiency, and η_o is output mirror coupling. R_{21} is the rate of stimulated emission and R_{12} is the rate of stimulated absorption. The two are related to the modal gain using:

$$(R_{21} - R_{12}) V_p = \Gamma_{QW} G_m(n_e) n_p V_p \quad (9.2)$$

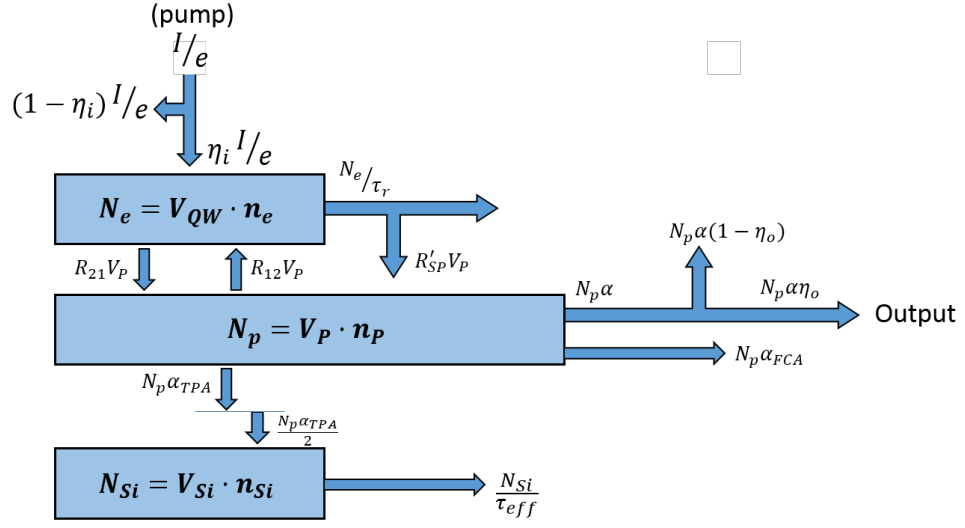


Figure 9.1: Particle reservoir picture of the system

The following relationships can be inferred from the steady-state solution:

$$N_p \alpha_{TPA} = \beta_T h \nu v_g^2 M_{TPA} \Gamma_{Si}^2 n_p^2 V_p \quad (9.3)$$

$$N_p \alpha_{FCA} = v_g \sigma_a n_{Si} \Gamma_{Si} n_p V_p \quad (9.4)$$

$$R'_{SP} V_P = \Gamma_{QW} G_m(n_e) n_{sp} \quad (9.5)$$

$$R_{21} V_P = R'_{SP} V_P \cdot n_p V_P \quad (9.6)$$

$$N_P (\alpha_{TPA} + \alpha_{FCA} + \alpha) + R_{12} V_P = R_{21} V_P + R'_{SP} V_P \quad (9.7)$$

By normalizing the differential rate equations to total numbers, as done in the particle reservoir picture, we can infer the magnitude of the noise simply through the shot-noise. The PSD of a shot-noise process can be deduced from the delta function correlation assumed for shot-noise:

$$\langle F_i(t) F_j(t - \tau) \rangle = S_{ij} \delta(\tau) \quad (9.8)$$

where S_{ij} defines the correlation strength between the two noise sources. The spectral density of such a process is white (constant) with magnitude equal to the correlation

strength:

$$W_{F_i F_j} = S_{ij} \quad (9.9)$$

Our small-signal analysis was conducted in the Fourier domain, such that all quantities are frequency dependent. A convenient way to calculate spectral densities using quantities that are expressed in the frequency domain can be obtained by first considering the ensemble average:

$$\begin{aligned} \langle F_i(\omega) F_j^*(\omega') \rangle &= \left\langle \int F_i(\tau_1) e^{-j\omega\tau_1} d\tau_1 \int F_j^*(\omega') e^{j\omega'\tau_2} d\tau_2 \right\rangle \\ &= \int \int \langle F_i(\tau_1) F_j^*(\tau_2) \rangle e^{-j(\omega\tau_1 - \omega'\tau_2)} d\tau_1 d\tau_2 \end{aligned} \quad (9.10)$$

Assuming stationary and ergodic processes the cross-correlation only depends on the time difference $\tau = \tau_1 - \tau_2$ and we can write:

$$\begin{aligned} \langle F_i(\omega) F_j^*(\omega') \rangle &= \int \langle F_i(t + \tau) F_j^*(t) \rangle e^{-j\omega\tau} d\tau \int e^{-j(\omega - \omega')t} dt \\ &= \int \langle F_i(t + \tau) F_j^*(t) \rangle e^{-j\omega\tau} d\tau \cdot 2\pi\delta(\omega - \omega') \end{aligned} \quad (9.11)$$

Using the Wiener–Khinchin theorem and the the expression in Equation 9.11 we can express the PSD of the dynamic variables Δn_i using [13]:

$$W_{\Delta n_i} = \frac{1}{2\pi} \int \langle \Delta n_i(\omega) \Delta n_i(\omega')^* \rangle d\omega' \quad (9.12)$$

for which the correlations of the Langevin noise source terms are given by:

$$\langle F_i(\omega) F_j(\omega')^* \rangle = 2\pi S_{ij} \delta(\omega - \omega') \quad (9.13)$$

If we write the solution of the matrix 9.1 using a sum:

$$\Delta n_i = \sum A_{ik}(\omega) F_k \quad (9.14)$$

then when we calculate the PSD using Equation 9.12, we end up with a summation

of the form:

$$W_{\Delta n_i} = \sum_{j=1}^3 S_{jj} |A_{ij}|^2 + 2 \sum_{k \neq j} \text{Re} \{A_{ik} A_{ij}\} S_{kj} \quad (9.15)$$

The correlations S_{ii} can be calculated simply by inspecting the rates of “particle” i flowing in (R_i^{in}) and out (R_i^{out}) of the reservoir:

$$\langle S_{ii} \rangle = \sum R_i^{in} + \sum R_i^{out} \quad (9.16)$$

and the cross correlations S_{ij} by the rates in which the two reservoirs, i and j , exchange particles:

$$\langle S_{ij} \rangle = - \left(\sum R_{i \rightarrow j} + \sum R_{j \rightarrow i} \right) \quad (9.17)$$

All in units of total number of particles, and the minus sign is due to the negative correlation (reservoir i receives a particle, while reservoir j loses one). For example, inspection of the particle reservoir picture in Figure 9.1 suggests the following correlation strength for the photon density fluctuations:

$$V_p^2 \langle F_{n_p} F_{n_p} \rangle = (R_{12} + R_{21}) V_P + R'_{SP} V_P + n_p V_p (\alpha + \alpha_{TPA} + \alpha_{FCA}) \quad (9.18)$$

Simplifying the expression using the steady-state conditions and following this procedure for the rest of the correlations yields:

$$\langle F_{n_p} F_{n_p} \rangle = 2R'_{SP} \left(n_P + \frac{1}{V_P} \right) \quad (9.19)$$

$$\langle F_{n_e} F_{n_e} \rangle = \frac{2\eta_i I}{eV_{QW}^2} + \frac{2R'_{SP} n_p}{\Gamma_{geom}^2} - \frac{2\Gamma_{QW} G_m n_p}{\Gamma_{geom} V_{QW}} \quad (9.20)$$

$$\langle F_{n_{Si}} F_{n_{Si}} \rangle = \frac{\beta_T h \nu v_g^2 M_{TPA} n_p^2}{V_P} \quad (9.21)$$

Notice that the auto-correlation of the Si carriers assumes that the effective lifetime τ_{eff} describes recombination-like processes only. This is an approximation that assigns a recombination lifetime to a diffusion process. Refined approximation will be introduced in relevant sections.

The cross-correlations can be shown to be:

$$\langle F_{n_e} F_{n_P} \rangle = -\frac{2R'_{SP} n_P}{\Gamma_{geom}} \left(1 + \frac{1}{2n_P V_P} \right) + \frac{\Gamma_{QW}}{\Gamma_{geom}} \frac{G_m n_P}{V_P} \quad (9.22)$$

$$\langle F_{n_P} F_{n_{Si}} \rangle = -\frac{\beta_T h \nu v_g \Gamma_{Si} M_{TPA} n_P^2}{\sqrt{2} V_P} \quad (9.23)$$

$$\langle F_{n_e} F_{n_{Si}} \rangle = 0 \quad (9.24)$$

The square root in the second equation is due to the fact that for each two-photon pair, only one Si electron is generated. The zero correlation between QW and silicon electrons (third equation) is due to the fact that the two only interact through the mediation of photons in a finite bandwidth, and the shot-noise impulses are assumed instantaneous.

Notice that we have assumed shot-noise statistics for all processes that involve generation or annihilation of particles. Though this is considered generally correct in the linear regime (or at least provides correct results), it wasn't proven in this work that this holds for nonlinear loss processes as well. In fact, it is not accurate for multi-particle processes such as TPA. For example, two-photon-absorption has been shown to produce sub-Poissonian light [23, 36]. An improved statistical model can be derived for TPA, at the cost of increased complexity. However, it is shown in this work that TPA is almost negligible compared to FCA, which is a linear process. Moreover, strong squeezing is only evident in resonant nonlinearities, or ultra-high light intensities [18]. The analysis implies that any squeezing-like effects in this platform would be weak, and in any case masked by free-carrier effects. I therefore treat fluctuations due to TPA as any other loss with shot-noise statistics.

9.2.1 Photon density

Next, I will solve the small-signal, Langevin-force-driven, linear set of equations (matrix 9.1) to get the photon density Δn_P , and calculate its PSD using Equation 9.12 and the correlation above. Recalling that $A_{31} = A_{13} = 0$, and using Cramer's rule,

we get the following expression:

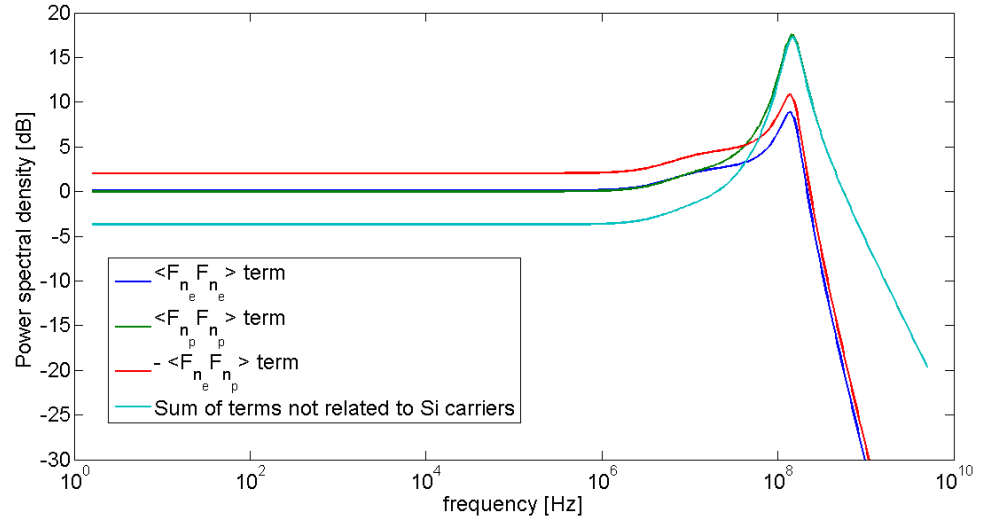
$$\begin{aligned}
W_{n_p} = & \frac{1}{|H_0(\omega)|^2} \{ |A_{21}A_{33}|^2 \langle F_{n_e} F_{n_e} \rangle + |A_{11}A_{33}|^2 \langle F_{n_p} F_{n_p} \rangle \\
& + |A_{23}A_{11}|^2 \langle F_{n_{Si}} F_{n_{Si}} \rangle - 2\text{Re} \{ A_{21}A_{33}A_{11}^* A_{33}^* \} \langle F_{n_e} F_{n_p} \rangle \\
& - 2\text{Re} \{ A_{11}A_{33}A_{11}^* A_{23}^* \} \langle F_{n_p} F_{n_{Si}} \rangle \}
\end{aligned} \tag{9.25}$$

where the function $H_0(\omega)$ is defined:

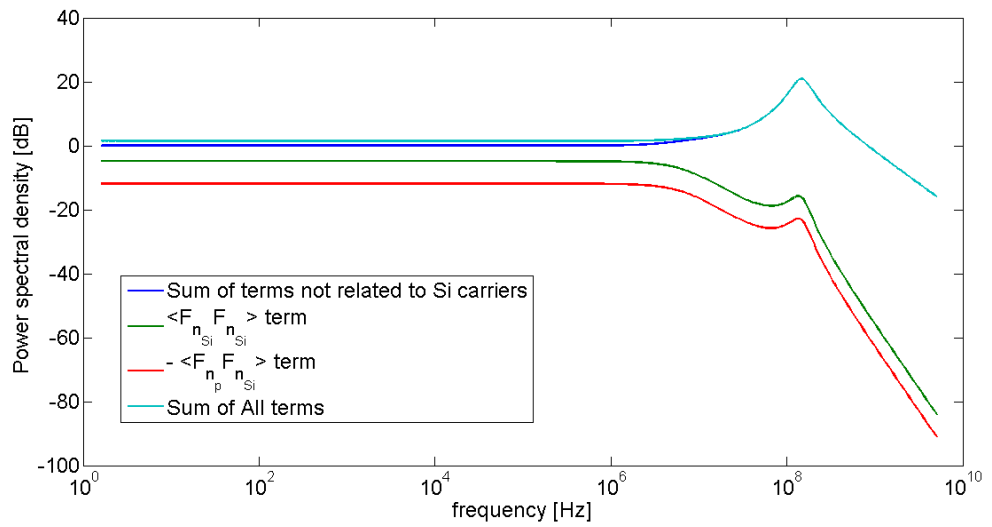
$$H_0(\omega) = (j\omega + 2\xi\omega_n) \left[(j\omega + Bn_{p,0}) \left(\frac{1}{\tau_{eff}} + j\omega \right) + 2CDn_{p,0}^2 \right] + \left(\frac{1}{\tau_{eff}} + j\omega \right) \omega_n^2 \tag{9.26}$$

for which parameters are defined in Equations 7.20-7.22.

The expression for the PSD of the photon density in Equation 9.25 has two terms which are unique to the hybrid platform, and link fluctuations of Si carrier density to fluctuations of photon density. The other terms, which don't involve the TPA-generated carriers, are compared in Figure 9.2(a). This figure demonstrates that the negative cross-correlation between QW-carrier and photons decreases fluctuations of photon density below its intrinsic level. This effect, which is related to gain saturation, is the reason that lasers have suppressed intensity noise. Figure 9.2(b) adds the contribution of free-carriers in Si. It shows that fluctuations of density of carriers in Si has a minor effect, and hardly changes the intensity noise from what we would expect in a conventional III-V laser.



(a)



(b)

Figure 9.2: PSD of the photon density (150nm spacer, $Q_{Si} = 10^6$, $I = 4I_{th}$) (a) Comparison of conventional terms (terms which don't involve TPA-generated free-carriers in Si) (b) Comparison of these conventional terms to free-carrier related terms

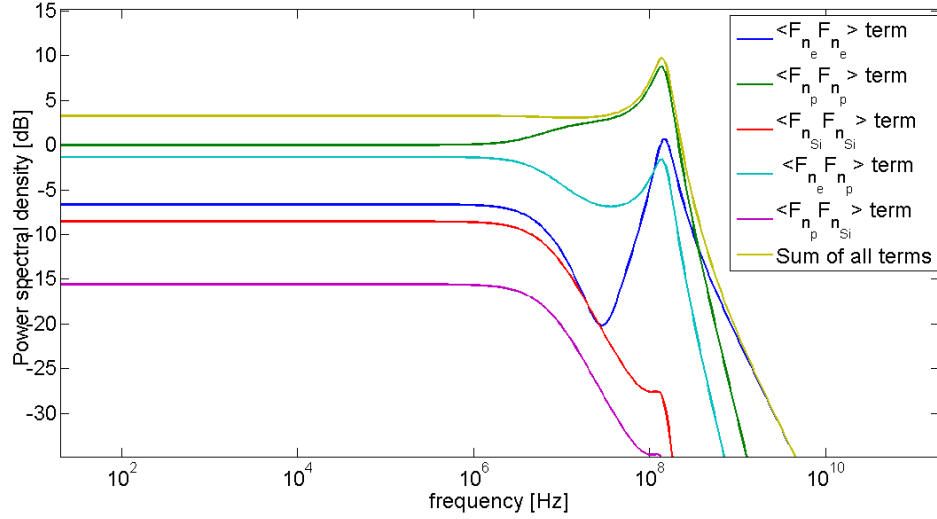


Figure 9.3: Comparison of the different terms of the PSD of QW-carrier density (150nm spacer, $Q_{Si} = 10^6$, $I = 4I_{th}$)

9.2.2 Carriers in the quantum wells

The same method that was used for the photon density will now be used for the QW carrier density. The following expression for the PSD is derived after some algebra:

$$\begin{aligned}
 W_{n_e} = & \frac{1}{|H_0(\omega)|^2} \{ |A_{22}A_{33} - A_{23}A_{32}|^2 \langle F_{n_e} F_{n_e} \rangle + |A_{12}A_{33}|^2 \langle F_{n_p} F_{n_p} \rangle \\
 & + |A_{12}A_{23}|^2 \langle F_{n_{Si}} F_{n_{Si}} \rangle - 2\text{Re} \{ (A_{22}A_{33} - A_{23}A_{32}) A_{12}^* A_{33}^* \} \langle F_{n_e} F_{n_p} \rangle \\
 & - 2\text{Re} \{ A_{12}A_{33}A_{12}^* A_{23}^* \} \langle F_{n_p} F_{n_{Si}} \rangle \}
 \end{aligned} \tag{9.27}$$

Figure 9.3 shows the magnitude of the different terms affecting the PSD of the density of QW carriers. Interestingly, the dominant term in that spectrum is the one due to fluctuation of photon-density $\langle F_{n_p} F_{n_p} \rangle$. Inherent fluctuations of QW electrons (the $\langle F_{n_e} F_{n_e} \rangle$ term) are small due to gain clamping. We will shortly see that this behavior gives the Henry linewidth-enhancement a multiplicative nature, rather than an additive one.

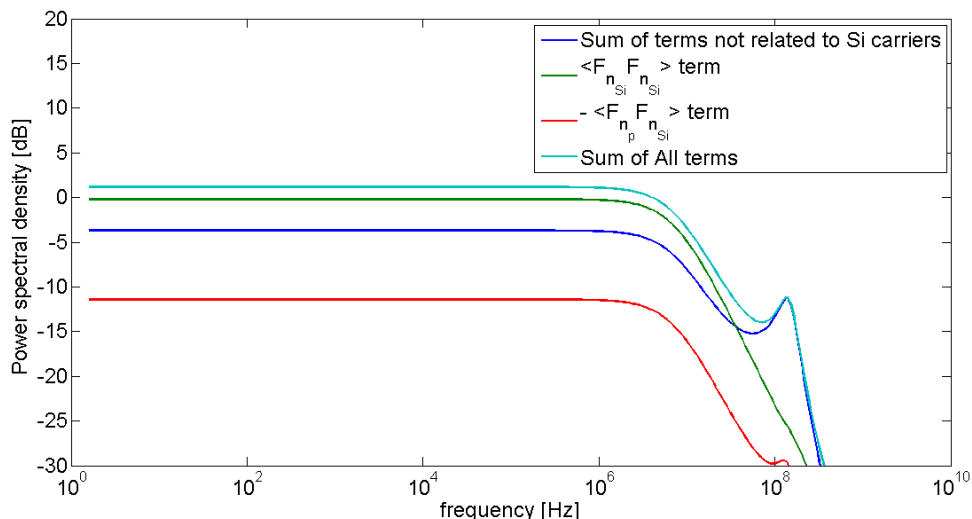


Figure 9.4: Noise spectrum of silicon carrier density for shot-noise model (150nm spacer, $Q_{Si} = 10^6$, $I = 4I_{th}$)

9.2.3 Free-carriers in silicon

In principle, the same treatment that was used above for the photons and the QW carriers could be used for the free-carriers in Si. However, this approach would incorrectly treat the effective lifetime in Si, τ_{eff} , as a time constant for recombination. As we recall from Chapter 3, this time constant also captures the average time in which carriers diffuse out of the mode's area. Though this was suitable for the steady-state analysis, it might not be adequate for noise estimation. Despite that fact, we will ignore diffusion for the time being, and examine the spectral content of the noise, assuming shot-noise statistics. The resulting PSD is shown in Figure 9.4. Note that in the case of the Si carriers, the dominant contribution is from the intrinsic fluctuation of Si carriers (the $\langle F_{n_{Si}} F_{n_{Si}} \rangle$ term). The other correlation terms contribute very little and can be neglected.

In the context of fluctuations, diffusion of particles have completely different statistics than recombination [118]. Recombination-generation has shot-noise statistics, with zero correlation between different points of space and time. Diffusion, however, a process that is stochastic in nature, has a unique and different correlation. If the

carrier density obeys the diffusion equation:

$$\frac{dn_{Si}}{dt} - D\nabla^2 n_{Si}(t, \mathbf{r}) = f_D(x, t) \quad (9.28)$$

Where the term on the RHS is the Langevin force, then the appropriate correlation for the diffusion-driven noise source is [122, 119]:

$$\langle f_D(t, r) f_D^*(t', r') \rangle = -2D \nabla_{\mathbf{r}} \cdot \nabla_{\mathbf{r}'} \left[n_{Si}(\mathbf{r}) \delta^3(\mathbf{r} - \mathbf{r}') \right] \delta(t - t') \quad (9.29)$$

From the previous discussion of Figure 9.4, we have concluded that only inherent fluctuations of the Si carrier should be considered, and all other contributions can be neglected. Therefore, I adopt the following strategy to refine the spectra of Si carrier density and consider diffusion, rather than just recombination:

1. Return to the original generation-recombination-diffusion equation (see Equation 3.23):

$$\frac{dn_{Si}}{dt} = \frac{\beta_T h \nu \Gamma_{Si} V_g^2}{2} n_p^2 - \left(\frac{1}{\tau_b} + 2 \frac{S}{H} \right) n_{Si} + D_a \nabla^2 n_{Si} \quad (9.30)$$

2. Take the Fourier transform in both time and space of a linearized small-signal equation, and introduce two Langevin forces:

$$\Delta n_{Si} = \frac{f_{n_{Si}}(\omega, \mathbf{k}) + f_D(\omega, \mathbf{k})}{j\omega + \frac{1}{\tau_{r, Si}} + D_a |\mathbf{k}|^2} \quad (9.31)$$

Where now $\frac{1}{\tau_{r, Si}}$ is time constant for recombination only (sum of bulk and surface recombination as in the bracket in Equation 9.30). $f_{n_{Si}}$ is the Langevin force due to generation-recombination, while f_D is due to diffusion. Notice that for purposes of simplicity, we have decoupled this equation from the other rate equations, by neglecting the dependence on the photon density. The generation term is considered a constant in this treatment. It will contribute to shot noise, but its dynamics are ignored. This is motivated by the previous analysis, that

showed that the spectra is dominated by the low-pass filter function, and only minor adjustments are required around the relaxation resonance.

I will use the result of Equation 9.31 to calculate the frequency noise in the following sections.

9.2.4 Temperature

Silicon has a large thermo-optic coefficient of about $\eta_T = \frac{dn}{dT} = 1.8 \cdot 10^{-4} [\text{K}^{-1}]$ at room temperature [45], comparable to that of InP and other III-V materials. Thermal fluctuations are therefore easily coupled to the frequency noise through the thermo-optic effect. This section will offer a model, based on the Langevin force approach, to take temperature fluctuations into account. I will consider both inherent temperature fluctuations, and those induced by thermal dissipation.

The temperature profile in the laser cavity obeys the non-steady-state heat equation [96]:

$$c_h \rho \frac{\partial T}{\partial t} = q + \kappa \nabla^2 T \quad (9.32)$$

where c_h is the specific heat in units $[\frac{\text{Joul}}{\text{kg} \cdot \text{K}}]$, κ is the thermal conductivity in units $[\frac{\text{Joul}}{\text{sec} \cdot \text{m} \cdot \text{K}}]$, and ρ is the density in units $[\frac{\text{kg}}{\text{m}^3}]$. The variable q represents the heat source. In this work, I will only consider heat that is generated due to dissipation in Si, such that q can be represented using the absorbance α_z (units of $[\frac{1}{\text{m}}]$) and the intensity I :

$$q = \alpha_z I \quad (9.33)$$

I will consider the following heat-generating mechanisms:

1. Every non-radiative recombination event generates heat by the amount of energy quanta absorbed.
2. Energy dissipated through free-carrier absorption fully converted to heat.

I will also assume that the temperature gradients are small enough within the mode's volume, such that it will be approximated as constant. No knowledge of the exact

temperature profile is required.

Expressing the two heat mechanisms explicitly, we get the following heat term:

$$q = h\nu v_g \sigma_a n_{si} \Gamma_{Si} n_p + \frac{2h\nu n_{si}}{\tau_{r,Si}} \quad (9.34)$$

where in the second term we used the two-photon energy instead of the silicon's bandgap energy, to take into account the thermalization process of carriers before they relax to the band-edge.

Linearizing the heat equation and introducing a Langevin noise force, we can write:

$$\frac{\partial \Delta T}{\partial t} = q_1 \Delta n_p + q_2 \Delta n_{Si} + D_T \nabla^2 \Delta T - \frac{1}{\tau_T} \Delta T + f_T \quad (9.35)$$

where $D_T = \frac{\kappa}{c_h \rho}$ is the temperature diffusion coefficient, f_T is the temperature Langevin force. The parameters q_1 and q_2 are defined as:

$$q_1 = \frac{h\nu v_g \sigma_a n_{si,0} \Gamma_{Si}}{c_h \rho} \quad (9.36)$$

$$q_2 = \frac{h\nu v_g \sigma_a \Gamma_{Si} n_{p,0} + \frac{2h\nu}{\tau_{r,Si}}}{c_h \rho} \quad (9.37)$$

The parameter $\frac{1}{\tau_T}$ is the temperature decay rate [55]. It was artificially inserted in the equation, to account for heat flow out of the cavity and into the heat sink. This was necessary since we don't treat the boundary conditions in the following derivation. The temperature fluctuations are effected by both photon density fluctuations and Si-carrier-density fluctuations, as described by the above equation. The correlations of the Langevin force for the temperature can be expressed as in other diffusion processes:

$$\langle f_T(t, r) f_T^*(t', r') \rangle = A \cdot \nabla_{\mathbf{r}} \cdot \nabla_{\mathbf{r}'} \left[T(\mathbf{r}) \delta^3(\mathbf{r} - \mathbf{r}') \right] \delta(t - t') \quad (9.38)$$

To find the unknown A , we require that for constant average temperature the root mean square (RMS) calculated using the above expression would agree with familiar

statistical physics results for a body in contact with a thermal bath [49]:

$$\langle \Delta T^2 \rangle = \frac{K_B T^2}{\rho c_h V} \quad (9.39)$$

By integrating expression 9.38 over volume V , for constant temperature T , and equating the result to the above RMS, we find the constant A :

$$A = \frac{2D_T K_B T}{\rho c_h} \quad (9.40)$$

9.3 Frequency noise

The lasing frequency is set by the average refractive index, as sensed by the optical mode. Fluctuations in the local refractive index will be averaged over the mode's area, and the fluctuations of the effective refractive index can be well-approximated using:

$$\Delta n_{eff}(t) = \iiint |e(x, y, z)|^2 \Delta n(x, y, z, t) dx dy dz \quad (9.41)$$

Where $e(x, y, z)$ is the electric field profile of the mode, normalized such that:

$$\iiint |e(x, y, z)|^2 dx dy dz = 1 \quad (9.42)$$

Fluctuations in the frequency can be approximated using the effective refractive index, as was done for the frequency response calculations:

$$\Delta \nu = -\frac{v_g}{\lambda_0} \Delta n_{eff} \quad (9.43)$$

These fluctuations can be broken apart to contributions from the dispersion plasma effect (of both QW carriers and Si carriers) and the thermo-optic effect. This can be approximated using the respective confinement factors:

$$\Delta \nu = -\frac{v_g}{\lambda_0} \left\{ \Gamma_{QW} \frac{\partial \Delta n_{eff}}{\partial n_e} \Delta n_e + \Gamma_{Si} \frac{\partial \Delta n_{eff}}{\partial n_{Si}} \Delta n_{Si} + \Gamma_{Si} \frac{\partial \Delta n_{eff}}{\partial T} \Delta T \right\} \quad (9.44)$$

Expressing the dispersion plasma effect in the QW using Henry's alpha parameter (see Equation 7.38), we get the following PSD of the frequency noise due to fluctuations in n_e , n_{Si} and T :

$$W_{\Delta\nu} = \left\{ \left(\Gamma_{QW} \alpha_H \frac{G'_m}{4\pi} \right)^2 W_{\Delta n_e} + \left(\frac{v_g}{\lambda_0} \xi \Gamma_{Si} \right)^2 W_{\Delta n_{Si}} + \left(\frac{v_g}{\lambda_0} \Gamma_{Si} \eta_T \right)^2 W_{\Delta T} \right\} \quad (9.45)$$

We have seen in previous sections that correlations between Δn_e and Δn_{Si} are very weak and hardly contribute to the total noise spectrum, and so I neglected them in the above expression. In the following sub-sections, I will use this expression to examine the contribution of the different fluctuation mechanisms, and attempt to predict the resulting PSD of the frequency noise. I will use the results from previous sections for the noise spectrum of carriers.

9.3.1 Spontaneous emission

The expression for the frequency noise that I have derived in the previous section considers the contribution of carriers and temperature fluctuations. However, it lacks a very important component: spontaneous emission. Spontaneous emission affects the frequency spectrum by "injecting" photons with random phase, which is uncorrelated to the mode's phase. In the spirit of this chapter, I will introduce a phase Langevin force, F_ϕ , to account for this random-walk of the phase:

$$\frac{d\Delta\phi}{dt} = 2\pi\Delta\nu = F_\phi \quad (9.46)$$

The RMS of the phase fluctuations is related to the photon density fluctuations using [13, 31]:

$$\langle F_\phi F_\phi \rangle = \frac{\langle F_{n_P} F_{n_P} \rangle}{4n_p^2} \quad (9.47)$$

Recall that we have previously calculated the correlation on the RHS of this equation. We therefore obtain a Lorentzian linewidth:

$$\Delta\nu = \frac{2R'_{SP} \left(n_P + \frac{1}{V_P} \right)}{2\pi \cdot 4n_p^2} \approx \frac{R'_{SP}}{4\pi n_p} \quad (9.48)$$

recreating the familiar S-T linewidth (see Equations 5.14,2.6).

9.3.2 Henry's linewidth enhancement

I have calculated the fluctuations of QW carrier density in section 9.2.2 and we have seen that the dominant term is the one proportional to $\langle F_{n_P} F_{n_P} \rangle$. The fact that the spontaneous emission noise is also proportional to this term gives rise to the linewidth enhancement factor. We can write the contribution of both spontaneous emission and dispersion plasma effect in the QW using:

$$W_{\Delta} = W_{\Delta\nu_{S-T}} \left\{ 1 + 4n_p^2 \left(\Gamma_{QW} \alpha_H \frac{G'_m}{2} \right)^2 \frac{|A_{12}|^2 |i\omega + \frac{1}{\tau_{eff}}|^2}{|H_0(\omega)|^2} \right\} \quad (9.49)$$

where $W_{\Delta\nu_{S-T}}$ is the S-T white noise level, and the term in bracket is the Henry enhancement. Figure 9.5 shows the contribution of spontaneous emission (which we derived using shot-noise model for the photon density) plus the contribution of QW carrier density fluctuations. This figure shows that, as expected, QW carrier fluctuations give rise to the Henry linewidth enhancement, which drops off to the Schawlow-Townes linewidth for frequencies above the relation resonance. It also demonstrates the advantage of having the resonance at very low frequencies, as in the thick spacer designs; the noise becomes truly quantum-mechanically limited (the S-T limit) at frequencies as low as ~ 1 GHz. Interestingly, the zero of the transfer function, which was predicted for the intensity modulation, doesn't appear in the noise spectrum. This is also evident in Figure 9.3, where the cross-correlation between fluctuations in photon and electron density (the $\langle F_{n_e} F_{n_P} \rangle$ term) cancels out the zero of the transfer function in the dominant term.

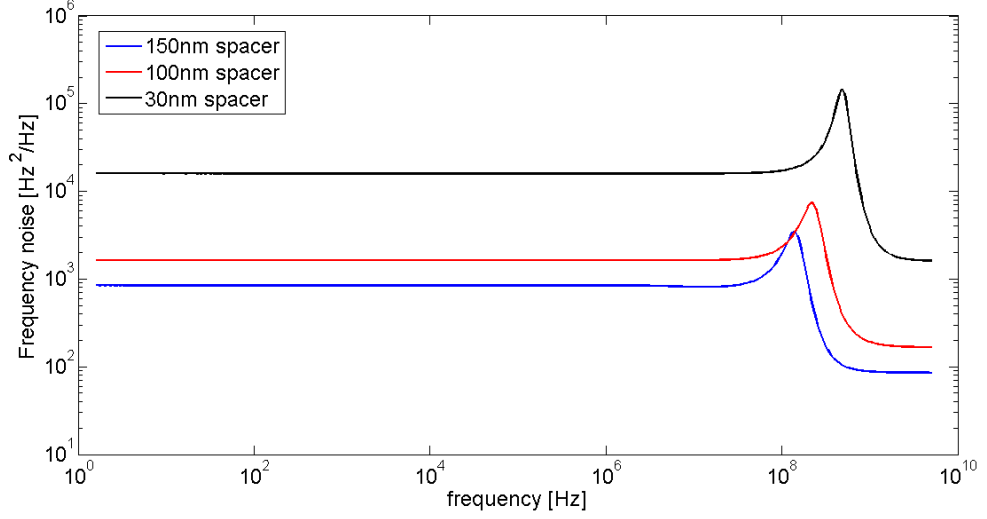


Figure 9.5: Frequency noise due to spontaneous emission and QW carrier density fluctuations using Langevin shot-noise model. $Q_{Si} = 10^6$, $I = 4I_{th}$, $\alpha_H = 3$

9.3.3 Noise due to the plasma effect in silicon

In this section I will consider only noise due to fluctuations of free-carriers in Si that affect the frequency noise spectrum through the plasma effect (free-carrier-dispersion):

$$\Delta\nu = -\frac{v_g}{\lambda_0} \left\{ \Gamma_{Si} \frac{\partial \Delta n_{eff}}{\partial n_{Si}} \Delta n_{Si} \right\} \quad (9.50)$$

I will compare the resulting spectrum from two different models:

1. Shot-noise only model - In this model I treat the effective lifetime of carriers in Si as a recombination lifetime. I will neglect carrier diffusion altogether, and assign recombination properties to the carriers that diffuse away from the mode.
2. Shot-noise and diffusion noise - I consider diffusion of carriers together with recombination (bulk and surface). However, I neglect noise due to cross-correlation of photons and Si carriers, and only treat intrinsic carrier fluctuations.

In the second model, we need to take into account spatial variation. The correlation of Langevin noise force (shot-noise) now becomes [50]:

$$\langle f_{n_{Si}}(t, r) f_{n_{Si}}^*(t', r') \rangle = \left\{ \frac{n_{Si}(\mathbf{r})}{\tau_{r, Si}} + \frac{\beta_T h \nu \Gamma_{Si} V_g^2}{2} n_p^2(\mathbf{r}) \right\} \delta^3(\mathbf{r} - \mathbf{r}') \delta(t - t') \quad (9.51)$$

while the correlation for the Langevin diffusion source is:

$$\langle f_D(t, \mathbf{r}) f_D^*(t', \mathbf{r}') \rangle = -2D_a \nabla_{\mathbf{r}} \cdot \nabla_{\mathbf{r}'} \left[n_{Si}(\mathbf{r}) \delta^3(\mathbf{r} - \mathbf{r}') \right] \delta(t - t') \quad (9.52)$$

To estimate the frequency fluctuation, I need to know the optical mode profile $i = |e(\mathbf{r})|^2$. For purposes of simplicity, I will assume a Gaussian profile with the same FWHM as the simulated mode. I will then compute the spatial Fourier transform of the energy distribution $I(k_x, k_y, k_z)$. Notice that the Langevin force correlations in the Fourier domain have the form:

$$\langle f_{n_{Si}}(\omega, \mathbf{k}) f_{n_{Si}}^*(\omega', \mathbf{k}') \rangle = \left\{ \frac{n_{Si}(\mathbf{k} + \mathbf{k}')}{\tau_{r, Si}} + \frac{\beta_T h \nu \Gamma_{Si} V_g^2}{2} G(\mathbf{k} + \mathbf{k}') \right\} 2\pi \delta(\omega - \omega') \quad (9.53)$$

$$\langle f_D(\omega, \mathbf{k}) f_D^*(\omega', \mathbf{k}') \rangle = -2D_a \mathbf{k} \cdot \mathbf{k}' n_{Si}(\mathbf{k} + \mathbf{k}') 2\pi \delta(\omega - \omega') \quad (9.54)$$

where $n_{Si}(\mathbf{k})$, $G(\mathbf{k})$ are the Fourier transforms of $n_{Si}(\mathbf{r})$, $n_P^2(\mathbf{r})$, respectively. The frequency fluctuations can be calculated by taking the Fourier transform of Equation 9.50, and by using the Fourier-domain Si carrier fluctuations from Equation 9.31. Finally, I will calculate the PSD of the frequency fluctuations using Equation 9.12, and plug in the correlations of Equations 9.51 and 9.52. Notice that this can be done numerically using no other assumptions. However, this brute-force approach requires calculating six nested integrals numerically. Performing this with sufficient resolution to obtain a reliable result is almost prohibitive, especially if one wishes to sweep other parameters, e.g., the pump power. I will therefore simplify this six-dimensional integral by using the following assumptions:

1. Instead of assuming a Gaussian profile I assume a three-dimensional sinc function for the optical mode with the same width. The Fourier transform of a sinc function is a window function. This will change the limits of integration to a finite window (an ellipsoid), and make the integrand manageable.
2. I assume that the Si carrier density profile $n_{Si}(\mathbf{r})$ is constant over the mode

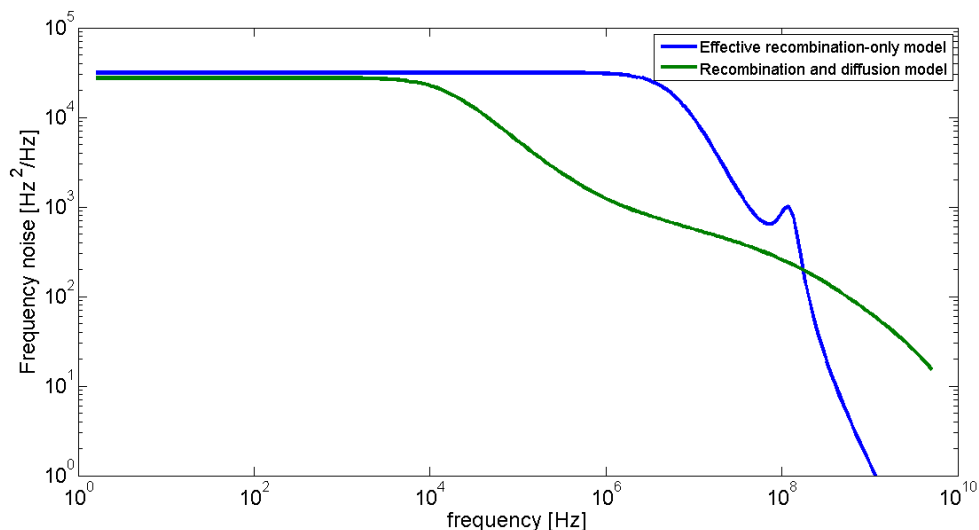


Figure 9.6: The effect of Si-carrier fluctuation on the frequency noise spectrum: Effective recombination model vs recombination-diffusion model. 150nm Spacer, $Q_{Si} = 10^6$, $I = 2I_{th}$

profile. We have previously seen in Chapter 3 that this is a good approximation due to the large diffusion length of carriers in Si. The Fourier transform will be a delta function (compared to the Fourier transform of the optical mode), which will reduce the dimensionality of the resulting integral.

3. I will work in spherical coordinates since the term $|\mathbf{k}|^2$ appears everywhere in the integration. The only non-spherical symmetric part of the integration is its boundary; the integration is over an ellipsoid and not a sphere.

Figure 9.6 compares frequency noise from the recombination-only model and the recombination-diffusion model. Some interesting conclusions can be drawn from this figure:

1. At the very low frequencies they both have same order of magnitude flat response. In the steady-state, the rate of carrier generation due to TPA equals the rate of carrier (effective) recombination. In both models, the generation term is identical so the shot-noise generated by this process is likewise identical.
2. The recombination-diffusion model has a pole at a much lower frequency. This

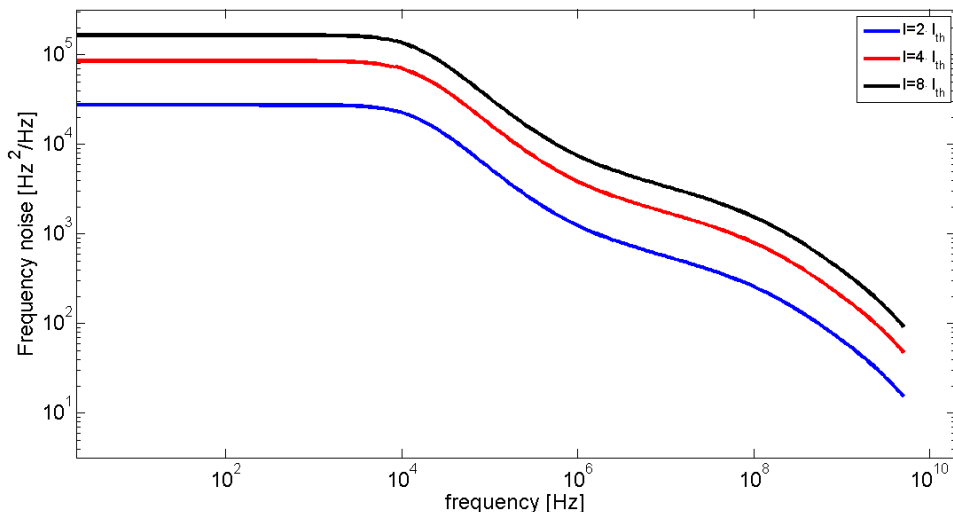


Figure 9.7: Frequency noise spectrum due to Si carrier fluctuations for different pump currents. 150nm Spacer, $Q_{Si} = 10^6$

is due to the much lower recombination lifetime of carriers in Si, compared to the effective lifetime that includes diffusion.

3. The high-frequency noise due to diffusion drops off much more slowly than that of the recombination-only model. This is a characteristic feature of diffusion noise. It demonstrates why it is so important to take the diffusion noise into consideration; at the high frequencies (~ 1 GHz) it might be dominant.

In the example of Figure 9.6 the diffusion noise at 1GHz for the 150nm spacer corresponds to a linewidth of 200Hz. In the high-Q platform, this is comparable to the S-T linewidth we would expect from this laser. This suggests that diffusion noise might be a dominant noise-source in our platform.

Figure 9.7 shows the effect of pump current on frequency noise due to Si carrier fluctuations. As we increase the pump current, the intra-cavity optical intensity increases together with the two-photon-absorption rate. This increases the free-carrier density in silicon, and their fluctuations increasingly degrade the frequency spectrum. The increase in noise level with pump current highlights an important feature of the high-Q hybrid Si/III-V platform: Noise that stems from fluctuations of carriers generated at the silicon slab due to TPA, does not behave as the noise of a conventional

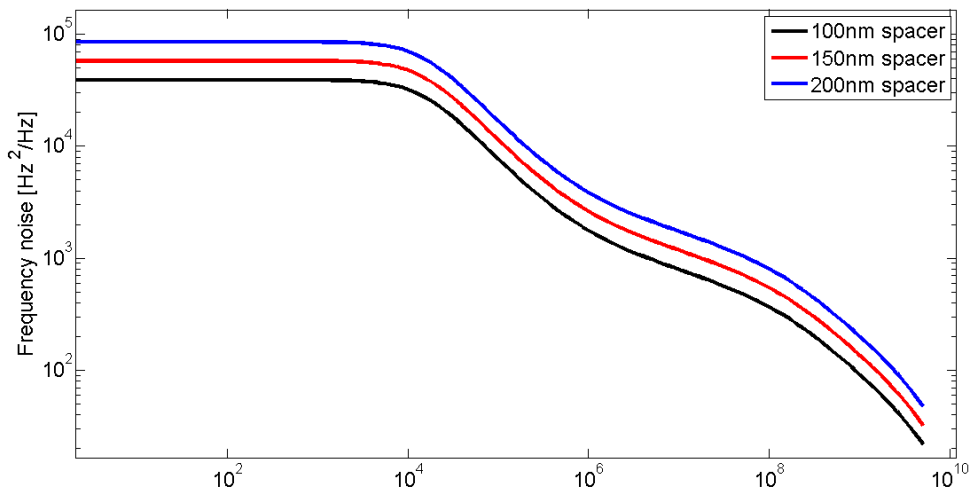


Figure 9.8: Frequency noise spectrum due to Si carrier fluctuations for different spacers. $Q_{Si} = 10^6$, $I = 2 \cdot I_{th}$

laser. In a conventional laser, the linewidth scales inversely with power. Fluctuation of the QW carriers yield the Henry linewidth enhancement, but the overall noise spectrum goes down at high frequencies with increasing power. However, in the high-Q hybrid platform the noise due to silicon carriers increases with power. This work therefore predicts that as we increase the laser's power, the linewidth will eventually start to broaden. This model predicts a sub-KHz equivalent linewidth as a rough limit. A better estimate will follow in the next sections. Figure 9.8 shows that this conclusion also holds for spacer thickness. For the thicker spacer, as we attempt to reduce loss and store more photons in the laser cavity, fluctuations of Si carriers limit the achievable linewidth.

9.3.4 Noise due to the thermo-optic effect in silicon

In previous sections I have considered the role of fluctuations in QW and Si carrier densities that contribute to the frequency noise through the plasma effect. However, the index of refraction of the laser's medium is also temperature-dependent, and it is important to investigate the role of temperature fluctuations on the frequency noise spectrum. Following the discussion on components of the frequency noise spectrum

in section 9.3, the contribution of temperature fluctuations can be written as:

$$W_{\Delta\nu} = \left(\frac{v_g}{\lambda_0} \Gamma_{Si} \eta_T \right)^2 W_{\Delta T}$$

where η_T is the thermo-optic coefficient of silicon, and $W_{\Delta T}$ is the temperature fluctuations PSD. The temperature diffusion formula in Equation 9.35 can be expressed in the Fourier plane as:

$$\begin{aligned} \Delta T(\omega, \mathbf{k}) = & \frac{q_1}{j\omega + \frac{1}{\tau_T} + D_T |\mathbf{k}|^2} \Delta n_p(\omega, \mathbf{k}) + \frac{q_2}{j\omega + \frac{1}{\tau_T} + D_T |\mathbf{k}|^2} \Delta n_{Si}(\omega, \mathbf{k}) \\ & + \frac{f_T(\omega, \mathbf{k})}{j\omega + \frac{1}{\tau_T} + D_T |\mathbf{k}|^2} \end{aligned} \quad (9.55)$$

The PSD of the temperature fluctuations is calculated as before, using Equation 9.12, with the Fourier domain correlation for the temperature derived from Equation 9.38:

$$\langle f_T(\omega, \mathbf{k}) f_T^*(\omega', \mathbf{k}') \rangle = \frac{2D_T K_B T^2}{\rho c_h} \mathbf{k} \cdot \mathbf{k}' \left[(2\pi)^3 \delta^3(\mathbf{k} + \mathbf{k}') \right] 2\pi \delta(\omega - \omega') \quad (9.56)$$

where I have assumed a constant temperature profile.

Equation 9.55 explicitly shows the contribution of three components to the temperature fluctuations:

1. Temperature fluctuations due to photon density fluctuations - Since heat is generated in the process of FCA, fluctuations in the photon density also contribute to temperature fluctuations.
2. Temperature fluctuations due to Si carrier density fluctuations - Heat is generated during the FCA process and non-radiative recombination in Si. Fluctuations in carrier density and the discrete nature of heat-generating recombination induce temperature fluctuations.
3. Inherent temperature fluctuations - The temperature of the laser cavity is set by the coupling to the thermal bath through a stochastic process. A cavity of finite volume will have a temperature probability distribution with a finite

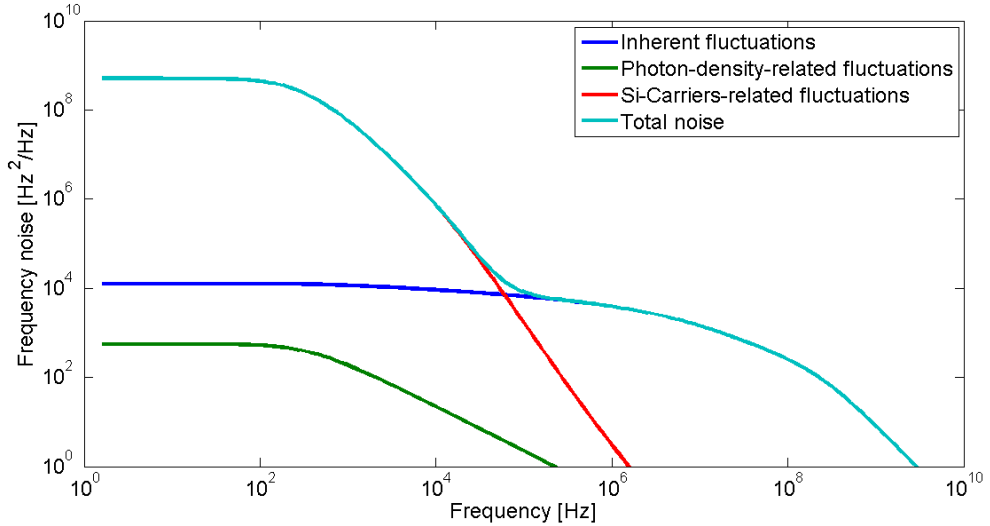


Figure 9.9: The different components of the frequency noise spectrum due to temperature fluctuations (150nm spacer, $Q_{Si} = 10^6$, $I = 2 \cdot I_{th}$)

width.

I can now numerically calculate the resulting frequency noise spectrum. I use the same approximations as in section 9.3.3. Figure 9.9 shows the different components of the frequency noise that are temperature related. It demonstrates that the noise at low frequencies is dominated by fluctuation of Si carriers that induce temperature fluctuations. The low frequency behavior quickly decreases with frequency, and at intermediate frequencies the noise is dominated by the inherent temperature fluctuations of the cavity. Figure 9.10 shows the temperature-related noise spectrum for different spacer designs. This figure shows that due to Si carriers, the low-frequency component of the frequency noise spectrum is higher at thicker spacers.

9.3.5 Total noise spectrum

I can now combine all the sources of fluctuations and calculate the total frequency noise spectrum. In previous sections I have broken the spectrum into three parts: spontaneous emission and QW carriers noise, free-carrier dispersion noise in Si, and temperature related noise. The latter included both temperature fluctuations that are inherent to the cavity and those which stem from Si carriers that have generated

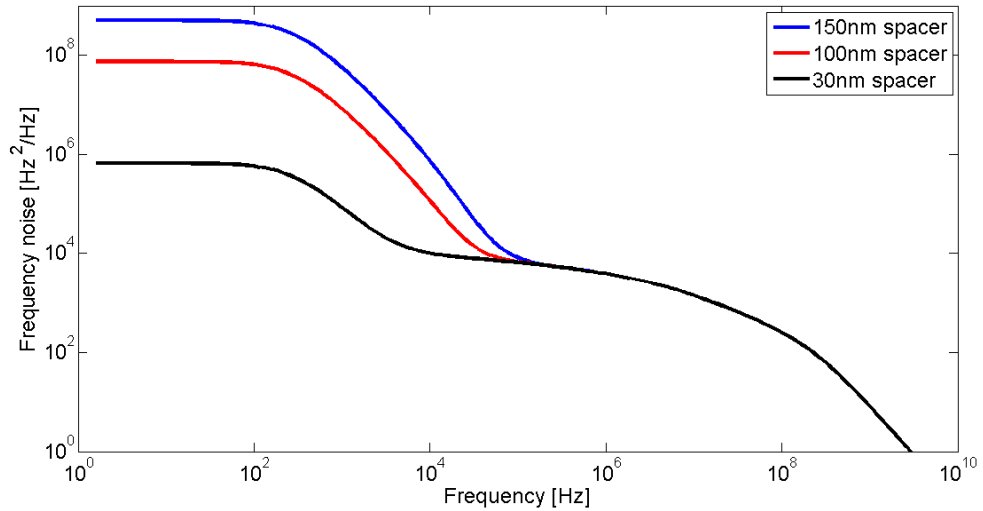
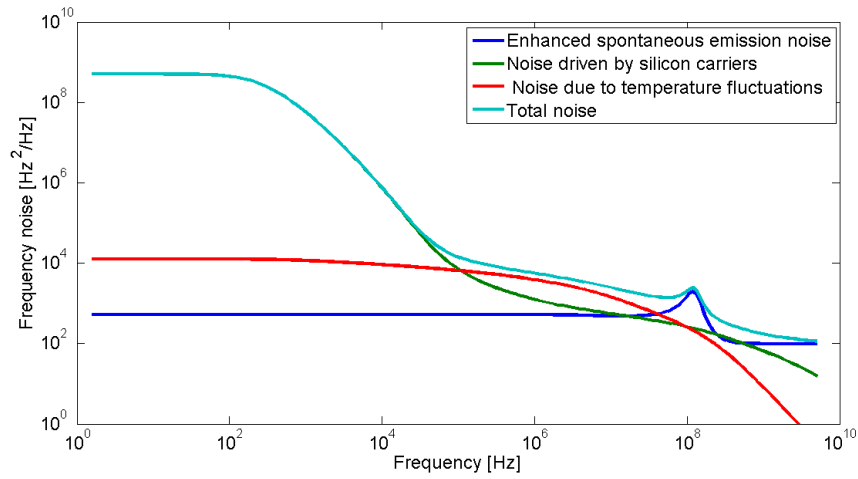


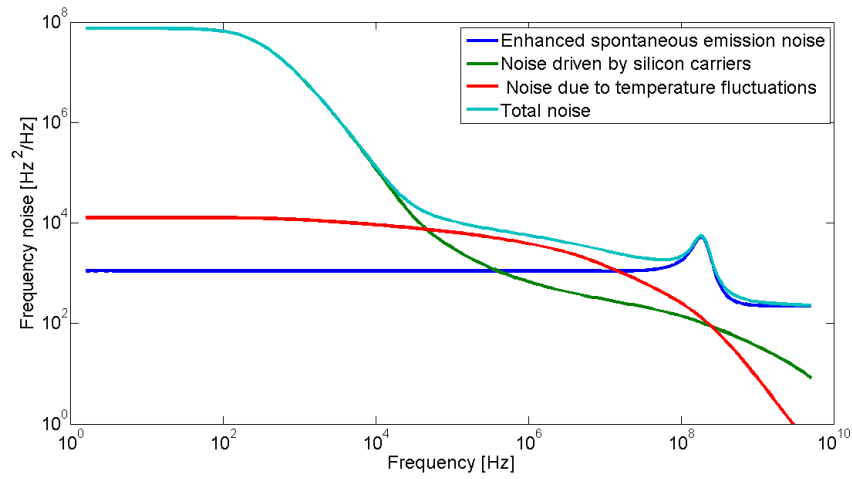
Figure 9.10: Frequency noise related to temperature fluctuations for different spacer designs ($Q_{Si} = 10^6$, $I = 2 \cdot I_{th}$)

heat. In this section, I will re-order those components and group together all the noise components that originate from free-carriers in Si, both through the plasma effect and through the thermo-optic effect. Figure 9.11 shows the predicted frequency noise spectrum and the contribution of different elements to that noise for different spacer designs. This figure demonstrates that for the thick spacer designs, temperature-related noise masks the S-T noise, which is revealed only at high frequencies (~ 1 GHz). Figure 9.12 compares predictions from different spacer designs, and reveals that thick spacer designs have very similar noise performance except at high frequencies, where the S-T is reached. Finally, Figure 9.13 compares predictions for the 150nm spacer at different pump powers. It is evident from this figure that for the aggressive 150nm design, this model predicts that increasing the pump power will broaden the linewidth instead of narrowing it. The S-T floor is not reached even at frequencies as high as 10GHz. It suggests that an equivalent linewidth of a few hundred Hertz might be the limit of this platform, due to free-carriers in silicon.

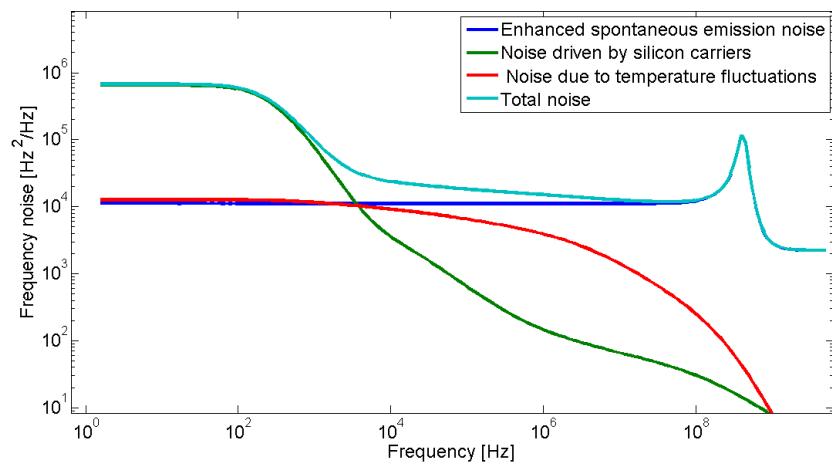
In this chapter I used the Langevin force approach to predict the noise performance of our lasers. It was found that both inherent temperature fluctuations and fluctuations of free-carriers in Si affect noise performance. It was predicted that free-



(a)



(b)



(c)

Figure 9.11: The different components of the total frequency noise spectrum ($Q_{Si} = 10^6$, $I = 2 \cdot I_{th}$). (a) 150nm spacer (b) 100nm spacer (c) 30nm spacer

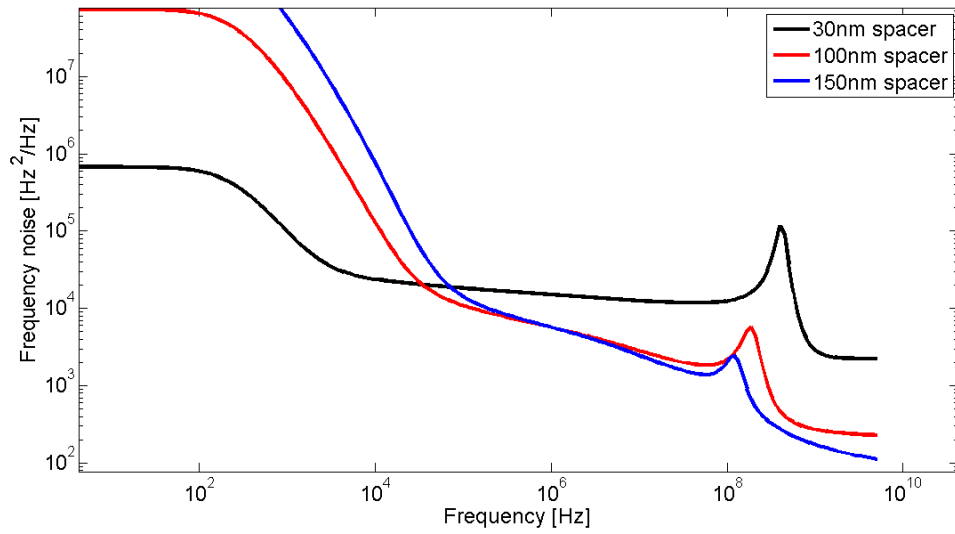


Figure 9.12: Predicted frequency noise spectrum of different spacer designs ($Q_{Si} = 10^6$, $I = 2 \cdot I_{th}$)

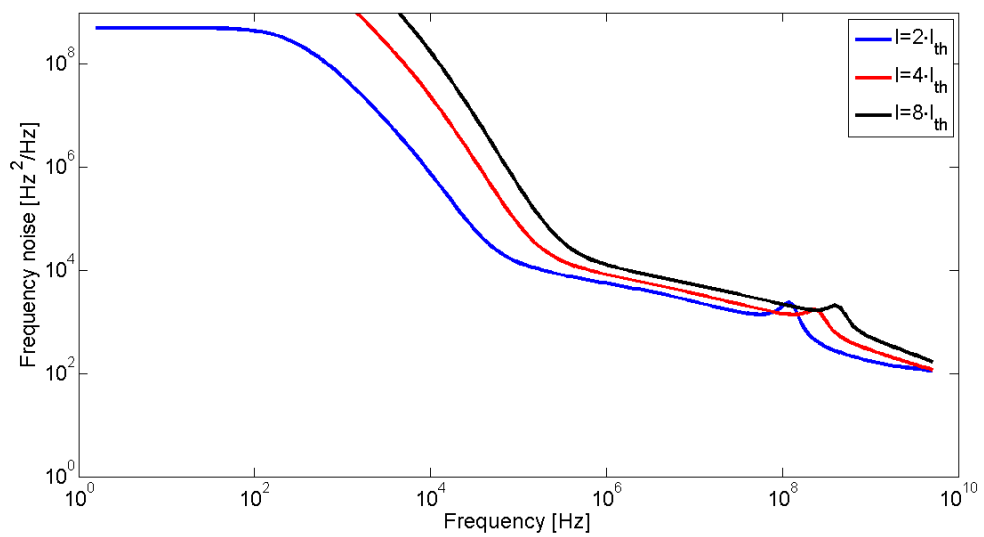


Figure 9.13: Predicted frequency noise spectrum for the 150nm spacer designs at different pump powers ($Q_{Si} = 10^6$)

carriers in Si will limit the achievable noise floor, especially at high pump powers. In the next chapter, I will present experimental frequency noise spectra and compare them to these predictions.

Chapter 10

Noise performance - Experimental results

Frequency noise spectra were measured for different spacer designs at different pump powers. The exact experimental setup and calibration process are described in detail in appendix B.5, while the laser design fabrication process is described in A.

The spectrum I measured using the RF spectrum analyzer is a single sided spectrum, whereas the analysis in the previous section is given as a double sided spectrum. In this section, I will convert the y-axis of the PSD of the frequency noise to an equivalent Lorentzian white-noise linewidth. The physical meaning of this metric can be interpreted using the following analogy: suppose that our laser has a certain level of noise at a given frequency. A (theoretical) laser, that has only white frequency noise of that level, would have had a Lorentzian line-shape, with width equivalent to the new y-axis. Such a conversion requires only multiplication by π for the single-sided spectrum, or by 2π for the double-sided spectrum (the reader can convert the predictions from the previous chapter to these units by multiplying the predicted spectrum by 2π).

The output power of the lasers varied from design to design. However, for many of the measured narrow-linewidth lasers, the output power (in the fiber) was less than 1mW. Since these narrow-linewidth lasers have very little noise at the high frequencies we are interested in, external amplification was needed to overcome the balanced-photodetector dark noise (for further discussion of that point, see appendix

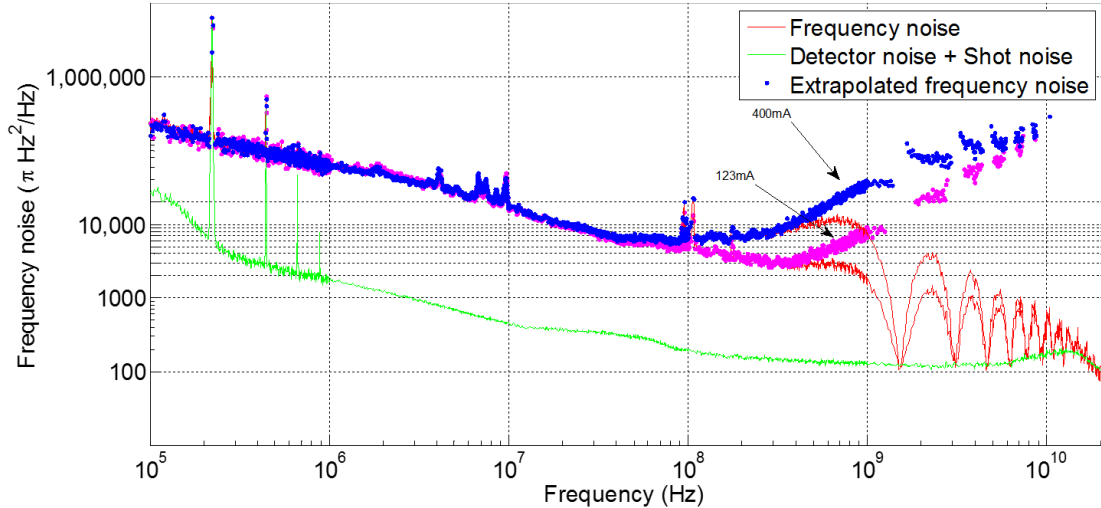


Figure 10.1: Effect of BOA amplification on frequency noise spectrum. All data was taken with the same 150nm spacer at constant laser pump current. Only BOA pump current changed from curve to curve

B). We have tested our devices with both booster-optical-amplifier (BOA) and Erbium-doped-fiber-amplifier (EDFA). As can be seen in Figure 10.1, the BOA adds phase noise to the signal. For the same input signal, higher amplification yields higher frequency noise. This noise is manifested as an increasing noise spectrum curve, that is only evident at the high frequencies. Unfortunately, this noise artifact due to amplification is at frequencies and noise levels that are of interest to us. Figure 10.1 also demonstrates the measurement calibration process. The red curves in the figure contain the MZI sinc^2 transfer function. The blue and pink curves are the calibrated spectra after deconvolving the sinc^2 from the measurement. This calibration process is further described in appendix B.5. In the spectra I present in the remainder of this chapter I will omit the raw oscillating data, and will only present the calibrated data. Figure 10.2 shows that the contaminating amplifier phase noise is also present with the EDFA amplification. However, the noise level is slightly lower with the EDFA. This is expected, as the EDFA has a lower specified noise-figure than the BOA. For that reason, all the results presented from now on are taken with EDFA amplification. However, the measurement is still limited by EDFA-induced noise for the 150nm spacer, as was evident from Figure 10.2, and the laser noise-floor cannot be observed.

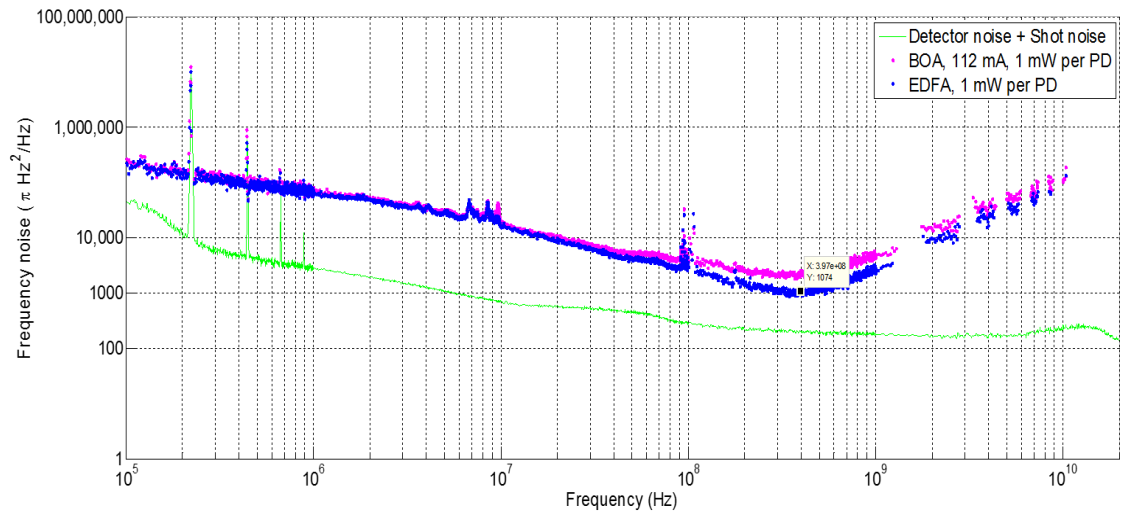
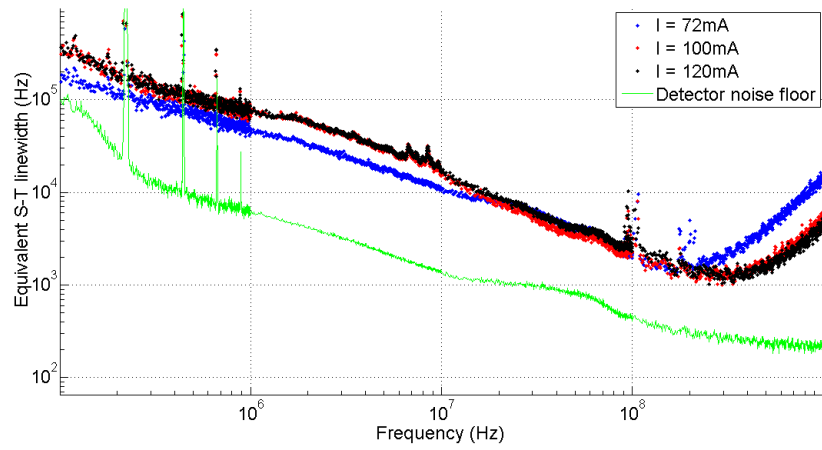


Figure 10.2: Frequency noise of 150nm spacer, amplified using BOA and EDFA

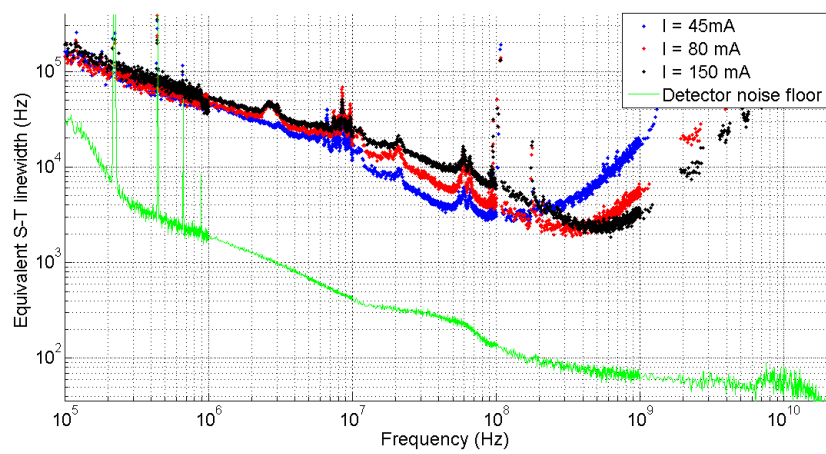
Therefore, the results presented here for the 150nm spacer should be interpreted as an upper limit of the noise.

Figure 10.3 shows frequency noise spectra at different pump powers for the three spacer designs. Several interesting observations can be made from this figure:

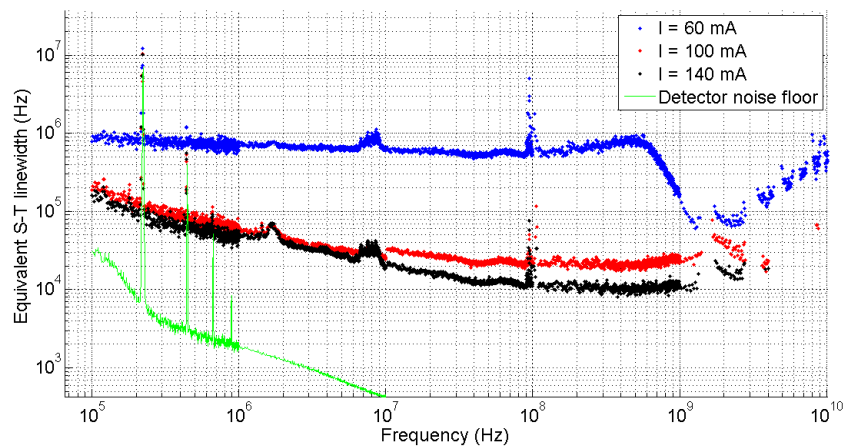
1. The 150nm spacer has an equivalent S-T linewidth of ~ 1 KHz. In fact, this is only limited by the amplifier noise. Since the amplifier noise becomes dominant for frequencies higher than the knee frequency, we can estimate that the laser's noise is sub-KHz (few hundred Hz). Such low noise for a semiconductor laser is unprecedented.
2. For both the 100nm and the 150nm spacers, increasing the pump current doesn't lower the noise floor at all. In fact, it increases the lower frequency noise level, in agreement with the theory that attributed that behavior to fluctuations of free-carriers in Si.
3. The 30nm spacer laser shows behavior that is closer to that predicted for a conventional laser. The (modified) S-T noise floor is observed, and decreases with increasing pump power, as expected from theory.
4. The 30nm spacer shows the relaxation resonance when operated close to thresh-



(a)



(b)



(c)

Figure 10.3: Frequency noise spectrum vs. pump current for different spacer designs (a) 150nm spacer (threshold @ 66mA) (b) 100nm spacer (threshold @ 28mA) (c) 30nm spacer (threshold @ 55mA)

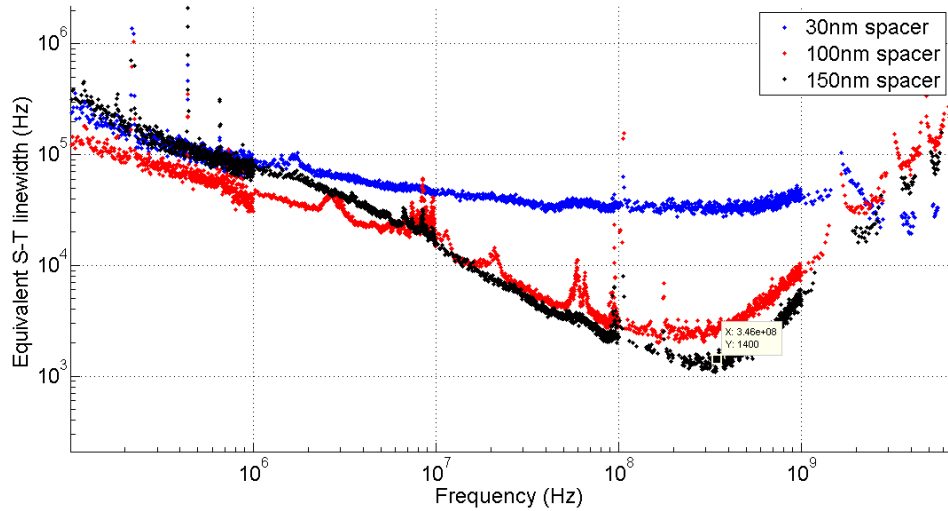


Figure 10.4: Frequency noise spectrum for different spacer designs at $I - I_{th} = 33\text{mA}$

old. We can't see the quantum S-T noise floor due to amplifier noise, but we do see that the enhanced S-T level drops by at least a factor of 16. We can therefore estimate a lower bound for the Henry linewidth enhancement factor for this laser:

$$\alpha_H > 4 \quad (10.1)$$

Figure 10.4 compares the three spacer designs for a constant offset from threshold. This figure demonstrates a few important trends:

1. As the spacer thickness increases, the noise floor level decreases. Spacers 30nm, 100nm and 150nm have equivalent linewidths at the noise floor of 30KHz, 3KHz, and 1 KHz, respectively, where the noise floor for the 150nm spacer is limited only by the measurement setup.
2. The low frequency noise ($< 100\text{MHz}$) decreases slowly with frequency. The thick 150nm spacer has a higher noise at the low frequencies than the 100nm spacer, in agreement with the nonlinear loss model presented in this work. Only at the high frequencies is it evident that the thicker spacer has lower noise.

The Schawlow-Townes noise floor is observed clearly in the 30nm spacer. In the 100nm spacer it seems that the noise has started to flatten at the knee area, though

this is not conclusive. The 150nm spacer clearly doesn't reach the noise floor before noise from the measurement setup becomes dominant.

In this chapter I have presented experimental frequency noise spectra from narrow-linewidth hybrid Si/III-V lasers. A record sub-KHz noise floor was demonstrated with a conclusive trend showing the effect of spacer thickness on the noise performance. It was also shown that though the noise floor is lower in the thicker spacer designs, the low-frequency components are noisier, in agreement with theoretical predictions attributing that trend to free-carriers in Si. The same trend was also evident when the pump power increased, as was predicted by the theory.

Chapter 11

Conclusion

11.1 Summary of key results

This work presented a theoretical model that takes into account extremely low III-V confinement, and nonlinear effects, such as TPA and FCA, that become increasingly dominant in the presence of a high-Q Si cavity. Predictions from this model were compared to experimental results from fabricated devices. Some of the key results in this work include:

1. Demonstration of a record-breaking sub-KHz semiconductor laser.
2. Demonstration of ultra-low frequency (~ 100 MHz) relaxation resonance. The theory developed in this work shows that this is due to the very low active confinement, and not due to the long cavity lifetime, as often suggested. It was argued and experimentally demonstrated that for frequencies above the resonance, the noise drops to the quantum noise floor. The low resonance frequency therefore lends itself to the realization of truly quantum-limited noise sources, at frequencies that are useful for optical communication.
3. The intensity modulation response of the laser was investigated experimentally. It was demonstrated that a zero of the transfer function is present at the thick spacer designs. This is in agreement with the theoretical model that attributes this phenomenon to the response of free-carriers in Si.

4. The frequency modulation response of the laser was investigated experimentally. It was shown that the response curve has a unique dip in addition to the conventional resonance peak. This was also explained by the theoretical model, which attributed these effects to free-carrier-dispersion in Si.
5. The frequency noise spectrum of these lasers was measured up to frequencies of a few GHz. It was shown that a very low S-T noise floor is reached, but only at high frequencies (>100 MHz). Furthermore, it was demonstrated that the low frequency portion of the spectrum becomes noisier with pump-power increase or with higher-Q. This is in agreement with the theoretical model, that attributes this behavior to fluctuation of free-carriers in Si.
6. The L-I curve for the high-Q designs was shown experimentally to be nonlinear, in agreement with the model that attributes this finding to nonlinear loss mechanisms, mainly TPA and FCA.

Qualitatively, all the predictions from the nonlinear loss model were observed experimentally, including the nonlinear L-I curve, the unique characteristics of laser dynamics, and the noise performance. The most convincing evidence for the role of free-carriers in Si may lie in the frequency response curve. Other predictions are less striking, and one could argue that although the experiments agree with the model, results may stem from other ignored physical processes. However, it is hard to argue that for the frequency response curve. The frequency response is due to changes of the effective refractive index of the lasing mode. In the high-Q hybrid platform, the optical energy of the lasing mode is about 99% confined in silicon. Since we are seeing a response that is comparable in magnitude to a conventional laser, it must come from the Si. Otherwise, we would have seen an orders of magnitude smaller response. And since the response has high frequency components, which cannot be explained by slow thermal processes, the result must be attributed to carriers in Si. This logical argument, together with the good overall agreement between theory and experiments, strengthen the case for the validity of the theoretical model, and for the role of free-carriers in Si.

11.2 Future directions

The record-low noise floor presented in this work is only an upper limit. The “real” laser noise could not be observed experimentally due to noise from the measurement setup, induced by necessary optical amplifiers due to the low output power of the lasers. A better estimation of the laser noise floor could be made by removing the optical amplifier altogether from the measurement setup. This would require higher power lasers. In Chapter 5 it was shown that the low output power is not a fundamental limit of the platform. Even though some trade-off between linewidth and wall-plug efficiency exists, it is predicted that achieving high-coherence lasers with reasonable efficiency is feasible.

The theoretical model in this work predicts that nonlinear effects such as TPA and photo-generated FCA will eventually limit the achievable linewidth of this platform. This prediction is a result of several physical processes:

1. Nonlinear loss that limits the achievable quality factor - When the intra-cavity photon density increases, the nonlinear loss processes become increasingly more dominant. The nonlinear loss limits the number of photons that are stored in the cavity, effectively lowering the quality factor. This will affect the S-T linewidth, which scales as the inverse of the quality factor squared.
2. Fluctuations of free-carriers in Si – It was shown theoretically that fluctuations of free-carriers in Si will couple to the frequency noise through both the free-carrier-plasma effect and the thermo-optic effect. Increase of free-carrier density due to increase in TPA will yield higher noise. This noise mainly affects the low and intermediate frequency range, but can still lower the achievable noise floor at frequencies of interest (~ 1 GHz).

The two performance-limiting mechanisms can be addressed using several approaches:

1. Lowering the temperature - Working at cryogenic temperature will dramatically lower the noise due to the thermo-optic effect. Inherent temperature fluctuations scale as T^2 [49], at temperatures above 100K the specific heat and the

thermo-optic coefficient scale roughly as T [20, 45], and the thermal conductivity scales roughly as T^{-2} [24]. This suggests that a factor of two reduction in temperature (i.e., from 300K to 150K) can result in noise reduced by an order of magnitude or more. Although operating the laser at cryogenics temperature might not be a commercially viable solution, it would provide a better understanding of the noise mechanisms and might reveal the S-T noise floor at lower frequencies. In this case, the noise floor might not be limited by amplifier noise. Furthermore, the measurement setup in this case might be constructed using a longer MZI that will provide higher gain, and might render the amplifier unnecessary.

2. The above approach only treats the temperature-related noise. It doesn't tackle noise due to the free-carrier plasma effect, which was estimated theoretically to have an observable impact on the noise performance. One can tackle all these noise limiting processes (except for inherent temperature fluctuations) by reducing the free-carrier density in silicon. The most straightforward path towards such a reduction is by reducing the effective lifetime of carriers in Si. Fortunately, since the carrier profile is much broader than the optical mode's profile, one can strongly affect the carrier population without introducing excess loss into the mode, by manipulating the carriers only outside the mode's area. This could be accomplished through two means:

- (a) Deliberate deterioration of surface quality - It was argued in Chapter 3 that surface recombination is a dominant factor in the determination of the effective lifetime. A reduction of carrier lifetime can be achieved by deliberately introducing surface defects. For example, dry etching arrays of deep holes or trenches could dramatically impact the effective lifetime. Another possibility is by ion implanting dopants to introduce excess SRH defects. As discussed above, this can be done outside the mode's area, so that the low-loss properties of this platform are maintained.
- (b) Construction of PN junction in Si - Another possible way to reduce the

lifetime of carriers in Si is by a fast sweep-out of carriers via a reversed-biased PN junction [16, 15]. An order of magnitude or more reduction in lifetime can be accomplished using this method [15]. Furthermore, the reverse bias voltage can provide a new “knob” for investigating the role of free-carriers in silicon.

In this work, Hybrid Si/III-V lasers were shown to have extremely unique characteristics. Not only do they support ground-breaking low-noise operation, which might render them the main candidate to replace the DFB laser, but they also provide a fruitful platform for research of new and exciting scientific phenomena. This work highlights the intriguing properties of this platform through both theory and experimentation. It also provides an attempt to estimate the limits of this platform, and offers several directions to overcome them. The hybrid Si/III-V platform promises to play an increasingly important and exciting role both in industry and in scientific research.

Bibliography

- [1] G.P. Agrawal. Gain nonlinearities in semiconductor lasers: Theory and application to distributed feedback lasers. *Quantum Electronics, IEEE Journal of*, 23(6):860–868, Jun 1987.
- [2] Donghwan Ahn, Ching yin Hong, Jifeng Liu, Wojciech Giziewicz, Mark Beals, Lionel C. Kimerling, Jurgen Michel, Jian Chen, and Franz X. Kärtner. High performance, waveguide integrated Ge photodetectors. *Opt. Express*, 15(7):3916–3921, Apr 2007.
- [3] Abdelkrim El Amili, Gaël Kervella, and Mehdi Alouini. Experimental evidence and theoretical modeling of two-photon absorption dynamics in the reduction of intensity noise of solid-state Er:Yb lasers. *Opt. Express*, 21(7):8773–8780, Apr 2013.
- [4] Paul Barclay, Kartik Srinivasan, and Oskar Painter. Nonlinear response of silicon photonic crystal microresonators excited via an integrated waveguide and fiber taper. *Opt. Express*, 13(3):801–820, Feb 2005.
- [5] Charles M. Bowden and Govind P. Agrawal. Generalized bloch-maxwell formulation for semiconductor lasers. *Optics Communications*, 100:147 – 152, 1993.
- [6] Robert W. Boyd. *Nonlinear Optics*. Academic press, 1992.
- [7] Ozdal Boyraz and Bahram Jalali. Demonstration of a silicon raman laser. *Opt. Express*, 12(21):5269–5273, Oct 2004.

- [8] Alan D. Bristow, Nir Rotenberg, and Henry M. van Driel. Two-photon absorption and kerr coefficients of silicon for 850-2200nm. *Applied Physics Letters*, 90(19), 2007.
- [9] Jaime Cardenas, Carl B. Poitras, Jacob T. Robinson, Kyle Preston, Long Chen, and Michal Lipson. Low loss etchless silicon photonic waveguides. *Opt. Express*, 17(6):4752–4757, Mar 2009.
- [10] Roger Chen, Thai-Truong D. Tran, Kar Wei Ng, Wai Son Ko, Linus C. Chuang, Forrest G. Sedgwick, and Connie Chang-Hasnain. Nanolasers grown on silicon. *Nature Photonics*, 5(3):170–175, feb 2011.
- [11] Yew Tai Chieng and G.J. Cowle. Suppression of relaxation oscillations in tunable fiber lasers with a nonlinear amplified loop mirror. *IEEE Photonics Technology Letters*, 7(5):485–487, may 1995.
- [12] G. Cocorullo, F. G. Della Corte, and I. Rendina. Temperature dependence of the thermo-optic coefficient in crystalline silicon between room temperature and 550 k at the wavelength of 1523 nm. *Applied Physics Letters*, 74(22):3338–3340, 1999.
- [13] L. A. Coldren and S.W Corzine. *Diode lasers and photonic integrated circuits*. Wiley, 1995.
- [14] Francesco G. Della Corte, Giuseppe Cocorullo, Mario Iodice, and Ivo Rendina. Temperature dependence of the thermo-optic coefficient of InP, GaAs, and SiC from room temperature to 600 k at the wavelength of 1.5 μm . *Applied Physics Letters*, 77(11):1614–1616, 2000.
- [15] D. Dimitropoulos, S. Fathpour, and B. Jalali. Limitations of active carrier removal in silicon raman amplifiers and lasers. *Applied Physics Letters*, 87(26), 2005.

- [16] D. Dimitropoulos, R. Jhaveri, R. Claps, J. C. S. Woo, and B. Jalali. Lifetime of photogenerated carriers in silicon-on-insulator rib waveguides. *Applied Physics Letters*, 86(7), 2005.
- [17] M. Dinu, F. Quochi, and H. Garcia. Third-order nonlinearities in silicon at telecom wavelengths. *Applied Physics Letters*, 82(18):2954–2956, 2003.
- [18] Avik Dutt, Kevin Luke, Sasikanth Manipatruni, Alexander L. Gaeta, Paulo Nussenzveig, and Michal Lipson. On-chip optical squeezing. *Phys. Rev. Applied*, 3, Apr 2015.
- [19] Alexander W. Fang, Hyundai Park, Oded Cohen, Richard Jones, Mario J. Paniccia, and John E. Bowers. Electrically pumped hybrid AlGaInAs-silicon evanescent laser. *Opt. Express*, 14(20):9203–9210, Oct 2006.
- [20] P. Flubacher, A. J. Leadbetter, and J. A. Morrison. The heat capacity of pure silicon and germanium and properties of their vibrational frequency spectra. *Philosophical Magazine*, 4(39):273–294, 1959.
- [21] J.G. Fossum, R.P. Mertens, D.S. Lee, and J.F. Nijs. Carrier recombination and lifetime in highly doped silicon. *Solid-State Electronics*, 26(6):569 – 576, 1983.
- [22] W. Gerlach, H. Schlangenotto, and H. Maeder. On the radiative recombination rate in silicon. *physica status solidi (a)*, 13(1):277–283, 1972.
- [23] Christopher C. Gerry and Edwin E. Hach III. Enhanced squeezing from a kerr medium combined with two-photon absorption. *Optics Communications*, 100(1-4):211–214, 1993.
- [24] C. J. Glassbrenner and Glen A. Slack. Thermal conductivity of silicon and germanium from 3°k to the melting point. *Phys. Rev.*, 134:A1058–A1069, May 1964.

- [25] Austin Griffith, Jaime Cardenas, Carl B. Poitras, and Michal Lipson. High quality factor and high confinement silicon resonators using etchless process. *Opt. Express*, 20(19):21341–21345, Sep 2012.
- [26] C.C. Harb, M.B. Gray, H.A. Bachor, R. Schilling, P. Rottengatter, I. Freitag, and H. Welling. Suppression of the intensity noise in a diode-pumped neodymium:YAG nonplanar ring laser. *Quantum Electronics, IEEE Journal of*, 30(12):2907–2913, Dec 1994.
- [27] Charles C. Harb, Timothy C. Ralph, Elanor H. Huntington, Ingo Freitag, David E. McClelland, and Hans-A. Bachor. Intensity-noise properties of injection-locked lasers. *Phys. Rev. A*, 54:4370–4382, Nov 1996.
- [28] C. Harder, J. Katz, S. Margalit, J. Shacham, and A. Yariv. Noise equivalent circuit of a semiconductor laser diode. *IEEE J. Quantum Electron.*, 18(3):333–337, Mar 1982.
- [29] T. R. Hart, R. L. Aggarwal, and Benjamin Lax. Temperature dependence of Raman scattering in silicon. *Phys. Rev. B*, 1:638–642, Jan 1970.
- [30] Guang S. He. *Nonlinear optics and photonics*. Oxford university press, 2015.
- [31] C.H. Henry. Theory of the linewidth of semiconductor lasers. *Quantum Electronics, IEEE Journal of*, 18(2):259–264, Feb 1982.
- [32] Lianping Hou, Mohsin Haji, Jehan Akbar, and John H. Marsh. Narrow linewidth laterally coupled $1.55\mu\text{m}$ AlGaInAs/InP distributed feedback lasers integrated with a curved tapered semiconductor optical amplifier. *Opt. Lett.*, 37(21):4525–4527, Nov 2012.
- [33] Robert Hull, editor. *Properties of Crystalline Silicon*. INSPEC, The Institute of Electrical Engineering London, UK, 1999.
- [34] J. C. Hulme, J. K. Doylend, and J. E. Bowers. Widely tunable vernier ring laser on hybrid silicon. *Opt. Express*, 21(17):19718–19722, Aug 2013.

- [35] S.K. Hwang, J.M. Liu, and J.K. White. 35GHz intrinsic bandwidth for direct modulation in $1.3\mu\text{m}$ semiconductor lasers subject to strong injection locking. *Photonics Technology Letters, IEEE*, 16(4):972–974, April 2004.
- [36] R.G Ispasoiu and T Goodson III. Photon-number squeezing by two-photon absorption in an organic polymer. *Optics Communications*, 178:371–376, 2000.
- [37] Thomas J. Johnson, Matthew Borselli, and Oskar Painter. Self-induced optical modulation of the transmission through a high-Q silicon microdisk resonator. *Opt. Express*, 14(2):817–831, Jan 2006.
- [38] Paul W. et al Juodawlkis. High-power ultralow-noise semiconductor external cavity lasers based on low-confinement optical waveguide gain media. *Novel In-Plane Semiconductor Lasers IX. Ed. San Francisco, California, USA: SPIE*, 2010.
- [39] Dawon Kahng. *Silicon integrated circuits: Advances in material and device research*. Number 3. Academic press, 2013.
- [40] Mark J. Kerr and Andres Cuevas. General parameterization of Auger recombination in crystalline silicon. *J. Appl. Phys.*, 91(4):2473, 2002.
- [41] Mark J Kerr and Andres Cuevas. Very low bulk and surface recombination in oxidized silicon wafers. *Semiconductor Science and Technology*, 17(1):35, 2002.
- [42] S. Keyvaninia, M. Muneeb, S. Stanković, P. J. Van Veldhoven, D. Van Thourhout, and G. Roelkens. Ultra-thin DVS-BCB adhesive bonding of III-V wafers, dies and multiple dies to a patterned silicon-on-insulator substrate. *Opt. Mater. Express*, 3(1):35–46, Jan 2013.
- [43] S. Kobayashi, Y. Yamamoto, M. Ito, and Tatsuya Kimura. Direct frequency modulation in AlGaAs semiconductor lasers. *Quantum Electronics, IEEE Journal of*, 18(4):582–595, Apr 1982.

- [44] T.L. Koch and J.E. Bowers. Nature of wavelength chirping in directly modulated semiconductor lasers. *Electronics Letters*, 20(25):1038–1040, December 1984.
- [45] J. Komma, C. Schwarz, G. Hofmann, D. Heinert, and R. Nawrodt. Thermo-optic coefficient of silicon at 1550nm and cryogenic temperatures. *Applied Physics Letters*, 101(4), 2012.
- [46] Eiichi Kuramochi, Hideaki Taniyama, Takasumi Tanabe, Kohei Kawasaki, Young-Geun Roh, and Masaya Notomi. Ultrahigh-Q one-dimensional photonic crystal nanocavities with modulated mode-gap barriers on SiO₂ claddings and on air claddings. *Opt. Express*, 18(15):15859–15869, Jul 2010.
- [47] Toshio Kuwayama, Masaya Ichimura, and Eisuke Arai. Interface recombination velocity of silicon-on-insulator wafers measured by microwave reflectance photoconductivity decay method with electric field. *Applied Physics Letters*, 83(5):928–930, 2003.
- [48] L. Lai and E. A. Irene. Limiting Si/SiO₂ interface roughness resulting from thermal oxidation. *Journal of Applied Physics*, 86(3):1729–1735, 1999.
- [49] L.D Landau and E.M Lifshitz. *Statistical physics*. Elsevier Ltd, 1980.
- [50] Robert J. Lang, K.J. Vahala, and A. Yariv. The effect of spatially dependent temperature and carrier fluctuations on noise in semiconductor lasers. *Quantum Electronics, IEEE Journal of*, 21(5):443–451, May 1985.
- [51] M. Lax. Quantum noise VII: The rate equations and amplitude noise in lasers. *Quantum Electronics, IEEE Journal of*, 3(2):37–46, Feb 1967.
- [52] Melvin Lax. Quantum noise IV: Quantum theory of noise sources. *Phys. Rev.*, 145:110–129, May 1966.
- [53] Melvin Lax. Classical noise. v. noise in self-sustained oscillators. *Phys. Rev.*, 160:290–307, Aug 1967.

- [54] Don S. Lemons and Anthony Gythiel. Paul Langevin's 1908 paper on the theory of Brownian motion ("Sur la théorie du mouvement brownien" C.R Acad. sci. (Paris) 146, 530-533 (1908)). *American Journal of Physics*, 65(11):1079–1081, 1997.
- [55] Jiang Li, Scott Diddams, and Kerry J. Vahala. Pump frequency noise coupling into a microcavity by thermo-optic locking. *Opt. Express*, 22(12):14559–14567, Jun 2014.
- [56] Di Liang, A.W. Fang, and J.E. Bowers. 100 mm wafer-scale InP-based ($\lambda = 1.6\mu\text{m}$) epitaxial transfer for hybrid silicon evanescent lasers. In *Electronic Components and Technology Conference, 2008. ECTC 2008. 58th*, pages 979–984, May 2008.
- [57] T. K. Liang and H. K. Tsang. Role of free carriers from two-photon absorption in Raman amplification in silicon-on-insulator waveguides. *Applied Physics Letters*, 84(15):2745–2747, 2004.
- [58] Q. Lin, Oskar J. Painter, and Govind P. Agrawal. Nonlinear optical phenomena in silicon waveguides: modeling and applications. *Opt. Express*, 15(25):16604–16644, Dec 2007.
- [59] Lina Ma, Yongming Hu, Shuidong Xiong, Zhou Meng, and Zhengliang Hu. Intensity noise and relaxation oscillation of a fiber-laser sensor array integrated in a single fiber. *Opt. Lett.*, 35(11):1795–1797, Jun 2010.
- [60] V. Malina, E. Hájek, J. Zelinka, M. Dapor, and V. Micheli. Non-alloyed Ti/Au and Ti/Pt/Au ohmic contacts to p-type InGaAsP. *Thin Solid Films*, 223(1):146 – 153, 1993.
- [61] Gregory S. Marlow and Mukunda B. Das. The effects of contact size and non-zero metal resistance on the determination of specific contact resistance. *Solid-State Electronics*, 25(2):91 – 94, 1982.

- [62] Y. Matsui, H. Murai, S. Arahira, S. Kutsuzawa, and Y. Ogawa. 30-GHz bandwidth 1.55 μm strain-compensated InGaAlAs-InGaAsP MQW laser. *Photonics Technology Letters, IEEE*, 9(1):25–27, Jan 1997.
- [63] D. E. McCumber. Intensity fluctuations in the output of CW laser oscillators. I. *Phys. Rev.*, 141:306–322, Jan 1966.
- [64] Z. Mi, P. Bhattacharya, J. Yang, and K.P. Pipe. Room-temperature self-organised In_{0.5}Ga_{0.5}As quantum dot laser on silicon. *Electronics Letters*, 41(13):742–744, June 2005.
- [65] C.M. Miller. Intensity modulation and noise characterization of high-speed semiconductor lasers. *LTS, IEEE*, 2(2):44–50, May 1991.
- [66] Edoardo Milotti. 1/f noise: a pedagogical review, 2002.
- [67] D. J. Morgan and M. J. Adams. Quantum noise in semiconductor lasers. *Physica Status Solidi (a)*, 11(1):243–253, may 1972.
- [68] Hadis Morkoc, T.J. Drummond, and C.M. Stanchak. Schottky barriers and ohmic contacts on n-type InP based compound semiconductors for microwave FET's. *Electron Devices, IEEE Transactions on*, 28(1):1–5, Jan 1981.
- [69] D.J. Moss, L. Fu, I. Littler, and B.J. Eggleton. Ultrafast all-optical modulation via two-photon absorption in silicon-on-insulator waveguides. *Electronics Letters*, 41(6):320–321, March 2005.
- [70] M. Nedeljkovic, R. Soref, and G. Z. Mashanovich. Free-carrier electrorefraction and electroabsorption modulation predictions for silicon over the 1-14 μm infrared wavelength range. *IEEE Photonics J.*, 3(6):1171–1180, dec 2011.
- [71] Makoto Okai, Makoto Suzuki, Tuyoshi Taniwatari, and Naoki Chinone. Corrugation-pitch-modulated distributed feedback lasers with ultranarrow spectral linewidth. *Japanese Journal of Applied Physics*, 33(5R):2563, 1994.

- [72] Ali Kemal Okyay. *Si/Ge photodetection technologies for integrated optoelectronics*. PhD thesis, Stanford university, 2007.
- [73] Özdal Boyraz, Prakash Koonath, Varun Raghunathan, and Bahram Jalali. All optical switching and continuum generation in silicon waveguides. *Opt. Express*, 12(17):4094–4102, Aug 2004.
- [74] O. Palais and A. Arcari. Contactless measurement of bulk lifetime and surface recombination velocity in silicon wafers. *Journal of Applied Physics*, 93(8):4686–4690, 2003.
- [75] H. Park, A. W. Fang, D. Liang, Y.H. Kuo, H.H. Chang, B. R. Koch, H.W. Chen, M. N. Sysak, R. Jones, and J. E. Bowers. Photonic integration on hybrid silicon evanescent device platform. *Advances in Optical Technologies*, March 2008.
- [76] Hyundai Park, Alexander Fang, Satoshi Kodama, and John Bowers. Hybrid silicon evanescent laser fabricated with a silicon waveguide and III-V offset quantum wells. *Opt. Express*, 13(23):9460–9464, Nov 2005.
- [77] Jr. Peter S. Zory. *Quantum well lasers*. Academic press, 1993.
- [78] K. Petermann. *Laser Diode Modulation and Noise*. Kluwer academic publisher, 1991.
- [79] Joachim Piprek, P. Abraham, and J.E. Bowers. Self-consistent analysis of high-temperature effects on strained-layer multiquantum-well InGaAsP-InP lasers. *Quantum Electronics, IEEE Journal of*, 36(3):366–374, March 2000.
- [80] Joachim Piprek, J.K. White, and A.J. SpringThorpe. What limits the maximum output power of long-wavelength AlGaInAs/InP laser diodes? *Quantum Electronics, IEEE Journal of*, 38(9):1253–1259, Sep 2002.
- [81] G. T. Reed, G. Mashanovich, F. Y. Gardes, and D. J. Thomson. Silicon optical modulators. *Nature Photonics*, 4(8):518–526, jul 2010.

- [82] G.K. Reeves. Specific contact resistance using a circular transmission line model. *Solid-State Electronics*, 23(5):487–490, 1980.
- [83] E.H. Rhoderick and R.H. Williams. *Metal-semiconductor contacts*. Oxford university press, 1988.
- [84] Haisheng Rong, Richard Jones, Ansheng Liu, Oded Cohen, Dani Hak, Alexander Fang, and Mario Paniccia. A continuous-wave Raman silicon laser. *Nature*, 433(7027):725–728, feb 2005.
- [85] Haisheng Rong, Ansheng Liu, Remus Nicolaescu, Mario Paniccia, Oded Cohen, and Dani Hak. Raman gain and nonlinear optical absorption measurements in a low-loss silicon waveguide. *Applied Physics Letters*, 85(12):2196–2198, 2004.
- [86] Haisheng Rong, Shengbo Xu, Oded Cohen, Omri Raday, Mindy Lee, Vanessa Sih, and Mario Paniccia. A cascaded silicon Raman laser. *Nature Photonics*, 2(3):170–174, feb 2008.
- [87] M. Rosling, H. Bleichner, P. Jonsson, and E. Nordlander. The ambipolar diffusion coefficient in silicon: Dependence on excess carrier concentration and temperature. *Journal of Applied Physics*, 76(5):2855–2859, 1994.
- [88] Christos Theodoros Santis, Scott T. Steger, Yaakov Vilenchik, Arseny Vasilyev, and Amnon Yariv. High-coherence semiconductor lasers based on integral high-Q resonators in hybrid Si/III-V platforms. *Proceedings of the National Academy of Sciences*, 111(8):2879–2884, 2014.
- [89] C.T. Santis. *High-Coherence Hybrid Si/III-V Semiconductor Lasers*. PhD thesis, California Institute of Technology, 2013.
- [90] Naresh Satyan, Arseny Vasilyev, George Rakuljic, Victor Leyva, and Amnon Yariv. Precise control of broadband frequency chirps using optoelectronic feedback. *Opt. Express*, 17(18):15991–15999, Aug 2009.

- [91] A. L. Schawlow and C. H. Townes. Infrared and optical masers. *Phys. Rev.*, 112:1940–1949, Dec 1958.
- [92] P. E. Schmid. Optical absorption in heavily doped silicon. *Phys. Rev. B*, 23:5531–5536, May 1981.
- [93] Dieter K. Schroder. *Semiconductor Material and Device Characterization*. Hoboken, NJ, USA: Wiley-Interscience, 3 edition, 2006.
- [94] M. Seimetz. Laser linewidth limitations for optical systems with high-order modulation employing feed forward digital carrier phase estimation. In *Optical Fiber communication/National Fiber Optic Engineers Conference, 2008. OFC/NFOEC 2008. Conference on*, pages 1–3, Feb 2008.
- [95] Hiroshi Sekoguchi, Yasushi Takahashi, Takashi Asano, and Susumu Noda. Photonic crystal nanocavity with a Q-factor of 9 million. *Opt. Express*, 22(1):916–924, Jan 2014.
- [96] S. J. Sheldon, L. V. Knight, and J. M. Thorne. Laser-induced thermal lens effect: a new theoretical model. *Appl. Opt.*, 21(9):1663–1669, May 1982.
- [97] Heedeuk Shin, Wenjun Qiu, Robert Jarecki, Jonathan A. Cox, Roy H. Olsson, Andrew Starbuck, Zheng Wang, and Peter T. Rakich. Tailorable stimulated brillouin scattering in nanoscale silicon waveguides. *Nat Comms*, 4, jun 2013.
- [98] W. Shockley and W. T. Read. Statistics of the recombinations of holes and electrons. *Phys. Rev.*, 87:835–842, Sep 1952.
- [99] Anthony E. Siegman. *Lasers*. University science books, 1986.
- [100] H. Soda, Y. Kotaki, H. Sudo, H. Ishikawa, S. Yamakoshi, and H. Imai. Stability in single longitudinal mode operation in GaInAsP/InP phase-adjusted DFB lasers. *IEEE J. Quantum Electron.*, 23(6):804–814, Jun 1987.
- [101] Richard A. Soref and Bria. Electrooptical effects in silicon. *IEEE Journal of Quantum Electronics*, QE-23(1):123–129, January 1987.

- [102] W.V. Sorin, Kok Wai Chang, G.A. Conrad, and P.R. Hernday. Frequency domain analysis of an optical FM discriminator. *Lightwave Technology, Journal of*, 10(6):787–793, Jun 1992.
- [103] D.K. Sparacin, S.J. Spector, and L.C. Kimerling. Silicon waveguide sidewall smoothing by wet chemical oxidation. *Lightwave Technology, Journal of*, 23(8):2455–2461, Aug 2005.
- [104] W. Spitzer and H. Y. Fan. Infrared absorption in *n*-type silicon. *Phys. Rev.*, 108:268–271, Oct 1957.
- [105] S. Stankovic, R. Jones, M.N. Sysak, J.M. Heck, G. Roelkens, and D. Van Thourhout. Hybrid III-V/Si distributed-feedback laser based on adhesive bonding. *Photonics Technology Letters, IEEE*, 24(23):2155–2158, Dec 2012.
- [106] S. T. Steger. *A fundamental approach to phase noise reduction in hybrid Si/III-V lasers*. PhD thesis, California Institute of Technology, 2014.
- [107] Jonathan Stohs, D.J. Bossert, David J. Gallant, and S.R.J. Brueck. Gain, refractive index change, and linewidth enhancement factor in broad-area GaAs and InGaAs quantum-well lasers. *Quantum Electronics, IEEE Journal of*, 37(11):1449–1459, Nov 2001.
- [108] David J. M. Stothard and Malcolm H. Dunn. Relaxation oscillation suppression in continuous-wave intracavity optical parametric oscillators. *Opt. Express*, 18(2):1336, 2010.
- [109] Xiankai Sun, Avi Zadok, Michael J. Shearn, Kenneth A. Diest, Alireza Ghaffari, Harry A. Atwater, Axel Scherer, and Amnon Yariv. Hybrid electrically pumped evanescent Si/InGaAsP lasers. In *Optical Fiber Communication Conference and National Fiber Optic Engineers Conference*, page OThN1. Optical Society of America, 2009.

- [110] Katsuaki Tanabe, Katsuyuki Watanabe, and Yasuhiko Arakawa. III-V/Si hybrid photonic devices by direct fusion bonding. *Sci. Rep.*, 2, April 2012.
- [111] C. L. Tang. On maser rate equations and transient oscillations. *Journal of Applied Physics*, 34(10):2935–2940, 1963.
- [112] En-Kuang Tien, Nuh S. Yuksek, Feng Qian, and Ozdal Boyraz. Pulse compression and modelocking by using TPA in silicon waveguides. *Opt. Express*, 15(10):6500–6506, May 2007.
- [113] Ming-Chun Tien, Jared F. Bauters, Martijn J. R. Heck, Daryl T. Spencer, Daniel J. Blumenthal, and John E. Bowers. Ultra-high quality factor planar Si_3N_4 ring resonators on Si substrates. *Opt. Express*, 19(14):13551–13556, Jul 2011.
- [114] H. K. Tsang, C. S. Wong, T. K. Liang, I. E. Day, S. W. Roberts, A. Harpin, J. Drake, and M. Asghari. Optical dispersion, two-photon absorption and self-phase modulation in silicon waveguides at $1.5\mu\text{m}$ wavelength. *Applied Physics Letters*, 80(3):416–418, 2002.
- [115] Rodney S. Tucker. High-speed modulation of semiconductor lasers. *Electron Devices, IEEE Transactions on*, 32(12):2572–2584, Dec 1985.
- [116] K. Vahala and A. Yariv. Semiclassical theory of noise in semiconductor lasers - part I. *Quantum Electronics, IEEE Journal of*, 19(6):1096–1101, June 1983.
- [117] Kerry J. Vahala. *Dynamic and spectral features of semiconductor lasers*. PhD thesis, California Institute of Technology, 1985.
- [118] N. G. van Kampen. Fluctuations in continuous systems. *AIP Conference Proceedings*, 27(1):153–186, 1976.
- [119] K. M. Van Vliet and H. Mehta. Theory of transport noise in semiconductors. *physica status solidi (b)*, 106(1):11–30, 1981.

- [120] A. Vasiliev. *The optoelectronic swept-frequency laser and Its applications in ranging, three-dimensional imaging, and coherent beam combining of chirped-seed Amplifiers*. PhD thesis, California Institute of Technology, 2013.
- [121] T.D. Visser, H. Blok, B. Demeulenaere, and D. Lenstra. Confinement factors and gain in optical amplifiers. *Quantum Electronics, IEEE Journal of*, 33(10):1763–1766, Oct 1997.
- [122] K.M. Van Vliet and A. Van der Ziel. On the noise generated by diffusion mechanisms. *Physica*, 24:415 – 421, 1958.
- [123] R. S. Vodhanel, N. K. Cheung, and T. L. Koch. Direct frequency modulation of vapor phase transported, distributed feedback semiconductor lasers. *Applied Physics Letters*, 48(15):966–968, 1986.
- [124] Ting Wang, Huiyun Liu, Andrew Lee, Francesca Pozzi, and Alwyn Seeds. 1.3 μm InAs/GaAs quantum-dot lasers monolithically grown on Si substrates. *Opt. Express*, 19(12):11381–11386, Jun 2011.
- [125] S. Weisser, E.C. Larkins, K. Czotscher, W. Benz, J. Daleiden, I. Esquivias, J. Fleissner, J.D. Ralston, B. Romero, R.E. Sah, A. Schonfelder, and J. Rosenzweig. Damping-limited modulation bandwidths up to 40 GHz in undoped short-cavity In_{0.35}Ga_{0.65}As-GaAs multiple-quantum-well lasers. *IEEE Photonics Technology Letters*, 8(5):608–610, may 1996.
- [126] D. Welford and S. Alexander. Magnitude and phase characteristics of frequency modulation in directly modulated GaAlAs semiconductor diode lasers. *Light-wave Technology, Journal of*, 3(5):1092–1099, Oct 1985.
- [127] Ming Wu, Connie Chang-Hasnain, Erwin K. Lau, and Xiaoxue Zhao. High-speed modulation of optical injection-locked semiconductor lasers. In *Optical Fiber Communication Conference/National Fiber Optic Engineers Conference*, page OThK3. Optical Society of America, 2008.

- [128] Tsuyoshi Yamamoto. High-speed directly modulated lasers. In *Optical Fiber Communication Conference*, page OTh3F.5. Optical Society of America, 2012.
- [129] Jun Yao, Govind P. Agrawal, Philippe Gallion, and Charles M. Bowden. Semiconductor laser dynamics beyond the rate-equation approximation. *Optics Communications*, 119:246–255, 1995.
- [130] A. Yariv and William M. Caton. Frequency, intensity, and field fluctuations in laser oscillators. *Quantum Electronics, IEEE Journal of*, 10(6):509–515, Jun 1974.
- [131] Amnon Yariv. *Quantum electronics*. Wiley, 3rd edition, 1989.
- [132] Amnon Yariv and Xiankai Sun. Supermode Si/III-V hybrid lasers, optical amplifiers and modulators: A proposal and analysis. *Opt. Express*, 15(15):9147–9151, Jul 2007.
- [133] Lianghong Yin and Govind P. Agrawal. Impact of two-photon absorption on self-phase modulation in silicon waveguides. *Opt. Lett.*, 32(14):2031–2033, Jul 2007.
- [134] Changyuan Yu, Shaoliang Zhang, Pooi Yuen Kam, and Jian Chen. Bit-error rate performance of coherent optical m-ary psk/qam using decision-aided maximum likelihood phase estimation. *Opt. Express*, 18(12):12088–12103, Jun 2010.
- [135] J.S. Yu, S.H. Kim, and T.I. Kim. PtTiPtAu and PdTiPtAu ohmic contacts to p-InGaAs. In *Compound Semiconductors, 1997 IEEE International Symposium on*, pages 175–178, Sep 1998.
- [136] J. Zhang, Q. Lin, G. Piredda, R. W. Boyd, G. P. Agrawal, and P. M. Fauchet. Anisotropic nonlinear response of silicon in the near-infrared region. *Applied Physics Letters*, 91(7), 2007.
- [137] X. Zhang, A. Gutierrez-Aitken, D. Klotzkin, P. Bhattacharya, C. Caneau, and R. Bhat. 0.98 μm multiple-quantum-well tunneling injection laser with 98-GHz

intrinsic modulation bandwidth. *Selected Topics in Quantum Electronics, IEEE Journal of*, 3(2):309–314, Apr 1997.

- [138] G. Zhu, Q. Wang, H. Dong, and N. K. Dutta. Fiber laser relaxation oscillation noise suppression through the use of self-biased intracavity loss modulator. *Journal of Applied Physics*, 96(4):1790–1793, 2004.

Appendix A

Fabrication process

This work followed previous endeavors to fabricate narrow-linewidth lasers on the hybrid Si/III-V platform. A detailed description of the design of the Si resonator can be found in [89], while details on the spacer platform and the III-V processing can be found in [106]. This appendix will summarize the fabrication process and design used in this current work, but the reader is referred to [106] for more details.

The device's schematics is shown in Figure A.1 for which the dimensions are detailed on table A.1 . The III-V wafer was obtained from Archcom Technology inc. Details on the wafer structure are described in table A.2.

A.1 Silicon processing

A flow diagram of the Si processing steps are shown in Figure A.2. Detailed description of the resonator's design methodology can be found in [89], and details on the design and dimensions can be found in [106].

A.1.1 Chrome deposition

Chrome was deposited using CHA Industries (custom made tool based on the mark-40 model) e-beam evaporator. Conditions are depicted in table A.3.

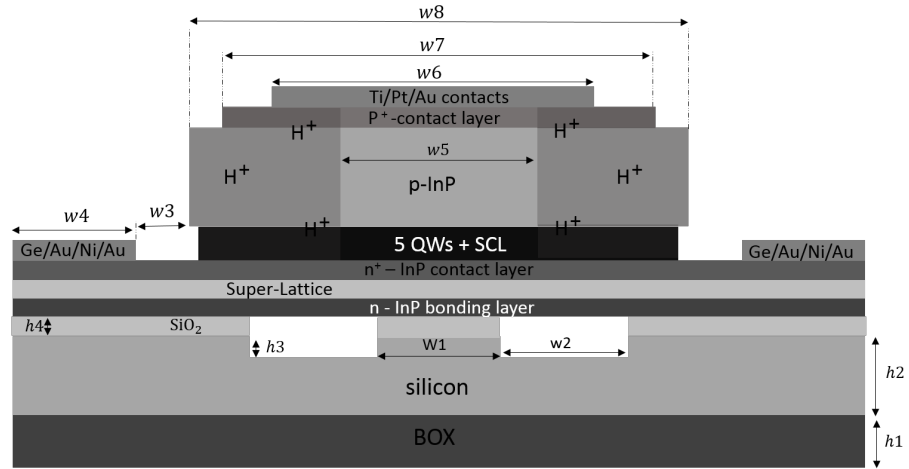


Figure A.1: Spacer laser device Schematics

Description	Notation	Dimension
BOX thickness	h_1	$1\mu m$
Silicon slab thickness	h_2	$0.5\mu m$
Silicon etch depth	h_3	100nm for spacer 30nm; 50nm for other spacers
Spacer thickness	h_4	30nm, 100nm, 150nm, 200nm
Waveguide width	w_1	$2.5\mu m$
Trench width	w_2	$15\mu m$
Mesa-metal separation	w_3	$7.5\mu m$
N-metal stripe width	w_4	$75\mu m$
Ion implant window	w_5	$5\mu m$
P-metal stripe width	w_6	$40\mu m$
P-contact layer width	w_7	$45\mu m$
Mesa width	w_8	$60\mu m$

Table A.1: Device dimensions. Notations is based on Figure A.1

Layer	Thickness	Comment
n-InP buffer	500nm	stripped in substrate removal step
p-In _{0.53} Ga _{0.47} As ($p > 10^{19} \text{cm}^{-3}$) contact layer	200nm	
p-InP cladding (p graded $10^{18} - 5 \cdot 10^{17} \text{cm}^{-3}$)	$1.5 \mu\text{m}$	
SCL InGaAsP (1.15Q)	40nm	Confinement layer
SCL InGaAsP (1.25Q)	40nm	
QW 1% compressive strain InGaAsP	7nm	5 QWs, and 4 barriers in between each well
QW barrier 3% tensile strain InGaAsP	10nm	
SCL InGaAsP (1.25Q)	40nm	Confinement layer
SCL InGaAsP (1.15Q)	40nm	
n-InP contact layer ($n = 10^{18} \text{cm}^{-3}$)	110nm	
Super Lattice, n-In _{0.85} Ga _{0.15} As _{0.327} P _{0.673}	7.5nm	x2; $n = 10^{18} \text{cm}^{-3}$
Super Lattice, n-InP	7.5nm	
n-InP bonding layer	10nm	$n = 10^{18} \text{cm}^{-3}$

Table A.2: III-V wafer structure

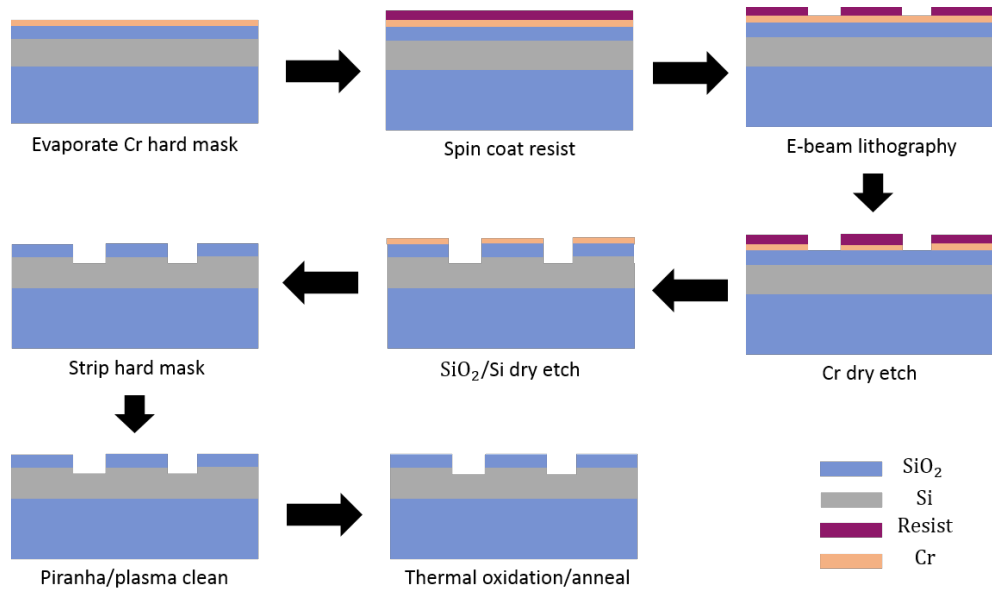


Figure A.2: Flow diagram of the silicon processing steps

Parameter	Value
Cr thickness	20nm
Temperature	Uncontrolled
Rate	0.5 A/s
Base pressure	7E-6 Torr

Table A.3: Conditions of Cr evaporation

Step	Conditions
Spin Coat ZEP 520A	5000 RPM for 90 seconds
Soft bake	180 C for 10 minutes
E-beam lithography (Leica EBPG 5000+)	Grating and 1 μ m of waveguide trench close to the sidewall (sleeve) at 340 μ C/cm ² with 300 pA current and 2.5nm beam step size and resolution. The rest using 10 nA beam with 270 μ C/cm ² , and 10 nm beam step size and resolution
Resist developement	1 minute dip of ZED-50N developer followed by 30 sec IPA-MIBK solution

Table A.4: Steps for E-Beam lithography

A.1.2 Lithography

E-Beam lithography was performed to pattern the hard Cr mask. All features (gratings, waveguides, markers, etc...) were patterned in a single e-beam lithography run. Steps and conditions depicted in table A.4.

A.1.3 Etch

The e-beam resist pattern was transferred to the Cr hard mask using ICP etch. The resist was stripped and the Oxide and Si layers were further etched. Steps and conditions are described in table A.5.

Step	Conditions
Cr etch	using Oxford ICP380 III-V etcher, at 15 C; chamber pressure 60mTorr; 60 sccm of Cl ₂ , 3 sccm of O ₂ ; 1000 W ICP power, 100W RF power
Resist strip	using Oxford ICP380 III-V etcher, at 15 C; chamber pressure 10mTorr; 100 sccm of O ₂ ; 3000 W ICP power, 20W RF power
Silicon and SiO ₂ etch	using Oxford ICP380 III-V etcher, at 15 C; chamber pressure 7mTorr; 35 sccm of C ₄ F ₈ , 5 sccm of O ₂ ; 2100 W ICP power, 200W RF power
Cr strip (wet etch)	Submerge in CR-7S chrome etch until fully removed

Table A.5: ICP etch steps and conditions

A.1.4 Oxidation

Following etch and clean steps the device was annealed and oxidized to reduce sidewall roughness and minimize optical losses [103, 48]. Preparation steps and furnace conditions are described in table A.6.

A.2 Wafer bonding

Direct low-temperature wafer bonding [19, 76] is used to bond the InP to Si/SiO₂. The Si and SiO₂ were patterned with an array of 10 μ m x 10 μ m out-gassing channel (50 μ m pitch) to allow hydrogen to outgas and avoid formation of interface bubbles [56]. Further details on the exact bonding recipe and considerations can be found in [106].

Steps	Conditions
Surface wet chemical clean	80 C Sulfuric acid / Hydrogen peroxide mix, 3:1, for 10 minutes;
Surface plasma clean	using Oxford ICP380 III-V etcher, at 15 C; chamber pressure 10mTorr; 100 sccm of O ₂ ; 3000 W ICP power, 20W RF power
Furnace oxidation	Ramp from 700C to 1000C in 60 minutes with 100 sccm O ₂ flow, and 3000 sccm N ₂ flow. 15 minutes at 1000C with 3000 sccm O ₂ , followed by 30 minutes of 3000 sccm N ₂ anneal

Table A.6: Oxidation/Anneal steps and conditions

A.2.1 Surface treatment

Both Si and InP surfaces were Solvent cleaned and activated/cleaned using oxygen plasma treatment. The same surface plasma clean recipe that is described in table A.6 was used.

A.2.2 Bonding

Chip were aligned manually by holding the InP back-side with vacuum tweezers and pressing it against the Si chip. The chips were partially bonded at this stage using Van der Waals forces, and were then covalently bonded at elevated temperature and pressure using Suss SB6 wafer bonder. Condition are described in table A.7.

A.2.3 Substrate removal

The InP handle was removed using chemical etch. The III-V sidewalls were protected using a thick wax layer to prevent under cutting. Two layers of protective resist were spun to prevent acid from flowing in the waveguide trenches and undercutting the bonding layer. Exact steps and conditions are depicted in table A.8.

Step	Conditions
Set pressure	205 mBar tool pressure (force) for one hour. Chamber air pressure lower than $3 \cdot 10^{-3}$ mBar (typically $\sim 10^{-4}$)
Low temperature	ramp to 150 C and hold for one hour
High temperature	Ramp to 285 C and hold for 5 hours

Table A.7: Steps and conditions for wafer bonding

Step	Conditions
Spin resist protection coating	spin PMMA A4 at 2000 RPM followed by 5 minutes hotplate soft bake at 180C. Spin PMMA A11 at 2000 RPM followed by 10 minutes hotplate soft bake at 180 C
Wax protection layer	Melt wax on the entire chip at ~ 150 C
Wax removal from III-V	Scrape wax and resist from bonded III-V using razor blade
Chemical etch	Etch using HCL/DI water mix (3:1) at room temperature until bubbles stop (typically 45 minutes)

Table A.8: Substrate removal steps and conditions

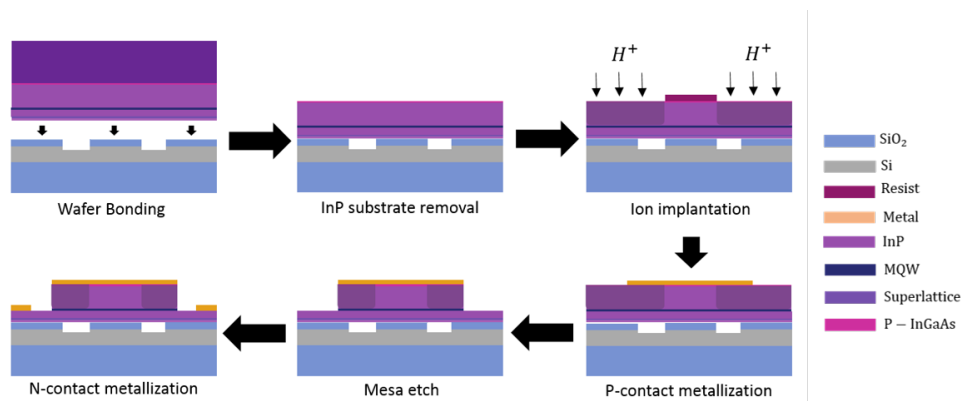


Figure A.3: Flow diagram of the III-V processing steps

A.3 III-V processing

After the bonding process, ion implantation, mesa formation, and metalization are performed. The mesa and contact dimensions are not critical, and therefore wet chemical etch is used. A flow diagram describing the III-V processing is shown in Figure A.3.

A.3.1 Ion implantation

The mesa and metal contacts are tens of microns wide, while the optical mode is only a few microns wide. To make a more efficient electrical pump process, where the QWs are pumped only at the vicinity of the optical mode, ion implantation is used to define narrow current path. We have patterned ion-implant photo-mask and sent the chips to be ion implanted at Kroko Inc. The steps and conditions used are described in table A.9.

A.3.2 P-metal deposition

For ohmic contacts of low resistance a highly-doped layer of InGaAs was used for the p-metal. $In_{0.53}Ga_{0.47}As$ has the smallest bandgap among the InP lattice-matched materials [135]. This yields a small energy barrier for carriers and allows for efficient field-thermionic emission of carriers from the metal to the semiconductor [83]. A

Step	Conditions
Spin photo-resist	Spin AZ5214 positive photoresist at 2000 RPM. Bake 90 seconds at 95 C
Exposure	expose 9 seconds using 25 mW/cm ² @g-line; hard contact mode
Develop	30 seconds in CD-26 developer puddle
Hard bake	115 C for 90 seconds on hotplate
Ion implant	Implant of Protons (H ⁺) with a dose of 5·10 ¹⁴ cm ⁻² and 170KeV energy at 7 degrees tilt with $\frac{20\mu A}{97.5cm^2}$ ion beam
Strip resist	Solvent clean with hot (80 C) Remover PG, and O2 plasma (same conditions as plasma clean in table A.5)

Table A.9: Parameters used for ion implantation

Ti/Pt/Au metal stack is used with low anneal temperature that is compatible with the bonded platform. A temperature higher than 300 C that is often encountered in metal contact recipes would jeopardize the integrity of the bonding interface. The recipe depicted in table A.10 have been tested using a circular test pattern setup [61] and yielded contact resistance $5 \cdot 10^{-5} [\Omega cm^2]$ with anneals temperature of 200 C. This is comparable with values reported in literature for similar contacts [60].

A.3.3 Mesa formation

The mesa formation is done using a three-steps etch that utilizes two different photo-masks. After the first etch process, in which the p-contact layer is etched, a larger photo-mask is spun and patterned for the mesa. The second mask is of bigger area than the first one to make sure the sidewalls of the InGaAs layer are protected, such that it is not attacked by the QW etch solution. Photo-lithography is used despite the aggressive acids used in the etch that erode the mask. The etch time is short enough that mask erosion is tolerable. Table A.12 describes the mesa formation wet

Step	Conditions
Pattern lift-off mask	See table A.11
Descum	Using Branson barrel asher, 1 minute at 150 W in 0.6 Torr O ₂ plasma
De-oxidize	15 seconds in HCl:DI water (1:10)
Deposit metals	Using CHA e-beam evaporator deposit 20nm of Ti at 1 A/sec , 50nm of Pt at 1 A/S and 150nm of Au at 2 A/S. Pressure lower than 8E-7.
Lift-off	Overnight in Acetone puddle
Anneal	using Jiplec RTA, anneal 30seconds at 200 C (N and P metals annealed together after N-metal deposition)

Table A.10: Steps and conditions used to deposit P metal stack

Step	Conditions
Spin Coat	spin AZ5214 @ 3000 RPM for 45 seconds
Soft bake	hotplate 50 sec at 110 C
expose	expose 2 seconds using 25 mW/cm ² @g-line; hard contact mode
Image reversal bake	hot plate 2 minutes at 107 C
Flood expose	16 seconds using 25 mW/cm ² @g-line
Develop	30 seconds dip in CD-26 developer puddle

Table A.11: Steps and conditions for lift-off photo-lithography

Step	Conditions
Pattern mask for InGaAs layer etch	Same PL process as in table A.9
InGaAs etch	7 seconds etch in room-temperature Sulfuric acid/Hydrogen peroxide/DI water (1:1:10)
Strip photo-mask	Acetone and hot (80 C) remover PG clean
Pattern mask for InP mesa	Same PL process as in table A.9
InP mesa etch	22 seconds in HCl(bottle strength = 37%)
QW etch	45 seconds etch in room-temperature Sulfuric acid/Hydrogen peroxide/DI water (1:1:10)
Strip resist	Acetone and hot (80 C) remover PG clean

Table A.12: steps and conditions used to form the mesa

etch process. The resulting mesa profile is shown in the SEM images of Figure A.4. The InGaAs contact layer has rough sidewall due to resist erosion in the Piranha etch process. However, only its sidewalls, which are of no significance, are affected.

A.3.4 N-Metal deposition

For the N-metal we are using alloyed Ge/Ni/Au contacts [68]. The metal structure and deposition condition are described in table A.13. The metal contacts fabricated

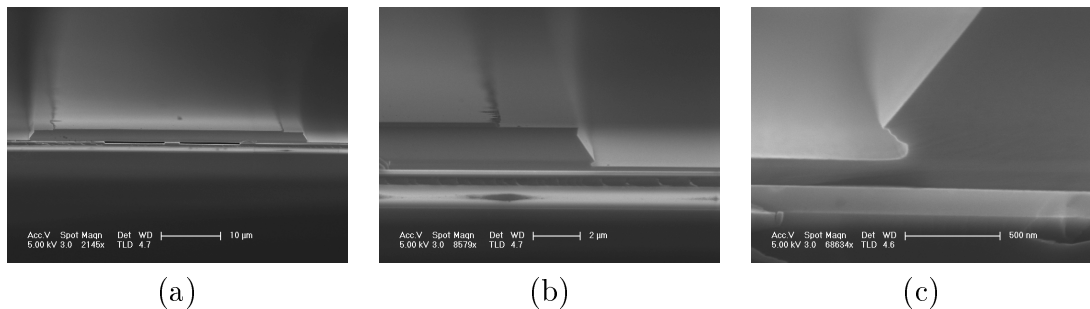


Figure A.4: SEM images of mesa formed using the two mask process (a) Entire mesa and Si waveguide (b) Sidewalls of mesa and InGaAs layers (c) Etch and under-cut of the QW layer

Step	Conditions
Pattern lift-off mask	See table A.11
Descum	Using Branson barrel asher, 1 minute at 150 W in 0.6 Torr O ₂ plasma
Deoxidize	5 seconds in BHF water (1:10)
Deposit metals	Using CHA e-beam evaporator deposit 30nm of Ge at 0.5 A/sec , 50nm of Au at 0.5 A/S, 12nm of Ni at 0.5 A/S and 225nm of Au at 1 A/S. Pressure lower than 8E-7.
Lift-off	Overnight in Acetone puddle
Anneal	using Jiplec RTA, anneal 30seconds at 200 C

Table A.13: Steps and conditions used for N-metal deposition

using this low-anneal temperature recipe were tested using the setup described in [82]. Contact resistance of $5 \cdot 10^{-5} [\Omega\text{cm}^2]$ was measured, comparable to industry standard for similar technique and materials.

A.3.5 Cleaving

The devices were cleaved using a diamond scribe, and were broken into bars manually. The diamond tip only scribed $\sim 1\text{-}2\text{mm}$ of the bar, and the cleave propagated along the crystal axis. This yielded devices with optically smooth facets that need not be polished.

Appendix B

Characterization setups

One of the major challenges in this work is the characterization of the lasers. The lasers were fabricated at Caltech, and were not packaged in any way. The lasers in each bar were probed and measured one by one manually without any automated aligning process. Furthermore, the task at hand was fundamentally challenging for several reasons:

1. Measurement of phase - The phase and frequency of the lasers had to be measured to characterize both the noise and the frequency response. Measuring phase required the usage of an MZI that had to be stabilized and locked to the laser. Locking the MZI to a free running, unpackaged laser was challenging.
2. Noise measurements - The lasers were designed and demonstrated to be extremely clean. Sub-KHz linewidth was demonstrated. Measuring noise in devices with very little noise signal is a major challenge. Special attention to the minimization of excess instrumentation noise was required. On top of that the laser's output power was low, making it even harder to measure, and forced us to fanatically worry about minimizing optical losses in the measurement setup.
3. Modulation response - The lasers were designed for high coherence and not for high speed modulation. The devices are big, about 1 mm of length, and no special attention was given to its capacitance, or to impedance matching in the laser design. Despite those facts high speed (few GHz) modulation experiments were performed.

In this chapter we will divide the lasers measurement setups into different tasks. In each task a full description of the methodology, experimental setup, equipment and calibration processes are discussed.

B.1 Mounting and probing the lasers

Each laser bar was roughly 1mm wide and 5mm long. All the measurements in this work used the same probe station and thermal management techniques described in this chapter.

B.1.1 Mounting of laser bars

Two techniques were used to mount laser bars to the probe station: mounting on a C-mount using indium soldier, or on a copper block using thermal paste. Characterization of spacer 30nm and 150nm was done using C-mounts, and of spacer 100nm using thermal paste. The lasers were probed using Cascade Microtech's ACP40-GSG-100 RF probe tip and MPHM micro-positioner. All measurements in this work were taken with this probe setup. The whole setup was enclosed in a fiber-glass box and sat on a Sorbothane anti-vibration pad to reduce fluctuations due to the environment.

B.1.2 Thermal management

In all mounting options the laser or the C-mounts were in thermal contact with a large copper block using thermal paste. Only the bottom side of the laser bar (the silicon wafer) was in thermal contact with the temperature-controlled stage. The copper block was in thermal contact with a Peltier cooler that was connected to a Newport 350 thermoelectric cooler (TEC). All measurements in this work were performed at 20°C unless otherwise stated.

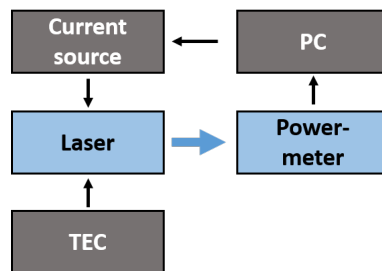


Figure B.1: Schematics of L-I curve characterization setup

B.2 L-I curves

L-I curves were measured in both CW and pulsed operation. In both cases a free-space integrating sphere ILX Lightwave OMM 6810B power meter was positioned at the output facet of the laser under test. It was verified that the alignment is robust to small spatial deviations, such that thermal expansion of the laser under test did not result in measured power loss. A schematic of the measurement setup is shown in Figure B.1.

B.2.1 CW excitation

All experiments were performed using CW excitation, unless otherwise stated. Laser diode current driver Newport 525B was controlled using a personal computer via USB. The computer also sampled the detected power on the power meter using GPIB. Five measurements were averaged to obtain the measured power, and outliers due to communication or transient problems were removed from the averaging. The power reading from the power-meter was assumed to be calibrated, and no post processing was done to the measured value.

B.2.2 Pulsed excitation

Spacer 150nm was also measured in pulsed operation to minimize thermal power roll-offs. We used ILX-Lightwave LDP 3840B pulsed current source, with a 40Ω impedance matching resistor. The power meter was set on slow operation mode and averaged the detected pulses. The measured average power was then divided by the duty-cycle

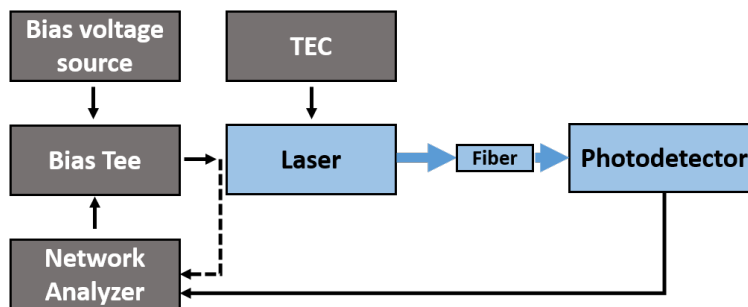


Figure B.2: Schematics of the experimental setup used for intensity modulation response measurements

to obtain an estimate of the average pulse power.

B.3 Intensity modulation response

The lasers were designed for narrow-linewidth operation and not for high speed. However, they were found to operate reasonably well under modulation of up to a few GHz. This section describes the experimental setup used to take intensity modulation response, as well the calibration processes used to isolate the response of the laser from that of auxiliary equipment.

B.3.1 Setup and equipment

A Schematics of the experimental setup appears in Figure B.2. A bias Tee (ZFBT-6GW, 0.1-6000MHz) was used to separate DC and high-frequencies and to allow for biasing of the laser above threshold. The laser was biased using E3611A DC voltage power supply. The input current to the laser was monitored using the built in current monitor. The RF+DC output of the bias-tee could be routed to either the laser probe or back to the network analyzer for calibration (see next section). Two different network analyzers (NA) were used interchangeably:

1. HP 8722C NA - for the high frequency components we used this 50MHz-40GHz analyzer. Each trace was averaged four times for consistent low-noise measurements.

2. Agilent 4395A NA - for the low frequency components we used this 10Hz to 500MHz analyzer.

The output of the laser was aligned to a lensed fiber (tapered SM fiber, AR coated TSMJ-X-1550-9/125-0.25-7-2.5-14-2-AR by OZ Optics), which was mounted on a five degrees-of-freedom (DOF) stage. The fiber was aligned with the aid of a power meter. The output SM fiber was connected to a photodetector (New focus 1544B, DC-12GHz, -600V/W peak conversion factor). The RF output signal of the PD connected to the return port in the NA. The NA measurement was captured using a computer through GPIB.

B.3.2 Calibration and measurement procedures

B.3.2.1 Photodetector response

The PD response, both magnitude and phase, was measured and subtracted from the laser response. The calibration of the PD response was performed by using a stable commercial laser, an amplitude modulator, and a separate broadband PD. The input of the PD was modulated using the NA and the response was measured. The same experiment was repeated with a broadband PD (HP 11982A, DC-15GHz). The HP 11982A PD was assumed (according to spec) to have very flat response, and so the NF 1544B was calibrated using it. The resulting response curve is shown in Figure B.3.

B.3.2.2 Driving circuitry response

The response of the driving circuitry (coax cables, bias tee, probe tip) was measured and subtracted from the measurement of the laser response. The following procedure was used:

1. The output of the bias tee was connected to return port of the NA (the dotted line in Figure B.2), and a modulation response curve was taken. The exact same cables that drive the laser were used.

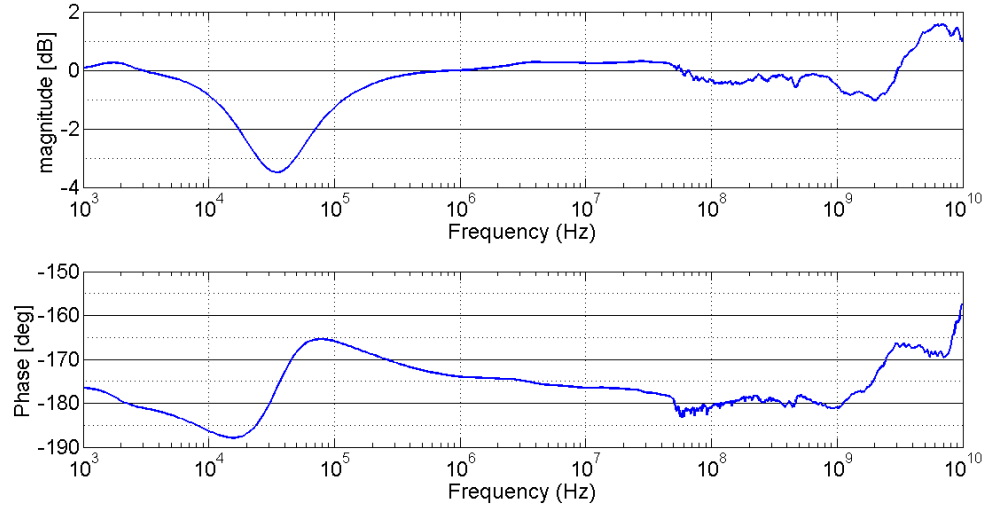


Figure B.3: Measured response of NF1544B photodetector. The PD response was subtracted from measured laser response

2. The response was registered into the internal memory of the network analyzers and was used as a calibration trace.
3. The output of the bias tee was disconnected from the NA and connected to the laser's probe tip. The circuit was then closed as in Figure B.2 and a measurement was taken (calibration trace used by the tool).

B.3.2.3 Calculating the small-signal current

To estimate the input current to the laser the following calculation was used:

$$I_{laser} = \frac{2}{\sqrt{10} (R_{laser} [\Omega] + 50\Omega)} 10^{\frac{P_{dBm}}{20}} \quad (\text{B.1})$$

where R_{laser} is the laser's small-signal resistance calculated from the slope of the I-V curve at the working current, and P_{dBm} is the set-point output power of the NA in Decibel mW, which gives the power falling on a 50Ω load.

B.3.2.4 Delay compensation

To accurately measure the phase of the transfer function compensation of the delay had to be performed. There are several meters of optical fiber and electrical wires and without delay compensations many 2π cycles of phase will accumulate at the high frequencies. As a first step, a guess of the delay length was used as an input to the NA delay compensation parameter. Fine tuning was done manually until the corrected phase response curve looked as expected (i.e., corresponding to a second order low-pass-filter). It is worth noting that this procedure leaves some room for interpretation by the user, and that different users might end up with slightly different response phases. However, experienced users will still get qualitatively similar results.

B.4 Frequency modulation response

The frequency response measurement is based on frequency-domain network analysis approach[126]. A schematics of the setup used is shown in Figure B.4. An MZI is used as a frequency discriminator that convert frequency modulation to intensity. One of the arms of the MZI is mounted on a fiber stretcher piezo. The piezo is used to lock the differential phase between the two MZI arms such that the MZI is locked in quadrature [102]. The two output of the MZI are connected to a fast balanced photodetector. The balancing is important in order to make sure that intensity modulation is not measured, and only the frequency response is detected. A network analyzer is used to modulate the laser and to register the balanced PD output. Conversion of the resulting response to units of $[\frac{GHz}{mA}]$ is done through post processing.

B.4.1 Setup and equipment

The driving circuitry (network analyzer, voltage source, bias tee, TEC) is similar to the one described in the intensity modulation setup of section B.3.1. The optical output of the laser is collected through a lensed fiber (tapered SM fiber, AR coated TSMJ-X-1550-9/125-0.25-7-2.5-14-2-AR by OZ Optics), which is mounted on a five

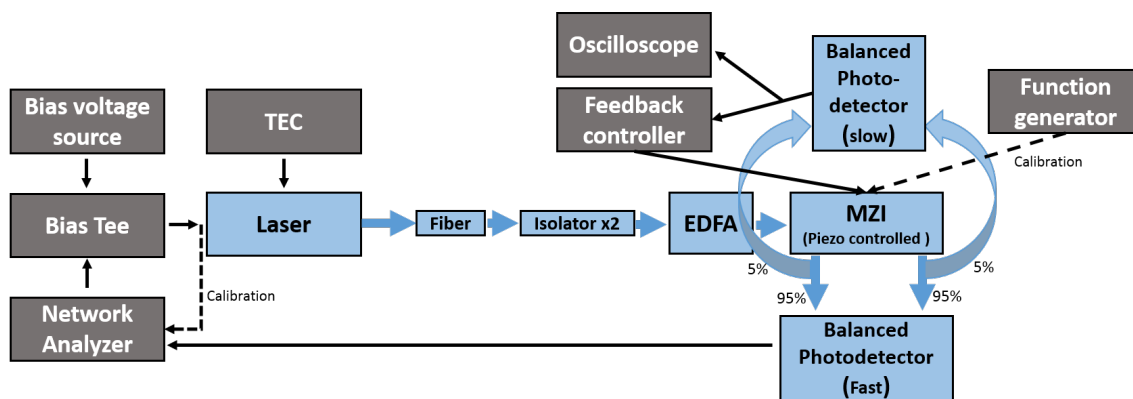


Figure B.4: Schematics of the experimental setup used for frequency modulation response measurements

DOF stage. The output is then amplified using an EDFA and launched into the input port of the piezo-driven MZI. The fiber in one of the MZI arms is mounted on a piezo fiber stretcher (Evanscent Optics 915B). The two outputs of the MZI (Q and I) are connected to a pair of couplers that couple 5% of the light to a (slow) balanced PD (New-Focus 1817 80 MHz photoreciever), and 95% to a fast balanced PD (23 GHz Optilab BPR 20M). Care was given to make sure that input fibers to the balanced PDs are length-matched to within a mm, to allow for maximal intensity modulation rejection, even at high frequencies. The slow balanced PD is connected to an electronic feedback PCB. A schematic of the feedback electronics is shown in Figure B.5. It was constructed such that it provides variable gain, and variable bandwidth through potentiometer and switchable capacitors. It also biases the MZI piezo driver at 2.5 Volts (the driver operate at 0-5 Volts). Another potentiometer that is connected between $\pm 5V$ allows for compensation of offset voltage at the input (ideally the slow balanced PD should have zero mean signal, but this is not always the case). The output of the feedback electronics PCB is connected to the MZI piezo driver (Evanscent Optics 914) to close the feedback circuit. The fast balanced PD is connected to the return port of the NA.

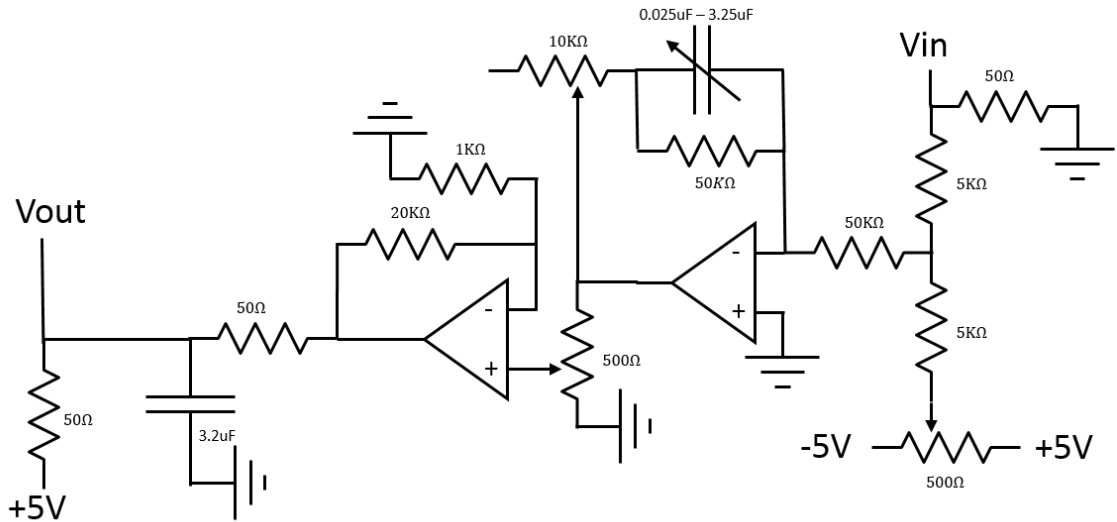


Figure B.5: Schematics of the electronic feedback PCB used to lock the MZI to quadrature

B.4.2 Calibration and measurement procedure

B.4.2.1 Balancing photodetectors

There are two photodetectors in the setup: a fast PD to measure the frequency noise, and a slow PD to lock the MZI in quadrature. The fast PD has to be balanced to eliminate the intensity noise, especially due to the presence of the amplifier, which introduces excess intensity noise. The slow PD has to be balanced to get a zero-mean small-signal feedback signal. It is worth noting that the feedback circuit can be constructed without balancing by comparing the DC output of an unbalanced PD to a reference voltage. However, drift of the output power, mainly due to drift of the optical alignment during the experiment will cause the MZI to drift away from quadrature. For that reason the balanced PD feedback setup was used.

Arbitrary loss in the fiber network yields unbalanced PD reading. To compensate for that the following procedure was used for balancing:

1. Modulate the MZI piezo at 100Hz and monitor the output of the slow balanced PD on the scope.
2. Manually adjust the fiber coupling to the PD until the scope reading has zero

mean.

3. Turn off the slow modulation and bring the system to lock. Adjust the offset potentiometer to make sure the system is locked at zero voltage.
4. Monitor the output power of the two PDs in the fast balanced detector using the power monitor connection.
5. Manually adjust the fiber coupling to the PDs until balanced.

This procedure should yield a balanced detection setup for both the measurement and the feedback.

B.4.2.2 Photodetector response

The photodetector response was measured and used to calibrate the frequency response, as well to calculate the voltage swing of the balanced PD. The response curves of Figure B.6 were obtained using the process described in section B.3.2.1.

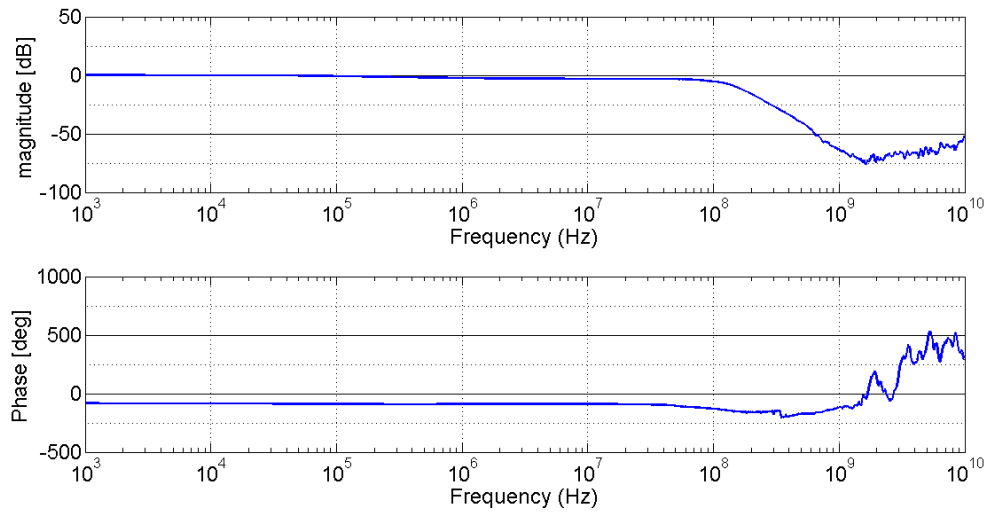
B.4.2.3 Voltage swing

The output of the fast balanced PD oscillates in response to the frequency modulation induced by the network analyzer. If the differential phase between the two MZI arms is $\Delta\phi$ then the output voltage of the PD is:

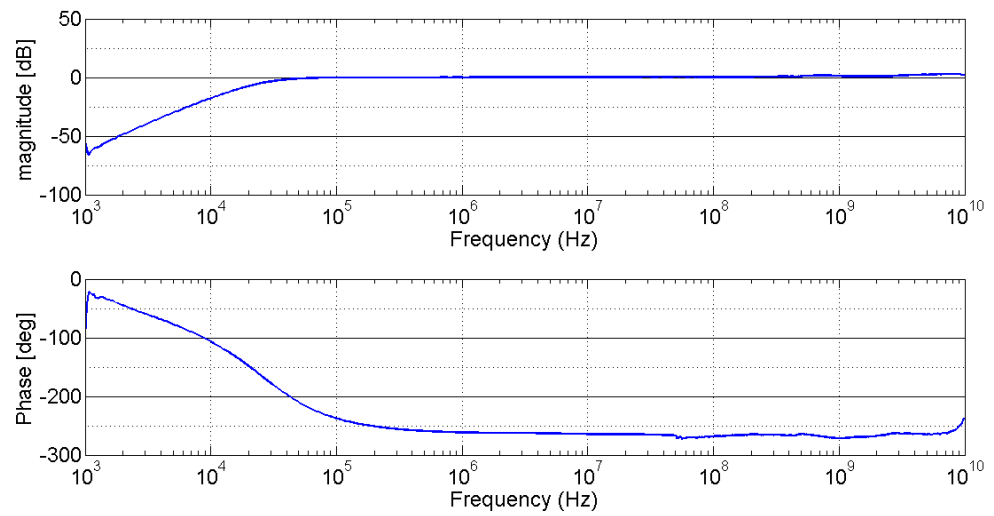
$$V_{PD} = V_q + V_g \sin(\Delta\phi) \quad (\text{B.2})$$

where V_q is some offset voltage (ideally zero in the balanced setup and in lock), and V_g is voltage swing.

For accurate calibration of the measurement, knowledge on V_g is required. This can conceptually be done by perturbing the system slightly and measuring the voltage swing. However, the balanced PD is equipped with a DC-block filter at its output, which alters the low-speed (<100 KHz) response. We therefore go through the following calibration procedure:



(a)



(b)

Figure B.6: Response curves of balanced PDs (a) New Focus 1817 (b) Optilab BPR 20-M

1. Replace the laser under test with a fast ($\sim 5 \cdot 10^{15} \frac{\text{Hz}}{\text{sec}}$) frequency chirped laser. We used a home-made frequency chirped semiconductor laser [90, 120].
2. Measure the resulting voltage swing on both fast and slow balanced PDs, using the two channels of the scope (make sure 50Ω load, as in the NA).
3. Register the ratio between the responses of the two PDs voltage swing:

$$\gamma = \frac{V_{fast}}{V_{slow}} \quad (\text{B.3})$$

4. Reconnect the laser under test to the setup.
5. Use a function generator, connected to the piezo driver, to modulate the MZI at 100Hz (make sure full voltage swings are achieved, and that PD is not saturated).
6. Measure voltage swing V_{pp} of slow balanced PD at 100 Hz modulation using the scope.
7. Obtain a conversion coefficient between the voltage swing read using the fast balanced PD at $\sim 2\text{MHz}$ and the slow balanced PD at 100 Hz.

$$V_g = \gamma \frac{V_{pp}}{2} \cdot R \quad (\text{B.4})$$

where R is the ratio between the slow PD response at $\sim 2\text{MHz}$ and 100 Hz known from the response curve of the PD (Figure B.6a).

B.4.2.4 Delay compensation

The same procedure used in section B.3.2.4 is used .

B.4.2.5 Measurement procedure

The following procedure is used to obtain a frequency response curve:

1. Turn on TEC and bias the laser using the voltage source.

2. Balanced the PDs as in section B.4.2.1.
3. Repeat calibration steps of section B.4.2.3 to obtain V_g .
4. Calibrate for the response of the driving circuitry as in B.3.2.2.
5. Calibrate for the delay as in B.3.2.4.
6. Take a calibrated measurement using the network analyzer. Make sure modulation current is small enough to maintain linearity and not to throw the system off lock.

B.4.2.6 Calculating the frequency response from the measurement

When the laser's pump current changes by a small amount $\Delta I(t)$ the frequency of the laser will change according to:

$$f \approx f_0 + \frac{\partial f}{\partial I} \Delta I(t) \equiv f_0 + G_f \Delta I(t) \quad (\text{B.5})$$

The output of the fast balanced PD which is connected to the MZI is given by:

$$V_{BPD} = V_g \sin \left(2\pi f_0 \tau + 2\pi \int_{t-\tau}^t G_f \Delta I(t') dt' \right) \quad (\text{B.6})$$

where V_g is the voltage swing of the PD determined by the input power and its internal transimpedance gain, τ is the MZI differential delay, and we have neglected noise. When the MZI is locked at quadrature:

$$f_0 \tau = m \quad (\text{B.7})$$

for some integer m . For small signal sinusoidal modulation, as in the one imposed by the NA:

$$\Delta I(t) = \Delta I \cdot \cos(2\pi \nu t + \phi_0) \quad (\text{B.8})$$

the laser's frequency is:

$$f \approx f_0 + G_f(\nu)\Delta I(t)\cos(2\pi\nu t + \phi(\nu) + \phi_0) \quad (\text{B.9})$$

If the signal is small enough such that:

$$V_{BPD} = V_g \sin \left(2\pi \int_{t-\tau}^t G_f \Delta I(t') dt' \right) \approx 2\pi V_g \int_{t-\tau}^t G_f \Delta I(t') dt' \quad (\text{B.10})$$

the resulting PD output is:

$$V_{PD} = V_g \Delta I \cdot \frac{\sin(\pi\nu\tau)}{\pi\tau} G_f(\nu) \cos(2\pi\nu t - \pi\nu\tau + \phi(\nu)) \quad (\text{B.11})$$

Equation B.11 shows that the detected signal contains both the desired contributions from the lasers response ($G_f(\nu)$, $\phi(\nu)$), but also contributions from the MZI finite FSR and its differential delay. These contributions will have to be deconvolved from the measurement to obtain calibrated result.

After going through the calibration process of subtracting the response of the driving circuitry and the PD response, we are left with system response in power dBm. The NA return port is terminated with a 50ohm resistor, such that the measured power for the sinusoidal modulation is given by $\frac{1}{2} \frac{V_{PD}^2}{50}$. The input current to the laser is related to the NA output power as described in Equation B.1. We therefore use the following transformation to convert to the desired units:

$$G(\nu) = \frac{\pi\nu(R_{laser} + 50)}{V_g |\sin(\pi\nu\tau)|} \cdot 10^{\frac{P_{cal}(\nu)}{20}} \left[\frac{\text{Hz}}{\text{A}} \right] \quad (\text{B.12})$$

$$\phi(\nu) = \phi_{cal}(\nu) + \pi\nu\tau \quad (\text{B.13})$$

Where P_{cal} is the already calibrated trace in power dBm, and ϕ_{cal} is the calibrated phase after delay compensation.

B.5 Frequency noise spectrum measurement

The frequency noise measurement setup described in this section enabled us to measure sub-KHz equivalent noise at frequencies of > 1 GHz. Many of the features of the measurement setup are similar to that of the frequency modulation response measurement setup described in section B.4. In both setups the measured signal is the laser's frequency. This required the use of an MZI as a frequency discriminator. In both setups an electronic feedback was used to lock the MZI in quadrature for the duration of the measurement. However, the noise measurement experiments possesses some unique challenges. The frequency noise level of these lasers is very low (sub-KHz), especially at the high frequencies where the noise reaches, or get close to the quantum noise floor. The transfer function of the MZI used as frequency discriminator has the form:

$$H_{MZI} = \tau^2 \frac{\sin^2(\pi\nu\tau)}{(\pi\nu\tau)^2} \quad (\text{B.14})$$

we can identify two regimes of the sinc function response:

1. The “flat” response - for frequencies below the FSR of the MZI the response is flat to a very good degree. The MZI at this regime has a gain of τ^2 .
2. The decaying oscillation - frequencies above the FSR will decay and oscillate with a period that is related to the FSR. The peaks of the oscillation are decaying at a rate of $\frac{1}{\nu^2}$.

This response sets a very fundamental limit on our ability to measure high frequencies with high gain due to the proportionality:

$$\text{gain} \sim \frac{1}{(\Delta\nu)^2} \quad (\text{B.15})$$

Increasing the bandwidth $\Delta\nu$ results in a reduction of available gain for the measurement. Notice that even if one works with high-gain (long) interferometer and wishes to extrapolate the laser frequency noise from the oscillating sinc function peaks at frequencies above its FSR, the response drops as $\frac{1}{\nu^2}$ at that regime, bringing the

gain down again. The low MZI gain at high frequencies, together with the relatively low power of our lasers, and the unavoidable noise from the measurement setup's instruments make it a challenging task.

B.5.1 Setup and equipment

The setup for frequency noise spectrum measurement is shown in Figure B.7. An ultra-low-noise current source (ILX lighwave LDX-3620) is used to bias the laser. A common mode filter (LNF-320) is connected to its output to reduce RF noise pickup. The optical output of the laser is collected through a lensed fiber (tapered SM fiber, AR coated TSMJ-X-1550-9/125-0.25-7-2.5-14-2-AR by OZ Optics), which is mounted on a five DOF stage. The output is amplified using an EDFA (to bring the signal above the detector noise floor) and launched into the input port of the piezo-driven MZI. The fiber in one of the MZI arms is mounted on piezo fiber stretcher (Evanescent Optics 915B) . The two outputs of the MZI (Q and I) are connected to a pair of couplers that couple 5% of the light to a (slow) balanced PD (New-Focus 1817 80 MHz photoreciever), and 95% to a fast balanced PD (23 GHz Optilab BPR 20M) . The input fibers to the balanced PDs are length-matched to within a mm, to allow for maximal intensity modulation rejection. The slow balanced PD is connected to an electronic feedback PCB. A schematic of the feedback electronics is shown in Figure B.5, and is described in section B.4.1. The output of the feedback electronics PCB is connected to the MZI piezo driver (Evanescent Optics 914) to close the feedback circuit. The fast balanced PD is connected to an RF spectrum analyzer (calibrated HP 8565E, 30Hz-50GHz) and the resulting spectrum is grabbed using a PC and post processed.

B.5.2 Calibration and measurement procedures

B.5.2.1 Balanced PD and amplifier

PD balancing procedure is done prior to measurement as described in section B.4.2.1. The response of the balanced PD used in the experiment is shown in Figure B.6b. The

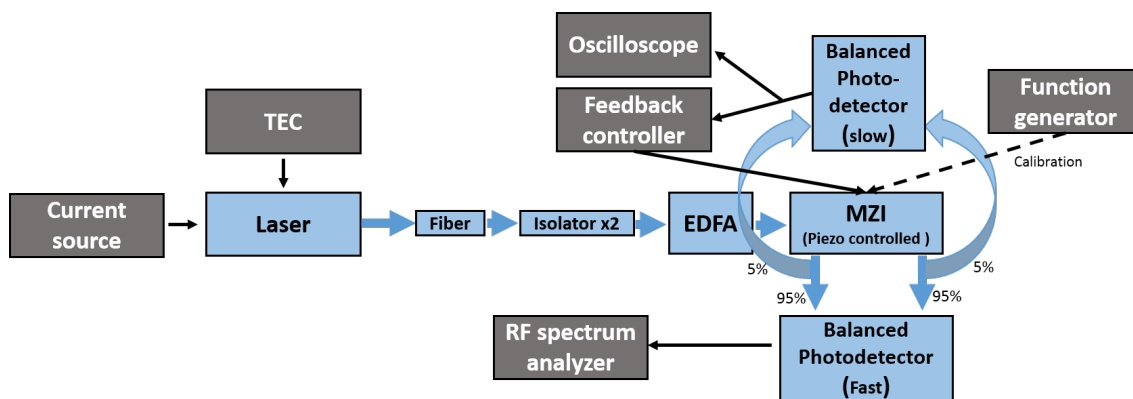


Figure B.7: Schematics of the experimental setup used for frequency noise spectrum measurements

dark noise of the PD set the ultimate noise signal that can be measured, and is shown in Figure B.8 (green curve). Due to the low power of the laser at test the desired noise signal is well below the dark noise, and therefore cannot be measured without amplification. Amplification is performed using an EDFA, which demonstrated superior phase noise performance over BOA. However, this limits our measurement setup to the C-band. Intensity noise of the laser+EDFA system is eliminated by the use of balanced PD. Figure B.8 shows intensity noise spectrums of the balanced PD for different input power. This was performed using the same laser seed power with changing EDFA gain. Figure B.9 shows the measured intensity noise vs the calculated dark+shot noise. The shot noise was calculated using the input power and assuming the internal trans-impedance (TI) amplifier of the balanced PD has the same shape as the dark noise curve. The comparison of the calculated noise floor vs the measured intensity noise (Figure B.9) shows that at high frequencies ($>100\text{MHz}$) the measurement is shot-noise limited. This verifies that the system is balanced, since otherwise the noise would have been higher due to the amplification (EDFA has noise-figure of at least 3dB). This also shows how crucial balancing is in this measurement. At low frequencies the high input power has a toll, and the TI amplifier add excess noise. However, the frequency noise at low frequencies is high enough, and easy to measure even with the excess TI noise. We therefore choose to work with high input powers of 1 mW per detector, for which the PD is not saturated yet, and is shot noise limited

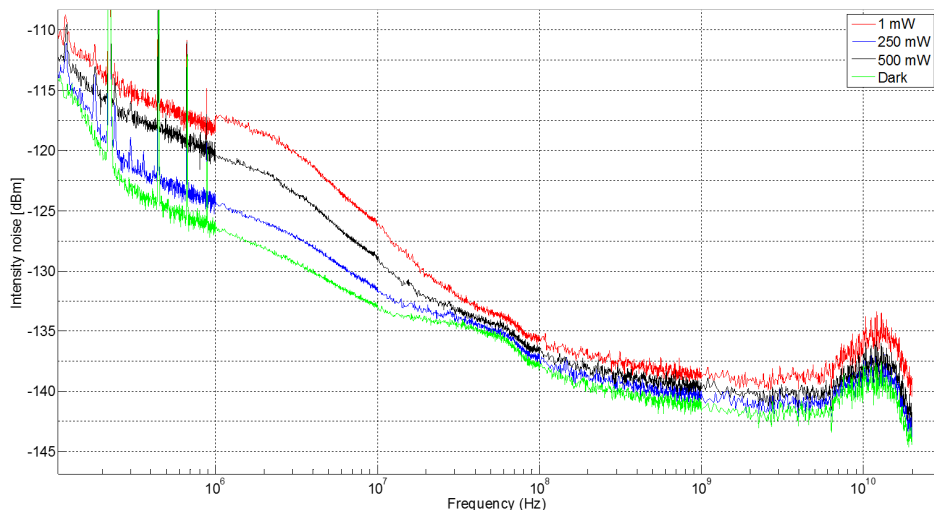


Figure B.8: Intensity noise measured for different input powers by the balanced photodetector (Optilab BPM-20)

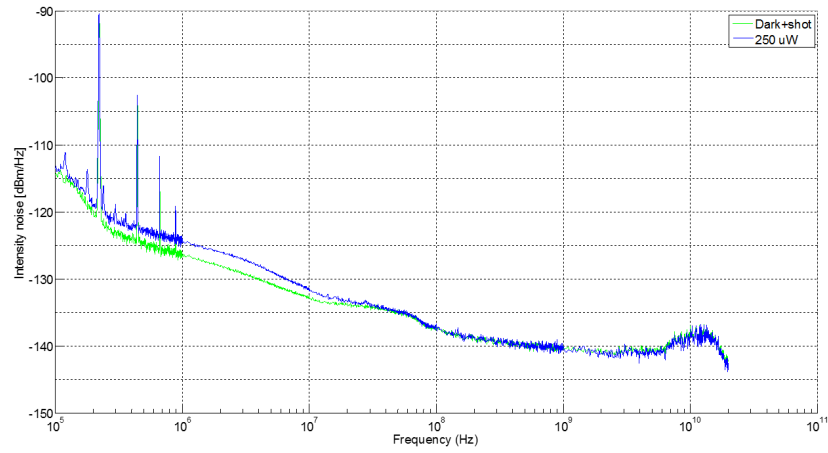
at the high frequencies.

The full output voltage swing of the PD is required to calculate voltage/frequency ratio to calibrate the noise measurement. This is done as described in section B.4.2.3.

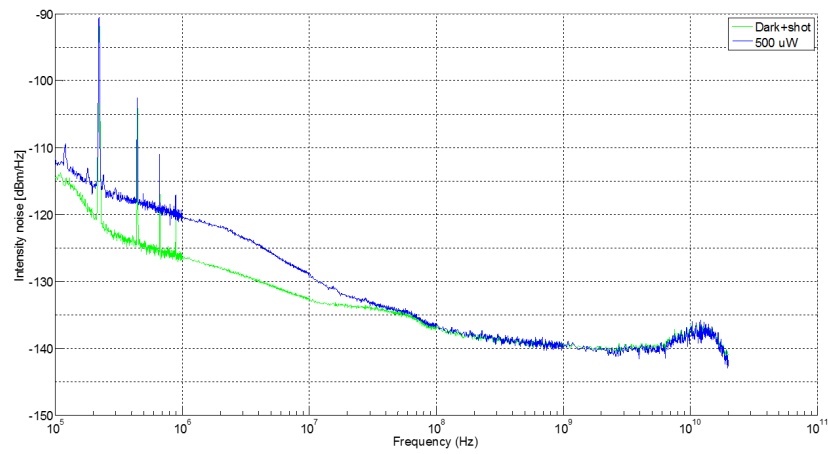
B.5.2.2 Measurement procedure

The following procedure is used to obtain the frequency noise spectrum:

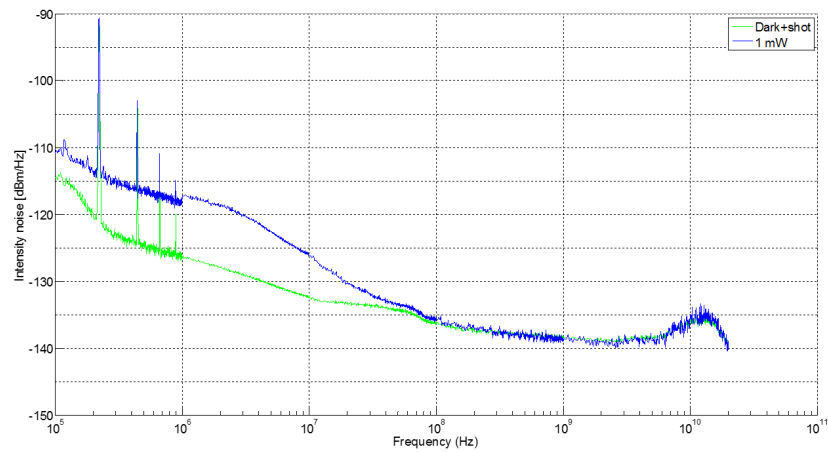
1. Turn on TEC and bias the laser using the voltage source.
2. Balance the PDs as in section B.4.2.1.
3. Adjust EDFA gain to obtain 1mW of power per detector (measured using the the monitor of the balanced PD).
4. Repeat calibration steps of section B.4.2.3 to obtain V_g .
5. Make sure the MZI is locked to quadrature and take a spectrum measurement using RF spectrum analyzer.
6. Post-process the measured spectrum to convert to meaningful units using the procedure in section B.5.2.3.



(a)



(b)



(c)

Figure B.9: Intensity noise vs calculated dark+shot noise for different input power to the balanced PD (a) 0.25mW per detector (b) 0.5mW (c) 1 mW

B.5.2.3 Calculating the noise spectrum from the measurement

When the MZI is locked in quadrature and the phase noise signal is small (RMS $\ll \pi$), as in our case (since the MZI delay is much shorter than the coherence time), the output of the balanced PD is given by:

$$V_{BPD} = V_g \Delta\phi(t, \tau) \quad (\text{B.16})$$

The resulting spectrum at the RF spectrum (single sided PSD in W/Hz) is related to the spectrum of $\Delta\phi$ by calculating the power that falls on its 50 ohm termination load:

$$W_{BPD} = \frac{V_g^2}{50} W_{\Delta\phi}^{(\text{single-sided})} \quad (\text{B.17})$$

and the PSD of the frequency noise is related to the PSD of $\Delta\phi(t, \tau)$ using [78]:

$$W_{\Delta\phi} = W_{\dot{\phi}} \tau^2 \frac{\sin^2(\pi\nu\tau)}{(\pi\nu\tau)^2} \quad (\text{B.18})$$

The frequency noise can be obtained directly from the PD spectrum at frequencies well below the FSR of the MZI. However, there is information about the frequency noise even at frequency above the FSR, where the response is falling and oscillating. To obtain that information in a readable form we need to deconvolve the sinc function from the measurement. The following procedure is used for that end:

1. Omit all points that are within 5dB of the intensity noise curve. These points are contaminated too much with AM noise and cannot be reliably used.
2. Subtract the intensity noise level from the remaining spectra. This results in a signal \widetilde{W}_{BPD} that contains only phase noise information.
3. Calculate the single sided PSD of the frequency noise using:

$$W_{\dot{\phi}}^{(\text{single-sided})} = \frac{50}{V_g^2} \frac{(\pi\nu)^2}{\sin^2(\pi\nu\tau)} \widetilde{W}_{BPD} \quad (\text{B.19})$$

in units of $(\frac{\text{rad}}{\text{sec}})^2 / \text{Hz}$.

4. One can present the resulting PSD as the equivalent white noise linewidth by dividing by the resulting $W_{\dot{\phi}}$ by 4π (see Equation 5.14, and recall that this is a single-sided PSD).